ASDEX PAPERS AT THE 13TH EUROPEAN CONFERENCE ON CONTROLLED FUSION AND PLASMA PHYSICS

(Schliersee, April 14 - 18, 1986)

IPP III/110 May 1986

MAX-PLANCK-INSTITUT FÜR PLASMAPHYSIK

8046 GARCHING BEI MÜNCHEN

MAX-PLANCK-INSTITUT FÜR PLASMAPHYSIK

GARCHING BEI MÜNCHEN

ASDEX PAPERS AT THE 13TH EUROPEAN CONFERENCE ON CONTROLLED FUSION AND PLASMA PHYSICS

(Schliersee, April 14 - 18, 1986)

IPP III/110 May 1986

Die nachstehende Arbeit wurde im Rahmen des Vertrages zwischen dem Max-Planck-Institut für Plasmaphysik und der Europäischen Atomgemeinschaft über die Zusammenarbeit auf dem Gebiete der Plasmaphysik durchgeführt.

ASDEX PAPERS AT THE 13TH EUROPEAN CONFERENCE ON CONTROLLED FUSION AND PLASMA PHYSICS

(Schliersee, April 14 - 18, 1986)

COMBINED APPLICATION OF NEUTRAL INJECTION, LOWER HYBRID, AND ION CYCLOTRON RESONANCE HEATING IN ASDEX AND SYNERGETIC EFFECTS

F. Wagner, F.X. Söldner, K. Steinmetz, G. Becker, H. S. Bosch, H. Brocken, G. Dodel[1], A. Eberhagen, D. Eckhartt, G. Fussmann, O. Gehre, J. Gernhardt, G.v.Gierke, E. Glock, O. Gruber, G. Haas, J. Hofmann, E. Holzhauer[1], A. Izvozchikov[2], G. Janeschitz, F. Karger, M. Keilhacker[3], O. Klüber, M. Kornherr, K. Lackner, M. Lenoci, F. Leuterer, G. Lisitano, F. Mast, H.M. Mayer, K. McCormick, D. Meisel, V. Mertens, E.R. Müller[3], H.Murmann, J.Neuhauser, H. Niedermeyer, J.-M. Noterdaeme, A. Pietrzyk[4], W. Poschenrieder, H. Rapp, H. Riedler, H. Röhr, J. Roth, F. Ryter[5], F. Schneider, C. Setzensack, G. Siller, P. Smeulders[3], E. Speth, K.-H. Steuer, O. Vollmer, F. Wesner, D. Zasche

Max-Planck-Institut für Plasmaphysik
EURATOM Association, D-8046 Garching

ABSTRACT

Confinement properties of ASDEX discharges are studied when NI and ICRH or NI and LH were applied simultaneously. ICRH leads to a larger change in plasma energy content when applied together with NI. At high power the β_p-increases of NI and ICRH are additive corresponding to the total heating power. In the combination of NI and LH the β_p-increase is the same when NI is applied to inductively or non-inductively driven plasma current despite the different current profiles. The effect of sawteeth on central confinement is described in detail in ohmically and beam heated plasmas as is the suppression of sawteeth by LH. The suppression of sawteeth by LH in low q_a beam heated plasmas leads to a substantial increase of β_p. The H-mode can be realized with NI under current drive conditions. ICRH can cause the H-transition in combination with NI. The H-mode, however, can also be realized with ICRH alone.

INTRODUCTION

ASDEX is equipped with neutral injection (NI), ion cyclotron resonance (ICRH) and lower hybrid (LH) heating. The operational parameters of the different heating systems are specified in Table 1. In this paper we present and discuss observations which were made when the different heating methods were applied simultaneously. Because of their importance for the continuation of the fusion programme and their appeal to plasma physicists, we will concentrate on confinement aspects.

TABLE 1

HEATING METHOD	OPERATIONAL MODE	POWER MW	PULSE LENGTH s	TECHNICAL SPECIFICATION
NI	D^o	4.2	0.4	45 kV
	H^o	3.5	0.4	40 kV
ICRH	$2\Omega_{CH}$	2.6	1.5	67 MHz
	D(H)	2.3	0.5	33.5 MHz
LH	LHCD	1	1.5	1.3 GHz
	LHH	1	1.5	1.3 GHz

Table 1: Technical parameters of the heating systems on ASDEX. NI is carried out with either deuterium (D^o) or hydrogen (H^o) injection. ICRH is used with 2nd harmonic heating on hydrogen ($2\Omega_{CH}$) or in the hydrogen minority mode (D(H)) applied to basically deuterium plasmas; LH is used in the current drive (LHCD) or in the heating (LHH) mode.

[1]University of Stuttgart, Germany; [2]Academy of Sciences, Leningrad, USSR; [3]Present address: JET Joint Undertaking, England; [4]University of Washington, Seattle, USA; [5]CEN Grenoble, France

A comparison of different heating methods clarifies the role of the microscopic heating mechanisms, which are different in the three cases on plasma confinement: With NI, the plasma is heated by classical Coulomb collisions with the beam ions; in the hf-cases, the plasma is heated by the interaction of a fraction of either ions or electrons from the Maxwellian distribution, which is in resonance with the wave. Unlike the hf-cases, NI heating refuels the plasma and transfers parallel momentum to it, thus giving rise to plasma rotation. Both NI and ICRH in the D(H) minority heating mode introduce non-thermal ions in either the parallel or perpendicular direction; at low density LH gives rise to a non-thermal electron distribution. Both cases of deviating Maxwellian velocity distributions introduce additional free energy to drive velocity space instabilities at the risk of degraded confinement. NI and ICRH-D(H) directly heat electrons and ions; ICRH-2 Ω_{CH} heats primarily ions, while LH is found to heat electons at low density. The power deposition profile with NI is broad, depending on the plasma density; ICRH and LH exhibit narrow power deposition; in the case of ICRH its location changes with the toroidal field B_T.

Combining NI and LH (in a k-spectrum setting which allows current drive (LHCD)) affords the possibility of studying global confinement at a different current distribution. In particular, with LHCD the resistive coupling between $j(r)$ and $T_e(r)$ is broken. In this scenario it can be clarified whether $T_e(r)$ and, as a corollary to it, the confinement properties can develop differently during NI in comparison with the case with the additional constraint of resistive coupling. Another aspect of this combination is that LH can suppress sawteeth (Söldner and co-workers, 1986). This offers the possibility of exploring the limitation of sawteeth on central plasma parameters and ultimately on the fusion reactivity of the plasma core. Finally, there is of course an obvious reason for combining different heating methods namely to achieve a high heating power.

Experimentally, an important motivation for combining the different heating methods has been the observation that injected beam ions interact with both the LH and the ICRH waves, causing an energy upshift of the energetic beam component (Ryter and co-workers, 1986). The low energy beam components and the bulk plasma (apart from bulk heating) are not affected. The slow decay time of the energy-upshifted ions when the beams are switched off indicates good confinement and nourishes the hope of detecting synergetic effects.

2. SUMMARY OF THE INDIVIDUAL ACHIEVEMENTS OF THE THREE HEATING SYSTEMS

The most successful heating system on ASDEX is NI, which yields the highest plasma temperatures ($T_i \sim 5 - 6$ keV), the best confinement times in the H-mode ($\tau_E \simeq 120$ ms) even at high power (Gruber and co-workers, 1985) and allows the ß-limit to be reached (Keilhacker and co-workers, 1985). Generally, NI gives rise to the H-mode unless too low or too high a density or too low a beam power is chosen. The lower density limit for the H-mode is $\bar{n}_e = 1.7 \cdot 10^{13}$ cm^{-3}; the high density limit depends on the refuelling technique, being $7 - 8 \times 10^{13}$ cm^{-3} with gas puffing and beyond $\bar{n}_e = 1.1 \cdot 10^{14}$ cm^{-3} with multiple pellet injection. Under optimal conditions the power limit is 1.2 MW with co- and 0.8 MW with counter-injection. Beyond these limits, NI gives rise to L-type behaviour with confinement times and scaling features comparable to those of ohmic limiter plasmas.

ICRH has been applied both in the 2nd-harmonic ($2\,\Omega_{CH}$) and the hydrogen minority D(H)-schemes (Steinmetz and co-workers, 1986a). The plasma generally reacts with degraded confinement, indicating L-mode characteristics. Figure 1 shows the increase of the plasma energy content W_p due to an NI-pulse and a subsequent ICRH-pulse of the same power (both in the L-mode). The W_p-trace of Fig. 1 is supplemented by the central line average density and four T_e-traces at different radial positions. The $ß_p$-increase with ICRH is somewhat higher, indicating an improvement over the L-confinement of beam heated discharges. The ICRH confinement times are systematically in excess of those with NI; the differences, however, are still within the combined error bars on τ_E[1].

Like the other two heating methods, LH leads to degraded confinement when applied at a density above $\bar{n}_e = 1 \times 10^{13}$ cm^{-3} (Söldner and co-workers, 1985). (At low density, in the suprathermal electron regime a slight improvement of τ_E with LH was observed (ibid.)) The importance of LH

[1] A systematic difference in the τ_E-analysis is introduced by the different methods, by which the heating power actually absorbed by the plasma is determined. In case of NI, P_{abs} is calculated independently from a Monte Carlo routine; in the case of ICRH, P_{abs} is determined from the rate of change of the plasma energy content when the ICRH-pulse is applied or switched off.

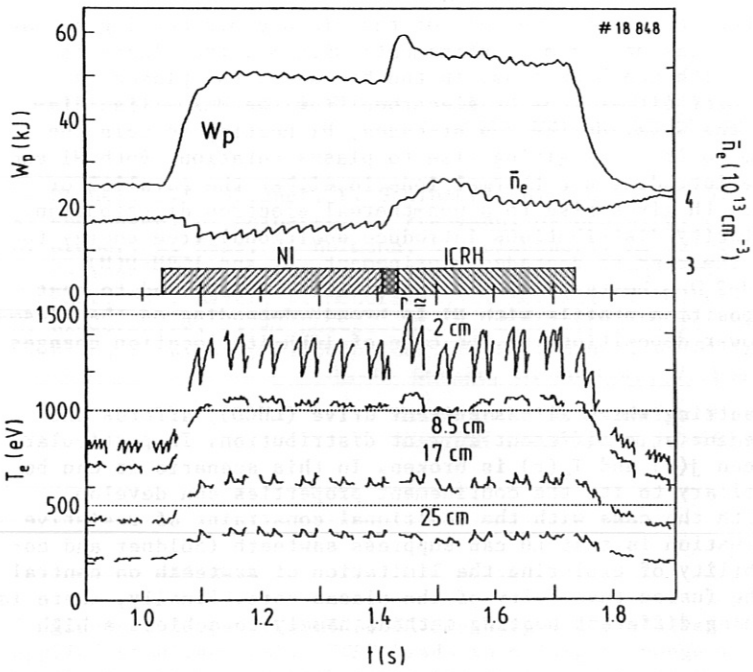

Fig. 1.
Plasma energy content W_p, line average density $\bar{n}_e$ (origin suppressed) and electron temperature T_e at 4 radial positions during an NI and a subsequent ICRH-pulse both of 1.75 MW power. (I_p = 380 kA, B_T = 2.3 T, $2\Omega_{CH}$).

in the context of this paper is its non-inductive current drive capability. At P_{LH} = 0.6 MW a current of 300 kA can be driven at $\bar{n}_e = 1 \cdot 10^{13}$ cm^{-3} for t = 1 s (Leuterer and co-workers, 1985). The different current distributions of inductive or non-inductive current drive, respectively, are measured by the Li-beam technique (McCormick and co-workers, 1986). Figure 2a compares an ohmic and an LHCD current profile in parameter settings which were used when LH and NI were combined (as described below). On application of LHCD the current profile is indeed maximally changed from the ohmic extreme, where the peaking of the curent density is limited by sawteeth, to the LHCD extreme, where its broadening is limited by the current density gradients at the q = 2 surface: With LHCD the plasma shows a tendency to develop a large saturated m = 2 mode.

Figure 2b compares the corresponding T_e-profiles obtained under OH or LHCD conditions. Contrary to the broadening of j(r), T_e(r) peaks with LHCD, thus demonstrating the decoupling of current and electron temperature profiles.

3. EFFECTS ON GLOBAL CONFINEMENT

3.1 Combination of ICRH with NI

The combination of ICRH with NI has some obvious technical advantages. With NI preheating, it is possible to apply the full ICRH-power up to P_{IC} = 2.3 MW (0.8 MW of NI-preheating is sufficient). In the case of an ohmic target plasma the ICRH power is limited to P_{IC} = 1.2 MW owing to excessive impurity radiation caused by ICRH (Steinmetz and co-workers, 1985). With NI, the power flux in the discharge is sufficiently increased so that high radiation levels can be tolerated without causing disruptions. On the other hand, disruptions and strong bulk radiation can also be prevented and ICRH can be applied to full power without NI assistance after the vessel wall has been carbonized (Janeschitz and co-workers, 1986). In a similar way, titanium evaporation in the divertor chamber removes oxygen from the discharge so that a higher impurity influx due to ICRH application can be tolerated. Under these circumstances, the full ICRH power can be applied to an ohmic discharge even under regular (stainless-steel) wall conditions. In the application of ICRH to an ohmic plasma, the power launched by the antennae P_{IC} is ~80 % of the generator power. In the case of an NI preheated plasma 90 % of the generator power can be launched. Also the fraction of the launched power, which is actually absorbed by the plasma improves from a maximum of ~60 % in the OH-case to a maximum of ~70% with NI-preheating (Steinmetz and co-workers, 1986b)..[1] (See footnote on next page.)

The improved application of ICRH power in a beam heated discharge is demonstrated in Fig. 3. Plotted is the rise in plasma energy content ΔW_{IC} due to ICRH normalised to the launched ICRH

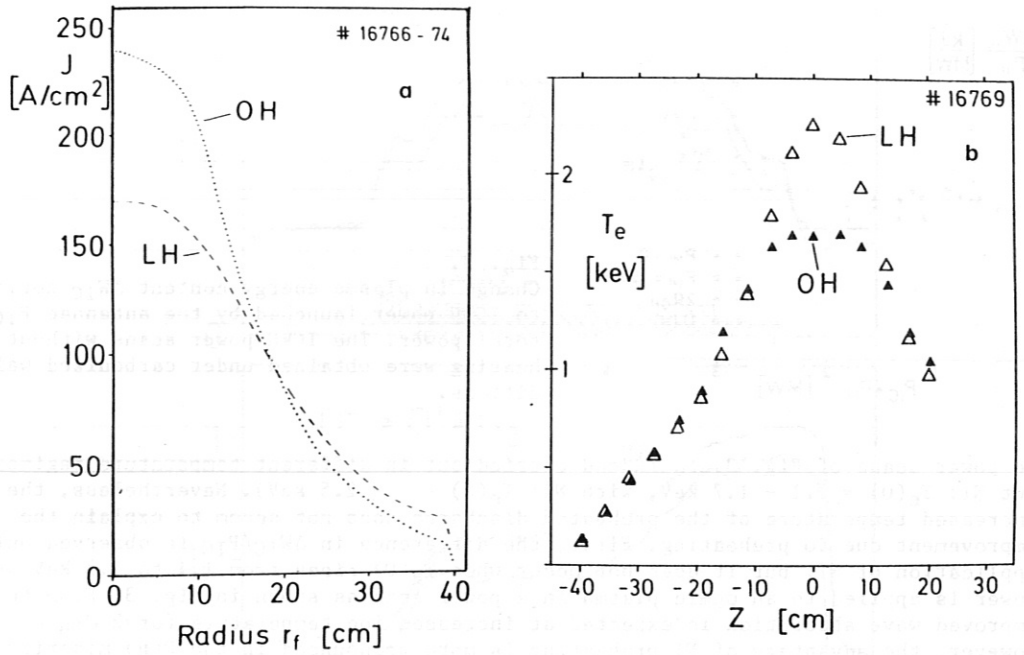

Fig. 2. Current density (a) and T_e profiles (b) (vertically measured) of an ohmic and a lower hybrid current driven discharge. ($\bar{n}_e$ = 1.2 x 10^{13} cm^{-3}, I_p = 312 kA, B_T = 2.3 T, P_{LH} = 0.87 MW).

power P_{IC} versus the total power $P_{IC} + P_{NI}$. Two cases are considered: (1) ICRH is applied to an ohmic target plasma and (2) ICRH is applied to a beam heated plasma. Figure 3 shows that ICRH-power is more efficiently used in a plasma which is preheated by NI. The difference in $\Delta W_{IC}/P_{IC}$ cannot be fully explained by the trivial reason that the ohmic power input decreases as soon as ICRH heats the plasma. (With NI-preheating, the reduction of P_{OH} reduces the NI heating efficieny.) Impurity radiation losses also cannot fully explain the differences in ICRH heating efficiency. Impurities, however, play a role because $\Delta W_{IC}/P_{IC}$ is lower with carbonized walls. The advantage of NI preheating might be (1) a favourable interaction of the ICRH wave with the energetic beam particles to the extent that gross plasma parameters are affected, or (2) improved wave absorption at higher ion temperature of the target plasma.

Re (1): The possibility of a favourable coupling of the ICRH wave ($2\,\Omega_{CH}$) to the beam ions was studied in a case where first the ICRH power was applied to a deuterium plasma preheated by hydrogen beams. The results were compared with a case where deuterium was injected into a deuterium plasma where no beam ion-ICRH wave interaction could be expected. Indeed, plasmas without hydrogen content quickly disrupted when ICRH ($2\,\Omega_{CH}$) was applied. Therefore, H_2 was blown into the $D^o \rightarrow D^+$ case to provide wave absorption. A hydrogen concentration of 20 % was found to provide good $2\,\Omega_{CH}$ heating. Figure 4 compares the β_p-development of the two cases $H^o \rightarrow D^+$ + ICRH ($2\,\Omega_{CH}$) and $D^o \rightarrow D^+$ + ICRH ($2\,\Omega_{CH}$) + H_2-addition. Contrary to expectation, the second case (without high energy hydrogen) displays the larger β_p. (The difference can only be partly explained by the slightly higher ICRH-power in the second case.) Obviously, the favourable beam-ion-wave interaction observed in the beam ion distribution is insufficient to give rise to synergetic improvements in the plasma energy content. If this effect is present, it is masked by the isotope effect on confinement (Stäbler and co-workers, 1984) which causes the larger β_p-rise in the second case with deuterium as the abundant plasma species.

[1]The absorption coefficient α is deduced from dW/dt (W = energy content) when ICRH is switched on or off. In the analysis, assumptions have to be made on the variation of τ_E in the initial phase of the ICRH-pulse or after it. A systematic error can be introduced in the determination of α (and consequently of τ_E) when ICRH is applied to an ohmic plasma (when τ_E rapidly degrades with auxiliary heating power) or together with NI at already degraded confinement conditions.

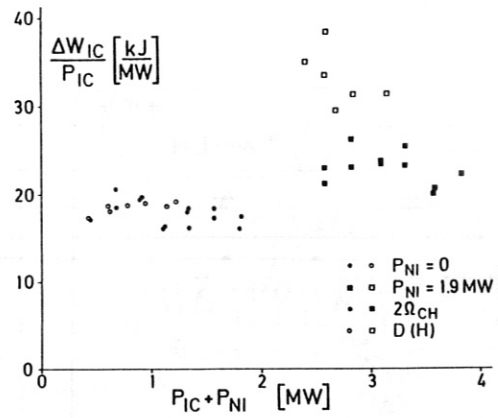

Fig. 3.
Change in plasma energy content ΔW_{IC} normalized to ICRH power launched by the antennae P_{IC} versus total power. The ICRH-power scans without NI preheating were obtained under carbonized wall conditions.

Re (2): The power scans of Fig. 3 are indeed carried out in different temperature regimes (without NI: $T_e(0)$ = 1.1 - 1.7 keV, with NI: $T_e(0)$ = 2 - 2.5 keV). Nevertheless, the increased temperature of the preheated discharge does not seeem to explain the improvement due to preheating. First, the difference in $\Delta W_{IC}/P_{IC}$ is observed only on application of NI, but it does not occur when $T_e(0)$ rises from 1.1 to 1.7 keV when ICRH power is applied to an ohmic plasma in a power scan as shown in Fig. 3. From theory, improved wave absorption is expected at increased ion temperature for 2 Ω_{CH}-heating. However, the advantage of NI preheating is more pronounced in the D(H) minority mode, where no such dependence is expected.

The rise in $\Delta W_{IC}/P_{IC}$ with beam heating might be due to better rf coupling at modified plasma parameters in the scrape-off-layer in front of the antennae. Indeed, the increase in $\Delta W_{IC}/P_{IC}$ corresponds to a similar increase in dW/dt - the rate with which the plasma energy content W rises when the ICRH pulse is initiated. In the case of D(H) minority heating, the total improvement in $\Delta W_{IC}/P_{IC}$ cannot thereby be explained. It might partly be a bulk property and depend on the hydrogen minority concentration.

0.8 MW of NI power is sufficient for the manifestation of the favourable effects of NI preheating as shown in Fig. 3. No substantial further improvement is achieved at higher P_{NI} (Steinmetz and co-workers 1985). Even at high heating power, the increase in β_p by ICRH and NI is additive. Figure 5 demonstrates the linear superposition of ICRH and NI power both for 2 Ω_{CH}- and D(H)-heating. In both cases, the discharge is preheated by 0.8 MW beam heating to operate under optimal absorption conditions, in a power range of the L-mode where τ_E is already rather insensitive to heating power and where the ohmic power input can be neglected. $\Delta\beta_p$ (NI) and $\Delta\beta_p$ (ICRH) are the same irrespective of the sequence of application. (In addition to the diamagnetic $\beta_{p\perp}$, the electron β_{pe}, deduced from Thomson scattering (Meisel and co-workers, 1986), is plotted to rule out falsifications by non-thermal contributions to $\beta_{p\perp}$ during ICRH.) The diagram documents that at high power the rise in β_p does not depend on the preparation of the target plasma irrespective of whether it is basically an NI or ICRH-heated discharge. The most important parameter for the gross confinement properties of the discharge is the total heating power. Additional features of the heating method (e.g. momentum transfer causing plasma rotation) seem to play a minor role. The overall higher β_p-values of D(H) in comparison with 2 Ω_{CH} are again mostly due to the isotope effect on confinement.

3.2 Combination of LH and NI

This scenario concentrates on the effects of different current distributions (OH or LHCD) on global confinement when NI is additionally applied. Another aspect is that, in the OH-case thermal electrons and, with LH, suprathermal electrons carry the current. Low density ohmic discharges with mostly suprathermal current carriers showed improved energy confinement (Fußmann and co-workers, 1981).

Figure 6a compares the plasma current, loop voltage and density for a case with NI (P_{NI} = 1.6 MW) alone and one with 0.8 MW LHCD and NI of the same power. Note the decrease of the loop

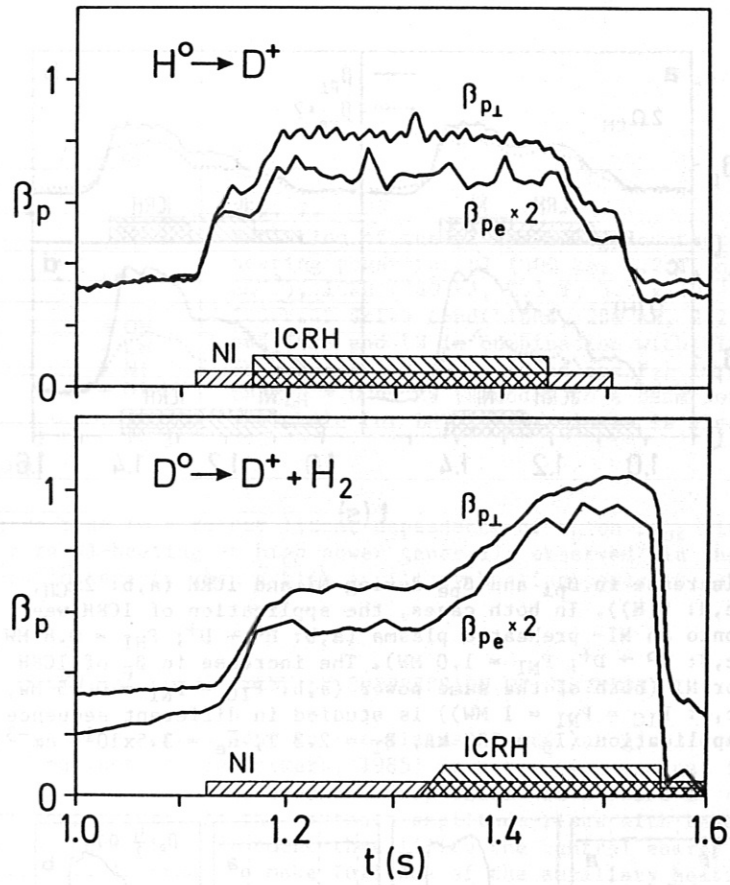

Fig. 4. Variation of diamagnetic $\beta_{p\perp}$ and β_{pe} of the electrons during the ICRH ($2\Omega_{CH}$) and NI-pulse. In case a, hydrogen was injected into a deuterium plasma (P_{IC} = 1.0 MW, P_{NI} = 1.8 MW); in case b, deuterium was injected into a deuterium plasma (P_{IC} = 1.2 MW, P_{NI} = 2.0 MW) with additional H_2-gas puffing (I_p = 380 kA, B_T = 2.3 T, $\bar{n}_e = 4.2 \times 10^{13}$ cm $^{-3}$).

voltage when LH is applied, which indicates that most of the current is non-inductively driven. Figure 6b plots the β_p-values for the two cases. Shown is $\beta_{p\perp}$ from the diamagnetic loop, $\beta_p^{equ} + l_i/2$ from plasma equilibrium and β_{pe} of the electrons as measured by laser scattering. The rise in $\beta_{p\perp}$ when LHCD is added is small, mostly because the ohmic input power of P_{OH} = 0.28 MW is instantly turned off. $\beta_p + l_i/2$ decreases after an initial increase when LHCD is turned on. The rise of β_p is offset by the drop in l_i as soon as the plasma current distribution broadens. The increase in $\beta_{p\perp}$ during the injection phase is the same for the two cases with different current distribution. The electron temperature profiles of the four cases of OH-, LHCD-, and NI into OH and LHCD are shown in Fig. 6c. The T_e-profiles in the OH- and LHCD-phases differ in the known fashion; during beam heating, the T_e profiles are rather similar for inductive and non-inductive current drive. During NI, the current profile remains broad under LH drive conditions (l_i remains low); the suprathermal electron population, however, seems to be reduced (as indicated by decreasing non-thermal ECE radiation).

Figure 7 summarizes the results obtained when either ICRH or LH is combined with NI. Plotted is the energy content of the discharge versus the total heating power. The results of combined heating are compared with those when NI or ICRH alone is applied. (The vessel wall was carbonized for these cases.) This diagram confirms what has been discussed in detail above, namely that ICRH and NI power can be superimposed linearly and that the heating results are independent of the method of current drive. The improvement of ICRF-heating when simultaneously applied

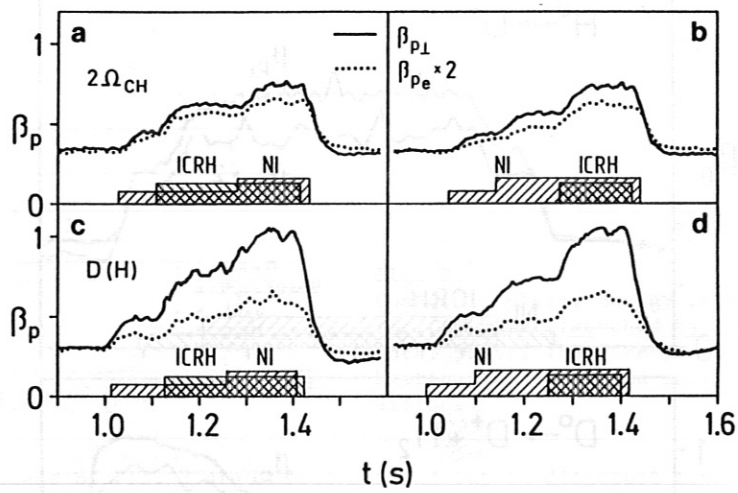

Fig. 5. Increase in $\beta_{p\perp}$ and β_{pe} during NI and ICRH (a,b: $2\Omega_{CH}$, c,d: D(H)). In both cases, the application of ICRH was onto an NI- preheated plasma (a,b: $H^o \rightarrow D^+$; P_{NI} = 0.8 MW, c,d: $D^o \rightarrow D^+$; P_{NI} = 1.0 MW). The increase in β_p of ICRH or NI (both of the same power (a,b: $P_{IC} = P_{NI}$ = 0.95 MW, c,d: $P_{IC} = P_{NI}$ = 1 MW)) is studied in different sequence of application (I_p = 380 kA, B_T = 2.3 T, $\bar{n}_e = 3.5\times10^{13}$ cm^{-3})

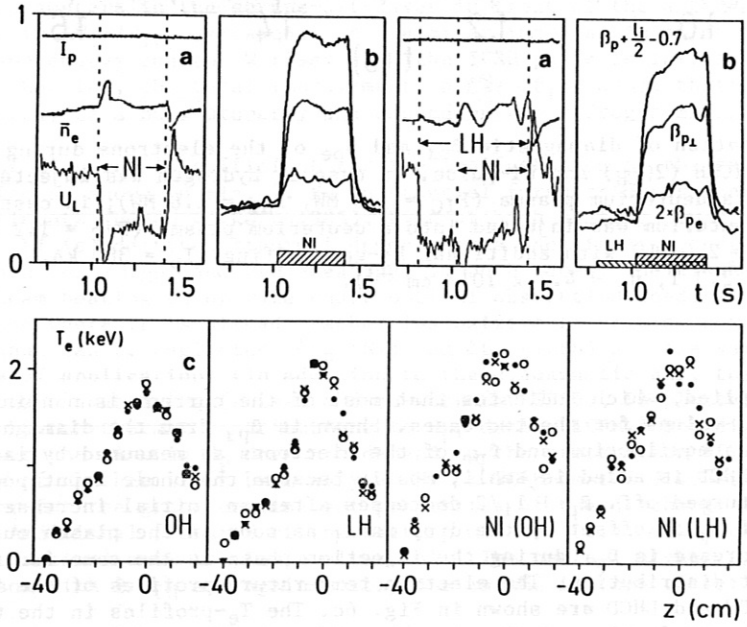

Fig. 6. Variation of $\beta_{p\perp}$, $\beta_p + l_i/2$ (from equilibrium) and β_{pe} during NI once into an ohmic and once into an LH (current drive) phase. The two diagrams are supplemented with plasma current (300 kA), loop voltage (2.5 x full scale) and density (2 x 10^{13} cm^{-3} full scale). To facilitate comparison, $\beta_p + l_i/2$ is shifted by 0.7 (a typical value for $l_i/2$). Note the increase in $\beta_{p\perp}$ and the decrease of $\beta_p + l_i/2$ when LH is applied. c shows the T_e-profiles for the four scenarios.

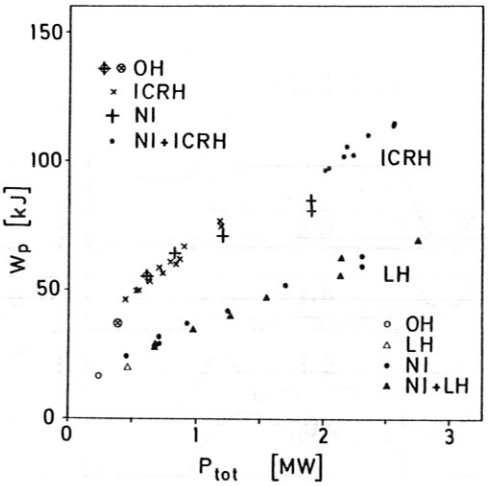

Fig. 7.
Variation of the plasma energy content with total heating power for NI (400 kA, 2.2 T, $\bar{n}_e = 5 \times 10^{13}$ cm^{-3}), ICRH (380 kA, 2.3 T, 3.5×10^{13} cm^{-3}) and LH (current drive conditions, 280 kA, 2.2 T, 1.2×10^{13}) and ICRH and LH in combination with NI. In case of ICRH $P_{NI} = 1.9$ MW is added and P_{IC} is varied; in case of LH $P_{LH} = 0.45$ MW is added to a beam power scan. W_p of the ohmic (or LH) target plasma is also shown.

together with NI may give rise to a rather linear dependence of W_p on P_{tot} without the slight saturation in W_p with pure NI-heating at high power generally observed in the L-mode. This result indicates favourable aspects when a high auxiliary heating power is split up into ICRH and NI.

4. EFFECTS ON CENTRAL CONFINEMENT BY SUPPRESSION OF SAWTEETH

Localized power deposition in a narrow zone in the plasma centre can give rise to rather violent sawtooth activity (Jacquinot and co-workers, 1985) as a reaction against further pinching of the current channel. In most cases the sawtooth drop occurs in a phase of still linearly rising central electron temperature. As the sawtooth amplitude rises with beam power, sawteeth represent a degradation of central confinement that limits the central energy density and ultimately the fusion reactivity. In order to make full use of the auxiliary heating power and to achieve high central temperatures, means of suppressing sawteeth have to be developed. Sawteeth can be suppressed by LH preferentially with the current drive wave-spectrum (Söldner and co-workers, 1986). The T_e-profiles shown in Fig. 2 are obtained in an OH-discharge with and an LHCD-discharge without sawteeth. In the following section we discuss the effect of sawteeth on the central energy density, the possibility of increasing it when sawteeth are suppressed and finally the aspects when LH is applied to NI heated discharges with large sawteeth to begin with.

First of all we describe some of the differences between sawtoothing and sawtooth-free ohmic discharges in ASDEX. Figure 8 compares the plasma current, line average density along different chords and central electron temperature of two consecutive discharges, one with and one without sawteeth. The second discharge starts also with sawteeth; they are suppressed during the second current ramp-up phase; the current was ramped up once more to study the plasma behaviour at different q_a-values (1st, 2nd, 3rd plateau: $q_a = 4.2, 3.3, 2.8$). During each plateau, steady-state conditions are established. Without sawteeth the central T_e is slightly above T_e averaged over the sawteeth and roughly agrees with the peak values of T_e just prior to the sawtooth drop. Figure 8 shows also the T_e- and n_e-profiles for the two q_a-values. The n_e-profile shows a clear peaking without sawteeth; the T_e-profiles remain largely unaffected and in particular broaden with decreasing q_a, as in the case with sawteeth (see Table 2). It is interesting to note the change in n_e-profile shape when the effects of the anomalous inward velocity are no longer balanced by the sawtooth turbulence.

TABLE 2

q_a	4.2	3.3	2.8
$T_{eo}/\langle T_e \rangle$	3.1	2.4 (2.2)	2.0 (1.7)
$n_{eo}/\langle n_e \rangle$	2.3	1.9 (2.5)	1.6 (2.4)

Table 2: Peak to volume averaged electron temperature and density for the sawtoothing and sawtooth free discharges (in brackets) of Fig. 8. At $q_a = 4.2$ both discharges were with sawteeth.

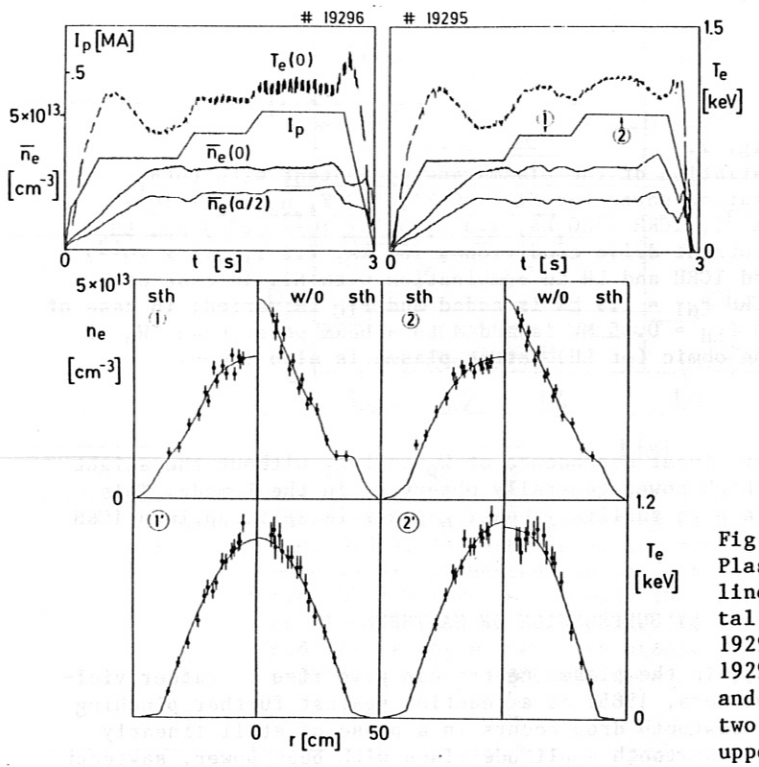

Fig. 8.
Plasma current, central temperature and line averaged density along two horizontal chords for a sawtoothing (sth, # 19296) and a sawtooth-free w/0 sth, # 19295) discharge. Electron temperature and density profiles are shown for the two moments marked by 1 and 2 in the upper right picture.

The energy content of the two cases is the same at all current values. The central energy density, however, rises by about 25 % when sawteeth disappear. The central confinement time, (defined as the ratio of the central energy density to heating power density) increases much more, however, if the central heating power is corrected for impurity radiation. There is a substantial rise in impurity radiation from the plasma core (~ 1 order of magnitude) when sawteeth disappear. The impurity radiation saturates at a high level (comparable to the central ohmic power density). Nevertheless the central energy density remains high and no thermal collapse occurs. It is unclear at present whether the enhanced core radiation prevents a peaking of T_e, similar to the peaking observed for the density.

In beam heated divertor discharges, the sawtooth repetition time τ_{st} is a strong function of beam power. Figure 9a shows the line average density during the beam pulse at different P_{NI}. The plasma density decreases because of the degraded confinement properties of the L-mode. τ_{st} increases with the beam power and for $P_{NI} > 2$ MW the discharge is sawtooth-free (apart from a possible sawtooth just after NI was started). At higher density or lower q_a more heating power is necessary to suppress sawteeth. The suppression of sawteeth with beam heating has only been observed in the divertor configuration. In limiter discharges of ASDEX, sawteeth occur up to the highest power with only a slight increase in τ_{st} (Fig. 9b).

Figure 10a plots $\tau_{E,st} = \tau_{st}\ \bar{T}_e/\Delta T_e$ versus total heating power for high q_a and low q_a NI heated and a low q_a NI + ICRH heated discharge ($\bar{T}_e$ is the mean temperature averaged over sawtooth excursion with amplitude ΔT_e). $\tau_{E,st}$ represents the central electron confinement time due to the repetitive sawtooth oscillations. $\tau_{E,st}$ is found to increase rapidly with the heating power; a further increase of the total power beyond the values shown in Fig. 10a yielded sawtooth-free discharges. The central electron energy density for NI and NI + ICRH power scans is plotted in Fig. 10b for two q_a-values. There is no change in the central electron energy density W_o at the transition from the NI-sequence with rare sawteeth to the NI + ICRH-sequence with frequent and high-amplitude ones. Unlike in the ohmic case, no distinct increase of the central energy density W_o occurs when sawteeth disappear. In particular, the nearly sawtooth-free NI-discharges do not markedly differ in W_o from those with NI + ICRH, which still have frequent sawteeth at the same total power (encircled data points in Fig. 10b).

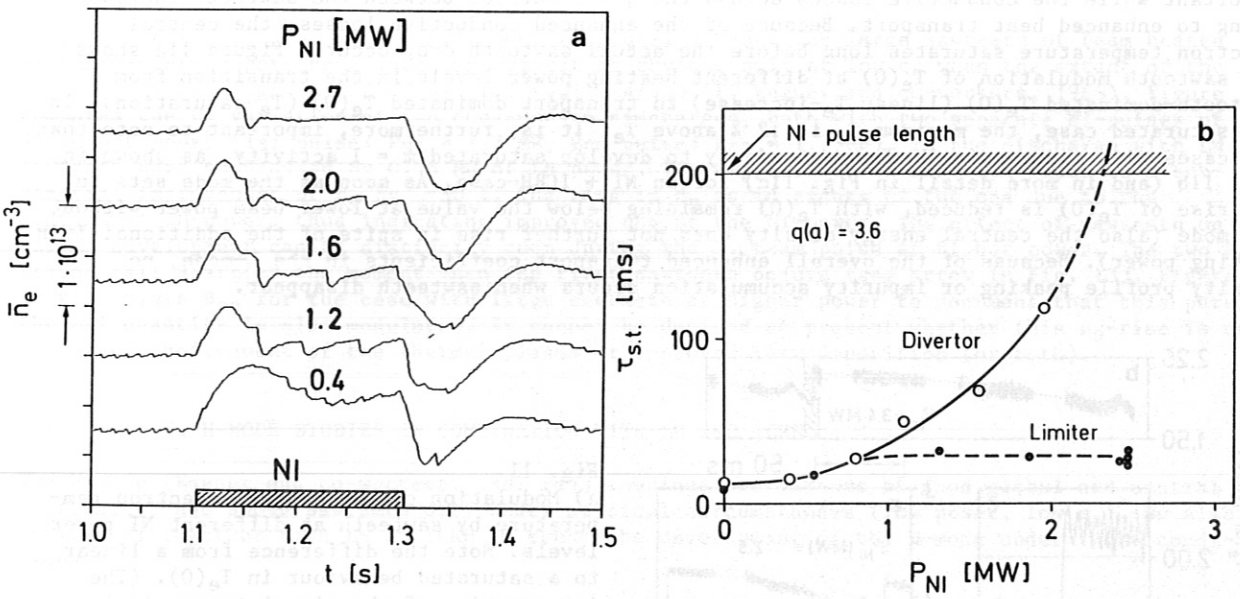

Fig. 9. a) Variation of the line averaged density indicating sawteeth during the NI phase for different heating powers. The density traces are shifted vertically for clarity; the densities during the ohmic phase agree in all cases ($\bar{n}_e$ = 2 x 10^{13} cm^{-3}; I_p = 300 kA).
b) Sawtooth repetition time τ_{st} versus beam power for divertor and limiter discharges. The NI pulse length is 200 ms as indicated.

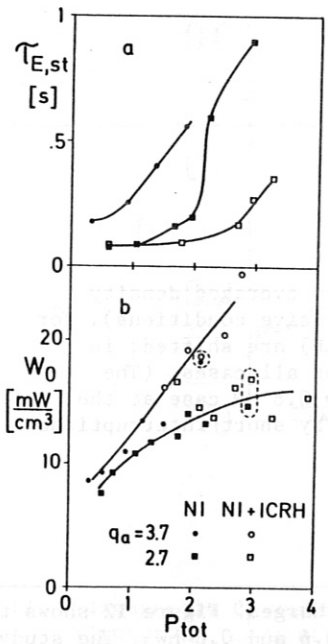

Fig. 10.
Central electron energy confinement time $\tau_{E,st}$ due to repetitive sawtooth relaxations defined as $\tau_{E,st} = \tau_{st} \cdot \bar{T}_e/\Delta T_e$ ($\bar{T}_e$ = mean central electron temperature, ΔT_e = sawtooth amplitude) and central electron energy density W_o versus total heating power. The results of two different q_a-values and with NI and NI + ICRF heating are shown. The encircled data points show W_o without sawteeth for NI alone and with frequent sawteeth in case of NI + ICRH. (In case of NI + ICRH at q_a = 3.7, $\tau_{E,st}$ could not be measured because the ECE spectrometer did not view the plasm centre.)

The different effect that sawteeth have on the central energy density in ohmic and auxiliary heated discharges is the result of two different mechanisms limiting the central energy density, namely the sawtooth relaxations and the steady-state power flux across the q=1 surface.

In ohmic discharges, sawteeth are the limiting process. With beam heating sawteeth become less important while the conductive losses across the q = 1 surface between the sawteeth increase owing to enhanced heat transport. Because of the enhanced conductive losses, the central electron temperature saturates long before the actual sawtooth drop occurs. Figure 11a shows the sawtooth modulation of $T_e(0)$ at different heating power levels in the transition from sawtooth-dominated $T_e(0)$ (linear T_e-increase) to transport dominated $T_e(0)$ (T_e-saturation). In the saturated case, the maximum T_e is 12 % above $\bar{T}_e$. It is, furthermore, important to note that the cases with rare sawteeth show a tendency to develop saturated m = 1 activity, as shown in Fig. 11b (and in more detail in Fig. 11c) for an NI + ICRH-case. As soon as the mode sets in, the rise of $T_e(0)$ is reduced, with $T_e(0)$ remaining below the value at lower beam power without the mode (also the central energy density does not further rise in spite of the additional ICRH heating power). Because of the overall enhanced transport coefficients in the L-mode, no density profile peaking or impurity accumulation occurs when sawteeth disappear.

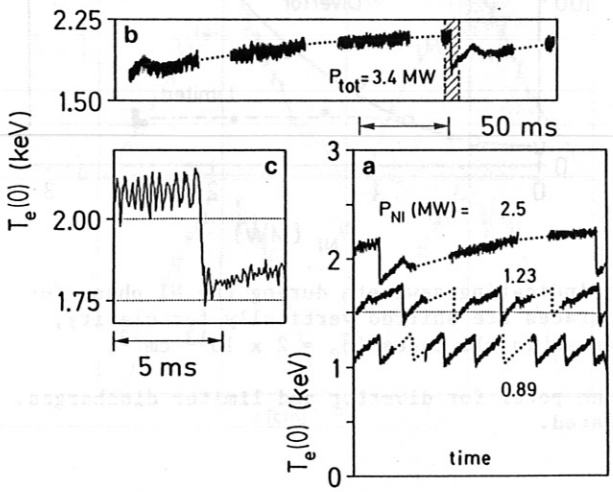

Fig. 11.
a) Modulation of the central electron temperature by sawteeth at different NI power levels. Note the difference from a linear to a saturated behaviour in $T_e(0)$. (The interruption of the signal traces is instrumental.)
In case b, 1.2 MW ICRH-power is added to the beam heated plasma with the result of long sawteeth with a saturated m = 1 mode. The hatched interval is blown up in c.
(a and b have the same time scale; I_p = 420 kA, q_a = 2.7).

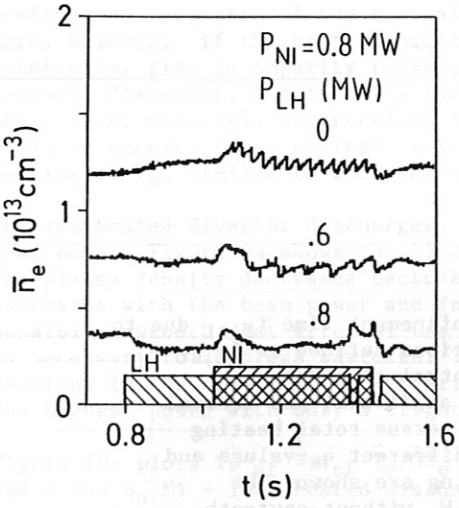

Fig. 12.
Sawtooth modulation of the line averaged density with NI and LH (under current drive conditions). For clarity, the $\bar{n}_e$ traces (with LH) are shifted; in the OH-phase $\bar{n}_e$ is the same for all cases. (The density variation in the P_{LH} = 0.8 MW case at the end of the NI-pulse is caused by short interruptions of the LH-pulse.)

LH current drive suppresses sawteeth both in OH and beam heated discharges. Figure 12 shows the density variation with NI (P_{NI} = 0.8 MW) and with additional LHCD (0.6 and 0.8 MW). The study of sawtooth suppression was concluded in the density range $\bar{n}_e < 2 \times 10^{13}$ cm^{-3}, where the current drive efficiency of the present LH-system is sufficiently high. W_o ($T_e(0)$) increases from 65 mW/cm^3 (1970 eV) with NI alone to 76 mW/cm^3 (2210 eV) with additional 0.8 MW LH. Unlike the ohmic case, no large improvement in the central energy density is achieved (the slight increase is due to the additional LH heating power). The distinct T_e-profile changes of LH applied to ohmic plasmas are not observed in beam heated plasmas. The T_e-profiles are rather invariant when sawteeth are suppressed (a slight peaking is still indicated). Their form still

depends on q_a. The low overall confinement properties (at low density or with beam heating) prevent impurity accumulation.

There is, however, a notable improvement in global β_p when the large sawteeth of beam heated discharges are suppressed. This improvement is obvious only at low q_a when the extent of the q=1 surface is large (in ADSEX we find $r_{q=1} \sim a/q_a$) (F. Wagner and co-workers, 1986). Figure 13 compares the β_p variation of two consecutive discharges, both with two separate NI-pulses of different power (1st pulse: P_{NI} = 1.3 MW, 2nd pulse: P_{NI} = 1.7 MW). In the discharge with LH, sawteeth were suppressed by 0.55 MW of LH power. The suppression of sawteeth leads to a substantial improvement of β_p by ~30 %. The rise in β_p is in excess of the one due to the additional LH-power, thus indicating improved use of the NI-power. The effect of sawteeth on the β_p-development can be distinctly seen during the 2. beam pulse at higher power. The two β_p-traces fall apart at the moment when the first sawtooth occurs (see arrow in Fig. 13). Figure 13 also plots β_{pe} for the case with large sawteeth at higher power to document that this purely thermal quantity is also modulated. It cannot be decided at present whether this β_p-rise is due to better confinement of the thermal plasma or improved beam deposition (or both).

5. H-MODE STUDIES IN COMBINATION WITH LH AND ICRH

The H-mode (Wagner and co-workers, 1982 (a)) combines the virtues of good global and central confinement and shows sawteeth only under atypical circumstances (low power, low q_a). We also applied NI together with LH or ICRH to study the development of the H-mode under these conditions.

The H-mode can be realized under current drive conditions (with loop voltage U_L = 0) at a density above the H-mode density threshold ($1.7 \cdot 10^{13}$ cm^{-3}) but still in a range of sufficient current drive efficiency. After the H-mode transition, however, when the density increases owing to the improved particle confinement, the current decreases (U_L = 0!). The realization of the H-mode under conditions of no inductive toroidal electric field (E_{tor} = 0) have contributed to a clarification of potential mechanisms to cause the H-transition. It does not seem to be caused by drift effects which depend on E_{tor}/B_{pol} (as in the neoclassical pinch) and influence particle transport. This effect has been considered in the past because of the vanishing B_{pol} at the stagnation point (Hinton, 1984).

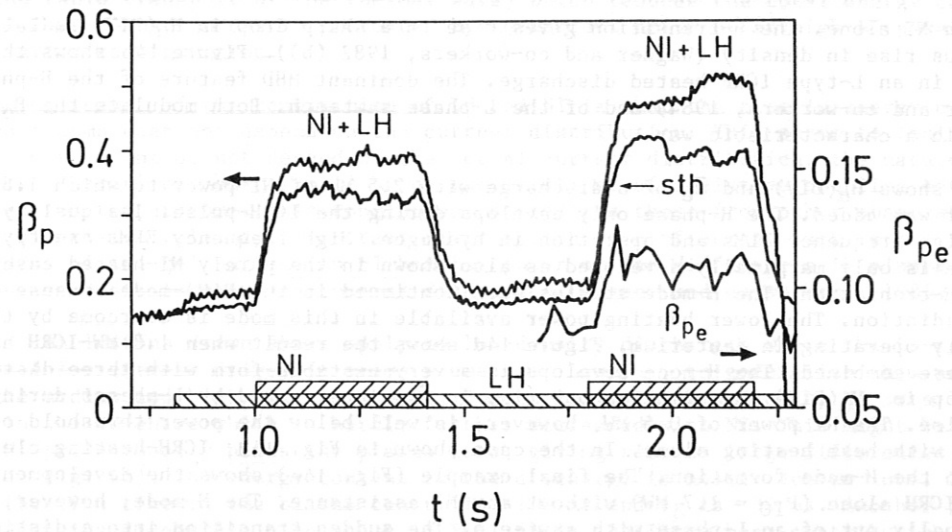

Fig. 13. Diamagnetic β_p variation during NI (1st pulse 1.3 MW, 2nd pulse 1.7 MW) with and without LH (current drive, P_{LH} = 0.55 MW). LH suppresses sawteeth yielding higher β_p. For the second NI pulse β_{pe} is plotted to document also sawtooth modulation of this parameter.

NI and ICRH were combined in an effort to achieve the H-mode with as little NI heating power as possible and with the ultimate goal of realizing it with ICRH alone. Figure 14a compares the H_α(DIV)-radiation in the divertor chamber and the line average density of an H- and an L-dis-

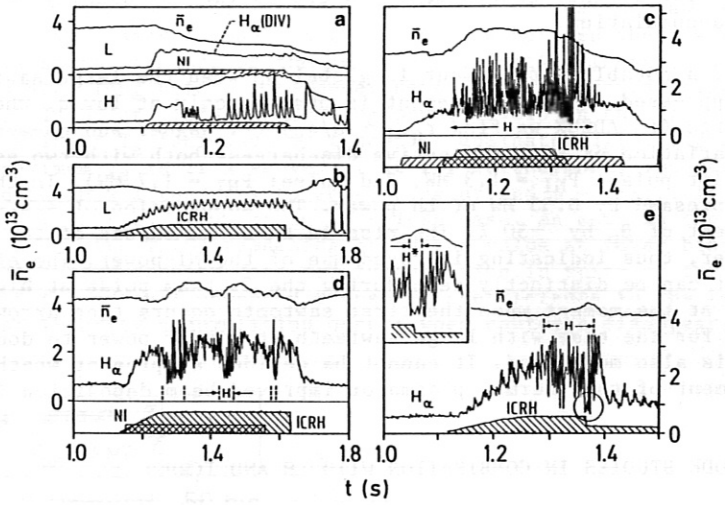

Fig. 14. Line average density and the H_α-radiation in the divertor chamber during NI and ICRH
a) NI, L and H-case; P_{NI} = 2.5 MW
b) ICRH, L-case; P_{IC} = 1.7 MW.
Note the modulation of density and H_α-radiation by ELMs in the H-phase and by sawteeth in L-discharges.
c) NI + ICRH - $2\Omega_{CH}$ yielding an H-phase with frequent ELMs
d) NI + ICRH - D(H) yielding an H-phase at a beam power (P_{NI} = 0.5 MW) where the H-phase is not possible with beam heating alone.
e) ICRH alone yielding an H-phase at marginal conditions. (The encircled section is enlarged in the insert).

charge with NI alone. The H-transition gives rise to a sharp drop in H_α(DIV)-radiation and a simultaneous rise in density (Wagner and co-workers, 1982 (b)). Figure 14b shows the same parameters in an L-type ICRF heated discharge. The dominant MHD feature of the H-phase are ELMs (Keilhacker and co-workers, 1984) and of the L-phase sawteeth. Both modulate the H_α(DIV)-radiation in a characteristic way.

Figure 14c shows H_α(DIV) and $\bar{n}_e$ of a discharge with 2.5 MW of NI-power to which 1.8 MW ICRH - $2\,\Omega_{CH}$ power was added. The H-phase only develops during the ICRH-pulse. Its quality is low owing to high-frequency ELMs and operation in hydrogen. High frequency ELMs are tpyical when the H-phase is only marginally developed as also shown in the purely NI-heated case (a) just after the H-transition. The H-mode studies were continued in the D(H)-mode because of reduced impurity radiation. The lower heating power available in this mode is overcome by the advantage of basically operating in deuterium. Figure 14d shows the result when 1.8 MW-ICRH and 0.5 MW NI-power were combined. The H-mode develops in a very unstable form with three distinct H-phases (drop in H_α(DIV) and simultaneous rise in $\bar{n}_e$) interrupted by L-phases during the heating pulse. The NI power of 0.5 MW, however, is well below the power threshold of 1.2 MW for the H-mode with beam heating alone. In the case shown in Fig. 14d, ICRH-heating clearly contributes to the H-mode formation. The final example (Fig. 14e) shows the development of the H-mode with ICRH alone (P_{IC} = 1.7 MW) without any NI assistance. The H-mode, however, develops only marginally out of an L-phase with sawteeth. The sudden transition into a distinct H-phase (see insert to Fig. 14e) changes (in a known fashion (Wagner and co-workers, 1985)) the boundary layer properties and therefore the coupling conditions for the antennae. As the rf-system was operated at maximal voltage, the sudden change in wave coupling caused failure in the operation of one antenna. Unfortunately, this technical difficulty has not yet been overcome.

The different stages in the development of the H-mode as shown in Fig. 14 demonstrates that the H-mode is accessible in combination with ICRH-heating but also with ICRH alone. More details on the H-mode with ICRH are provided by K. Steinmetz (this conference). In order to produce long and stable H-phases which allow the assessment of its confinement properties, however, more ICRH power than presently installed on ASDEX is required.

6. DISCUSSION

NI and ICRH heating power give rise to similar confinement regimes (L and H). In particular, the manifestation of the H-mode only with ICRH-heating could be of great importance both for the understanding of confinement physics and the development of controlled fusion research. On simultaneous application of ICRH and NI the plasma energy content increases linearly according to the total heating power. The synergetic improvement as observed in the combination of NI and ICRH may prevent the deviation of W_p versus P_{tot} from linearity at high power as is generally observed in the L-mode with beam heating alone.

The confinement characteristics of the tokamak plasma seem to be an intrinsic plasma property and not to depend on the microscopic nature of the heating method. It also seems to be irrelevant for the gross confinement structure whether particles and momentum are transferred together with the heating power or whether the particle distribution functions are distorted by energetic tails in the parallel or perpendicular degrees of freedom. The lack of importance of the plasma collisionality on heating and confinement is again confirmed. It does not matter whether the plasma is heated at high collisionality (when the heating method under consideration is applied alone) or - at the same power - at low collisionality when applied together with another heating method. This result might be of interest in conjunction with direct particle orbit losses or in considerations of the extent to which dissipative trapped particle modes influence transport and confinement. The comparison of the D(H)- with the $2\Omega_{CH}$-ICRF heating modes reflect the isotope effect on confinement (Stäbler and co-workers, 1984) and confirm once more the importance of large ion Larmor radii or slow ion sound velocity for low electron heat diffusivity (Wagner and co-workers, 1986).

The combination of LHCD and NI yields a synergetic effect only at low q_a: The plasma energy content, increased by NI, is further raised when sawteeth are suppressed. This is a surprising result because sawteeth are an internal instability which should affect the central confinement but not the global one. On the other hand, the sawtooth drop in the plasma centre transiently increases runaway electron losses and the level of high-frequency B_r-fluctuations outside the plasma and gives rise to energy losses into the scrape-off layer. The same signatures are observed at the OH-L transition in the initial beam heating phase. Obviously, the plasma reacts with enhanced transport after the sawtooth drop during the phase of increased power flux (as indicated by the rapid transport of the thermal wave) which reduces the total energy content. This additional loss mechanism can be prevented by LH-current drive or at high NI power in the case of the divertor configuration.

Another surprising result of the combination of LH and NI is that the rise in energy content of the beam heated plasma does not depend on the current distribution. This seems to indicate that NI heating and confinement do not depend on the actual current distribution, the nature of the current carriers (thermal or non-thermal) or on the existence of resistive coupling between the current and electron temperature. This conclusion contradicts those from other observations, which indicate a decisive role of the current distribution on confinement such as the invariance of the radius of the q=1 surface on NI heating power or the differences in plasma profiles between (currentless) stellarator and tokamak discharges (Wagner and co-workers, 1986).

The results and conclusions drawn above apply to low-density discharges where the LH-system of ASDEX can be used for current drive. It seems premature, however, to generalize them and apply them also to the medium and high density ranges. A peculiarity of low-density NI is a low τ_E-value already in the OH-phase which is hardly further decreased with NI. This might be due to the fact that NI predominantly heats the plasma ions, giving rise to large differences between $\beta_{p\perp}$ and β_{pe} (see Fig. 6b). The energy content in the discharge is mostly due to ions. The ion-electron equilibration time in the plasma centre is ~100 ms and τ_E is ~30 ms. Another problem of NI into low-density discharges also shown in Fig. 6b is the large beam contribution to β_p. This is obvious from the large difference in $\Delta(\beta_p + l_i/2)$ and $\Delta\beta_{p\perp}$ with NI. The ion slowing-down time is about 80 ms. Part of the $\beta_{p\perp}$-rise will also be due to the perpendicular non-thermal beam-ion contribution. Because of these peculiarities at low density, changes in the electron confinement on account of decoupled current- and temperature profiles might escape observation. On the other hand, the measured β_{pe}-values are the same in the two cases (see Fig. 6b), ruling out at least large changes in the electron confinement.

Similarly, sawtooth suppression might exhibit new aspects at higher density which are not observed at low density. At high density the suppression of sawteeth by auxiliary heating might also improve core confinement (as in the OH-case), but only when good global confinement is provided, too. Then, however, means of preventing impurity accumulation, as observed in OH

plasmas, or the quiescent H-mode (Keilhacker and co-workers, 1984, Müller and co-workers, 1986) or the development of saturated m = 1 modes have to be found.

The discussion of the LH-experiments, as presented here, indicates the necessity of applying LH in a more relevant density range with a LH system operating at higher frequency.

ACKNOWLEDGEMENT

The excellent work of the technical staffs of ASDEX and the neutral injection, ion cyclotron and lower hybrid heating systems are gratefully acknowledged. Thanks are due to I. Hermann, H. Sittig and H. Volkenandt for preparing the manuscript and to Dr. A. Gibson for critically reading it.

REFERENCES

Fussmann, G., and co-workers (1981). Long-pulse suprathermal discharges in the ASDEX tokamak. Phys. Rev. Lett., 47, 1004.

Gruber, O., W. Jilge, and co-workers (1985). Radial energy balance analysis of ASDEX H-mode discharges. Proc. 12th Europ. Conf. on Contr. Fus. and Plasma Phys., 9F, Part I, 18.

Hinton, F.L., M. S. Chu, R.R. Dominguez, and co-workers (1986). Physics of the H-mode. Plasma Physics and Controlled Fusion Research, 1984, IAEA, Vienna, Vol. II, p. 71.

Jacquinot, J., R.J. Anderson, J. Arbez, and co-workers (1985). ICRF studies on JET. Plasma Physics and Contr. Fus., 28, 1.

Janeschitz, G., and co-workers (1986). Impurity production during ICRF-heating. This conference.

Keilhacker, M., and co-workers (1984). Confinement studies in L and H-type ASDEX discharges. Plasma Phys. and Contr. Fus., 26, 49.

Keilhacker, M., and co-workers (1985). Confinement and beta-limit studies in ASDEX H-mode discharges. Plasma Phys. and Contr. Nucl. Fus. Res., 1984, IAEA, Vienna, Vol. II, p. 71.

Leuterer, F., and co-workers (1985). Lower hybrid experiments in the ASDEX tokamak. Plasma Phys. and Contr. Fusion, 27, 1399.

McCormick, K., and co-workers (1986). Influence of the lower hybrid wave spectrum on the current distribution in ASDEX. This conference.

Meisel, D., and co-workers (1986). Periodic Thomson scattering diagnostic with 16 spatial channels on ASDEX. This conference.

Müller, E.R., G. Janeschitz, P. Smeulders, and co-workers (1986). Evolution of radiation power profiles in ASDEX H-mode discharges. This conference.

F. Ryter, and co-workers (1986). Comparison of ICRH and LH generated fast ions in NI heated ASDEX plasmas. This conference.

Söldner F.X., D. Eckhartt, F. Leuterer, and co-workers (1985). Power absorption studies for lower hybrid heating and current drive in ASDEX. Proc. 12th Europ. Conf. on Contr. Fus. and Plasma Phys., 9F, Part II, 244.

Söldner, F.X., D. Eckhartt, F. Leuterer, and co-workers (1986). Stabilisation of sawtooth oscillations by lower hybrid waves in ASDEX. This conference.

Stäbler, A., F. Wagner, and co-workers (1984). Energy confinement time scaling of ASDEX L and H-discharges. In H. Knoepfel and E. Sindoni (Eds.). Proc. 4th Int. Symp. on Heating in Toroidal Plasmas, Vol. 1, p. 3.

Steinmetz, K., and co-workers (1985). High-power ICRF heating on the divertor tokamak ASDEX. Plasma Phys. and Contr. Fus., 28, 235.

Steinmetz, K., F. Wagner, F. Wesner, and co-workers (1986a). ICRF H-mode and 2 Ω_{CH}/D(H)-heating on ASDEX. This conference.

Steinmetz, K., Wesner, F., Niedermeyer, H., and co-workers (1986b). Ion cyclotron studies in the divertor tokamak ASDEX. Journal of Vacuum Science and Technology (A), to be published.

Wagner, F., O. Gruber, K. Lackner, and co-workers (1986). An experimental study on the principles governing tokamak transport. Accepted for publication in Phys. Rev. Lett.

Wagner, F., and co-workers (1985). The H-mode of ASDEX. Proc. of the Workshop on Basic Physical Processes of Toroidal Fusion Plasmas, Varenna (1985).

Wagner, F., G. Becker, K. Behringer, and co-workers (1982a). Regime of improved confinement and high beta in neutral beam heated divertor discharges of the ASDEX tokamak. Phys. Rev. Letters, 49, 1408.

Wagner, F., G. Becker, K. Behringer, and co-workers (1982b). Confinement and β_p-studies in neutral-beam-heated ASDEX plasmas. Proc. 9th Int. Conf. on Plasma Physics and Contr. Nucl. Fusion Research, Baltimore 1982, Vol. I, IAEA, Vienna (1982) 43.

REVIEW ON PELLET FUELLING

M. Kaufmann

Max-Planck-Institut für Plasmaphysik, EURATOM Association,
D-8046 Garching, Fed. Rep. of Germany.

ABSTRACT

Injection of frozen hydrogen pellets was already proposed as a means of fuelling plasmas at an early stage of fusion research. After an extended period of technical development, gas gun pellet injectors are now available with speeds of up to 2000 m/s (in single-shot operation and in series of up to 7 shots per discharge). Centrifuges can deliver up to 80 pellets per discharge with speeds of up to 800 m/s.

Substantial progress in understanding pellet ablation was achieved with the description of a cold gas mantle shielding the pellet against the hot plasma. For ohmic discharges with sufficiently high density, good agreement between this "neutral shielding model" and the experimental observation of ablation was found. In the case of non-thermal electrons much faster ablation has been observed. The pellets explode at the plasma edge in extreme cases. With neutral injection part of the pellets often seems to be ablated outside the plasma. Inside the plasma enhanced ablation by fast ions has to be taken into account.

For several years now a growing number of experiments with pellet injection have been conducted on hot plasmas. So far different influences on the plasma performance have been reported: Strong peaking of the density profile is usually also seen in cases where the pellet does not penetrate to the centre. In ohmic discharges with sufficient edge recycling it was observed that the averaged density increases and in parallel the particle and energy confinement are substantially improved. With growing neutral injection power, this improvement degrades, while the central particle and energy confinement remain enhanced.

The peaked density profile is accompanied by a strong inward drift of high-Z material. The resulting radiation from the centre keeps the increase of the density limit below or equal to 100%.

1. INTRODUCTION

Early in fusion research Spitzer [1] (1954) advocated injection of hydrogen pellets for the fuelling of a stellarator. He argued that fuelling close to the walls by gas puffing is extremely inefficient: this fuel would be the first to be withdrawn by the divertor.

It took about two decades to introduce experiments with pellet injection and about another decade to get reliable pellet injectors at least for a fair number of the larger fusion devices. This relatively slow development was caused, on the one hand, by the difficult technical problems in preparing and accelerating pellets of frozen hydrogen. The unexpected success, on the other hand, of fuelling a fusion plasma by gas puffing played a role in limiting the requirements for pellet injectors. A lack of confidence that frozen hydrogen pellets can penetrate deep into hot plasmas might finally have contributed to reducing the efforts made. These difficulties have now been overcome. Pellet injectors with velocities of up to 2000 m/s and up to 80 pellets per discharge are feasible and pellets can travel deep into hot plasmas, the ablation is - to a fair degree - theoretically understood, and pellet injection experiments have demonstrated the capacity for improving refuelling, for diagnosing plasmas and, most essential, for improving plasma performance. Furthermore, there is hope that the systematic changes of plasmas by pellet injection will contribute to the understanding of confinement.

This review of pellet injection work only briefly summarizes the technical development and status of injectors. Ablation theory and comparison with experiments are also reported in condensed form. The report concentrates more on contributions to

plasma confinement. In the following the most essential highlights of pellet experiments will be reviewed without any claim to completeness. In the next section an attempt is made to derive a common picture of these experiments and to discuss it. The report closes with some remarks on status and prospects.

2. STATUS OF PELLET INJECTORS

For the acceleration of pellets the thermal and mechanical properties of solid deuterium or hydrogen have to be taken into account. Acceleration methods have to be chosen which couple nearly no thermal energy to the pellet: the atomic binding energy in deuterium is $\sim$ 0.01eV, while the kinetic energy at 1 km/s is of the order of 0.02 eV. The tensile strength of solid hydrogen imposes a strong limitation on acceleration. Hydrogen of 4.2 K has a very small tensile strength of 5.5×10^5 Pa only, which even decreases to 4.5×10^5 Pa at about 12 K [2]. Taking into account these limitations, two types of pellet injectors have been successfully developed: the gas gun and the centrifuge.

Different types of gas guns using hydrogen or helium with pressures of up to 10 MPa of the propellant gas were developed at Risø [3], at ORNL[4,5] and at IPP Garching [6, 7]. In an Oak Ridge gun the pellet is frozen from the gas phase into one or more holes in a rotatable disc (Fig. 1a). The pellet is brought to the entrance of the barrel by rotation. In the pellet guns of Risø and Garching (Fig. 1b), the pellet is formed by extrusion from stored solid deuterium. The high extrusion pressure leads to a more homogeneous ice. The formation of the pellet itself is done by cutting with a rotatable cylinder or punching with a moveable barrel. Extrusion and punching with the barrel are also used in the repeating pellet injector of ORNL. Guns of these types produce pellets from 0.3mm in diameter up to 4.6 mm in diameter and accelerate them up to velocities of 1600 m/s.

Pellet centrifuges were developed at ORNL and Garching. The pellet velocities available are not limited by the tensile strength of the rotor material but by the strength of the solid deuterium. The ORNL centrifuges [8] (Fig. 2a) using carbon fibre or Kevlar rings would be able to accelerate pellets to a velocity of up to 2000 m/s with about 40 Hz. However, above a pellet velocity of 800 m/s, the pellets are damaged. The IPP centrifuge (Fig. 2b) [9] uses a non-optimized disc rotor and was operated up to pellet velocities of 720 m/s. It ejects up to 80 pellets at minimum time intervals of 20 ms. While in the ORNL centrifuge at maximum pellet velocity a stress of $\leq 3.3 \times 10^5$ Pa can be estimated, in the IPP centrifuge one finds, correspondingly, the extremely high value of $\approx 10^6$ Pa. This difference might be explained by the different temperatures at which the pellets are fed into the centrifuge. The pellets in the ORNL centrifuge are inserted at extrusion temperature (typically 12 K), while in the IPP centrifuge the pellets are fed in at about 6 K.

The injection of pellets can be facilitated by the use of guide tubes, which were suggested by Risø [10]. With limited curvature of the tubes pellets remain undestroyed and survive without substantial loss of mass and velocity, and the scatter angle remains acceptable. These guide tubes facilitate the application of injection in plasma experiments.

Today, development is mainly directed at higher pellet velocities for multiple and repeating gas guns. Higher velocities can only be reached by a higher temperature of the propellant gas. In a recent development at Risø high temperature was obtained by an electric arc (Fig. 3). The pellet reached a velocity of close to 2000 m/s [11]. Other investigations include rail gun technique (University of Illinois) [12] or two-stage gas guns (JET, [13]). These developments aim at velocities of 5 – 10 km/s.

3. PELLET EXPERIMENTS

In a very first experiment with frozen hydrogen, (Risø [14]) a pellet (diameter 0.25 mm) was dropped with a velocity $v_p = 10$ m/s into an $E \times B$ rotating plasma PUFFATRON. In a somewhat similar way pellets were dropped into the PULSATOR vessel [15]. The tokamak was ignited when the pellet was in the centre of the vessel. The pellet could replace part of the gas filling.

The first experiment with a "fast" pellet shot into the ORMAK tokamak was carried out at Oak Ridge National Laboratory in 1976 [16]. Droplets were formed by liquid hydrogen streaming through a nozzle. The subsequently frozen pieces were accelerated by a helium gas flow to about 100 m/s. The relatively small pellet with a diameter of 200μ could only increase the plasma mass by 1% while travelling about 8 cm deep into the plasma. The comparison with ablation theory clearly showed the existence of a shielding cloud. Otherwise the electrons of the hot plasma would much sooner have destroyed the pellet with its sublimation energy of only 0.01 eV per particle. The H_α light signal was set proportional to the local ablation rate and good agreement with the neutral shielding model [17] was observed (Fig. 4).

In the following period of pellet experiments on ISX-A and ISX-B the pellet velocity and especially the pellet mass relative to the target plasma mass were increased. Injection using a single-shot gas gun with $v_p = 330\,\mathrm{m/s}$ on ISX-A [18, 19] led to an increase of the plasma mass by 100%. An increase of the order of 30% as measured by the central interferometer signal (curve A in Fig. 5) showed, after the fast rise caused by the pellet, a continuing slow increase. The enhanced, temporal increase seen in some cases (curve B) was attributed to inward diffusion of the material deposited in an outer shell. We shall come back to a discussion of this important phenomenon. Relatively high density jumps ($\sim$ 100%) starting from a low-density target showed no remaining density build-up (Fig. 5, lower curve) and were accompanied by strong m=2 oscillations.

With the experiments on ISX-B [20] the range of operation was again substantially increased. Single pellets with $v_p \leq 1\,\mathrm{km/s}$ of 3.7×10^{19} hydrogen atoms per pellet were fired into the ISX-B tokamak with ohmic (OH) and neutral injection (NI) heating. These discharges already showed most of the features of high-performance pellet injection: the ablation path was accompanied by H_α radiation with about $2H_\alpha$ photons per 100 ionization processes. The H_α light showed oscillation, which was attributed to an instability, and the path was bent in the direction of the electron current (OH discharge). If the pellet could travel across the axis, a strong reduction of H_α light beyond the axis was seen: the large pellets cool the plasma down on their way to the centre and beyond the magnetic axis find a meanwhile reduced temperature on the magnetic surfaces. OH discharges at low densities ($\bar{n}_e \leq 10^{19}\,\mathrm{m^{-3}}$) show a distinct increase of ablation which is attributed to the runaway electrons. In NI discharges enhanced ablation by the beam ions was also observed. In OH experiments the density could be raised by up to 300%. The particle confinement time rose from 18 to 50 ms, and - following the Alcator scaling - the energy confinement time went from 9 to 25 ms. No considerable loss due to radiation or charge exchange particles at the moment of injection was observed. In an OH discharge where runaway electrons were present, the pellet did not travel to the centre. In this case a fast drop of the temperature (1 ms time scale) was observed in front of the pellet. Also a fast redistribution of the density profile led to a pronounced peaking 20 ms after injection. The pellet was present 100% in the plasma compared with an efficiency of only 30% in the case of gas puffing.

Following these experiments, pellet injectors were used on a large number of devices. Pellet injection played an important role in producing a stellarator plasma in W VII-A. [21]. Starting from a tokamak the plasma current was decreased, the external rotational transform increased, and the neutral injection switched on. Pellet injection was used to improve the target for neutral injection. It led to a higher plasma density, and hence to better absorption of beam neutrals and beam ions and finally a faster plasma energy build-up (Fig. 6). The good particle confinement of the stellarator ($\tau_p \approx 200\,\mathrm{ms}$) kept practically all the pellet mass inside the plasma.

A double gas gun allowed two pellets ($v_p \leq 1150\,\mathrm{ms}$) to be injected into ASDEX [22]. Photographic observation revealed the peaked structure in the H_α signal to be associated with bright and dark stripes extending parallel to the magnetic field. The location of the stripes was usually reproducible. In some cases the dark stripes could be associated with magnetic surfaces with a rational q-number. However, recent observations on W VII-A [23] showed a clear stripe structure even in a case strictly without shear. The explanation in terms of an instability of the ablation therefore seems to be the most probable one.

Pellet injection in ASDEX was used for a detailed analysis of the particle transport Γ_p. The decay of the incremental density rise [25] and of the total density [26] after a pellet could be described by $\Gamma_p = -D[\frac{\partial n}{\partial r} + \alpha(r)\frac{2r}{a^2}n]$, with $D \approx 0.4\,\mathrm{m^2/s}$ and $\alpha(r) \approx 1$ (Fig. 7). This means that the increased particle confinement time in this case reflects the deeper fuelling, while the diffusion coefficient remains essentially unchanged compared with discharges without pellets [27]. Pellets doped with 1% neon showed in ASDEX diffusion again with $D \approx 0.4\,\mathrm{m^2/s}$ for neon [26, 7].

In the PDX divertor tokamak three pellets fired shortly after each other led to deeper penetration [28, 29]. In OH discharges where pellets reached the centre $n_e(0) \approx 3 \times 10^{20}\,\mathrm{m^{-3}}$ was achieved, and the very peaked density profiles decayed within 100 to 200 ms (Fig. 8). No improvement of confinement was seen. With moderate NI heating (600 kW), a peaked density profile could also be obtained and an increase in τ_e from 20 to 30 ms was reported. At high beam power only a fraction of the pellet mass could be found after injection in the plasma.

In the ALCATOR C high-field tokamak injection of up to four pellets [30–32] could considerably raise the density to record values of $\bar{n}_e \leq 10^{21}\,\mathrm{cm^{-3}}$ and $n_e(0) \leq 2 \times 10^{21}\,\mathrm{m^{-3}}$. A peaked density profile was found although the pellet did not penetrate to the centre. An analysis of the decay of the peaked profiles showed an unusually high ratio $v/D \approx 10r/a^2\,\mathrm{cm^{-1}}$ in the plasma centre (v: inward drift, D: particle diffusion coefficient). At the same time energy confinement improved at the high density: the $\tau_e(\bar{n}_e)$ curve did not show the saturation effect but reached with its highest values the ALCATOR scaling. A detailed investigation [32] showed the ion confinement to become neoclassical, while in gas puff cases ion confinement was worse by a

factor of about 3...4. It was argued that the improvement might be caused by a more peaked density profile compared with the temperature profile. The larger values of τ_e at very high densities led to record values of $\bar{n}_e \times \tau_e$ beyond the Lawson criterion (Fig. 9). The peaking of the hydrogen density was accompanied by a strong central peaking of light (C) and heavy (Mo) impurities, as detected by soft-X-ray radiation [33].

Pellets from a Risø gas gun [34] were injected into TFR plasmas and the redistributions of density and temperature during and after ablation were investigated [35, 36]. With pellets of about 10^{19} particles and $v_p = 500\,\mathrm{m/s}$ the density rose by 30%. In contrast to experiments with a larger relative increase, no fast inward drift of material was observed while a cooling wave travelled with 1400 m/s faster than the pellet into the centre (Fig.10 [35]). This is comparable to the speed of temperature changes in a minor disruption. The profile $T_e(r)$ $800\mu s$ before and after ablation had the same relative shape. In a recent study the stripes of the H_α light, which extend in the toroidal direction, were used to identify the direction of the magnetic field [37]. The determination of a q profile was easier if the stripes were coloured with neon.

First experiments using a centrifuge were carried out on DOUBLET III [38, 39]. Pellets with 7×10^{19} deuterons each and with a velocity of 800 m/s could be injected at time intervals of 31 or 39 ms. Pellets were injected into limiter discharges with ohmic and neutral injection heating, where the pellets penetrated 33 and 20 to 25 cm deep, respectively, into the plasma with a radius of 40 cm. Bremsstrahlung indicated density peaking, which was attributed to inward diffusion of inverted profiles. The typical behaviour of the averaged density $\bar{n}_e$ can be seen from the interferometric signal of Fig. 11: during the OH phase $\bar{n}_e$ increased in stairsteps. After two more pellets with increase in the NI phase, no further increase can be seen. Thus the long particle confinement time in the ohmic phase has become small in the case of neutral injection. The energy confinement with OH heating was similar to the ALCATOR C observation: saturation at higher densities with gas puff ($\tau_e \leq 55\,\mathrm{ms}$) but proportional increase with $\bar{n}_e$ up to 120 ms with pellets. With neutral injection the energy confinement time degraded with time and with growing heating power. Compared with gas puff, an increase of 70% was reported for 2.4 MW while no increase can be seen for larger heating powers. The authors attribute the improvement by pellet injection to deep refuelling and reduced edge recycling.

First pellet injection on a large tokamak was carried out on TFTR with a multiple gas gun [40–44]. Up to seven pellets with particle numbers of 0.7×10^{21} and 2.1×10^{21} for deuterium and hydrogen, respectively, could be fired with velocities of 1000 to 1500 m/s. Typical penetration was half the plasma radius of 0.8 m. The pellets were used to produce a target for neutral beam injection (80 keV D-injection). In the ohmically heated phase an increase of the average density limit by up to 100% and a central density $n(0) = 4 \times 10^{20}\,\mathrm{m}^{-3}$ were observed. The global energy confinement time went up to 400 ms. This value continues the trend of saturation of the $\tau_e(\bar{n}_e)$ curve at high $\bar{n}_e$ values. A $n_e(0) \times \tau_E$ value of $1.5 \times 10^{20} s/m^3$ was reached [45]. The peaked density profile was accompanied by a flat T_e profile. Central radiation losses, with bremsstrahlung a good part of them, came close to the local heat production. Beam deposition in these pellet-prepared discharges was strongly shifted to the plasma edge. In spite of that the centre reheats fast (Fig. 12), and the authors quote a local energy confinement time of above 1 s for radii of below 0.4 m. The global energy confinement time with 5.4 MW NI was not increased beyond the value of 200 ms with gas puff.

For about one year a centrifuge [42] has been in operation on ASDEX. The centrifuge delivers up to 80 pellets with 200 to 720 m/s (typically 650 m/s). The pellets with about 4.5×10^{19} deuterons each can be fired at time intervals of 20 ms or more. Pellets were used in ohmic discharges and with different additional heating. With ohmic heating and divertor operation, two regimes with distinct differences were observed:

- In the first case [47, 48] pellets were injected early in the discharge, without gas puff in parallel and with moderate plasma target densities ($\bar{n}_e \approx 2 \times 10^{19}\,\mathrm{m}^{-3}$). In these very low recycling cases the density in the centre was higher compared with gas-fuelled discharges, although the pellet was ablated in the outer 15 cm of the radius. The attempt to get to high averaged densities ended with deep penetration up to the centre, very peaked profiles and high radiation there, and finally led to an internal disruption with m=2 activity. A TRANSP analysis showed the local thermal conductivity and particle transport to be close to the values of gas puff discharges. The energy confinement time was even smaller for the same $\bar{n}_e$ for pellets because of the additional convection and partly the radiation.
- In a second series of experiments [49, 50], the target plasma already had a high density ($\bar{n}_e \approx 6 \times 10^{19}\,\mathrm{m}^{-3}$), pellets started later in the discharge, and the gas puff was optimized to reach maximum densities. While the density limit could only be increased by somewhat more than 50%, an interesting phase of high central density was observed, which remained nearly stationary after the pellets were switched off (Fig. 13a). Comparison of the two nearly stationary and source-free density

profiles with gas puff only (curve G) and after pellet injection (curve P) (Fig. 13b), showed that the particle confinement must have changed. One can deduce $v/D \approx 2.7 \times 10^{-6} \times r^3\,\mathrm{m}^{-1}$ for the gas puff case and $v/D \approx 3.1 \times 10^{-3} \times r\,\mathrm{m}^{-1}$ for the "after pellet phase". It seems to be possible to initiate the central peaking even with slow pellets of 200 m/s penetrating only 5 to 8 cm deep. During the period of rising density and the stationary phase the energy confinement time went up to a high value of about 145 ms in this case and remained there for 400 ms (Fig. 13a). In another case $\tau_E \approx$ 160ms was reached. The discharge ended - although diverted and wall-carbonized - with an increase of radiation in the centre, a flattening of the T_e profile and an internal disruption at the time when the ballooning criterion [51] was locally violated in the centre. τ_E as a function of $\bar{n}_e$ during and after pellet injection is compared with gas puff only in Fig. 14. A clear improvement compared with the saturation curve can be seen.

4. DISCUSSION AND SUMMARY

a) Ablation

Comparison of experimental studies of ablation with theory (for references see [48, 49]) demonstrates in most cases that the pellets are shielded from the hot electrons of the plasma. Ohmically heated discharges with moderate or high density show good agreement with the neutral shielding model [17, 54, 55]. The model describes the fast self-regulation of a 3-dimensional quasi-continuous expansion of a neutral cloud around the pellet: a higher bombardment of the pellet surface by plasma electrons led to more ablation and therefore to more shielding.

Fast, non-thermal electrons in runaway discharges, in slide-away discharges [56], and with lower hybrid heating at low densities showed drastically increased ablation and reduced penetration. The deep penetration of the fast electrons into the pellet destroys the solid structure: A blow-off of the solid pellet to a volume twenty times larger was nicely detected on ISX-B[57].

In experiments with neutral injection enhanced ablation is also observed and is attributed to the beam ions. Codes describing the additional ion ablation have been developed [58, 59]. The physical process of ablation seems to be changed with neutral injection. Instead of dominant H_α light, continuous light in the outer regions of the plasma can be observed [50]. Beside the faster ablation inside the plasma, a substantial part of the mass can already be lost on the outside and does not appear in the bulk plasma. This is probably due to a fast ion population outside the separatrix.

In some areas open questions remain with respect to ablation:

- There is a basic contradiction in the neutral shielding model. The assumption of stationarity only holds for a free 3-D expansion. The fact that the ablatant will freeze to the magnetic field lines close to the pellet (distance typically a few millimetres) and should then flow one-dimensionally parallel to the field lines should lead to a substantial reduction of ablation: the ablatant should form a shielding hose of warm plasma (T_e typically a few 10 eV), [60, 63]. The obvious non-existence of this shielding might be toroidal drift of the high-beta plasma close to the pellet, and might be associated with the peaks observed in H_α light.

- The pellets on their path in the plasma bend in the toroidal direction (electron current direction in OH discharges and the opposite direction for neutral beam co-injection). They bend only weakly in the poloidal direction. It remains to be clarified whether this motion is caused by a rocket effect or whether the pellet is coupled to a plasma rotation. A possible explanation might be the following: while viscous coupling between the pellet and the plasma is small, it is much larger between the ablatant cloud and the plasma. A shielding cloud moving with the plasma would lead to asymmetric ablation, thus producing a rocket effect.

- The origin of the stripe structure is still to be revealed. The W VII-A stellarator also showed pronounced stripes in an almost shearless plasma.

- In the case of neutral injection the reduced filling efficiency and changes in the ablation processes need to be studied.

- From a spectroscopic investigation of the ablation process [61] a plasma of $n_e = 2.4 \times 10^{23}\,\mathrm{m}^{-3}$ and $T_e = 1.5$ eV was found, where the ionization takes place. From this a much higher ratio of H_α quanta to ionization processes can be calculated than experimentally observed.

b) Fast Plasma Response (1 ms time scale)

In most cases no global energy loss of the plasma during injection can be observed. In spite of that, often a locally non-adiabatic rearrangement of energy can be seen. Even if the pellet only travels to, for example, half the radius, fast cooling (100μ time scale) can be seen in the centre [25, 31, 35]. At the end of this fast process T_e profiles which are similar in their radial dependence to the profiles before injection can be seen. The nature of this process, which is part of the general observation of "profile consistency", is not clear. Fast redistribution of the plasma mass is observed in cases where pellets with a mass relatively large compared with the plasma mass do not travel to the centre (e.g. [62]). This redistribution seems to be a consequence of the non-adiabatic behaviour of the temperature: the cooling in front of the pellet produces a hollow pressure profile leading to a MHD instability.

c) Particle Transport

After numerous experiments, particle transport after pellet injection in ohmic discharges gives a relatively homogeneous picture:

- The global particle confinement time is always increased compared with cases of gas puff. This is partly a consequence of the deeper fuelling.
- In cases with low edge recycling a large part of the pellet mass leaves the plasma and does not contribute to density build-up. Detailed analysis estimates a diffusion coefficient D and an inward drift v close to values of the analysis of gas puff discharges.
- If pellet injection is accompanied by proper edge recycling, the plasma density builds up much faster (steplike behaviour of $\bar{n}_e(t)$) and a significant change in the parameters v and D can be found. Especially in the inner part of the plasma, v/D is much larger and an inward hydrogen drift can be seen. The density peaks centrally with moderate or even very shallow pellet penetration. Candidates for the change in plasma behaviour are an increase of ν^* and a relative change of the decay length of the n_e and T_e profiles. Also the change in plasma rotation [50] might be connected to this phenomenon. A final physical explanation has not yet been found, however.

  Neutral injection degrades the particle confinement as the heating power increases even with pellet fuelling. A steplike density increase was observed with counter-injection [50], indicating an improvement compared with gas puff fuelling only.

d) Impurity Transport and Density Limit

Peaked density profiles are accompanied or followed up by accumulation of impurities. Carbon, but especially heavy impurities, (e.g. [33]) accumulate in the centre. The limitation of the plasma density by edge effects ("marfes") can be eliminated by the pellets. The up to 100%higher density is limited by the accumulation of impurities. Finally, at a local radiation power close to the local heating power, the temperature profile broadens, ending in an internal disruption.

e) Energy Confinement

In all cases analyzed the energy confinement has a behaviour similar to that of the bulk plasma particle confinement. Improved global energy confinement times in ohmic discharges are always parallel to a successful build-up of averaged and especially central density by the pellets. In this way record values of $\bar{n}\tau_E$ [31, 45] were attained. A high plasma edge density obtained by sufficient recycling is again the prerequisite: too low a density at the edge leads to enhanced convection losses [48]. The high energy confinement time can be maintained until the radiation collaps occurs [49].

With neutral injection, the global energy confinement behaviour is again similar to the particle confinement behaviour: improvement was only found for limited heating power. In contrast to that - as a further demonstration of profile consistency - a dramatic improvement of the central energy confinement was found [40, 41] if the pellets shift the absorption of the neutral beam to the plasma edge.

Energy confinement in pellet-fuelled discharges is far from being optimized. Especially the combination of proper gas puffing with pellets at the right time interval should lead to further improvements.

5. PROSPECTS

Although pellet injection has so far not solved the problem of degradation with additional heating, pellets have opened up new prospects. It will have to be investigated under what conditions the improvement of particle and energy confinement observed in OH discharges can be transferred to a situation with additional heating. Besides the improvement of plasma performance, pellet-fuelled plasmas greatly extend the experimental parameter space and should thus contribute to a better understanding of transport phenomena. Attempts to improve confinement and greater attention to limit the impurities are required in parallel. The parallelism of particle and energy confinement might open the chance for ignition at relatively high n_e values.

Acknowledgement

The author would like to thank very much C. Andelfinger, K. Büchl, G. Fussmann, K. Lackner, R. Lang, V. Mertens, H. Niedermeyer, W. Sandmann, and F. Wagner for their help in preparing the material and for fruitful discussions.

References

[1] Spitzer et al., USAEC Report NYO-6047 (1954).

[2] D.N. Bol'shutkin et al., Sov. Phys. Solid State 9(1968) 1952.

[3] A. Nordskov et al., Report Risø -M-2245, (1980).

[4] S.L. Milora, C.A. Foster, Rev.Sci.Instrum. 50 (1979) 482.

[5] S.K. Combs et al., Rev.Sci.Instrum.56 (1985) 1173.

[6] H.-J. Forth et al., Vakuum-Technik 30(1981) 102.

[7] C. Andelfinger et al., Proc.13th SOFT Varese (1984)255.

[8] C.A. Foster, J. Vac. Sci. Techn. A1 (1983) 952.

[9] W. Amenda, R.S. Lang, Max-Planck-Institut für Plasmaphysik, Report No. 1/187 (1981).

[10] P.B. Jensen, V.J. Andersen, J. Phys.D: Appl. Phys.15 (1982) 785.

[11] V. Jensen, private communication.

[12] K. Kim, J. Honig, Fus. Techn. 6 (1984) 372.

[13] P. Kupschuß , private communication.

[14] L. W. Jørgensen, A. H. Sillesen, and F. Øster, Plasma Phys. 17 (1975), 453.

[15] W. Amenda, K. Büchl, R.S. Lang, L.L. Lengyel, W. Riedmüller, Proc. Pellet Workshop, Princeton (1977), 110.

[16] C. A. Foster, R. J. Colchin, S. L. Milora, Nucl. Fusion 17 (1977), 1067.

[17] P.B. Parks, R.J. Turnbull, C.A. Foster, Nucl. Fusion 17 (1977), 539.

[18] M. Murakhami et al., Proc. 7th Int. Conf. Plasma Phys. Contr. Nucl. Fus. Res., Innsbruck 1978, 1 (1979) 269.

[19] S. L. Milora, C. A. Foster, P. H. Edmonds, G. L. Schmidt, Phys. Rev. Lett. 42 (1979), 97.

[20] S. L. Milora et al., ORNL /TM-7422, and Nucl. Fusion 20 (1980), 1491.

[21] G. Cattanei et al., Proc. 9th Int. Conf. Plasma Phys. Contr. Nucl. Fus. Res., Baltimore 1982, 1 (1983) 241.

[22] K. Büchl et al., Proc. 9th Symp. Eng. Probl. Fus. Res. , Chicago 1981, 2 (1981) 1725.

[23] K. Büchl, H. Renner, IPP Annual Report (1985), IPP AR/1985.

[24] W. Engelhardt, Proc.Workshop on Diagnostics for Fusion Reactor Conditions, Varenna (1982), p.11.

[25] G. Vlases, K. Büchl, D. Campbell, Proc. 11th Europ. Conf. on Contr. Fusion and Plasma Physics, Aachen 1983, 1 (1983) 127.

[26] K. Behringer et al., DPG Tagung Regensburg, Verhandlungen 47 (1983) 395.

[27] O. Gruber, Proc. Invited Papers, Int. Conf. Plasma Physics, Lausanne (1984), Vol. 1, p. 67.

[28] S.L. Milora et al., Nucl. Fusion **22** (1982), 1263.

[29] R.J. Fonck et al., J. Nucl. Mater. **128+129** (1084), 330.

[30] M. Greenwald et al., Proc. 11th Europ. Conf. on Contr. Fusion and Plasma Physics, Aachen 1983, **1** (1983) 7.

[31] M. Greenwald et al., Phys. Rev. Lett. **53** (1984), 352.

[32] S.M. Wolfe et al., Nucl. Fusion **26** (1986), 329.

[33] R.D. Petrasso et al, MIT Report, PFC/JA-85-41 (1985).

[34] Sørensen et al., Proc.9th Int.Vacuum Congress, Madrid 1983, Ext. Abstracts, p.196.

[35] Equipe TFR, Proc. 10th Int. Conf. Plasma Phys. Contr. Nucl. Fus. Res., London 1984, **1** (1985) 103.

[36] Equipe TFR, Plasma Phys. 1984, **28**, (1986), 85.

[37] Equipe TFR, accepted for publication in Europhysics Letters.

[38] S. Sengoku et al., Proc. 10th Int. Conf. Plasma Phys. Contr. Nucl. Fus. Res., London 1984, **1** (1985) 405.

[39] S. Sengoku et al., Nucl. Fusion **25** (1985), 1475.

[40] G.L. Schmidt et al., Proc. 12th Europ. Conf. on Contr. Fusion and Plasma Physics, Budapest 1985, **1** (1985) 675.

[41] H.P. Furth, Proc. Workshop on Basic Physics for Fusion Plasmas, Varenna (1985).

[42] S.K. Combs et al., presented for publication.

[43] S.L. Milora et al., presented for publication.

[44] S.L. Milora et al, Proceedings this conference, to be published in Plasma Physics and Controlled Fusion.

[45] R. Goldston, private communication.

[46] W. Amenda, R.S. Lang, to be published in J.Phys.E: Sci.Instrum.(1986).

[47] G. Vlases et al., Proc. 12th Europ. Conf. on Contr. Fusion and Plasma Physics, Budapest 1985, **1** (1985) 78.

[48] G. Vlases, submitted for publication in Nuclear Fusion.

[49] H. Niedermeyer et al., FR-16, this conference.

[50] M.Kaufmann et al, to be published.

[51] D. Lortz, J. Nührenberg, Nucl. Fusion **19** (1979), 1207.

[52] C.T. Chang et al., Nucl. Fusion **20** (1980), 859.

[53] S.L. Milora, J.Fusion Energy **1** (1981) 15.

[54] D.F. Vaslov, IEEE Trans. Plasma Sci. PS-5(1977) 12.

[55] S.L. Milora, C.A. Foster, Oak Ridge National LaboratoryTM-5776(1977).

[56] G. Fussmann et al., Proc. 9th Int. Conf. Plasma Phys. Contr. Nucl. Fus. Res., Baltimore 1982, **1** (1983) 295.

[57] C.E. Thomas, Oak Ridge National LaboratoryTM-7486(1981).

[58] S.L. Milora, ORNL/Report TM-8616 (1983).

[59] L.L. Lengyel, Max-Planck-Institut für Plasmaphysik, Report No. 1/213 (March 1983).

[60] M. Kaufmann et al., Nucl. Fusion **26** (1986), 171.

[61] D.H. McNeill et al, Phys. Rev. Lett. **55** (1985), 1398

[62] M. Greenwald et al, Proc. of the 4th Int.—Symp. on Heating in Toroidal Plasmas, Rome (1984), Vol. II, 1033.

[63] W.W. Heidbrink et al, submitted to Nuclear Fusion.

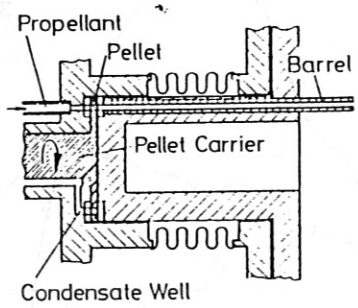

Fig. 1a: ORNL gas gun using a rotating pellet carrier.

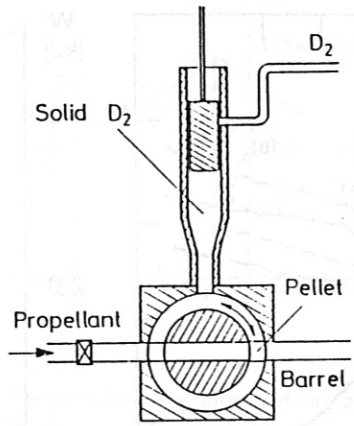

Fig. 1b: IPP extrusion-type gas gun.

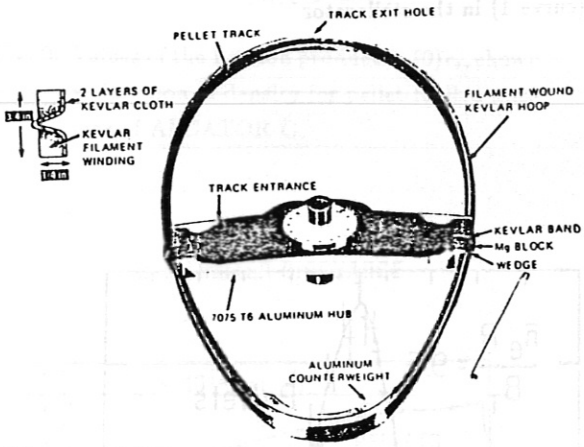

Fig. 2a: ORNL centrifuge.

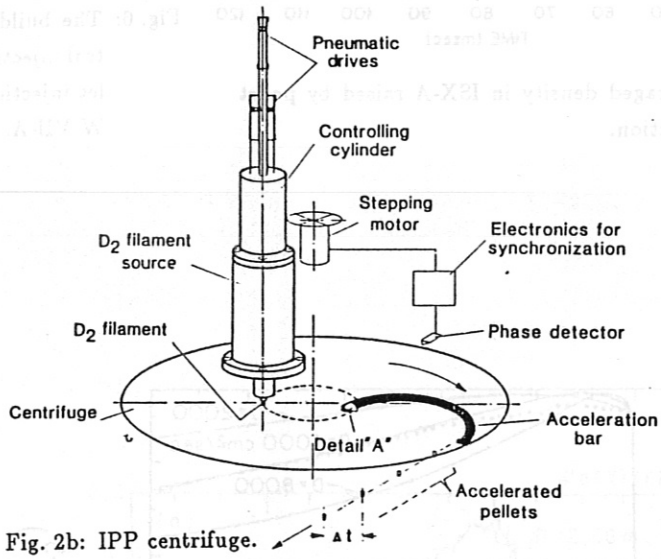

Fig. 2b: IPP centrifuge.

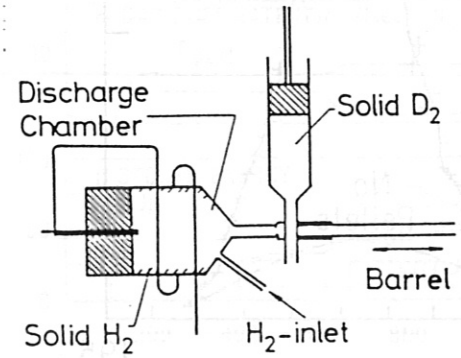

Fig. 3: Risø extrusion-type gas gun using a movable barrel. The propellant gas is heated by an electrical arc.

Fig.4: A comparison of ablation theory (neutral shielding model, solid line) with experimental data (H_α light intensity is set proportional to the ablation rate) on ORMAK.

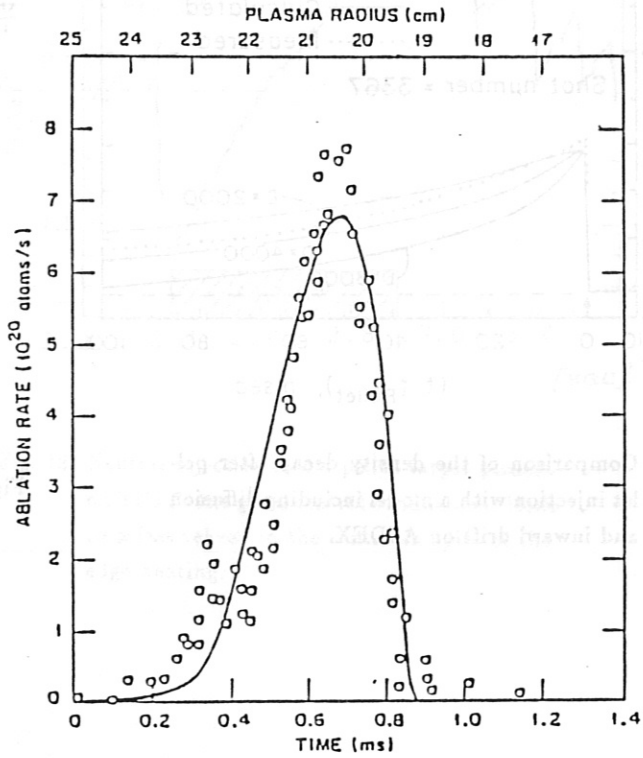

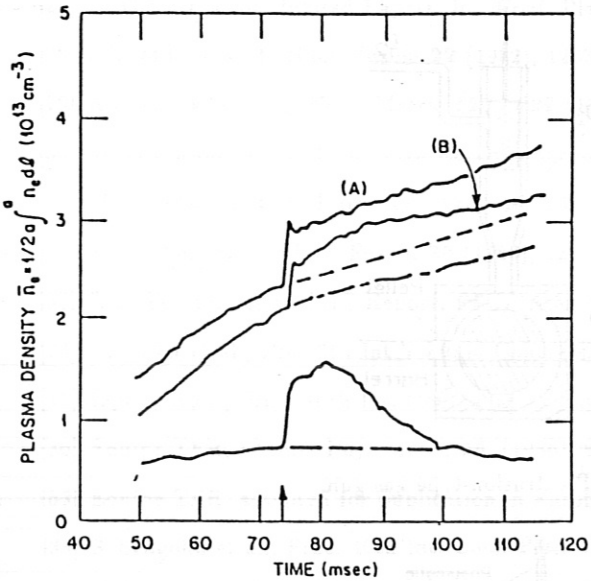

Fig. 5: Averaged density in ISX-A raised by pellet injection.

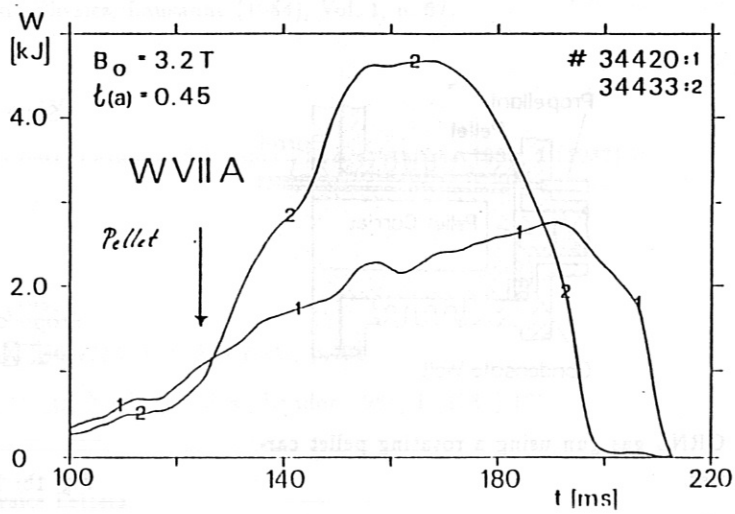

Fig. 6: The build-up of plasma energy during neutral injection with (curve 2) and without pellet injection (curve 1) in the stellarator W VII-A.

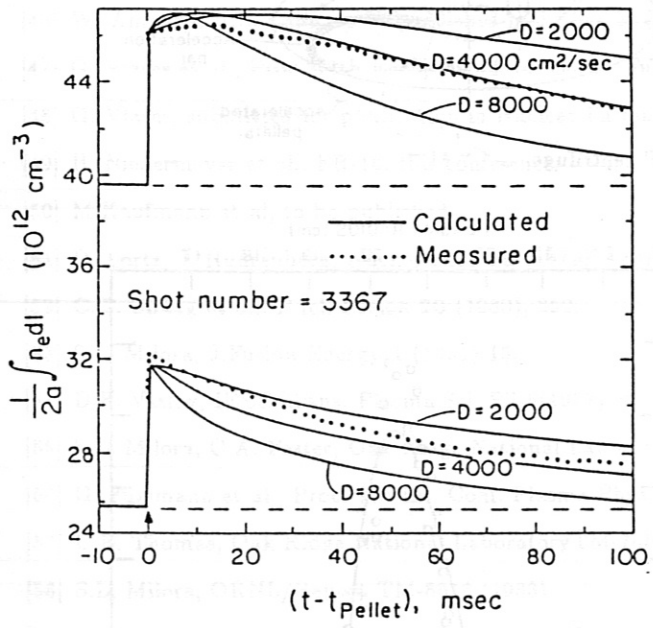

Fig. 7: Comparison of the density decay after pellet injection with a model including diffusion and inward drift on ASDEX.

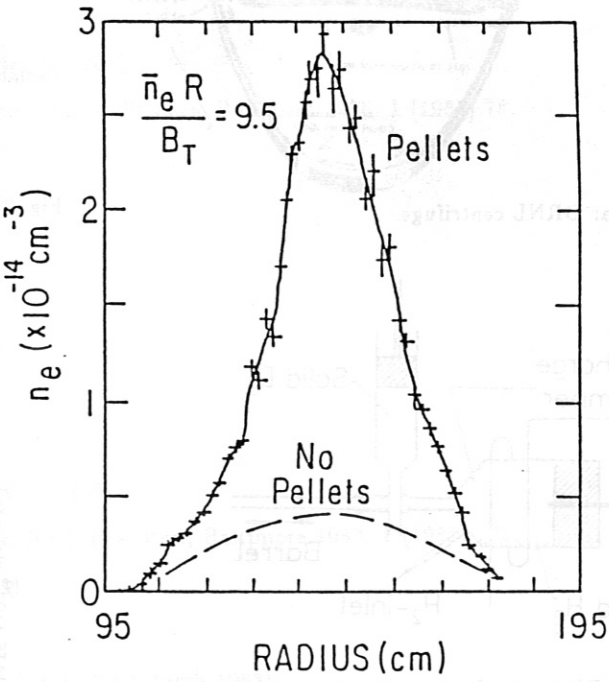

Fig. 8: Plasma density before and after pellet injection in PDX.

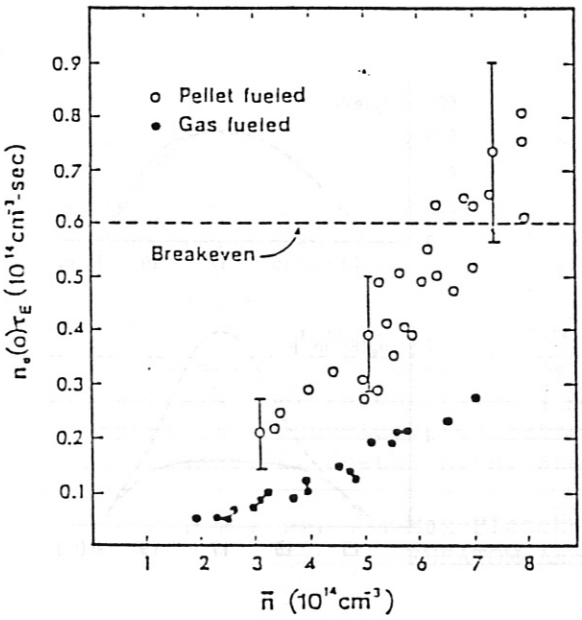

Fig. 9: Values of the Lawson product $n_e(0)\tau_e$, shown as function of density for pellet-fuelled plasmas of ALCATOR C.

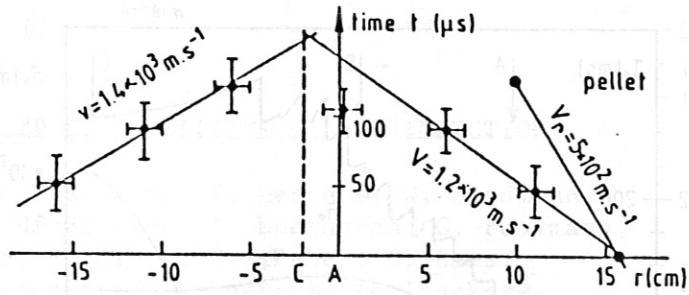

Fig. 10: Propagation diagramme of the pellet and of the cooling edge for TFR.

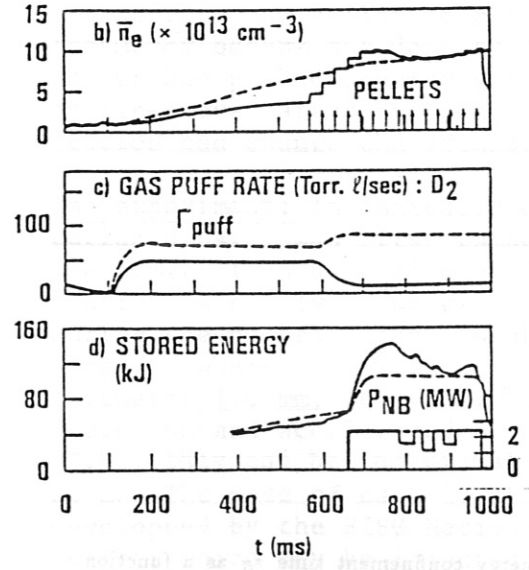

Fig. 11: Averaged density, gas puff signal and stored energy for cases with and without pellet in DOUBLET III. Neutral injection starts at about 660 ms.

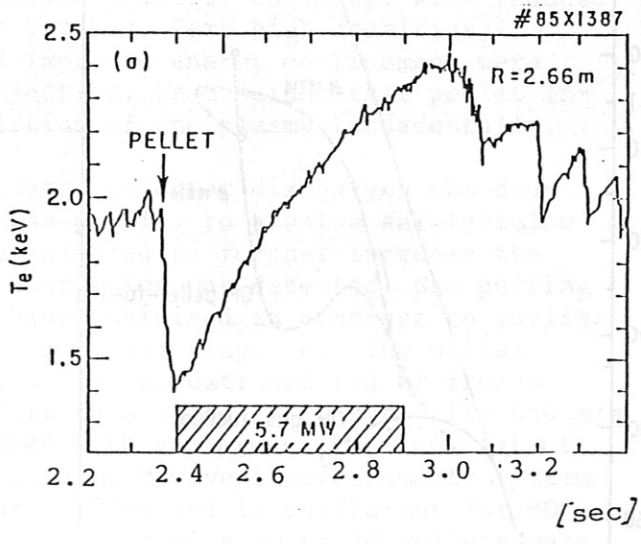

Fig. 12: Neutral injection into a pellet target plasma on TFTR: the good central confinement leads to a fast reheat in the centre in spite of the edge heating.

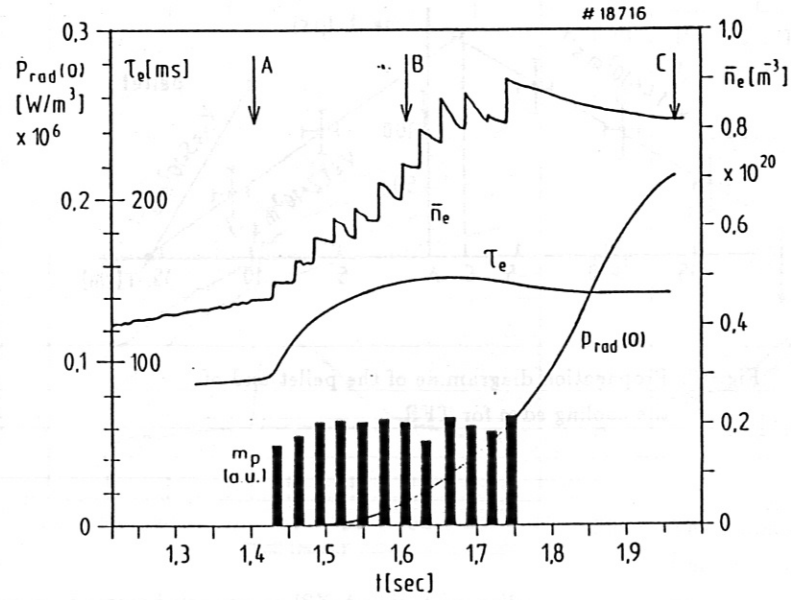

Fig. 13a: After a series of pellets injected into ASDEX the high density remained stationary for about 250 ms. τ_E reached 145 ms in this case.

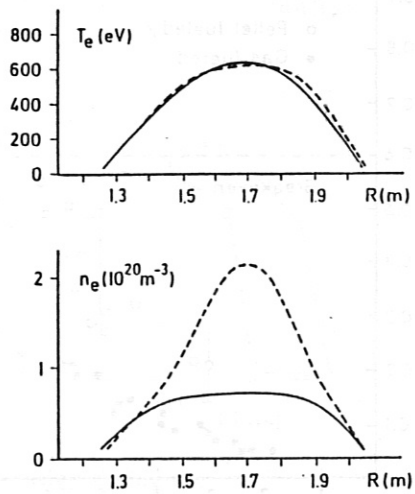

Fig. 13b: Comparison of T_e and n_e profiles in only gas-puff-fuelled (G) and a pellet-fuelled (P) cases. $n_e(r)$ is nearly stationary in time for both cases.

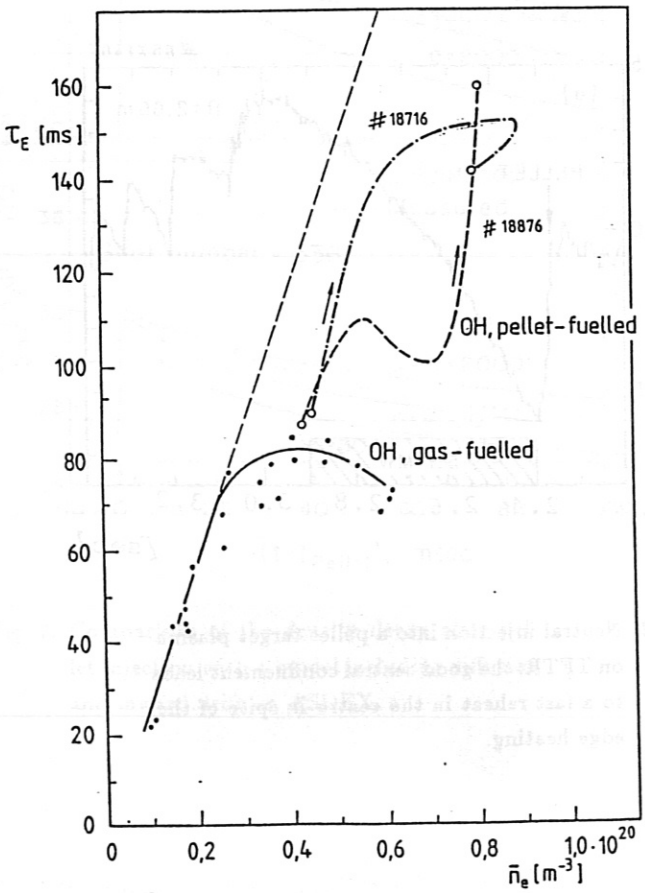

Fig. 14: Energy confinement time τ_E as a function of averaged density $\bar{n}_e$ for gas-fuelled and pellet-fuelled discharges on ASDEX (OH). Discharge No. 18876 shows the importance of recycling. In the first part pellets were injected without gas puff: τ_E improvement levels off. Together with gas puff (the second part of the trace) a significant increase of τ_E can be seen.

INCREASE OF THE DENSITY LIMIT IN ASDEX BY REPETITIVE PELLET INJECTION

H. Niedermeyer, K. Büchl, M. Kaufmann, R. Lang, V. Mertens, W. Sandmann, G. Vlases[1], G. Becker, H. S. Bosch, H. Brocken, A. Eberhagen, G. Fussmann, O. Gehre, J. Gernhardt, G. v. Gierke, E. Glock, O. Gruber, G. Haas, J. Hofmann, A. Izvozchikov[2], G. Janeschitz F. Karger, M. Keilhacker[3], O. Klüber, M. Kornherr, K. Lackner, M. Lenoci, G. Lisitano, F. Mast, H. M. Mayer, K. McCormick, D. Meisel, E. R. Müller[3], H. Murmann, A. Pietrzyk[1], W. Poschenrieder, H. Rapp, H. Riedler, H. Röhr, J. Roth, F. Ryter[4], F. Schneider, C. Setzensack, G. Siller, P. Smeulders[3], F.X. Söldner, E. Speth, K.-H. Steuer, O. Vollmer, F. Wagner, D. Zasche

Max-Planck-Institut für Plasmaphysik
EURATOM Association, D-8046 Garching

Introduction: Investigations performed on ASDEX in a large range of plasma parameters with and without neutral beam heating showed that the density limit is normally caused by energy losses at the plasma boundary /1/. The stronger gas influx needed to achieve higher densities leads to increasing recycling losses and increasing radiation at the edge. At a certain average density the discharge becomes unstable. It seems to be obvious that more efficient refuelling deeper inside the discharge, e.g. by injection of fast pellets, should result in a higher density limit. High densities have been achieved in several experiments by a fast density ramp up with a few pellets /2/,/3/,/4/,/5/. In ASDEX also slow ramp up with a large number of pellets was applied and pellet injection was switched off or continued with reduced frequency before the density limit was reached. Very high densities, favourable peaked density profiles and improved energy confinement were obtained even after stopping pellet injection. We conclude that pellet injection can change the transport properties of the plasma fundamentally.

The experiment: In ohmically or beam heated divertor discharges the deuterium density was first ramped up by gas puffing to a value safely below the limit. Then deuterium pellets were injected to further increase the density as slowly as possible until a disruption was detected. Gas puffing during the pellet injection phase has been optimized in contrast to earlier work /6/ where it has been attempted to minimise recycling. The pellets (diameter 1.0 mm, length 1.0 mm) are cut from an extruded rod of frozen deuterium and accelerated by a centrifuge to a velocity of typically 650 m/s /7,8/. They can be individually triggered with a minimum time interval of 20 ms. The mass of each is measured with a microwave interferometer system developped by the RISØ National Laboratory. One rod is sufficient for 80 pellets which may be injected in one burst. Normally 20 to 30 pellets were injected with a repetition rate of one per 30 ms. In some discharges the repetition rate was reduced after a few pellets or injection was switched off to keep the plasma density constant. The $5 \cdot 10^{19}$ particles of one typical pellet correspond to a volume averaged density of $1 \cdot 10^{13}$ cm^{-3}.

Line averaged densities: Figure 1 shows a Hugill plot of divertor discharges at the density limit. All ohmically heated discharges in non-carbonised

---

[1]University of Seattle, DOE contract; [2]Academy of Sciences, Leningrad, USSR; [3]Present address: JET Joint Undertaking, England; [4]CEN Grenoble, France

vessel with gas refuelling lie close to the solid line. The points marked with figures indicate the best discharges achieved so far with pellet refuelling in three different scenarios: ohmically and beam heated plasmas in non-carbonised vessel and ohmically heated plasma in carbonised vessel. For optimization the pellet frequency and the amount of additional gas puffing have been varied. The benefit of wall carbonisation for ohmically heated pellet discharges is clear and much higher than for gas puffed discharges (not shown in Fig. 1). Low power beam heating increased nR/B_T to about 9 in pellet refuelled discharges without wall carbonisation. It was not yet possible to exceed this value with wall carbonisation. High power co-injection did not permit to reach high densities without heavy gas puffing, so that no substantial improvement could be achieved with pellet injection at high beam powers.

Profiles: Pellet injection permits a much larger relative increase of the fusion relevant central density than of the line averaged density usually plotted in Hugill diagrams. A comparison of density and electron temperature profiles from two shots close to the density limit, one with gas puffing alone, the other one with pellet refuelling, reveals dramatic differences (Fig. 2). Density profiles with efficient pellet refuelling are strongly peaked in contrast to the rather flat gas puffing profiles. T_e profiles of gas puffing shots normally stay peaked up to the disruptive end while T_e profiles of pellet shots flatten shortly before the disruption. The time evolution of a pellet refuelled discharge which was driven close to but not into the density limit is shown in Figs. 3 and 4. Before pellet injection (A) we observe a flat n_e and a peaked T_e profile. The radiation profile (P_{rad}) is peaked at the edge with negligible radiation on axis. During pellet injection (B) the density profile peaks, the central radiation increases exponentially, the T_e profile stays peaked as long as the radiation profile is hollow. These characteristic features are observed during the pellet injection phase and even a few hundred milliseconds after its end. Finally (C) the central radiation has strongly increased to a value comparable to the local power input and flattened the temperature profile. T_e- and n_e-profiles are similar to the ones at the density limit shown in Fig. 2. Now the discharge disrupts at a density below the limit reached with continuous density increase. The radiation source has been spectroscopically identified as iron. An increase of low-Z impurities is not being observed, Z_{eff} stays close to 1.

The disruption: In contrast to gas refuelled shots a further increase of the density with pellets is not prevented by edge effects but by central radiation. With flattening T_e-profile the current density profile flattens until a stability limit is violated. A stability calculation based on fitted n_e- and T_e-profiles states that the ballooning limit is being reached. Wall carbonisation reduces the level of iron in the discharge by an order of magnitude, so that the critical level of central radiation is reached later at a higher density. It has been found that additional gas puffing also permits to reach a higher density at a certain level of radiation. We have identified high-Z impurity radiation as the limiting factor. The level of radiation observed cannot be explained by the higher density, but an increase of impurities has to be assumed. Enhanced impurity release can be excluded from spectroscopic measurements. The only possible explanation is accumulation of impurities.

Particle transport: The initial idea was to obtain peaked density profiles by moving the particle source from the boundary to the centre, but the measured profiles cannot be explained by a peaked source term. The pellets penetrate to slightly inside half the minor radius only. In the discharge phase after pellet injection the only particle source is at the edge. Assuming that the particle transport may be described by a diffusion term with a diffusion coefficient D(r) and an inward drift term with a drift velocity v(r), we analysed nearly stationary phases of a pellet shot (C in Fig. 4) and of a gas refuelled high density discharge (Fig. 2). One finds that the gas puffing profile is very well approximated with $v/D \sim r^3$, the pellet profile with $v/D \sim r$, however. Pellets, though not penetrating to the centre, apparently change the transport coefficients throughout the plasma. The effect begins with pellet injection and lasts until a few hundred milliseconds after its end, the magnitude of the effect varies, however, during the density ramp up: the density gain associated with each pellet scatters and is not proportional to the pellet size (the first ones are normally very efficient). High power co-injection seems to prevent switching of the transport properties. The impurity accumulation observed may be explained by an inward drift as well, if the ratio of drift velocity to diffusion constant is much higher for high-Z impurities than for deuterium. Because saturation has never been reached in the experiments a quantitative description is not possible.

Energy confinement: The modified transport properties do not only result in good particle confinement but also in strongly improved energy confinement. Improvement of the energy confinement is not caused by higher densities but is switched on by pellet injection as we see in Fig. 3. Absolute values of up to 160 ms were achieved in other discharges. An improvement of the global energy confinement time of 80 % was observed in ohmic discharges only. High power co-injection prevents an improvement of the energy confinement as it prevents peaking of the density profiles.

Conclusions: Pellet injection is able to switch the confinement properties of a tokamak discharge fundamentally. This switching is possible with pellets penetrating to the half-radius (there are indications that even much smaller penetration depths are sufficient). Improved particle confinement and triangular density profiles permit to achieve extremely high central densities. Substantially improved energy confinement is provided in this transport regime. The problem of impurity accumulation has to be solved which prevented to sustain this transport mode stationarily and a way has to be found to sustain the regime with high heating power.

References:

/1/ H. Niedermeyer, et al., Proc. 12th European Conf. on Contr. Fusion and Plasma Physics, Budapest 1985, part 1, p. 159.
/2/ M. Greenwald, et al., Proc. 11th European Conf. on Contr. Fusion and Plasma Physics, Aachen 1983, part 1, p. 7.
/3/ G.L. Schmidt, et al., Proc. 12th European Conf. on Contr. Fusion and Plasma Physics, Budapest 1985, part 2, p. 674.
/4/ S. Sengoku, et al., Nuclear Fusion, Vol. 25, No. 10 (1985), p. 1475.
/5/ R.J. Fonck, et al., Journal of Nuclear Materials 128 & 129 (1984), p.330.
/6/ G. Vlases, et al., submitted to Nuclear Fusion.
/7/ W. Amenda, R.S. Lang, Proc. 13th Symp. on Fusion Technology, Varese 1984, p. 243.
/8/ W. Amenda, R.S. Lang, to be published in J. Phys. E: Sci. Instrum. (1986).

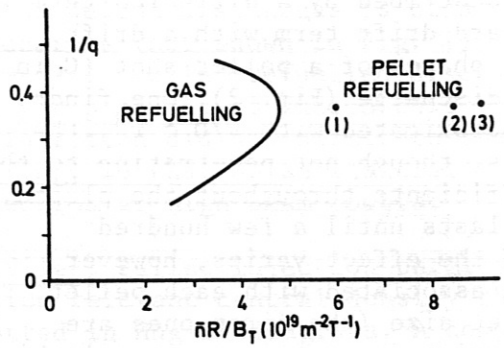

Fig. 1: Hugill plot of discharges at the density limit with gas refuelling (ohmic heating, solid line) and pellet refuelling
(1) OH non-carbonised wall
(2) OH carbonised wall
(3) NI 0.43 MW non-carbonised

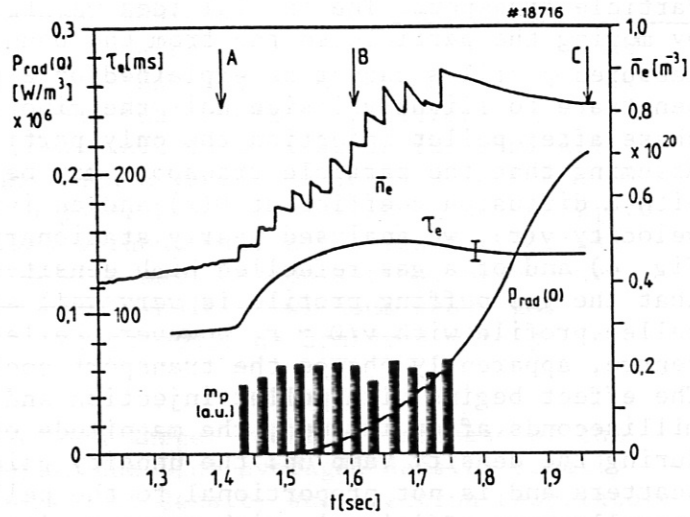

Fig. 3: Time evolution of the line averaged density n_e, radiation density on axis P_{rad}, global confinement time τ_E and pellet mass during a discharge with injection of 12 pellets.

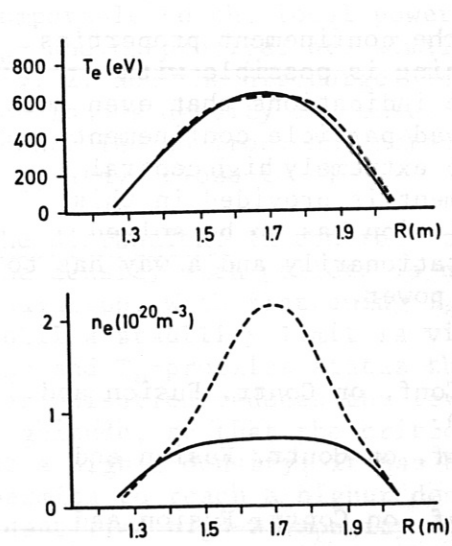

Fig. 2: T_e- and n_e-profiles of high density discharges with gas puffing (solid lines) and pellet injection (dashed lines).

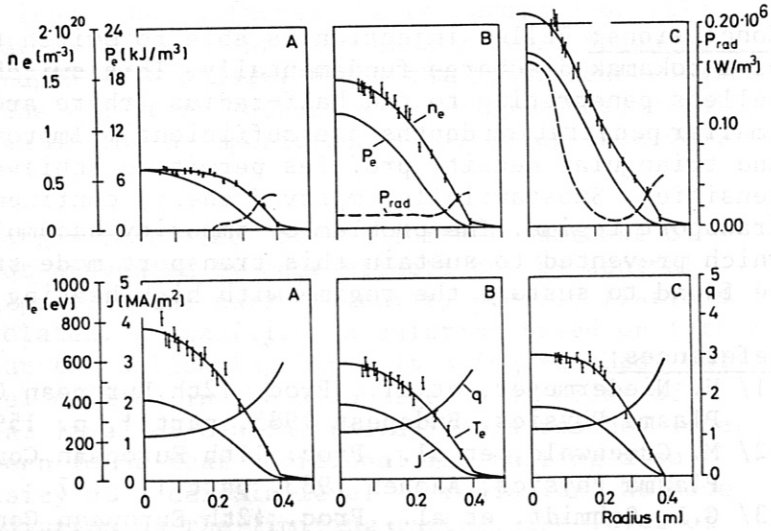

Fig. 4: Profiles of the electron density n_e, electron pressure p_e, radiation density P_{rad}, current density J, safety factor q at three times as indicated in Fig. 3.

ENERGY AND PARTICLE TRANSPORT IN MEDIUM-DENSITY ASDEX PELLET DISCHARGES

O. Gruber, W. Jilge, V. Mertens, G. Vlases, M. Kaufmann, R. Lang, W. Sandmann, K. Büchl, H.S. Bosch, H. Brocken, A. Eberhagen, G. Fussmann, O. Gehre, J. Gernhardt, G. v. Gierke, E. Glock, G. Haas, J. Hofmann, G. Janeschitz, F. Karger, M. Keilhacker, O. Klüber, M. Kornherr, K. Lackner, M. Lenoci, G. Lisitano, F. Mast, H. M. Mayer, K. McCormick, D. Meisel, E. R. Müller, H. Murmann, H. Niedermeyer, W. Poschenrieder, H. Rapp, H. Röhr, F. Ryter, F. Schneider, C. Setzensack, G. Siller, P. Smeulders, F. X. Söldner, K.-H. Steuer, F. Wagner, D. Zasche.

Max-Planck-Institut für Plasmaphysik, EURATOM Association,
D-8046 Garching, Fed. Rep. Germany.

1. INTRODUCTION

In ASDEX a comparison of ohmically heated divertor discharges with gas fuelling (GF) and pellet fuelling (PF), without any gas puffing after a gas puff "start-up" phase, has been done [1].

With a large interval between successive pellets ($\Delta t_p \approx 40\,\mathrm{ms}$) the density stayed below $2 \cdot 10^{19}\,\mathrm{m}^{-3}$ and only small differences resulted in the radial plasma parameter profiles and the transport behaviour comparing PF and GF discharges at the same density. With $\Delta t_p \approx 35\,\mathrm{ms}$ a medium density of $\overline{n}_e \approx 3.3 \cdot 10^{19}\,\mathrm{m}^{-3}$ resulted where the pellet penetration depth increased up to ≥ 25 cm, primarily a consequence of the continuously falling electron temperature (shot PM). The PM density profiles are much more peaked than the profiles of the gas-fuelled discharge GC at the same density $\bar{n}_e$, whereas the PM T_e profiles become only slightly broader compared with the GC T_e profiles (see Fig. 1). The corresponding $T_e(o)/\langle T_e \rangle$ values for both discharges are still within the scatter of the data showing pofile consistency at the corresponding $q_a^* = 3.4 : T_{e0}/\langle T_e \rangle = 2.2 \div 2.7$ [2]. In the PM discharge a distinct increase of the totally radiated power and of the radiation power density in the plasma centre is observed and sawteeth are absent after 1.1 s. With still further reduced $\Delta t_p < 33$ ms the density is limited to $< 5 \cdot 10^{19}\,\mathrm{m}^{-3}$ by a radiation collapse and is comparable with the density limit of a GF discharge. Only combining pellet injection and gas puffing and using wall carbonization considerably higher densities can be obtained [3].

This paper deals with a detailed comparison of the radial transport of the PM and the GC discharges with the transport analysis code TRANSP [4] using the measured radial profiles of n_e, T_e and radiation losses.

2. PARTICLE TRANSPORT

In the PF discharges the particle fluxes Γ inside $r < 0.75a$ are solely determined by the decrease of the particle content after the pellet injection event, which is equal to the pellet fuelling rate there. Only for larger $r > 3/4a$ has the particle recycling flux (and the gas puff rate in GF discharges) to be considered as an additional source term. From the calculated Γ at $r = 30\,\mathrm{cm}$ (Fig. 2) a $\dot{N} = \Gamma \cdot 2\pi R \cdot 2\pi r = 10^{21} s^{-1}$ is obtained therefore, which is equal to $\Delta N_{pellet}/\Delta t_p$. The total particle confinement time has been estimated from pressure measurements in the divertor chamber to increase from 60 ms (GC) to about 100 ms (PM), yielding only a small recycling flux $2 \cdot 10^{19}\,\mathrm{m^{-2}\,s^{-1}}$ at $r = a$ in the latter case.

The particle flux Γ can be modelled by the ansatz $\Gamma(r,t) = -D\frac{\partial n}{\partial r} - nv_{in}$, where v_{in} is an anormal "inward drift" velocity. Fits have been tried to yield a consistent description of D and v_{in} over a pellet cycle by using 1) $v_{in} = v(a)r^2/a^2$, yielding D(r,t), 2) $v_{in} = 3\frac{r^2}{a^3}D$, yielding D, 3) $D = 4000\,\mathrm{cm^2/s}$, yielding v(r,t) and 4) $D = 0.2 \div 0.4\chi_e$, yielding again v. The electron thermal diffusivity χ_e was determined from the energy transport analysis (s. Sec. 3). In practice scatter is large, but model 3) can be excluded and models 2) and 4) give about equal results for D and v, correspondingly. The same model, $D = 0.3\chi_e$ and $v_{in} = 3\frac{r^2}{a^3}D$, describes also GF discharges with constant or rising density [5].

3. ENERGY TRANSPORT

The global energy confinement time $\tau_E^* = W_{pl}/(P_{heat} - \dot{W}_p l)$ are degraded in the PM discharge from 72 ms (GC) to a pellet-cycle-averaged value of 44 ms due to three effects:

1. The total plasma energy is smaller in PM as the temperatures are decreased and the density profiles are strongly peaked (accounting for 20% of the decrease in τ_E^*).
2. Radiation losses are increased from 110 kW (GC) to 160 kW (PM) (accounting for 10%) (see Fig. 3).
3. Non-adiabatic fast losses ($\Delta W \leq 2\,\mathrm{kJ}$) occur after each pellet event constituting a time-averaged loss rate of about 50 kW for the quasi-steady PF discharge state (accounting for 10%). This energy loss is an order of magnitude higher than the energy required to ionize all injected particles. It is further equal to the time-averaged energy increase during the pellet cycle shown in Fig. 3a for the quasi-steady discharge phase.

Due to the deep pellet fuelling the convective energy losses $P_{conv} = \frac{5}{2}k(T_e + T_i)\Gamma$ exceed the electron conduction losses throughout the plasma in contrast to the GF discharges ($P_{cond,e} \gg P_{conv}, P_{rad}$ for $\bar{n}_e < 3 \cdot 10^{19}\,\mathrm{m^{-3}}$; Fig. 3b). The cycle-averaged β and $\beta_p + li/2$ values of the kinetic analysis agree with the magnetic measurements.

The local transport analysis shows further that within the error bars the cycle-averaged thermal heat diffusivity $\bar{\chi}_e^t$ can be described by the scaling $\chi_{GMG} \sim (n_e^{0.8} T_e q)^{-1}$ derived from GF discharges [5], showing no major change in the anomalous transport mechanism. But χ_e is larger than χ_{GMG} just after the pellet injection event ($t = t_p$) and smaller at the end of

the pellet cycle ($t = t_p + \Delta t_p$) (Fig. 4). On the other hand, the ohmic input power is strongly changing over one pellet cycle, too, due to the T_e decrease at the pellet injection event and the corresponding increase of the loop voltage U_L (e.g. t_p+5 ms: $P(\mathbf{OHM}) = 650\,\mathbf{kW}$, $t_p + \Delta t_p$: $P(\mathbf{OHM}) = 450\,\mathbf{kW}$). Therefore a description $\chi_e \sim (P_{cond,e}/2\pi R)/(n_e T_e \frac{r}{T_e}\frac{\partial T_e}{\partial r})$, where $P_{cond,e}$ is a certain fraction of the input power $P(\mathbf{OHM}) = U_L \cdot I$ and $\frac{r}{T_e}\frac{\partial T_e}{\partial r} \sim \frac{r^2}{r^{*2}}$ is fixed by the profile consistency (s. Fig. 1; r^* may be the $q = 2$radius), is strongly suggested and supported by the results given in Fig. 4b. One then obtains a local diffusivity $\chi_e \sim B_t U_L r^{*2}/(R^2 n_e T_e q)$ which is derived under the assumption of profile consistency and is essentially equal to $\chi_{CMG} = 3.4 \cdot 10^{15} B_t a/(R n_e^{0.8} T_e q)$ [$\mathrm{m}^2/s, T$, m , keV] with $U_L \sim a \cdot R/r^{*2}$. The ion heat conductivity is about one to two times the neoclassical one and much smaller than χ_e both for PM and GC discharges.

REFERENCES

[1] G. Vlases et al, Proc. 12th Europ. Conf. on Contr. Fusion and Plasma Physics, Budapest 1985, **1** (1985) 78.

[2] F. Wagner, O. Gruber et al, submitted to Phys.Rev.Letters.

[3] H. Niedermeyer et al. and M. Kaufmann et al, (Invited paper), this conference.

[4] R. Hawryluk, in *Physics of Plasmas Close to Thermonuclear Conditions*, Vol. 1, Varenna (1979) (EUR-FU-BRU/XII/476/80).

[5] O. Gruber, Proc. Invited Papers, Int. Conf. on Plasma Physics, Lausanne (1984) Vol. 1, p. 67.

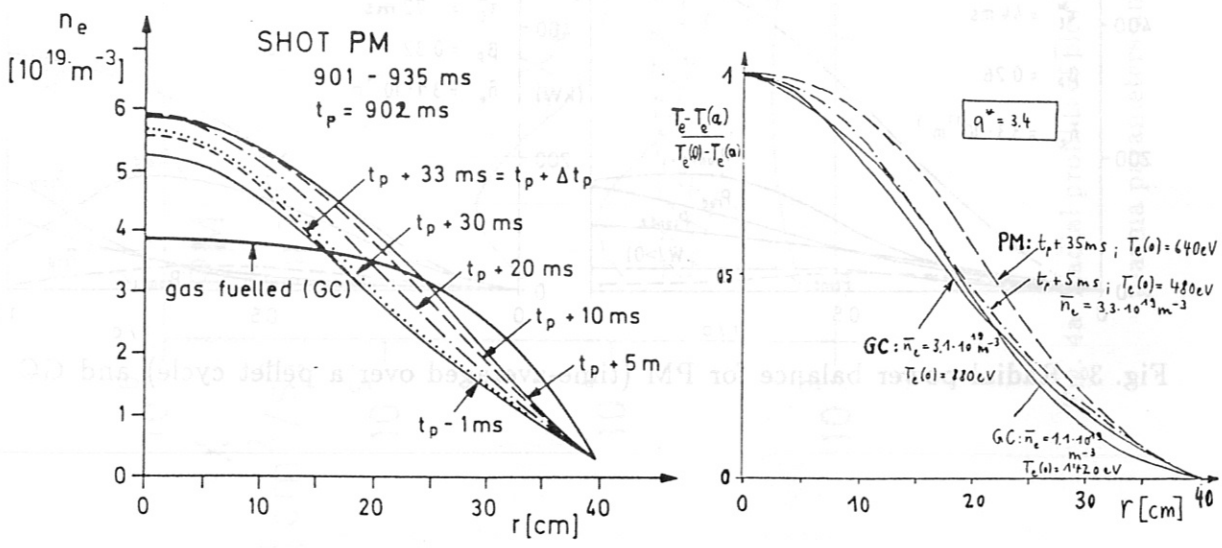

Fig. 1 Radial density and normalized temperature profiles for pellet-fuelled (PM) and a gas-fuelled (GC) discharge.

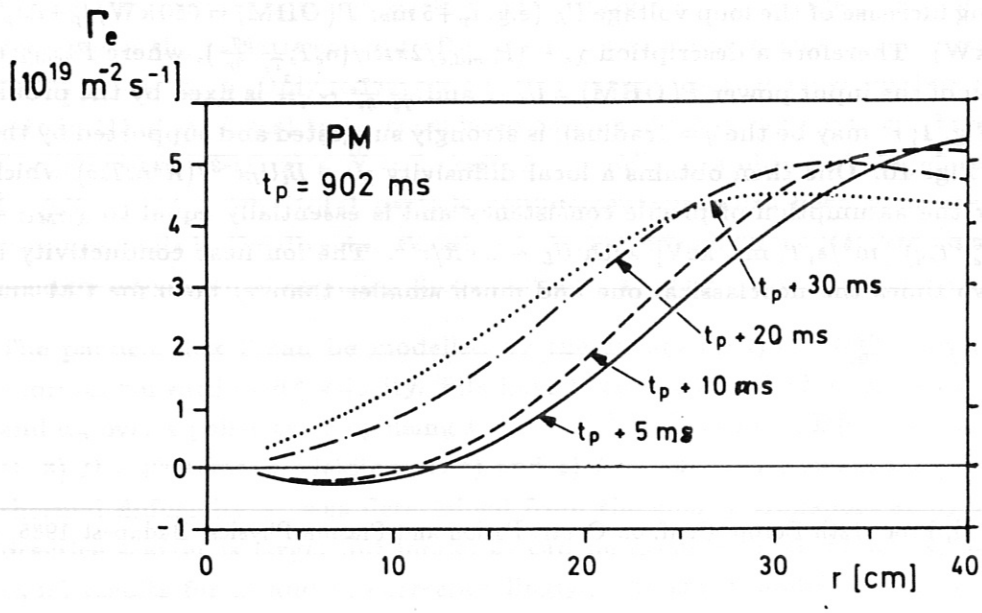

Fig. 2 Particle fluxes $\Gamma(r,t)$ for PM discharge.

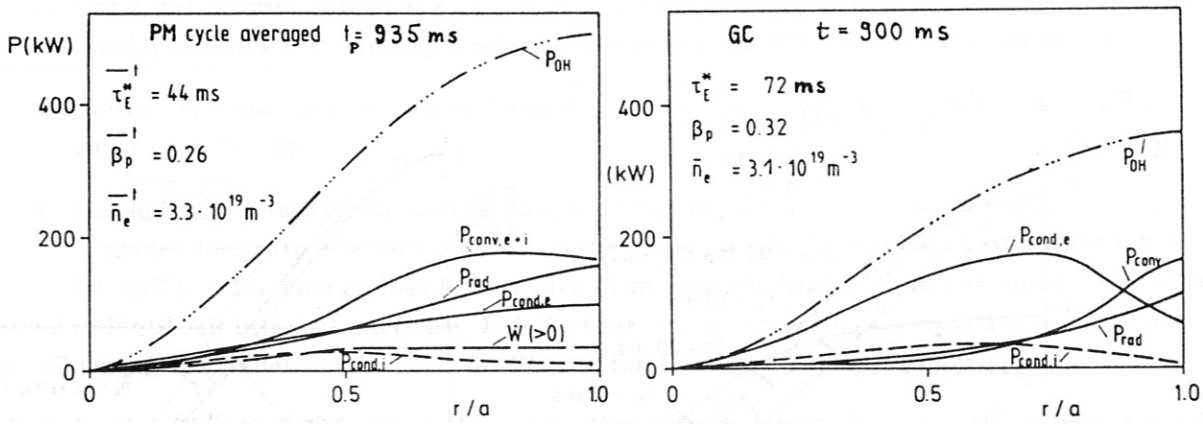

Fig. 3 Radial power balance for PM (time-averaged over a pellet cycle) and GC

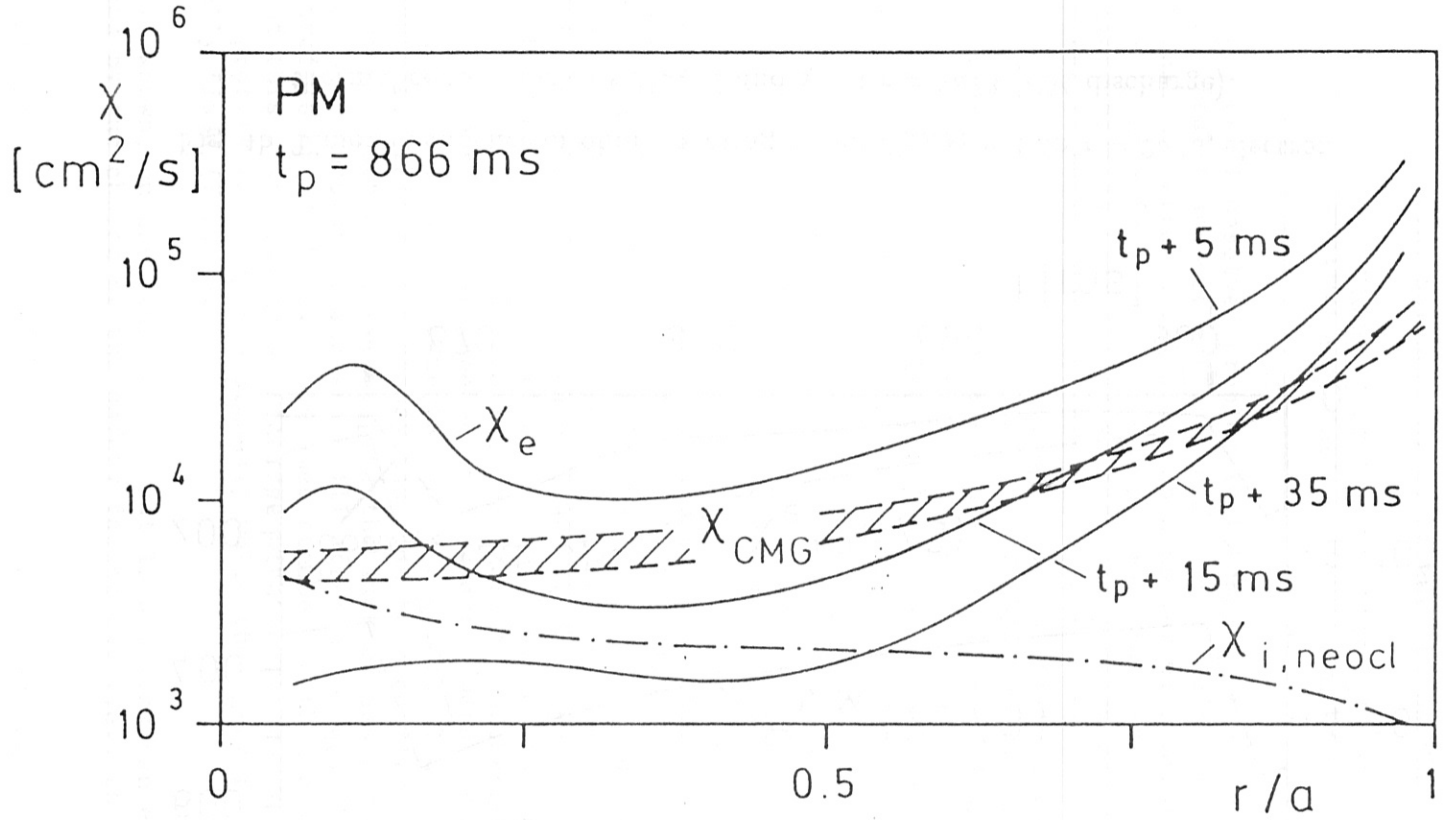

Fig. 4a Radial profiles of electron thermal diffusivity χ_e, χ_{CMG} [5] for the measured plasma parameters and the neoclassical ion heat conductivity $\chi_{i,neocl}$ (PM

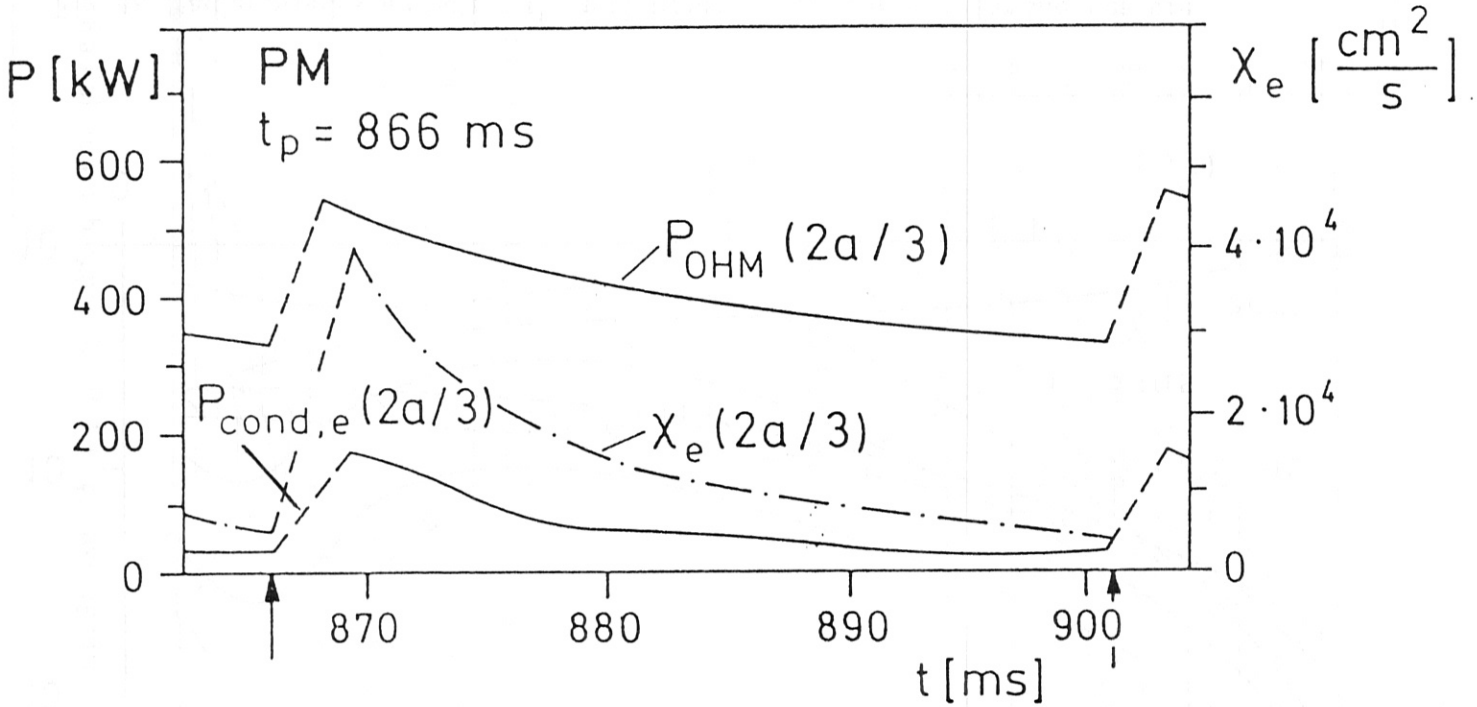

Fig. 4b Time dependence of ohmic heating power P_{OHM} within $r = 2a/3$, electron thermal conduction loss $P_{cond,e}$ and χ_e at $r = 2a/3$ (PM discharge).

ANALYSIS OF THE INVARIANCE PROPERTY OF THE ELECTRON TEMPERATURE DURING AUXILIARY HEATING IN ASDEX

H. Murmann, F. Wagner, G. Becker, H. S. Bosch, H. Brocken, A. Eberhagen, G. Fussmann, O. Gehre, J. Gernhardt, G.v.Gierke, E. Glock, O. Gruber G. Haas, J. Hofmann, A. Izvozchikov[1], G. Janeschitz, F. Karger M. Keilhacker[2], O. Klüber, M. Kornherr, K. Lackner, M. Lenoci, G. Lisitano, F. Mast, M. H. Mayer, K. McCormick, D. Meisel, V. Mertens, E. R. Müller[2], H. Niedermeyer, A. Pietrzyk[3], W. Poschenrieder, H. Rapp, H. Röhr, J. Roth, F. Ryter[4], F. Schneider, C. Setzensack, G. Siller, P. Smeulders[2], F.X. Söldner, K.-H. Steuer, D. Zasche

Max-Planck-Institut für Plasmaphysik
EURATOM Association, D-8046 Garching

A crucial and still unsolved problem in tokamak physics is the understanding of anomalous heat transport across the magnetic field via heat conduction of the electrons. All efforts to establish a universal expression for the diffusivity χ_e as a function of local plasma parameters which is valid also for auxiliary heating have failed so far. The problem has become even greater since it became evident that plasma confinement deteriorates during additional heating in a parameter range that is still very close to ohmic heating conditions. The conventional way of thinking is that additional heating of plasma affects its temperature locally according to the energy deposition profile. Consequently the electrical conductivity $\sigma \propto T^{3/2}$ will rise and thus the current density profile takes a new shape determined by the power deposition profile. This statement is, however, in clear contradiction to the experimental finding: electron temperature profiles exhibit a remarkable invariance to external influences and possess a very characteristic shape. An example is given in Fig. 1 showing temperature profiles as taken with a new Thomson scattering device with relatively high spatial resolution using a 60 Hz Nd:YAG laser. The profiles are normalized to the central value and represent four different cases: Ohmic heating (OH) alone, OH with additional neutral beam injection (NI) with different power deposition. In one case 29 keV D^o-particles were injected into a relatively high density target plasma. The beam power is then deposited at radii of 25 ... 30 cm. This is compared to the case of 40 keV D^o injection in a low density plasma with peaked power deposition. Although the central T_e values rise appreciably, the relative T_e-profile shapes remain unchanged. This profile invariance has been further checked in discharges with addition of Ne impurities, which clearly documents that rather $1/T \cdot dT/dr$ and not dt/dr keeps constant. Profile consistency has also been confirmed in cases with and without sawtooth activity. Despite the lack of sawteeth the T_e profiles are found to be consistent and are still affected by q_a. The electron density profile $n_e(r)$, however, becomes steeper in this case. Another example of this disparity is a discharge with pellet refuelling during which the $n_e(r)$ profile is changed enormously while the T_e-profile shape keeps practically fixed (Fig. 2).

It is well-known, on the other hand, that T_e-profiles can easily be influenced by the choice of the safety factor q_a, i.e., the ratio of the

---

[1]Academy of Sciences, Leningrad, USSR; [2]Present address: JET Joint Undertaking, England; [3]Univ. of Washington, Seattle, USA; [4]CEN Grenoble, France

toroidal magnetic field to the plasma current. Amazingly, this statement has also proved to hold for additionally heated plasma discharges: the T_e-profile shapes are influenced in the same manner by q_a as in the OH case, regardless where the heating power is deposited. This is demonstrated in Fig. 3 for two cases with identical plasma current but variable toroidal field with q_a = 2.9 and 4.7, respectively. Profiles are normalized to the peak value again and do not change shapes when NI-power is applied. The dependence on q_a, however, is quite evident and can be summarized impressively for a large variety of plasma conditions in a plot of $T_e(0)/\langle T_e\rangle$ versus q_a, where $\langle T_e\rangle$ is the volume averaged electron temperature (Fig. 4). $T_e(0)/\langle T_e\rangle$ represents a measure for the peakedness of a T_e profile and shows a characteristic q-dependence. The tendency is similar for $n_e(r)$ profiles but many exemptions exist which do not fit to the same characteristics, e.g. discharges with pellet injection or witout sawtooth activity /1/.

So far we concentrated on OH an NI conditions. When the plasma is additionally heated by high frequency radiation e.g. ion cyclotron resonance heating or lower hybrid heating, the profile invariance has to be restricted to a region $r > r_1$, where r_1 might be interpreted as the radius of the q = 1 surface. In both cases the heating effect is higher in the plasma center. Obviously this region $r \lesssim r_1$ is a confinement region of its own, and has to be treated separately in comparison to the region $r > r_1$. But if the T_e-profiles are normalized to a value at a radius where the influence of the q = 1 surface is negligible one observes that all profiles coincide amazingly for $r > r_1$ within the error bars of the diagnostic and yield an almost constant slope

$$(1) \qquad \frac{1}{T_{r/a = 0.45}} \cdot \frac{dT}{dr} = (4 \pm 0.3)\ m^{-1} \text{ for } r > r_1 \cdot \sqrt{2}$$

for all discharge conditions (see Fig. 5). If we apply the same procedure to merely OH and NI heated discharges, we note that eq. (1) is valid as well. In this case the deviation from eq. (1) for radii $r < r_1$ is only due to the different q_a values (Fig. 6). Thus, the profile steepening for large q_a values (Fig. 4) is mainly caused by phenomena within the q = 1 surface. Then the plasma turns into the high confinement regime during neutral injection (NI(H)) the T_e-profiles deriate slightly from the general shape due to an additional edge temperature rise.

The dominant role of q alone to constitute the T_e profile shape is quite obvious and points to the current density profile as a leading quantity to be invariant. This is also supported by the observation that the inversion radius of sawteeth is only a function of q_a and otherwise remarkably constant /2/. Via the coupling $T_e(r) \propto j(r)^{2/3}$, the temperature profile is then forced to become invariant, too. There are indeed reasons for j(r) to take a "natural shape" arising from very basic principles as minimization of magnetic field energy in a plasma column with a given toroidal current I.

References

/1/ Gehre, O., et al., this conference
/2/ Wagner, F., Phys. Rev. Letters, to be published

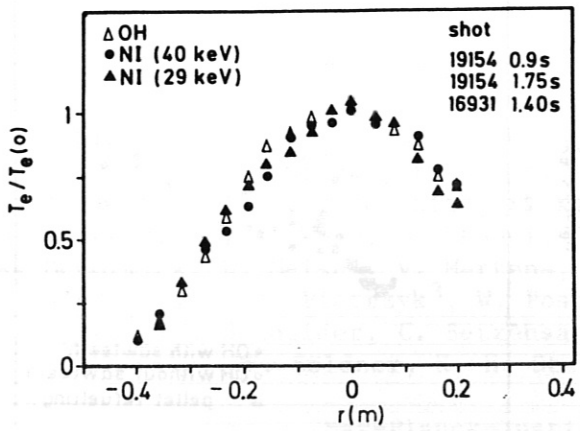

Fig. 1:
Variation of the deposition profile
Δ ohmic heating (OH)
q = 2.9; $T_e(0)$ = 0.65 keV
● 2 MW neutral injection (NI) D^o (40 keV) $\rightarrow H^+$ $\bar{n} = 2.9 \cdot 10^{13} cm^{-3}$; $T_e(0)$ = 1.68 keV; q = 2.9
▲ 1.3 MW NI, D^o(29 keV) $\rightarrow D^+$; q = 2.6 $\bar{n} = 5.6 \cdot 10^{13} cm^{-3}$; $T_e(0)$ = 1.1 keV

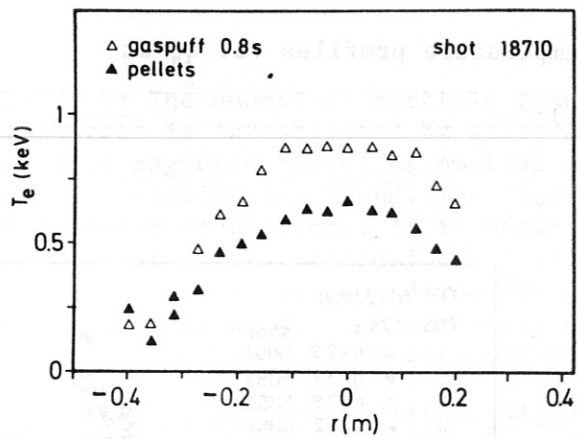

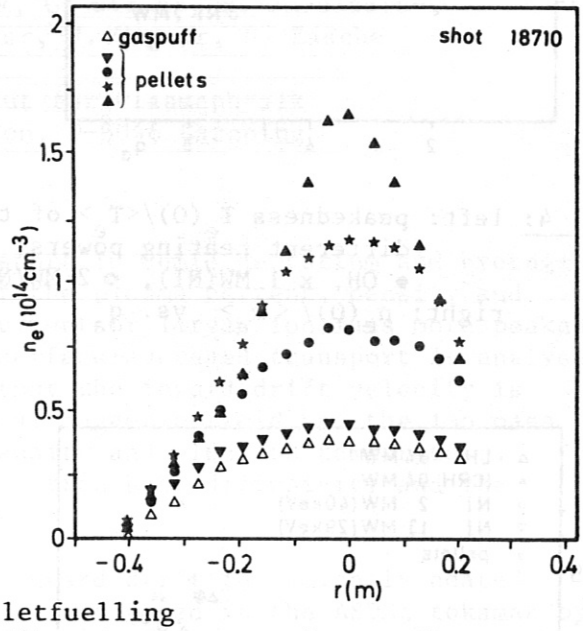

Fig. 2: Comparison: gasfuelling - pelletfuelling
left: $T_e(r)$ with gasfuelling (Δ) and after a series of 20 pellets (▲)
right: $n_e(r)$ during gasfuelling (Δ) and pellet fuelling (dark symbols) showing the time evolution of $n_e(r)$; (t = 1,3-1,5-1,7-2,1 s).

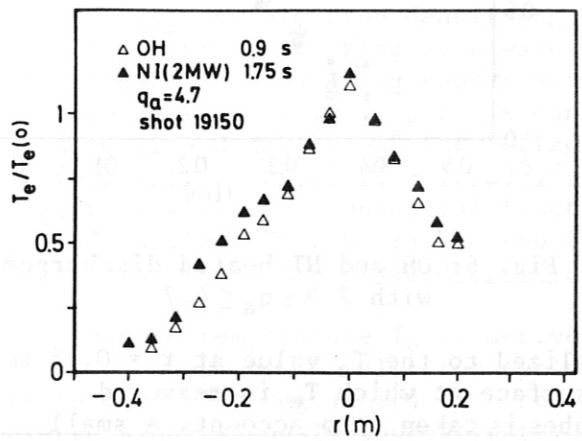

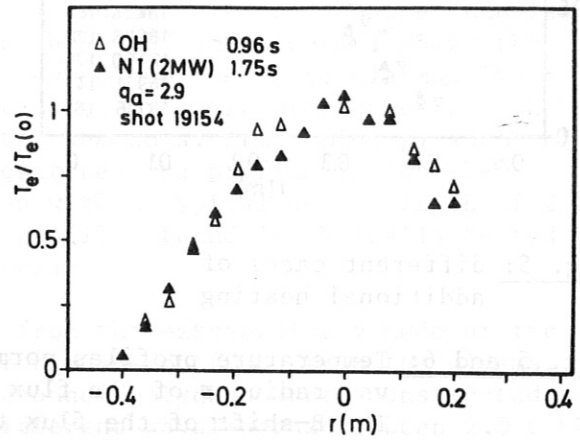

Fig. 3: Comparison of T_e profile shapes during ohmic heating (Δ) and 2 MW neutral injection (▲) at q_a = 2.9 and q_a = 4.7

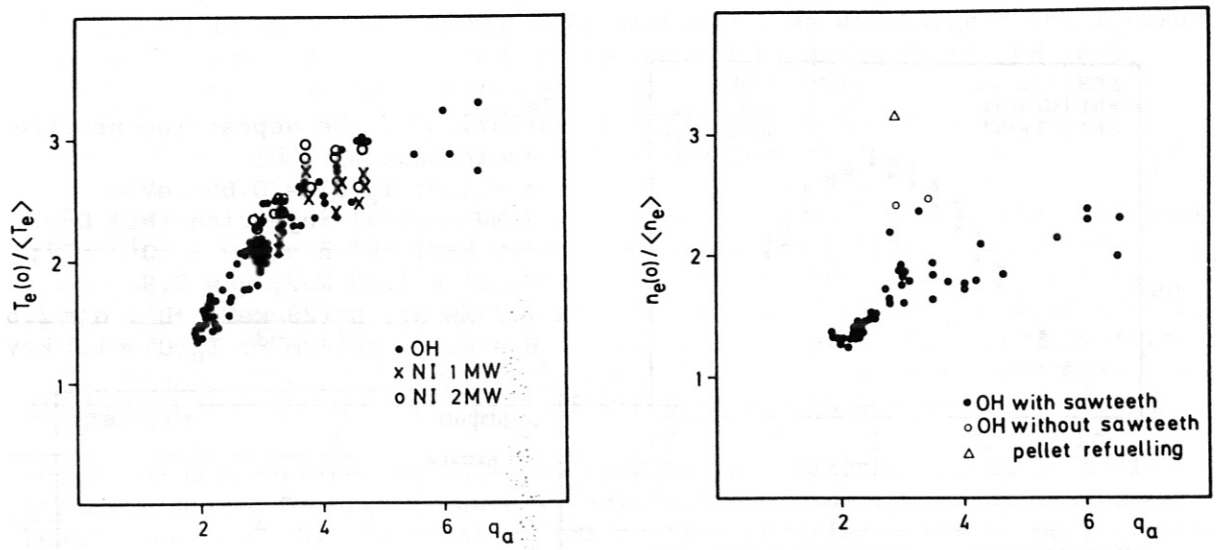

Fig. 4: left: peakedness $T_e(0)/\langle T_e\rangle$ of temperature profiles vs. q_a at different heating powers
• OH, x 1 MW(NI), o 2 MW(NI)
right: $n_e(0)/\langle n_e\rangle$ vs. q_a

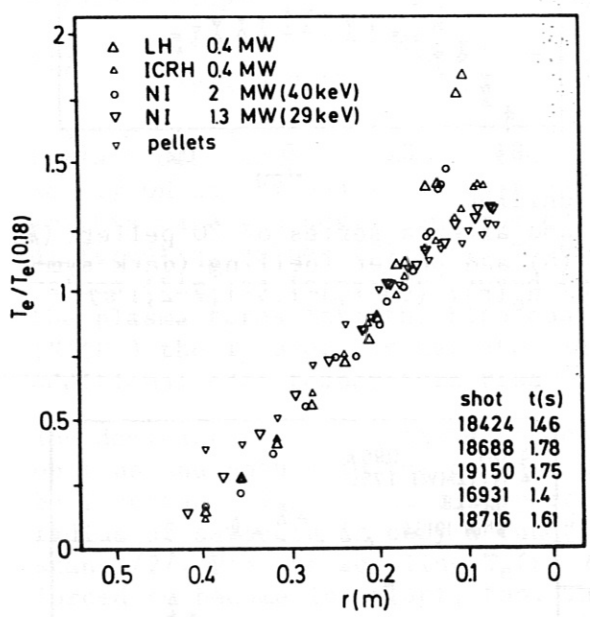

Fig. 5: different cases of additional heating

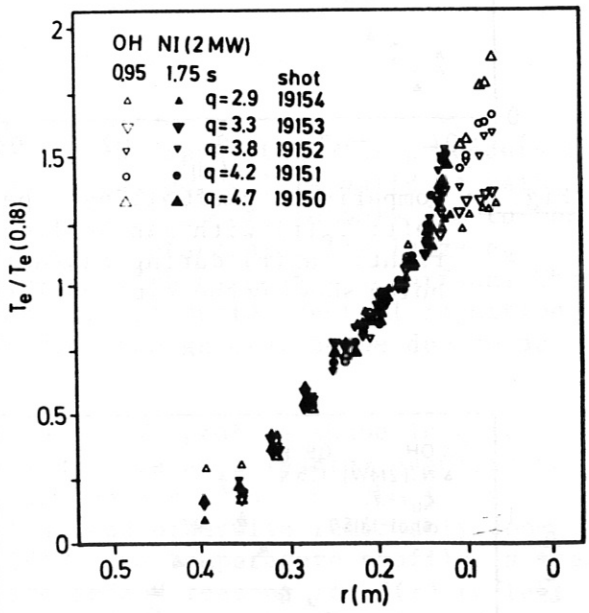

Fig. 6: OH and NI heated discharges with $2.9 \leq q_a \leq 4.7$

Fig. 5 and 6: Temperature profiles normalized to the T_e value at r = 0.18 m vs. radius r of the flux surface at which T_e is measured. The ß-shift of the flux tubes is taken into account. A small area around the magnetic axis is not covered by the laser beam of the scattering diagnostic.

PARTICLE CONFINEMENT IN OHMICALLY HEATED ASDEX PLASMAS

O. Gehre, G. Becker, A. Eberhagen and H. S. Bosch, H. Brocken, G. Fussmann, J. Gernhardt, G.v.Gierke, E. Glock, O. Gruber, G. Haas, J. Hofmann, A. Izvozchikov[1], G. Janeschitz, F. Karger, M. Keilhacker[2], O. Klüber, M. Kornherr, K. Lackner, M. Lenoci, G. Lisitano, H. M. Mayer, F. Mast K. McCormick, D. Meisel, V. Mertens, E. R. Müller[2], H. Murmann, H. Niedermeyer, A. Pietrzyk[3], W. Poschenrieder, H. Rapp, H. Röhr, J. Roth, F. Ryter[4], F. Schneider, C. Setzensack, G. Siller, P. Smeulders[2], F. Söldner, K.-H. Steuer, F. Wagner, D. Zasche

Max-Planck-Institut für Plasmaphysik
EURATOM Association, D-8046 Garching

Abstract: The anomalous particle transport in ohmic deuterium and hydrogen discharges is investigated by scans of the plasma current, density and toroidal magnetic field. At smaller current or larger ion mass more peaked density profiles are found. The flux-surface-averaged transport is analysed by computer simulations. It is shown that the inward drift velocity is independent of the poloidal and toroidal magnetic field and the ion mass number but inversely depends on the density and electron temperature. Empirical scaling relations for the electron heat diffusivity and the diffusion coefficient are also presented.

Introduction: Anomalous diffusion and inward drift in ohmically heated (double-null divertor) discharges are investigated in the ASDEX tokamak by extensive parameter studies. For deuterium and hydrogen plasmas the variation of the density profile with plasma current I_p, toroidal magnetic field B_t and line-averaged density $\bar{n}_e$ is explored. Several series of discharges are studied in which only one of these parameters has been scanned. In all cases, data measured during long current and density plateaus are analysed.

Diagnostics: The electron density n_e is measured by a multichannel HCN-laser interferometer /1/ working at a wavelength of 337 µm. Figure 1 shows the arrangement of the viewing chords with respect to the ASDEX plasma. The electron density profile $n_e(r)$ is constructed by a fit procedure for the measured line densities of the horizontal channels. A modified parabola of the form $n_e(r) = n_e(0)\,[1 - (r/a)^{\beta}]^{\alpha}$ describes the profile inside the separatrix while an exponential function with a typical decay length of 2 cm is used outside. For the rather smooth profiles found in ohmically heated discharges, this method yields good accuracy.

The electron temperature T_e is derived from the extraordinary mode of the second harmonic of the electron cyclotron emission (ECE) from the plasma. Its intensity is registered by a four-channel polychromator, constructed to observe simultaneously four slightly different wavelengths between $2.0 \lesssim \lambda \lesssim 3.0$ mm corresponding to four radial positions in the plasma about 6 - 8 cm apart from one another. The complete T_e profile can be established by a sequence of at least two identical discharges with properly varied wave

---

[1]Academy of Sciences, Leningrad, USSR; [2]Present address: JET Joint Undertaking, England; [3]Univ. of Washington, Seattle, USA; [4]CEN Grenoble, France

length settings of the polychromator. For details of the ECE diagnostic employed see e.g. Ref. /2/.

Analysis of the particle transport by computer modelling: The steady-state particle balance equation with anomalous outward diffusion and anomalous inward convection reads

$$- D \frac{dn_e}{dr} + v_{in}\, n_e = \Gamma_i, \qquad (1)$$

where Γ_i is the flux density due to ionization of cold atoms which mainly takes place near the plasma edge.
The experiments are simulated with the BALDUR transport code /3,4/. For deuterium and hydrogen plasmas the computations fit the measured $n_e(r)$ and $T_e(r)$, the central ion temperature $T_i(0)$ from CX diagnostics and the poloidal beta β_p from the diamagnetic loop. The following expressions for the electron heat diffusivity χ_e and the diffusion coefficient D are to be used for best fits in ohmically heated plasmas:

$$\chi_e(r) = 1.61 \times 10^{16}\, A_i^{-1/2}\, B_t\, n_e(r)^{-1}\, T_e(r)^{-1}\, q(r)^{-1}\ cm^2\ s^{-1} \qquad (2)$$

$$D(r) = 0.2\, \chi_e(r), \qquad (3)$$

where B_t is in kG, n_e is in cm^{-3} and T_e is in keV. A_i denotes the ion mass number. Note that the ion mass dependence given holds under pure deuterium and hydrogen plasma conditions after glow-discharge cleaning. The ion heat diffusivity χ_i used is one time the neoclassical values according to Chang and Hinton. For the anomalous inward drift velocity $v_{in} = \gamma(r/r_w)^2$ is applied instead of the Ware pinch. γ is a factor whose parameter dependences are investigated by scanning I_p and $\bar{n}_e$, and r_w is the wall radius (r_w = 49 cm). As illustrated by Fig. 2, this model yields the measured profile variation, characterized by $n_e(0)/\langle n_e\rangle$, on I_p, where $\langle n_e\rangle$ is the volume-averaged density. For deuterium $v_{in} = -550\ (r/r_w)^2$ cm s^{-1} is used while for hydrogen $v_{in} = -710\ (r/r_w)^2$ cm s^{-1} is applied. The inward drift velocity is found to be independent of the plasma current. In Figs. 3 and 4, examples of computed density and temperature profiles from these scans are compared with the measured results for deuterium and hydrogen, respectively.

Results of the density scan are presented in Fig. 5. For a given electron temperature the inward drift exhibits an inverse $\bar{n}_e$ scaling. Scanning the toroidal magnetic field (see Fig. 6) yields a weak rise of the measured $n_e(0)/\langle n_e\rangle$ values with increasing B_t which is ascribed to the variation of the q=1 radius. These scans show that v_{in} is independent of the poloidal magnetic field B_p, B_t and A_i but it depends inversely on n_e and T_e. Equations (2) and (3) and $B_t/q = R_o\, B_p/r$ yield

$$\frac{v_{in}(r)}{D(r)} \simeq - A_i^{1/2}\, B_p(r)^{-1}\, f(r) \qquad (4)$$

independently of B_t, n_e and T_e. Smaller currents and larger ion mass correspond to higher $|v_{in}|/D$, i.e. more peaked density profiles, in agreement with the measurements. The v_{in} scaling given by Eq. (4) differs from the previously used relation $v_{in}/D \simeq -2\alpha\, r/a^2$ with α being a constant. An explicit dependence of χ_e, D and v_{in} on Z_{eff} was not identified in the scans.

References

/1/ Gehre, O., Int. Journal of Infrared and Millimeter Waves, Vol. 5 (1984) 369.
/2/ Eberhagen, A., Campbell, D.J., Kissel, S.E., Mertens, V., EC-4, Fourth Int. Workshop on ECE and ECRH, Roma, 1984, p. 115.
/3/ Becker, G., ASDEX Team, Neutral Injection Team, Rep. IPP III/98 (1984).
/4/ Post, D.E., Singer, C.E., McKenney, A.M., PPPL Transport Group, TFTR Physics Group, Rep. 33 (1981).

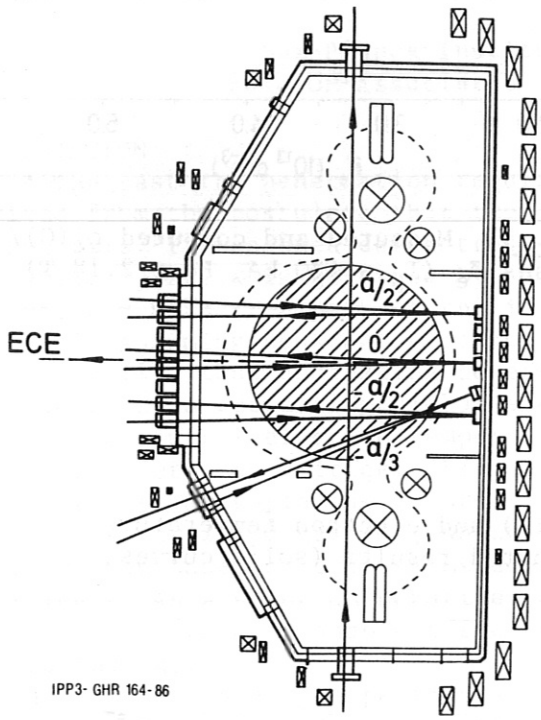

Fig. 1: Cross-section of the ASDEX device, showing the viewing chords of the HCN-laser interferometer (solid lines) and ECE diagnostics (dashed line).

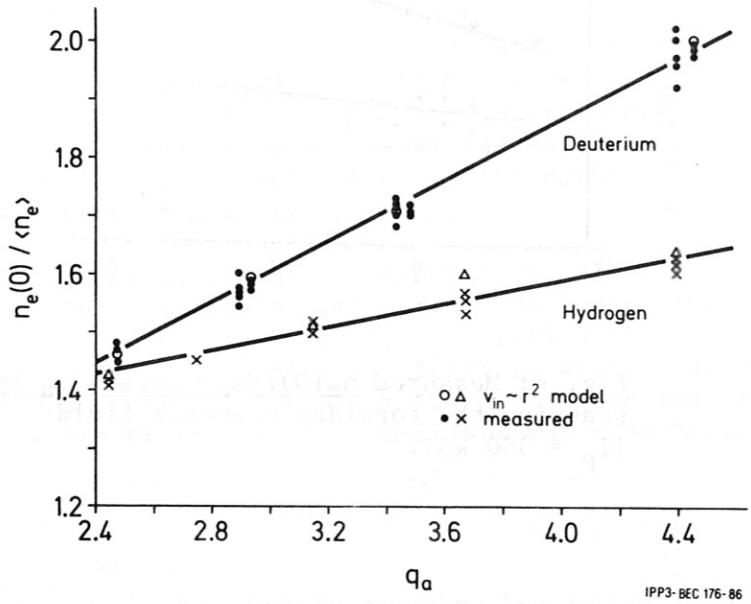

Fig. 2: $n_e(0)/\langle n_e \rangle$ versus q_a by scanning the plasma current between 250 and 450 kA (B_t = 2.25 T, $\bar{n}_e$ = 2.7 x 10^{13} cm^{-3}.

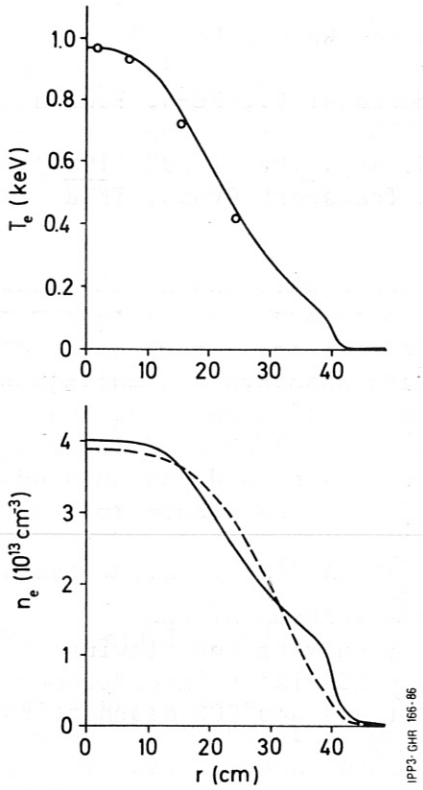

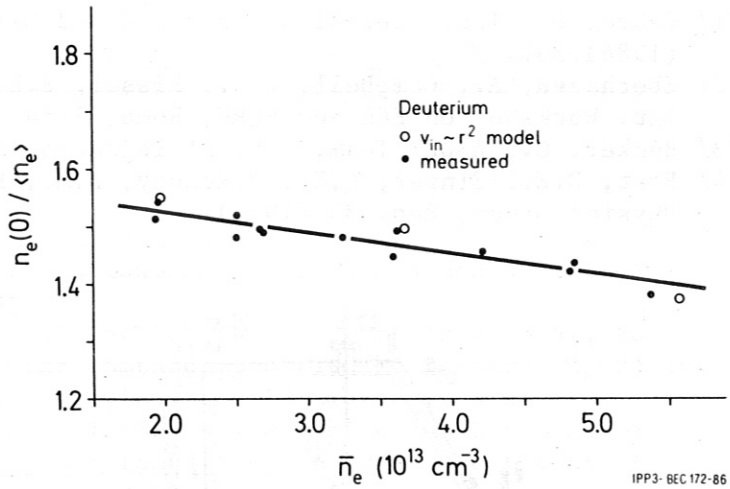

Fig. 5: Measured and computed $n_e(0)/\langle n_e \rangle$ versus $\bar{n}_e$ (I_p = 420 kA, B_t = 2.18 T).

Fig. 3: Measured density (dashed curve) and electron temperature (circles) profiles compared with computed results (solid curves, I_p = 320 kA and deuterium plasma).

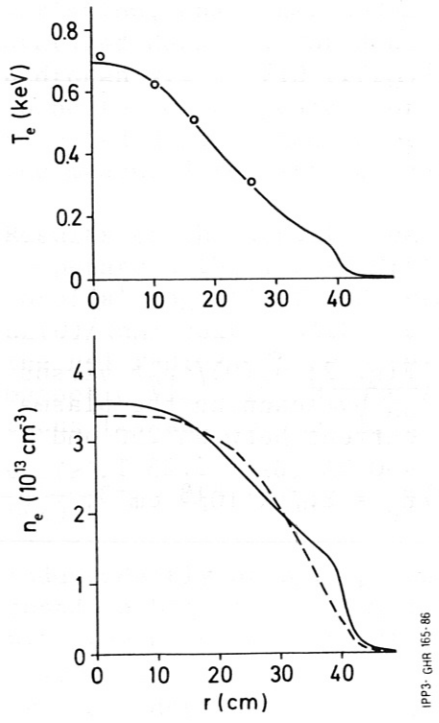

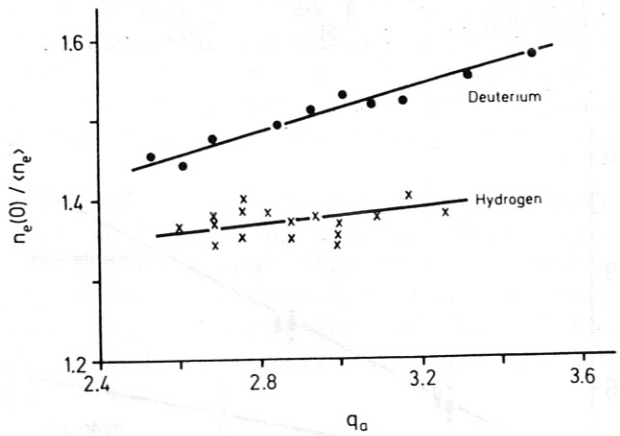

Fig. 6: Measured $n_e(0)/\langle n_e \rangle$ versus q_a by scanning the toroidal magnetic field (I_p = 380 kA).

Fig. 4: As in Fig. 3, but I_p = 350 kA and hydrogen plasma.

NEUTRAL BEAM DEPOSITION EXPERIMENTS AT ELEVATED DENSITIES IN ASDEX

E. Speth, O. Gruber, G. Janeschitz, H. Murmann, H. Niedermeyer, F. Wagner, O. Vollmer, G. Becker, H.S. Bosch, H. Brocken, A. Eberhagen, G. Fussmann, O. Gehre, J. Gernhardt, G. v.Gierke, E. Glock, G. Haas, J. Hofmann, A. Jzvozchikov[1], F. Karger, M. Keilhacker[2], O. Klüber, M. Kornherr, K. Lackner, M. Lenoci[3], G. Lisitano, F. Mast, H.M. Mayer, K. McCormick, D. Meisel, V. Mertens, E.R. Müller, A. Pietrzyk[4], W. Poschenrieder, H. Rapp, H. Riedler[5], H. Röhr, J. Roth, F. Ryter[6], J. Schneider, C. Setzensack, G. Siller, P. Smeulders, F. Söldner, K.H. Steuer, D. Zasche.

Max-Planck-Institut für Plasmaphysik,
EURATOM-Association, D-8046 Garching, FRG

INTRODUCTION

In the past the penetration requirements for neutral beams have been derived from the postulate that the beam power should be deposited near the plasma axis. It has been demonstrated theoretically that the shape of the deposition profile is governed by the parameter a/λ (a = minor plasma radius, λ = mean free path of the injected neutrals at line-averaged density). Assuming constant electron thermal conductivity, it can be shown theoretically, that decreasing penetration (i.e. increasing a/λ)of the beam results in decreasing global energy confinement time and decreasing attainable central electron temperature, values of a/λ in excess of 2 being considered as critical /1/. Consequently the beam energies necessary to penetrate large plasmas in order to heat the plasma centre lie in the range of several 100 keV /2/, which leads to serious difficulties for positive-ion-based neutral beams due to the decreasing neutralisation efficiency. As a solution negative-ion-based systems have been proposed, which would offer reasonable efficiency, but require the development of a new technology.

In order to make an experimental assessment of the required beam penetration a series of experiments were started in 1984 in ASDEX, in which neutral beam deposition was varied systematically. The first results reported at Budapest /3/ showed (in agreement with other experiments /4/) no degradation of heating and confinement within the parameter range accessible, but suffered from following drawbacks: the plasma density was too low ($\bar{n}_e = 6 \times 10^{13}$ cm^{-3}) for extremely hollow deposition profiles to be produced and the power level was only moderate (1.3 MW). This paper describes the continuation of the experiments at almost twice the density and three times higher power.

EXPERIMENTAL PARAMETERS AND RESULTS

The experiments were carried out under the following conditions: $I_{pl} = 420$ kA, $B_T = 2.2$ T, $\bar{n}_e = 1.15 \times 10^{14}$ cm^{-3}, D_2-plasma, double-null, diverted. The density was built up with D_2 gas-puffing before and during the injection pulse ($\tau = 400$ msec), and reached a stationary state towards the end of the pulse. Comparison was made between shots of different beam

---

[1]Academy of Sciences, Leningrad, USSR; [2]Assigned to JET Joint Undertaking, England; [3]ENEA Frascati, Italy; [4]University of Washington, Seattle, USA; [5]Fellow of the Schiedel-Stiftung, Austria; [6]CEN Grenoble, France

energy per nucleon, i.e. 40 kV acceleration voltage, H^o-injection, <E> = 25 keV/AMU (P_N = 3.6 MW) and 44 kV acceleration voltage, D^o-injection, < E> = 13 KeV/AMU (P_N = 4.1 MW), keeping everything else identical. All the shots were L-type discharges.

The global energy confinement time, evaluated from the diagmagnetic β_{pol} during the stationary phase, does not show a significant difference (see Fig. 1). The value of τ_E = 35 msec is consistent with ASDEX L-scaling. The electron temperature profiles during the stationary phase (taken from YAG-laser scattering and ß-shift corrected) are shown in Fig. 2. As can be seen, there is a reduction of about 10 % in $T_e(0)$ for the low-energy case (44 kV D^o) inspite of the somewhat higher power. The corresponding power deposition profiles are shown in Fig. 3.

DISCUSSION

If one interprets this reduction of $T_e(0)$ for the 44 kV D^o-case as the onset of degradation of heating, one may identify the corresponding profile parameter $a/\lambda = 6$ with the limit for off-axis deposition in tokamaks ($\lambda = (\bar{n}_e \sigma_{TOT})^{-1}$; $\bar{n}_e$ = line-averaged density, σ_{TOT} = total trapping cross-section).

In calculating $a/\lambda = 6$ a correction for steeper injection angles (15 - 20° on large machines instead of 45° on ASDEX) has been applied. Applying this scaling law to larger plasmas yields the curve shown in Fig. 4. It can be seen that e.g. 70 keV D^o in JET or 120 keV D^o in NET would be sufficient to produce deposition profiles of the same relative shape as in Fig. 3b and would hence result in non-degraded heating.

At low energy (E < 20 keV/AMU) the deposition limit may not be determined by heating but by impurity radiation due to enhanced charge-exchange wall erosion. Enhanced impurity (iron) influx was e.g. observed in the 44 kV D^o-case at the end of a 400 msec-pulse, but was absent in the 40 kV H^o-case. Low energy injection at $a/\lambda = 6$ may therefore be limited by an additional constraint, namely to E > 20 keV/AMU independently of plasma size and calls for a high proton ratio from the ion sources. From the present data it cannot be entirely excluded that this limit may even be higher ($\sim$ 30 keV/AMU).

It is important to note, that hollow deposition profiles as shown in Fig. 3b are sensitive to central impurity radiation leading to radiation collapse. The viability of hollow deposition profils must therefore be confirmed in long pulse experiments.

If the principle of "profile consistency", i.e. the invariance of the temperature profile with respect to power deposition /3,5,6/ will persist in larger tokamaks, it may even not be required to obey a/λ = const. in order to produce heating and confinement without degradation. Other scaling laws may have to be considered, e.g. relating λ to the width of the toroidal shell outside q = 2 /6/, or possibly λ = const., suggesting that it may be sufficient to deposit the power independently of plasma size at constant depth measured from the plasma edge and λ chosen just large enough to avoid enhanced charge exchange wall sputtering (see above).

It should be noted, that the conclusions contained in this paper are valid for injection into tokamaks and do not necessarily apply to stellarators.

Finally it may be appropriate to reconsider the development of power recovery and plasma sources with high atomic ion yield in comparison with negative ions.

REFERENCES

/1/ J.G. Cordey, Applied Atomic Collision Phyics, Vol. 2, Plasmas, Academic Press (1984), p. 327
/2/ J.W. Willis et al., ERDA-report 76-77
/3/ E. Speth et al., Proc. of the 12th Europ. Conf. on Contr. Fusion and Plasma Physics, Budapest (1985), part II, p. 284
/4/ M. Murakami et al., Plasma Physics and Controlled Fusion, Vol. 28, 1A (1986), 17/5/F. Wagner et al., to be published in Nucl. Fusion
/6/ G.L. Schmidt et al., Proc. of the 12th Europ. Conf. on Contr. Fusion and Plasma Physics, Budapest (1985), part II, p. 674.

FIGURE CAPTIONS

Fig. 1: Global energy confinement time τ_E vs. species-averaged beam energy <E> and full beam energy E_o respectively

Fig. 2: Electron temperature profiles

Fig. 3: Power deposition profiles for ohmic power (p_Ω), electrons (p_e), ions (p_i) and total power (Σ).
a) for 40 KV H^o, 3.6 MW
b) for 44 kV D^o, 4.1 MW

Fig. 4: Opacity $\bar{n}_e \cdot a$ vs. species-averaged beam energy <E> ;
injection angle < 20°,
$\bar{\sigma}_{TOT}$ = total trapping cross section,
$\bar{T}$ = average plasma temperature

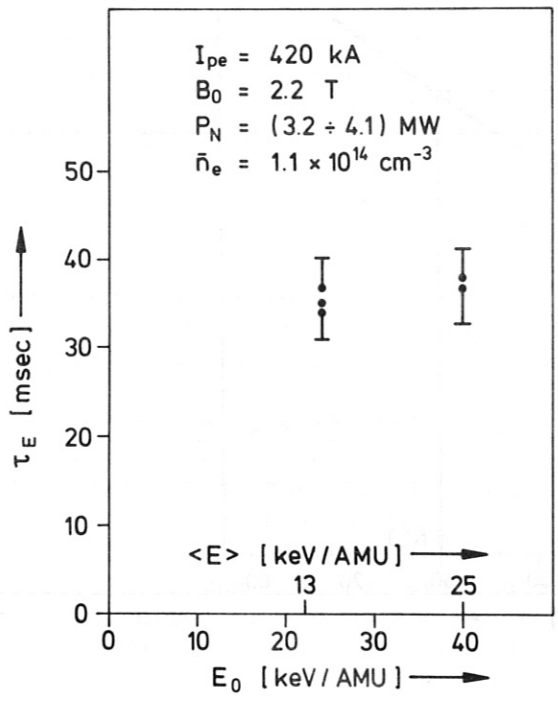

Fig. 1

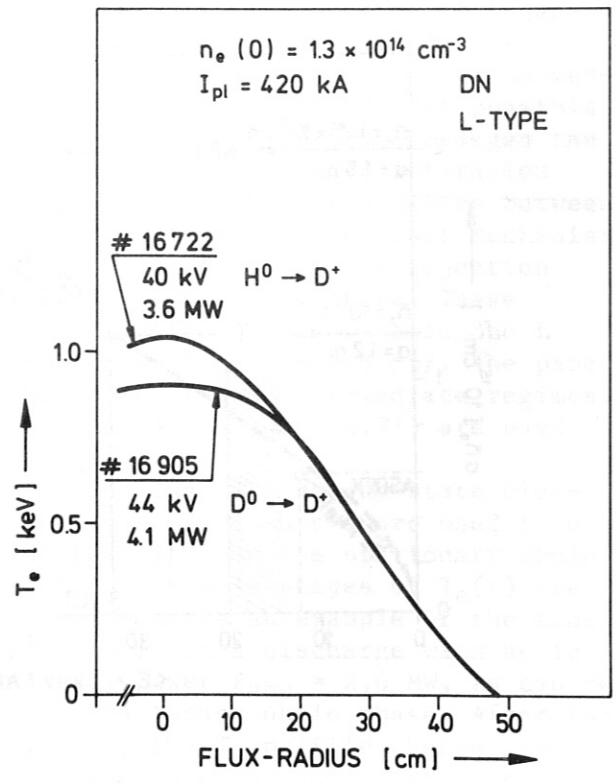

Fig. 2

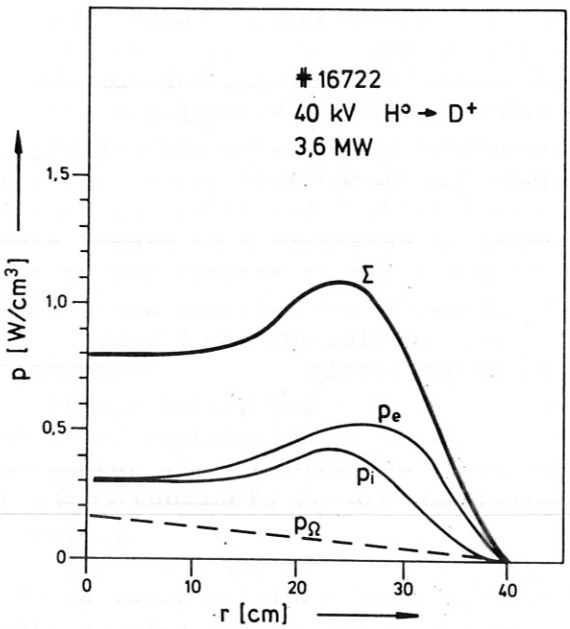

Fig. 3a

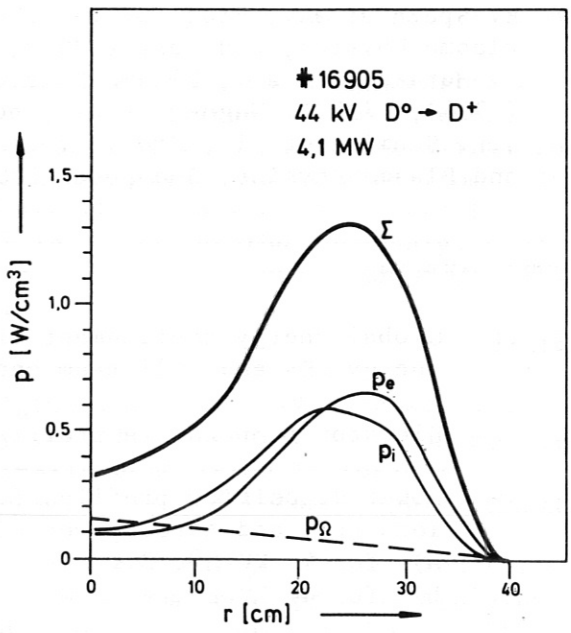

Fig. 3b

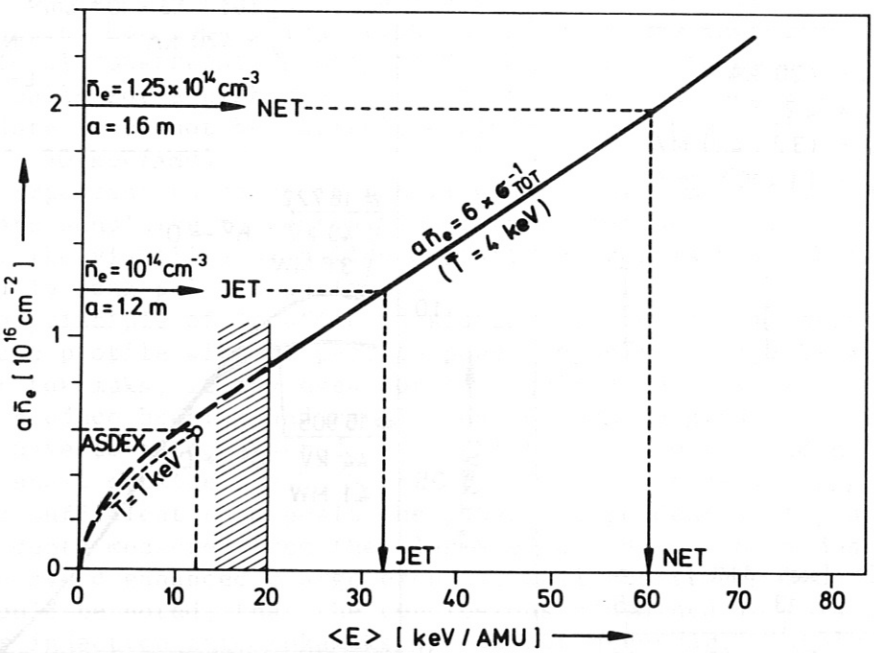

Fig. 4

LOCAL TRANSPORT IN TOKAMAKS WITH OHMIC AND INJECTION HEATING

G. Becker

Max-Planck-Institut für Plasmaphysik
EURATOM Association, D-8046 Garching

Abstract: The anomalous electron heat diffusivity χ_e is investigated by a power scan of the injection heating and by the time evolution of L (low confinement) discharges. It is shown that deviations from the ohmic scaling occur if the non-ohmic electron heating locally exceeds the ohmic power density. The change in scaling is attributed to the injection heating with its different dependence on the plasma parameters rather than to other instabilities or saturation effects. Constraints on χ_e are derived from the electron and ion energy equations and the shape of the measured electron temperature profiles. For small injection power complex χ_e scalings result which cannot be represented by superposing the ohmic and L scalings.

Introduction: As reliable microinstability-based diffusivities are not available at present for tokamaks with ohmic and auxiliary heating, preference is given to empirical scalings determined by means of transport modelling of many series of discharges. The flux-surface-averaged electron heat diffusivity χ_e and the diffusion coefficient D exhibit a scaling in injection-heated plasmas which greatly differs from that with ohmic heating /1-4/. It was demonstrated that the ohmic transport scaling is not a universal plasma quality which is independent of the heating method. One possible explanation for the different scaling is that neutral injection changes the transport mechanism, i.e. the underlying instabilities and/or saturation effects. There might exist a threshold parameter which distinguishes between the confinement regimes. Another possibility is that the transport mechanism itself remains unchanged and the χ_e scaling is modified by the injection heating with its different variation with the plasma parameters. These questions will be pursued by studying the transition between ohmic and L transport and by following the time evolution of L discharges /5/. The paper deals with the anomalous transport in the ohmic, L and intermediate regimes. Results from transport computations (with the BALDUR code /6,7/) are used.

Constraints on χ_e with ohmic and injection heating: The steady-state electron and ion energy equations and measured T_e profile shapes are used to derive constraints for the electron heat diffusivity. In the stationary ohmic and neutral-beam-heated phases of ASDEX characteristic shapes of $T_e(r)$ are observed. This is illustrated by Fig. 1, which shows an example of the time evolution of the electron temperature profile in an L discharge with an injection period of 400 ms and an absorbed beam power P_{abs} = 2.0 MW. As can be seen, a Gaussian shape is found during the stationary ohmic phase. After the beginning of neutral injection (t_{on} = 1.12 s), the T_e profile changes to an approximately triangular shape which is then maintained during the whole injection period. The 'confinement zone' (hatched in Fig.1) is defined by $r_{q=1} < r < 0.9a$, where the plasma radius a is equal to the separatrix radius of 40cm.

Neglecting the ion heat conduction, the steady-state electron and ion energy equations yield

$$\frac{1}{r}\frac{d}{dr}\left(rn\,\chi_e\frac{dT_e}{dr}\right) + \eta j_t^2 + P_b \approx 0 \qquad (1)$$

with $\eta j_t^2 = E_t j_t$. The power density of the ASDEX neutral injection system can be approximated by $P_b(r) = \alpha_b/r$ with $\alpha_b = P_{abs}/(4\pi^2 R_o a)$ and major radius R_o. After integration it follows that

$$\chi_e(r) = \left[\frac{c}{4\pi} E_t B_p(r) + \alpha_b\right] n(r)^{-1} \left|\frac{dT_e}{dr}\right|^{-1} . \qquad (2)$$

With $P_b = 0$ and $T_e(r) = T_e(0)\exp(-\alpha r^2/a^2)$ one obtains the constraint

$$\chi_e^{OH}(r) = \frac{c}{8\pi}\,\frac{a^2}{\alpha}\,E_t\,\frac{B_p(r)}{rn(r)T_e(r)} . \qquad (3)$$

Large injection power and $T_e(r) \simeq T_e(0)(1-r/a)$ yield the constraint

$$\chi_e^{L}(r) \simeq a\,\alpha_b\,T_e(0)^{-1}\,n(r)^{-1} . \qquad (4)$$

Comparing the constraints shows that the χ_e scalings depend on the heating method and its variation with the plasma parameters. Neutral injection does not introduce a $B_p(r)$ dependence in contrast to ηj_t^2. Owing to $j_t(r) \sim T_e(r)^{3/2}$ the ohmic heating and electron temperature profiles are stongly coupled, whereas $P_b(r)$ depends on the target density and injection energy. It is obvious from Eq. (2) that the transport in the intermediate range cannot simply be represented by superposing the ohmic and L scalings, but that rather complex, mixed χ_e scalings occur. The beam heating modifies the ohmic contribution by changing E_t and the T_e profile shape and the ohmic heating modifies the beam contribution.

Transition between ohmic and L transport: The confinement in the intermediate range between OH and L scaling is studied by simulating a series of discharges at $\bar{n} = 2.5 \times 10^{13}$ cm^{-3}, $I_p = 380$ kA, $Z_{eff} = 1.5$ and $P_{OH} = 0.52$ MW with various injection powers. Figure 2 shows the increase of the electron heat diffusivity with rising absorbed beam power. Obviously, at small P_{abs} equal to 0.3 and 0.6 MW the χ_e values clearly exceed the ohmic result (cross) in the middle of the confinement zone at r = 2a/3. This explains the observed decrease of the global energy confinement time τ_E /2/. The χ_e profiles with ohmic heating and $P_{abs} = 0.6$ MW are presented in Fig. 3. Special attention is paid to the local ratio of the injection and ohmic heating power densities. Results for various absorbed beam powers are shown in Fig. 4. It is obvious that $P_b/(\eta j_t^2) \simeq 0.3$, where the influence of beam heating should become important, is already exceeded with $P_{abs} = 0.3$ MW. As shown above, the corresponding χ_e and τ_E are indeed found to deviate from the ohmic scaling. With $P_{abs} = 0.6$ and 0.9 MW, neutral injection becomes dominant in the confinement zone. This explains the observed fast transition of τ_E to the L scaling. For $P_{abs} \gtrsim 1.2$ MW the beam power density is large compared with ηj_t^2, which agrees with the essentially pure L confinement found. The power scan shows that the transition to the L regime correlates with the ratio $P_b/(\eta j_t^2)$. Both the deviation from the ohmic scaling and the approach to the L confinement occur at power density ratios which agree with the expected values. According to the electron energy equation, injection powers of this level perturb the ohmic state. The associated change in

confinement suggests that the χ_e scaling responds to the auxiliary heating. The fact that the coupling between the ohmic heating profile and $T_e(r)$ is broken up with neutral injection should play an important role. As the smallest injection power scarcely modifies the plasma parameters, such as density and temperature gradients and poloidal beta, a transition to other instabilities and/or saturation effects, i.e. to a different transport mechanism, is very unlikely.

Transport behaviour after neutral injection: A characteristic time development of the diffusivities χ_e and D in L discharges was found by means of transport simulations /1,2/. It was shown that the L phase persists for about 100 ms after the end of injection. As the slowing-down time of the fast beam ions is only about 10 ms, the injection power rapidly decays. It is thus concluded that the L transport does not require the presence of injection heating, beam fuelling and direct ion heating. Simulations of many L discharges revealed that the phase with the ion-electron energy transfer rate $P_{ie} > 0$ also lasts for a time span of about 100 ms, which suggests that the L phase is maintained by non-ohmic electron heating.

The time development of the electron temperature profiles measured after injection is shown in Fig. 5. Although the beam power is negligibly small, the Gaussian-shaped T_e profiles typical of the ohmic phase are only reached after about 80 ms. The central steepening of the profiles results from the electron heating due to P_{ie}, which is largest in the plasma centre. Profiles of $P_{ie}/(nj_t^2)$ after neutral injection which were determined by simulating the L discharge with P_{abs} = 2.1 MW in Figs. 2 and 4 are presented in Fig. 6. The absorbed beam power is negligibly small at $t-t_{off}$ = 43 ms, so that the only non-ohmic heating is due to P_{ie}. Owing to P_{ie} a transport scaling different from the ohmic one should thus persist in a considerable fraction of the plasma cross-section. Close to the end of the L phase, however, the ratio of the power densities has become so small that the scaling becomes almost purely ohmic. It is concluded that deviations from the ohmic scaling occur if the non-ohmic electron heating (due to neutral injection or ion-electron energy transfer) locally exceeds the ohmic power density.

References

/1/ Becker, G., ASDEX Team, Neutral Injection Team, Nucl. Fusion 22 (1982) 1589.
/2/ Becker, G., Campbell, D., Eberhagen, A., Gehre, O., Gernhardt, J., et al., Nucl. Fusion 23 (1983) 1293.
/3/ Becker, G., Nucl. Fusion 24 (1984) 1364.
/4/ Kaye, S.M., Goldston, R.J., Bell, M., Bol, K., Bitter, M., et al., Nucl. Fusion 24 (1984) 1303.
/5/ Becker, G., Report IPP III/109 (1986).
/6/ Post, D.E., Singer, C.E., McKenney, A.M., BALDUR: A One-dimensional Plasma Transport Code, PPPL Transport Group, TFTR Physics Group, Report 33 (1981).
/7/ Becker, G., ASDEX Team, Neutral Injection Team, Report IPP III/98 (1984).

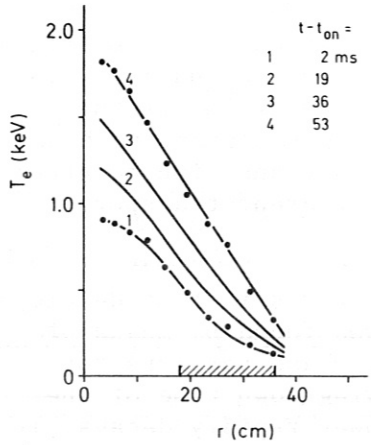

Fig. 1: $T_e(r,t)$ after the beginning of neutral injection (t_{on} = 1.12 s) measured by multi-pulse Thomson scattering in an L discharge with $\bar{n}$ = 2.4 x 10^{13} cm^{-3}, I_p = 280 kA and P_{abs} = 2.0 MW. The hatched area denotes the confinement zone.

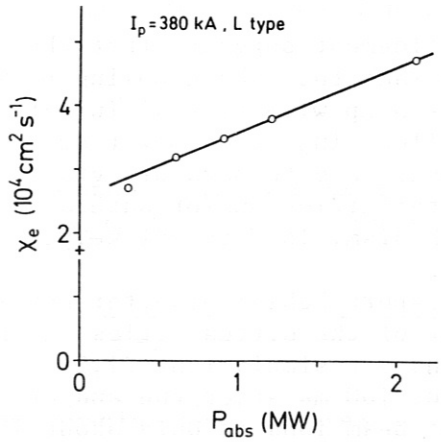

Fig. 2: Approximately homogeneous electron thermal diffusivity from simulations versus absorbed beam power ($\bar{n}$ = 2.5 x 10^{13} cm^{-3}). For comparison, the ohmic χ_e (2a/3) value (cross) is shown.

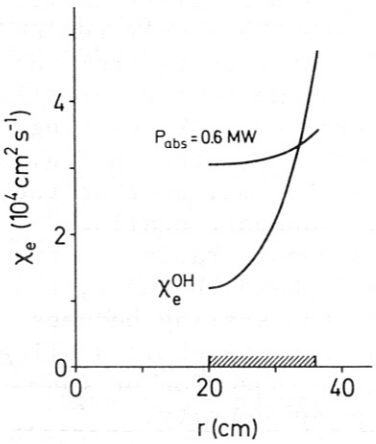

Fig. 3: $\chi_e(r)$ in the confinement zone (hatched) with ohmic heating and neutral-beam heating with two sources.

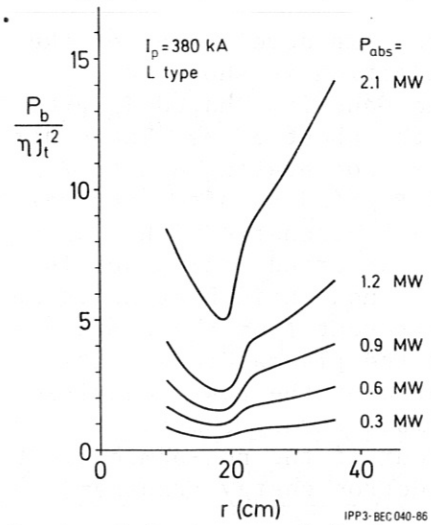

Fig. 4: Ratio of the beam and ohmic power densities versus radius from simulations of the power scan of Fig. 2.

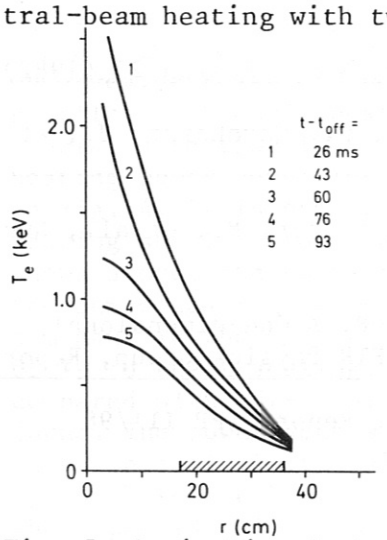

Fig. 5: As in Fig. 1, but after the end of neutral injection (t_{off} = 1.52 s).

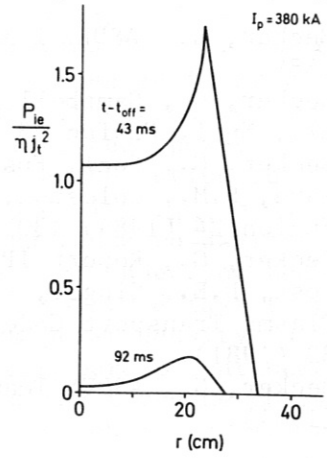

Fig. 6: Ratio of the power densities of ion-electron energy transfer and ohmic heating versus radius after t_{off}.

TRANSPORT IN BEAM-HEATED ASDEX DISCHARGES BELOW AND IN THE VICINITY OF THE BETA LIMIT

O. Gruber, W. Jilge, H.S. Bosch, H. Brocken, A. Eberhagen, G. Fussmann, O. Gehre, J. Gernhardt, G. v. Gierke, E. Glock, G. Haas, J. Hofmann, G. Janeschitz, A. Izvozchikov, F. Karger, M. Keilhacker, O. Klüber, M. Kornherr, K. Lackner, M. Lenoci, G. Lisitano, F. Mast, H. M. Mayer, K. McCormick, D. Meisel, V. Mertens, E. R. Müller, H. Murmann, H. Niedermeyer, W. Poschenrieder, H. Rapp, H. Riedler, H. Röhr, J. Roth, F. Ryter, F. Schneider, C. Setzensack, G. Siller, P. Smeulders, F. X. Söldner, E. Speth, K.-H. Steuer, O. Vollmer., F. Wagner,

Max-Planck-Institut für Plasmaphysik, EURATOM Association,
D-8046 Garching, Fed. Rep. Germany.

1. INTRODUCTION

Radial transport and confinement properties of ohmically and beam-heated ASDEX discharges are studied using the PPPL transport analysis code TRANSP[1] and measured radial plasma profiles and global parameters. Results are that the anomalous electron thermal transport is dominating in low-density ohmic as well as "L" beam-heated ASDEX plasmas. It leads, however, for these regimes to different scaling laws of the global energy confinement time [2]. At high-density ohmic and "H" mode beam-heated discharges the neoclassical ion heat conductivity and convective losses (H mode) are comparable to the electron losses and tend to dominate the energy balance.

The ion heat conduction χ_i is described by two times the neoclassical value calculated by C. Chang and F. Hinton in all discharge phases (OH, L, H, H^*). Thereby a χ_i of three times $\chi_{i,neocl}$ fits the central ion temperature measured by the energy spectrum of CX neutrals whereas a $\chi_i = \chi_{i,neocl}$ yields for the calculated T_i profiles the measured neutron fluxes.

Experiments show that the electron temperature profile shape in ohmically and beam-heated "L" discharges is only influenced by the safety factor $q^*(a)$[3]. According to this concept the elctron thermal diffusivity $\chi_e(r)$ depends directly on the electron thermal conductive loss $P_{cond,e}$ across the magnetic surface with radius r, which is a certain fraction of the input power. From the definition $\chi_e = -(P_{cond,e}/2\pi R)/(n_e T_e \frac{r}{T_e}\frac{\partial T_e}{\partial r})$ and from the "profile consistency" argument $\frac{r}{T_e}\frac{\partial T_e}{\partial r} \simeq -\alpha\frac{r^2}{r^{*2}}$ (where r^* may be the $q = 2$ radius, and α is a function of $q^*(a)$) one obtains $\chi_e(r) \sim P_{cond,e}(r)/(n_e(r)T_e(r)r^2)$. The definition of a local χ_e which depends on local plasma parameters does not seem to be appropriate. In this paper the χ_e values deduced from the transport analysis of OH, L and H mode discharges are used to show which description is applicable.

2. PROFILE CONSISTENCY IN OHMIC AND BEAM-HEATED "L MODE" PLASMAS

In nearly steady-state ohmic discharges χ_e can be described by a local parameter dependence $\chi_e(OH) = \chi_{CMG} \sim (B_t a/R)/(n_e^{0.8} T_e q)$ [2]. But in ohmically heated pellet discharges only the χ_e values averaged over one pellet cycle agree with χ_{CMG}, whereas a description in agreement with "profile consistency" depicts also the time-resolved χ_e measurements and yields an explanation for the scaling given by χ_{CMG} [4].

L-mode discharges at $q^*(a) \approx 2.6$ have been studied using $H^o \rightarrow D^+, D^o \rightarrow H^+, D^o \rightarrow D^+$ injection with 14.5–40 keV maximum energy/nucleon yielding about the same normalized T_e profiles (Fig. 1a), despite quite different heat deposition profiles (see Fig. 1b), total heating powers ($P_h = P_{bi} + P_{be} + P_{OH} = 1.5 \div 4.1 MW$) and densities ($\bar{n}_e = 4.10^{19} \div 11.3 \cdot 10^{19}\,\mathrm{m}^{-3}$). The electron heating ($P_{be} + P_{OH}$) exceeds slightly the ion heating (P_{bi}) and $T_i \gtrsim T_e$ is obtained. Accordingly the central confinement times $\tau_E^* = W_{pl}/(P_h - \dot{W}_{pl})$ are increasing with off-axis heating deposition, whereas the global confinement times are about the same. The deduced $\chi_e(r)$ values given in Fig. 1d can well be described by $\chi_e \sim P_{cond,e}/(n_e T_e r^2)$ for $r_{q=1} < r < 0.8a$ for individual discharges, and at a fixed radius of $r = 2a/3$ the relation $(\chi_e n_e T_e)\,|_{2a/3} \sim P_{cond,e}(2a/3)$ holds for different discharges too. At that radius $P_{cond,e} \approx (0.5 \div 0.65) P_h$ holds, showing the dominance of electron thermal transport in the L mode over the entire density range.

Despite this good agreement a fit of χ_e depending on the local plasma parameters I_p, n_e and T_e has been tried with the limited data base at present available (not only the discharges described here). Good agreement is obtained with a scaling $\chi_e(L) \sim r^2/(I^{1.5}(r) n_e^{0.3}(r) T_e(r) A_i)$, where A_i is the ion mass. This parameter dependence will be tested using a simulation code to reproduce the measured temperatures. We are aware of the "explosive" nature of the $1/T_e$ dependence and that the limited parameter set may give a misleading tendency with inherent correlations of the chosen local parameters.

3. H-MODE CONFINEMENT BELOW AND AT THE BETA LIMIT

Beam-heated ASDEX discharges with $D^o \rightarrow D^+$ show an H mode confinement of $\tau_E^*(a) = 0.2 I$[MA, s] independent of the heating power for plasmas with $\beta < 0.9\beta_c$ and $\beta_c = 0.028 I/aB_t$[MA, m, T]. Reaching the β_c limit the energy confinement times decrease with increasing heating power. This confinement factor of 0.2 s/MA is more than a factor of 2 better than reported from D III and PDX discharges. At higher plasma currents ($I_p >$ 400kA) or lower q^* values (< 3) the confinement factor is decreased ($\tau_E^*(a) \lesssim 60ms \lesssim 0.15 I_p$) [5]. Together with $H^o \rightarrow D^+$ and $H^o \rightarrow H^+$ injection results, a scaling $\tau_E^*(H) = 0.1 I A_i$ is deduced.

At these high confinement times and therefore high plasma energies (see Fig. 2a) the convection losses ($P_{conv}/P_h \approx \frac{5}{2}\Gamma k(T_e + T_i)/\Gamma\langle E\rangle$, with the particle flux Γ and the medium energy $\langle E\rangle$ of the injected neutrals) and the ion conduction losses are comparable to the elctron conduction losses (see Fig. 2b). These are now only between $0.25((I_{pl} = 310kA, q^*(a) = 4)$ and $0.4(I_p = 410kA, q^*(a) = 2.7)$ of the total heating power over a large part of the plasma

cross-section. At the higher plasma current the neoclassical ion heat losses are reduced ($\chi_i \sim 1/I^2$). The ion heating by the beams exceeds the electron heating with $D^o \rightarrow D^+$ injection ($P_{bi} \lesssim 3P_{be}$) and the contribution of the beams to the total β value is about 25%. This fact results in the difference of the τ_E^* values with and without the beam contribution given in Fig. 2c. The confinement time τ_E includes only the conductive and convective losses and shows the influence of the radiation and CX losses on τ_E^*.

For these H-mode discharges no description compatible with "profile consistency" is available at present. But the local parameter dependence of $\chi_e(L)$ given above fits also the $\chi_e(H)$ values covering now a parameter range of $0.6 \lesssim \chi_e(L,H) \lesssim 3.7 m^2/s, 200 \lesssim I \lesssim 350\,\mathrm{kA}, 2.8 \cdot 10^{19} \lesssim n_e \lesssim 11 \cdot 10^{19}\,\mathrm{m}^{-3}, 300 \lesssim T_e \lesssim 1100\,\mathrm{eV}, 1.3 \lesssim A_i \lesssim 2$. The χ_e for the discharge near the β limit described in Fig. 2 is above this scaling derived from discharges below the β limit.

4. CONCLUSIONS

In OH and L mode discharges the concept of "profile consistency" is supported by pellet injection and strongly varied deposition profiles, respectively. In H-mode discharges no consistent picture has evolved up to now. But also a dependence of χ_e on local parameters seems possible in both L and H mode. $D^0 \rightarrow D^+$ injection provides high confinement times with a scaling $\tau_E^* = 0.1 I A_i$[s, MA] for $q^*(a) > 3$ and with strong ion heating. At the β limit confinement degrades with increasing χ_e compared with χ_e below the β limit.

REFERENCES

[1] R. Hawryluk, in *Physics of Plasmas Close to Thermonuclear Conditions*, Vol. 1, Varenna (1979) (EUR-FU-BRU/XII/476/80).

[2] O. Gruber, Proc. Invited Papers, Int. Conf. on Plasma Physics, Lausanne (1984) Vol. 1, p. 67.

[3] F. Wagner, O. Gruber, K. Lackner et al, submitted to Phys.Rev.Letters.

[4] O. Gruber et al, this conference.

[5] M. Keilhacker et al, Plasma Phys. Contr. Fusion **28** (1986), 29

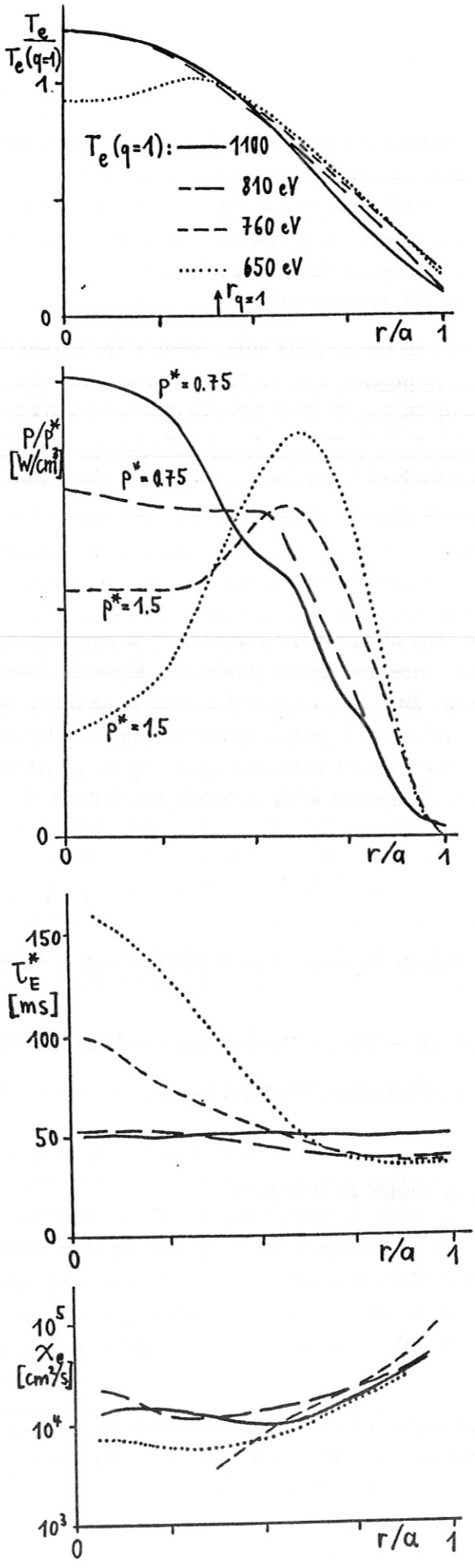

Fig. 1 Normalized T_e , heating power density p, energy confinement time τ_E^* and χ_e radial profiles of L-mode discharges with $q^*(a) = 2.6$.

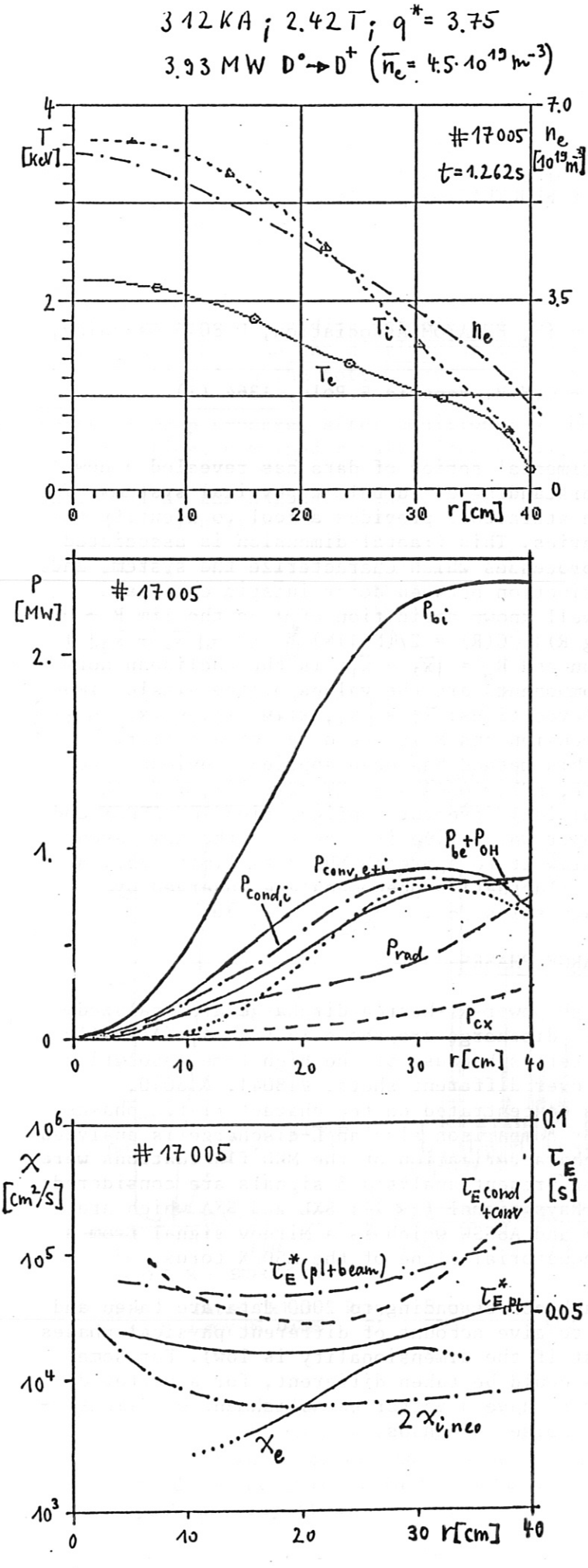

Fig. 2 Radial profiles of T_e, T_i and n_e, volume-integrated power balance, τ_E^* with and without beam contribution, $\tau_E = W_{pl}/(P_{cond}+P_{conv})$, χ_e and χ_i of H-mode discharge at the β limit ($\beta/\beta_c = 0.95$).

DIMENSIONALITY OF FLUCTUATIONS IN ASDEX

L. Battiston*, ASDEX-Team

Max-Planck-Institut für Plasmaphysik, EURATOM Association, D-8046 Garching, Fed. Rep. of Germany

*Istituto Dinamica Grandi Masse - C.N.R. Venezia S.Polo, 1364 (I)

INTRODUCTION

Dimensionality analysis of experimental series of data has revealed a new powerfull tool for a deeper understanding of turbulent physical systems. The analysis of the so-called strange attractors provides a tool to identify the fractal dimension ν of a time series. This fractal dimension is associated with the number of indipendent processes which characterize the system, and if it exists, it provides a distinction between deterministic chaos and noise /1/. Here it is used the well known definition of ν as the $\lim R \to 0$ of the ratio $(d \log C(R))/(d \log R)$; $C(R) = 2/((N-1)N) \cdot \sum_{ij} H(R - |\bar{x}_i - \bar{x}_j|)$ where H is the heaviside function and $R_{ij} = |\bar{x}_i - \bar{x}_i|$ is the Euclidean norm between all pairs of $\bar{x}_i$ whose components are the values of the single time series signal at D different delayed times: $\bar{x}_i = \{x_i, x_{i+M}, x_{i+2M}, \ldots x_{i+(D-1)M}\}$ D is the so-called embedding dimension and M is the delay time factor. In the context of fusion research this method has been applied previously to the study of fluctuations on DITE, RFP, TOSCA and JET /2/, /3/, /4/. The present analysis exploits the poloidal divertor configurations of ASDEX and its strong additional heating power which give it access to the new favourable H-confinement regime and allow it to approach MHD Beta limits /5/. As a consequence a wider variety of fluctuation phenomena are observed by Mirnov coils and soft X-Rays diagnostics /6/.

CHOICE OF DIAGNOSTICS AND DISCHARGE PHASES

Different phases of a typical high power NI-heated discharge are analyzed. The important time traces of this discharge are shown in fig. 1. (Actually four shots are used of the same series because of the high time-resolution diagnostics (250 kHz) recovered over different shots, #18041, #18040, #18026, #18039.) The analysis is concentrated on the characteristic phases indicated in the same fig. 1. For comparison also an L-discharge is analyzed (#18024). Diagnostics used for characterization of the MHD fluctuations were soft X-Rays and Mirnov coils. For present analysis 5 signals are considered: SXF and SXJ which are central X-Rays signal ($q < 1$); SXL and SXA which are peripheral X-Rays signals ($q > 1$) and A8SSW which is a Mirnov signal from a coil located externally in the equatorial plane of the ASDEX torus.

In general 10 windows of 8 ms each corresponding to 2000 data are taken and analyzed for each shot in order to give account of different physical phases and to have enough data (at least if the dimensionality is low). For some specific situations, the windows could be taken different, for a better definition or much longer in order to have a better establishment of dimensionality or to distinguish between noise and chaos.

If the dimensionality is low it is found indipendent of the number of data from 1000 to 10000. Also for the delay time it is found a range of independence of results with $5 \lesssim M \lesssim 10$, for N = 2000 (e.g.), but in general M = 5 is taken.

ASDEX RESULTS

According to the preceding definitions results are presented phase by phase. During an H-shot one can distinguish approximately four phases: They are shown in fig. 1 on the bottom border.

Phase 1: Deep L-phase, after additional NI heating and before L → H transition. Combined results from #18041 and #18040.

SXF: $\nu \sim 1$ at the beginning and then increases to $\nu \sim 2$ through splitting of dimensionality: $\nu - \begin{Bmatrix} 1.22 \\ 0.8 \end{Bmatrix}$

SXJ: $\nu \sim 1$ at the beginning and then increases to $\nu \sim 2.25$ through splitting of dimensionality: $\nu - \begin{Bmatrix} 2.25 \\ 0.75 \end{Bmatrix}$

SXL and SXA: $\nu \sim 1$

A8SSW: value of dimensionality $2.25 < \nu < 3.5$

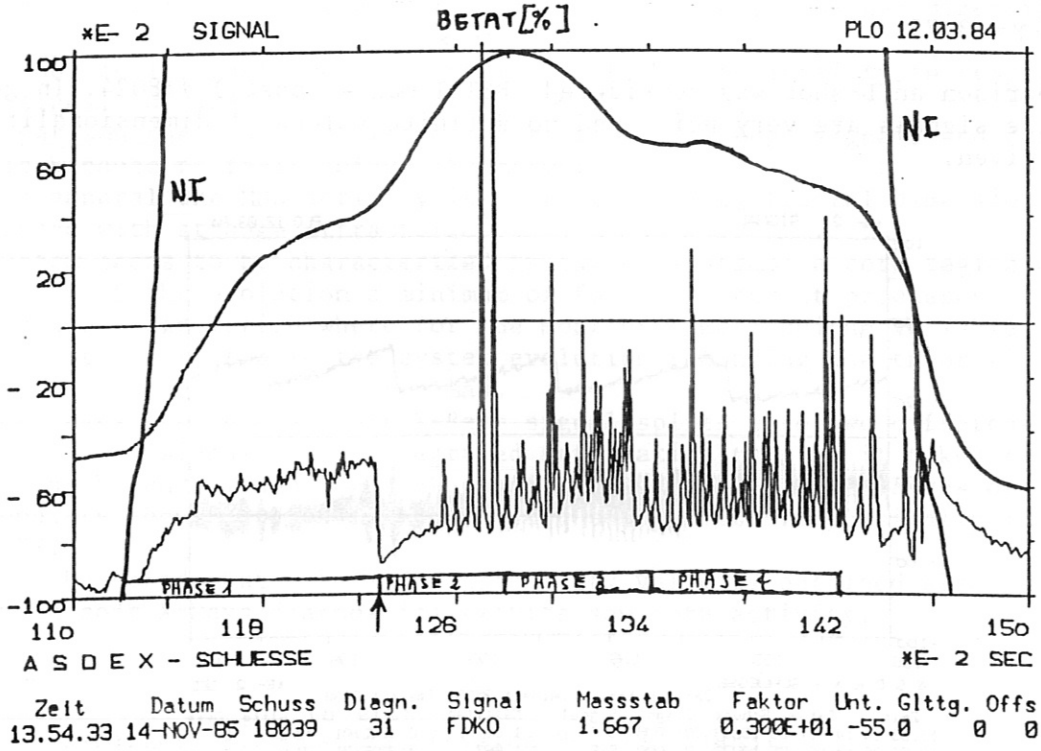

Fig. 1 shows some important parameters during a typical H-shot: NI is the neutral injection interval, FDKO is the signal connected with H_α activity which points the L → H transition (indicated with an arrow) and BETAT behaviour. In the bottom side the four phases of the analysis are reported.

Phase 2: After L → H transition, toward maximum BETAT. #18040. H-phase begins with sawtooth in edge region and fishbone like signal in central region.

SXF: $\gamma \sim 3.3$

SXJ: $\gamma \sim 0.75$

SXL and SXA: $\gamma \sim 1$

A8SSW: $\gamma \sim 3.5$

Phase 3: From BETAT maximum toward stationary phase with constant BETAT. #18026.

SXF: γ begins with value - 1 and then increases up to $\gamma \sim 3.6$

SXJ: $\gamma \sim 3$

SXL, SXA: $\gamma \sim 1$ in presence of well pronounced sawteeth

A8WNW: $2.6 < \gamma < 3.5$

Phase 4: Stationary H-phase at reduced but constant BETAT.#18039.

SXF: $\gamma \sim 1$ and after $2.5 < \gamma < 3.5$, Presence of a splitting of dimensionality at the beginning $\gamma \sim \begin{cases} 2.5 \\ 0.75 \end{cases}$

SXJ: noise

SXL: $\gamma \sim 0.85$, SXA: $\gamma \sim 1.2$ with well pronounced sawteeth (fig. 2 and 3)

A8SSW: $\gamma \sim 3.75$

In comparison an L-shot was considered (BETAT max - const.) #18024. In general the signals are very noisy and no definite values of dimensionality can be given.

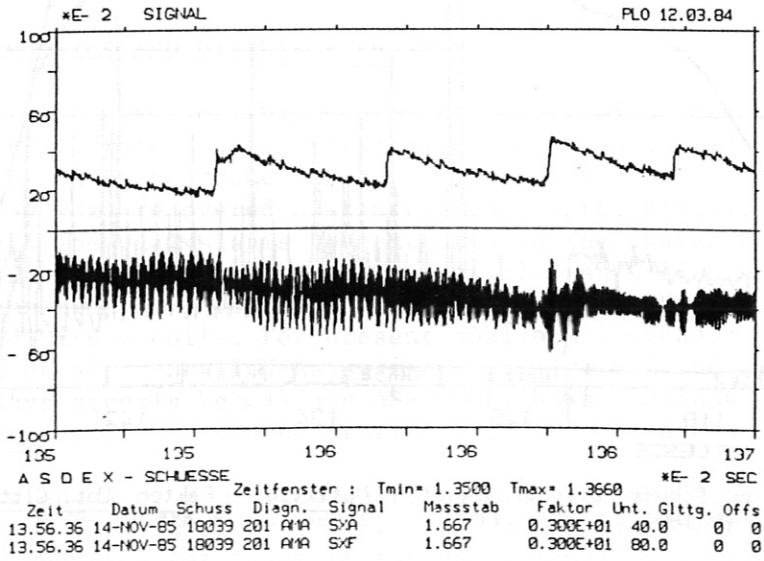

Fig. 2: Signals traces of two X-Rays chords during a time-window of 16 ms. SXA, the edge chord, shows definite sawteeth, while SXF, the core chord, exibits a fishbone-like structure. There seem to be no correlation between the two signals. #18039

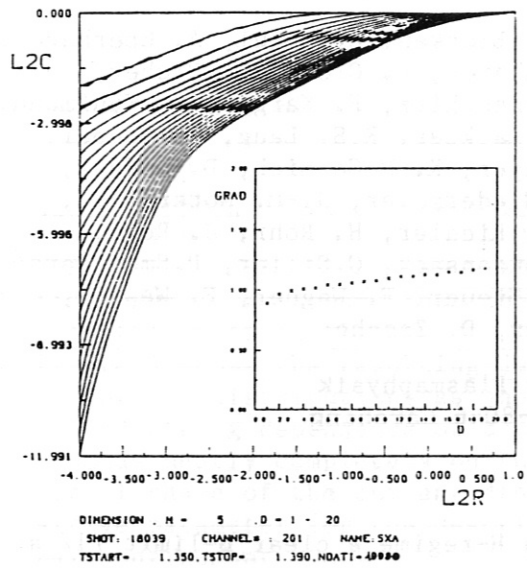

Fig. 3:
Dimensionality analysis for chord SXA signal. Same shot as in fig. 2 but for a longer period of 40 ms corresponding to 10000 data points. The result is identical for 1000 data point due to the very low dimensionality. M=5 is the delay time factor chosen. The embedding curves are simply connecting 50 calculated points (10 per decade). Logarithms in base 2 are used. The straight lines which show the D-depending slope are constructed with the least mean square method, starting from the same calculated points. In the square window the slopes, that is the gradients of the embedding curves as functions of embedding dimensions D are reported. The asymptotic saturation value of the slope is the dimension. $\nu \sim 1.2$ in this case.

CONCLUSIONS

The MHD activity present in ASDEX NI heated divertor plasma configurations, has in general a low dimensionality: $\nu < 3.75$. Signals with a non-strictly convergent saturation slope are ascribed to noise.
The edge soft X-Rays signals show a very low dimensionality: $\nu \sim 1$ during all phases.
The central soft X-Rays signals, in general, develope a higher dimensionality passing from L to H-phase and $1 < \nu < 3.5$.
The Mirnov coil signal seems to have an higher dimensionality in respect to other signals during all phases with $3 < \nu < 3.75$.
In comparison the L-shot shows no information from edge signals and central signals because of their noisy-like structure.
Thus in general the MHD activity is characterized by fractal dimensionality associated with strange attractors.
The system seems to be characterized by two subsystems: a core region where at the end of the evolution a minimum of four indipendent processes is necessary, and an edge region where for the most of time a unique variable could be enough to characterize the system evolution reminding the theoretical example of the non-linear logistic map.
In some cases the central soft X-Rays signal splits into two different value of ν. An X-Ray signal is an integrated information that is it takes into account both central and edge X-Ray emission. Two different values of dimensionality should indicate that the two subsystems are physically indipendent /7/.
It is to be noted that a $\nu = 1$ dimensionality value is obtained also in JET /3/, when soft X-Rays diagnostics exibits sawtooth activity.

REFERENCES

/1/ P.Grassberger, I.Procaccia, Physica 9D, 189 (1983).
/2/ S.J.Gee, J.B.Taylor, 12th Europ. Conf. Contr. Fus. and Plasma Physics, Vol. 2, 446 (1985).
/3/ A.Coté et al., ibid, 450 (1985).
/4/ W.Arter, D.N.Edwards, ibid, 442 (1985).
/5/ M.Keilhacker, ASDEX-Team, Nuclear Fusion, Vol. 25, 9 (1985).
/6/ R.Stambaugh, J.Gernhardt, O.Klüber, F.Wagner, (IPP III/103) (1984).
/7/ J.P.Eckmann, D.Ruelle, Rev. Mod. Phys. 57, 3, 617 (1985).

THE INFLUENCE OF THE CURRENT DISTRIBUTION ON THE ACHIEVABLE ß-VALUES IN ASDEX

G. v. Gierke and G. Becker, H. S. Bosch, H. Brocken, K. Büchl, A. Eberhagen, D. Eckhartt, G. Fussmann, O. Gehre, J. Gernhardt, E. Glock, O. Gruber, G. Haas, J. Hofmann, A. Izvozchikov[1], G. Janeschitz, F. Karger, M. Kaufmann, M. Keilhacker[2], O. Klüber, M. Kornherr, K. Lackner, R.S. Lang, M. Lenoci, F. Leuterer, G. Lisitano, F. Mast, H. M. Mayer, K. McCormick, D. Meisel, V. Mertens, E. R. Müller[2], H. Murmann, H. Niedermeyer, J.-M. Noterdaeme, A. Pietrzyk[3], W. Poschenrieder, H. Rapp, H. Riedler, H. Röhr, J. Roth, F. Ryter[4], W. Sandmann, F.Schneider, C. Setzensack, G.Siller, P.Smeulders[2], F.X. Söldner, E. Speth, K.Steinmetz, K.-H. Steuer, F. Wagner, F. Wesner, G. Vlases[3], O. Vollmer, D. Zasche

Max-Planck-Institut für Plasmaphysik
EURATOM Association, D-8046 Garching

Introduction:

In the divertor tokamak ASDEX we get in the H-regime a clear ß-limit /1/ at

$$ß_{cr} = 2.8 \frac{I}{a\ B} \ \% \ [MA,m,T] \qquad (1)$$

if we use for the volume averaged ß the ß-value measured by the diamagnetic loop. Below the ß-limit the highest ß-value during a shot, $ß_{max}$, is proportional to the normalized power

$$P_N = \frac{P}{0.33 \cdot b \cdot R \cdot B} \qquad (2)$$

where P[MW] is the total heating power, 2b the vertical diameter and B the magnetic field on axis. The confinement time at $ß_{max}$ is proportional to the plasma current I. The proportionality factor depends mainly on the isotope composition and slightly on current, impurity and other parameters not yet unraveled. The confinement time at $ß_{max}$ is $I_p/4 > \tau_E > I_p/7$, where the limits are for deuterium and hydrogen respectively. After $ß_{max}$ ß always decays to values about or even below 0.7 - 0.8 $ß_{cr}$. At this level nearly time independent ß-values could be observed. The ß-decay is usually the faster, the closer $ß_{max}$ is to $ß_{cr}$. There is no qualitative difference in any signal between discharges with $ß_{max} = ß_{cr}$ or $ß_{max} < ß_{cr}$.

After excluding all trivial reasons, like wall contact, radiation due to impurity accumulation etc, the only thinkable parameter which could change with time and would cause the observed ß decay is the current distribution. But only the longest observed decay times are in agreement with resistive current diffusion (calculated with classical resistivity throughout this paper). We hesitated for a long time to assume faster current redistributions then those.

In the numerical calculations, which result in a similar ß-limit as observed experimentally the limit seems to be caused by a combination of ballooning modes and surface kinks /2/. In a divertor tokamak the behaviour of surface kinks are unclear due to the unknown influence of the strong shear near the separatrix. In ASDEX the influence of the separatrix is very concentrated and therefore the influence should be restricted to higher n-modes. As we

---

[1]Academy of Sciences, Leningrad, USSR; [2]Present address: JET Joint Undertaking, England; [3]Univ. of Washington, Seattle, USA; [4]CEN Grenoble, France

observe no pronounced changes with varying q-values we assume tentatively that the ballooning mode is responsible mainly for the observed limit.

The influence of the current distribution

We therefore have calculated the influence of the current distribution on the ballooning mode stability limit using the inner inductivity l_i as a measure. We used the ballooning mode criterium

$$\frac{dp}{dr} = -\frac{B^2}{2\,R\,q^2} \cdot \alpha(s) \qquad s = \left(\frac{r}{q}\right)\frac{dq}{dr}$$

and the approximation $\alpha(s) = s/1.67$ /3/, but we neglected the usual condition $q_o = 1$. We assume that the ballooning mode criterium is marginal all over the cross-section.

Figure 1 shows the resulting dependence of $\beta/\varepsilon\, q^2$ on l_i for several families of current distributions as shown by the inserts ($\varepsilon = a/R$). We see the expected strong dependence of β on l_i, but the surprising result is that β depends nearly completely on the global l_i value and only marginally on the actual shape of the current distribution. We conclude that l_i is a very sensitive parameter for the description of the volume averaged β resp. the global confinement time.

The dependence found in fig. 1 can be described by the approximation:

$$\frac{\beta}{\varepsilon} = \frac{1}{q^2}\,(19\,l_i^{\,2} + 44.5\,l_i - 27). \qquad (3)$$

Comparing this formula with experimental l_i-values, evaluated as described later, we find that the general behaviour of the β-decay can be described, but that the calculated β-values are larger by 20 - 100 % depending on the q-value. Inserting the empirical law (1), found experimentally and numerically, for the β limit, transformed to $\beta_{cr}/\varepsilon = 14/q$ one finds that unreasonably small l_i-values belong to this β-limit especially at higher q-values. This is not surprising, because all the theoretical calculations have been done in the cylindrical large aspect ratio approximation. We therefore assume as a correction that the q in eq. (3) is not the cylindrical q but q_ψ . Figure 2 shows now the β/ε dependence on l_i with different q_ψ as parameter. The β-limit $\beta/\varepsilon = 14/q$ and q_{cyl}-curves are also shown. They have been calculated assuming a purely thermal β_p in the calculation of q_ψ, neglecting contributions by the beam or rotation.

By the measured $\beta(\beta_p^{dia})$ and the measured q_ψ a point in fig. 2 is defined and with it the corresponding l_i. q_ψ is evaluated from β_p^{equ} by

$$q = q_c\,[1 + \varepsilon^2(1 + 0.5\,(\beta_p^{equ})^2] \text{ with } q_c = \frac{5a \cdot b \cdot B}{R \cdot I}$$

taking into account the empirically found dependence of a on β_p^{equ}: $a = 0.375\,(1 + 0.07\,\beta_p^{equ})$ but limited to $a \leq 0.44$ m, due to our vessel dimensions, which was found roughly in agreement with equilibrium calculations, (quoted q_c values are always with a = 0.4 m).

In fig. 2 data points are shown measured in the described way of a power scan at 379 kA and $q_c = 2.79$, H^o injection (1.8-3.5 MW), where the crosses are values at β_{max} and the points intermediate β values during the β decay or the β values on the end of the heating pulses. Supplemented is this scan by shots at 311 kA, at q-values of 2.805, 2.71, and 2.85. The slightly stronger bent of the experimental curves compared with the calculated q_c = const. curves is due to the nonthermal contributions of the beam and the rotation to β_p^{equ} and by it to q_ψ and by the increasing diameter. As we shall see later the resulting l_i values agree quite well with l_i values evaluated

in quite another way beside the lowest point shown, an L-shot, where we, however, do not expect that the ballooning criterium is fulfilled all over the radius.
In fig. 3 we show q-scans at otherwise constant parameters (311 kA, 3.5 MW H_o-injection). The achieved l_i values (and consequently the ß values) are limited to values <1.5. With D_o injection (4.05 MW) otherwise the same parameters very high l_i values result and the ß-limit can be reached also at larger q_c values.

To compare the found l_i values we evaluate l_i out of the difference signal

$$ß_p^{equ} - ß_p^{dia} = \frac{l_i}{2} + \frac{ß}{2} \text{ „nontherm.}$$

neglecting $ß_{\perp nonth.}$. $ß_{\text{„nonth.}}$ is estimated from the injected beam, the slowing down time and an expression for the rotation, which is proportional to the energy confinement time. The absolute value of $ß_{\text{„nonth.}}$ is adjusted so that for long lasting shots where the difference signals approach a constant value, the so evaluated l_i value approaches the l_i value calculated out of the electron temperature profile. Time dependence of l_i, evaluated in this manner are shown in fig. 4. The crosses are the l_i values according to our modified ballooning criterum. The agreement is nearly in all cases satisfying in spite of the many inaccuracies involved and the difficulty of the absolute calibration. With deuterium injection the agreement can't be reached with constant proportionality factors in every case as the nonthermal contributions (probably the rotation) seems to depend nonlinearily on the beam parameters and the confinement. But the very large l_i-values and their decay are found.

Summary and discussion

We conclude that in the H-regime the ballooning mode is limiting the energy content of the discharge at $ß_{max}$ and afterwards always and already at very low ß-values. The ß-limit $ß/\varepsilon = 14/q$ can only be reached by favorable combinations of l_i and q_ψ. At large q values l_i must be larger than in the ohmic cases, which can only be reached transiently by inductive currents, for which we have some experimental hints. These currents are due to the injected beam, the plasma rotation and the $ß_p$-changes. The ß-decay after $ß_{max}$ is due to the disappearance of these inductive currents and the approach to the stationary current profile defined by the conductivity profile. As a change of $ß_p$ and the rotation induce changes of the confinement by altering the ballooning limitation, an increase as well as a decrease has a self-inforcing effect. Therefore high ß values decay faster and to values well below limits achieved with smaller power.

The ß-limit itself, but also the ballooning limited profiles below of it, are influenced by rational q_ψ-values (fig.5). This coupling of the ballooning mode with surface kinks seems to favour the current redistribution. But much finer scans are necessary to prove this convincingly as higher rational values are involved, too, and the self-inforcing effect mask the rationals.

References:

/1/ M. Keilhacker, et al., in Plasma Phys. Contr. Fusion (Spec. Issue: Proc. 12th Eur.Conf.Contr.Fus.and Plasma Phys., Budapest, 1985), 28 (1986) 29. G. v. Gierke, Europhys. Conf. Abstr., 12th Europ. Conf. on Contr. Fusion and Plasma Phys., Budapest, 1985, 9F, Part I, 331.
/2/ F. Troyon, Workshop on "The Basic Physical Processes of Toroidal Fusion Plasmas", Varenna (1985).
/3/ J.A. Wesson, A. Sykes, Nucl. Fus., 25, 85 (1985).

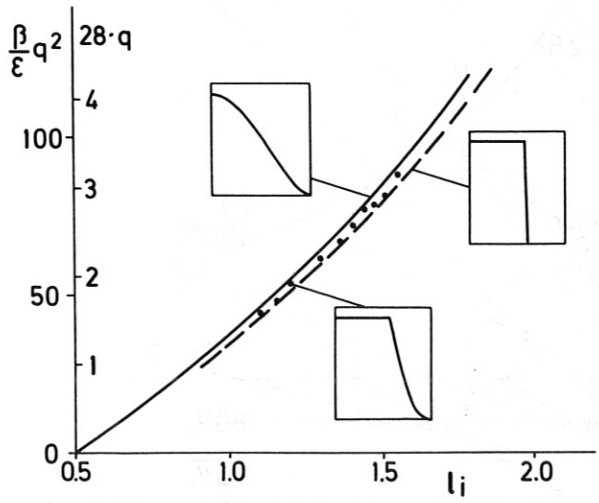

Fig. 1: Dependence of ballooning mode limited $<\beta_T>$ on the internal inductance li for different current distributions. The second scale gives the $q_o > 1$ limit for different q.

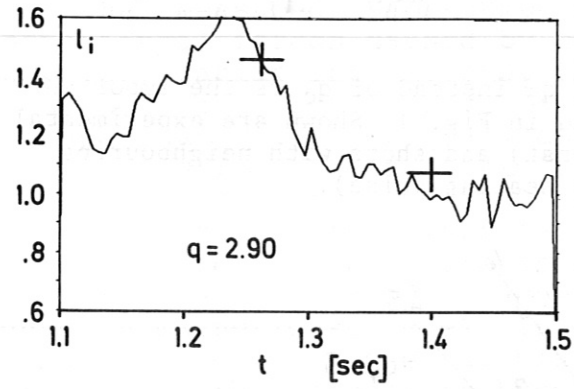

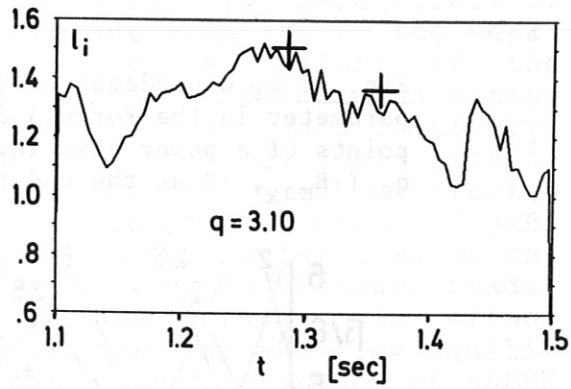

Figs 4: Time dependence of li evaluated from the difference of $\beta_p^{equ} - \beta_p^{dia}$ and an estimated beam contribution. The crosses are li-values calculated with the modified ballooning criterion.

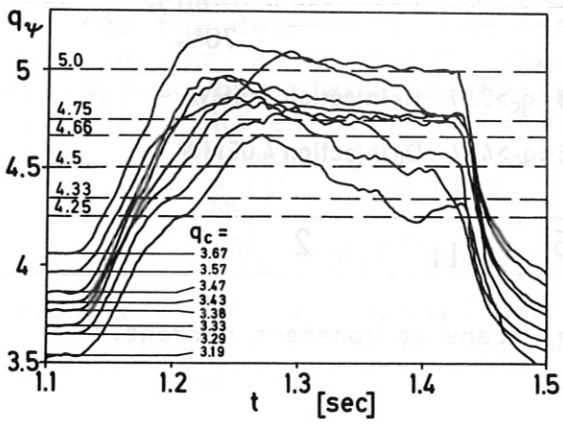

Fig. 5: q_ψ-values calculated with β_p^{equ} showing the influence of rational q_ψ-values.

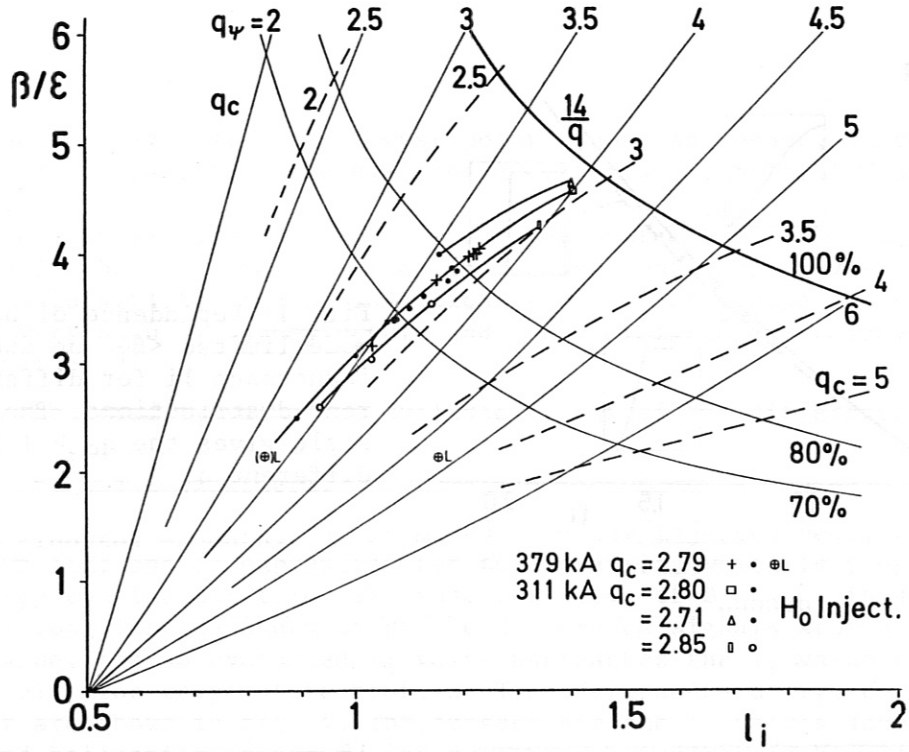

Fig. 2: β_T dependence on li, if q_ψ instead of q_c is the important parameter in the formula derived in Fig. 1. Shown are experimental points of a power scan (q_c = const) and shots with neighbouring q_c (+β_{max}, ·ß at the end of the heating pulse).

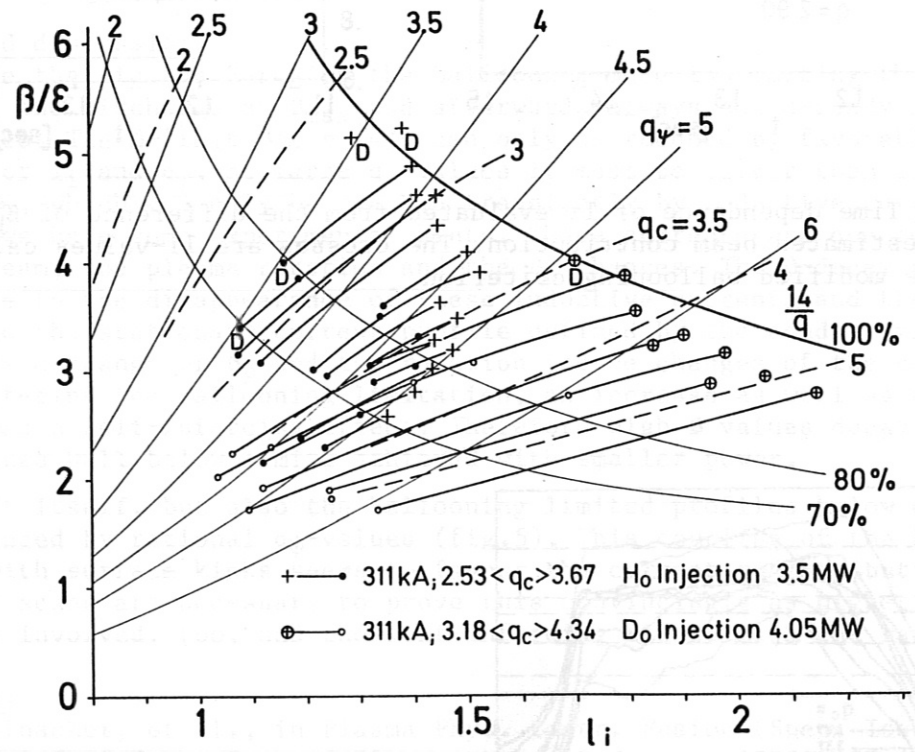

Fig. 3: The same as Fig. 2 but q_c-scans at constant current.

FREE-BOUNDARY FLOW EQUILIBRIA FOR ASDEX AND ASDEX-UG

H.P. Zehrfeld

Max-Planck-Institut fuer Plasmaphysik
EURATOM Association, D-8046 Garching

Neutral beam injection into magnetically confined plasmas is connected with plasma flow and a corresponding alteration of the equilibrium characteristics of the discharge. In particular density variations on magnetic surfaces were observed in neutral beam heated plasmas. This has led to attempts to explain them by toroidal rotation of the plasma. It has turned out that in view of the measured Mach-numbers for this flow the mere effect of centrifugal forces caused by only toroidal rotation is too weak. However, taking into account the more involved effect of the combined action of both toroidal and poloidal plasma motion changes the situation qualitatively as well as quantitatively: Due to the finite rotational transform of the flow field accelerating forces in toroidal direction appear. In an equilibrium state, they must be balanced by corresponding components of jxB. This requires plasma currents across magnetic surfaces which together with the toroidal magnetic field maintain pressure gradients in magnetic surfaces. In order to demonstrate this effect quantitatively we have calculated corresponding MHD flow equilibria for the separatrix-bounded plasma configurations of ASDEX and ASDEX-UG. For this purpose the partial differential equation

$$R^2 \, \mathrm{div}\left\{ \frac{D \nabla \Psi}{R^2} \right\} = \mathcal{S}(R, \Psi, |\nabla \Psi|, F) \quad , \qquad D = D(R, \Psi, |\nabla \Psi|, F) \tag{1}$$

must be solved for the poloidal flux Ψ. D and $\mathcal{S}$ are given functions. F represents five profiles

$$F = (H_M, C_M, J_M, \Psi_M, \Phi_M) = F(\Psi) \tag{2}$$

The first three quantities can be determined prescribing profiles for the density n, the temperature T and the poloidal current J on a straight line s leading from the magnetic axis ($\Psi = \Psi_A$) to the plasma boundary ($\Psi = \Psi_B$). Ψ_M is the poloidal mass flux, Φ_M the electric potential. We have chosen the distributions

$$n_S \sim (1 - \gamma_n x)^{\nu} \quad , \quad T_S \sim (1 - \gamma_T x)^{\mu} \quad , \quad J_S^2 = J_S^2(\Psi_A) + (J_B^2 - J_S^2(\Psi_A))\, G(x) \tag{3}$$

$$\Psi_M' \sim n_S T_S^{1/2} e^{-x} \quad , \quad \Phi_M' \sim T_S^{1/2} \quad , \quad ' \equiv d/d\Psi \tag{4}$$

where $x = (\Psi - \Psi_A)/(\Psi_B - \Psi_A)$ and $G(x)$ ($0 \leq G(x) \leq 1$) some function describing the diamagnetism of the plasma. γ_n, ν and γ_T, μ are profile constants.

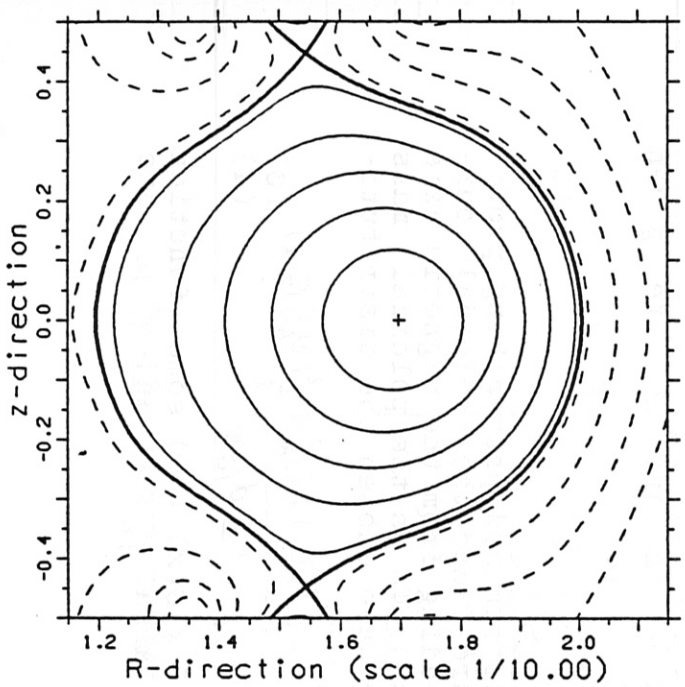

Fig. 1 ASDEX flux surfaces

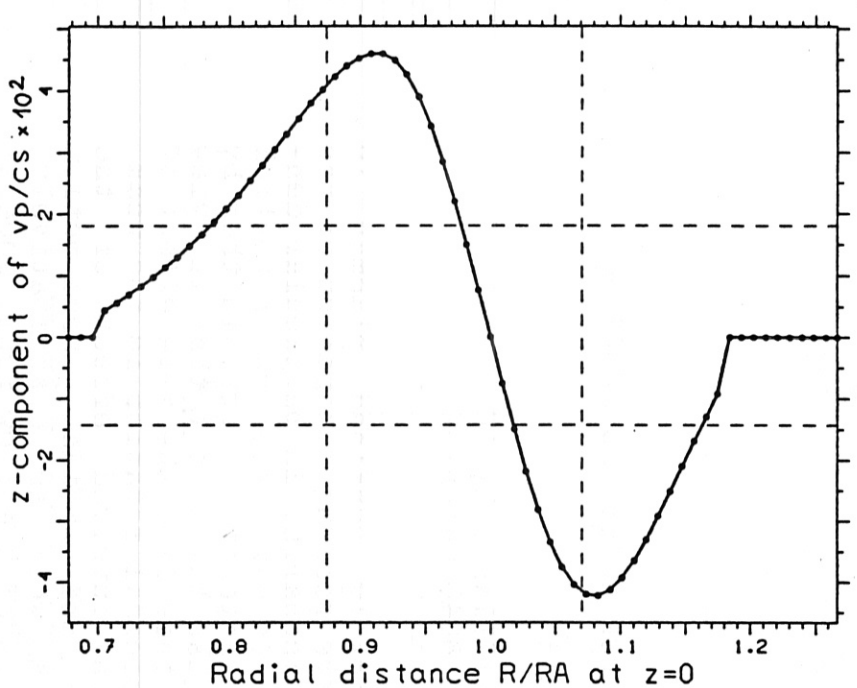

Fig. 2 Radial v_p/c_s-profile

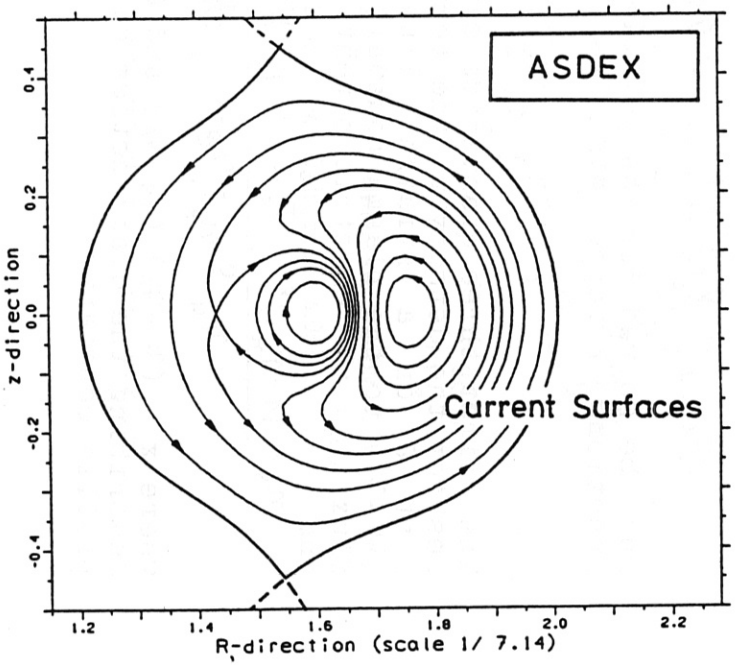

Fig. 3 ASDEX current surface

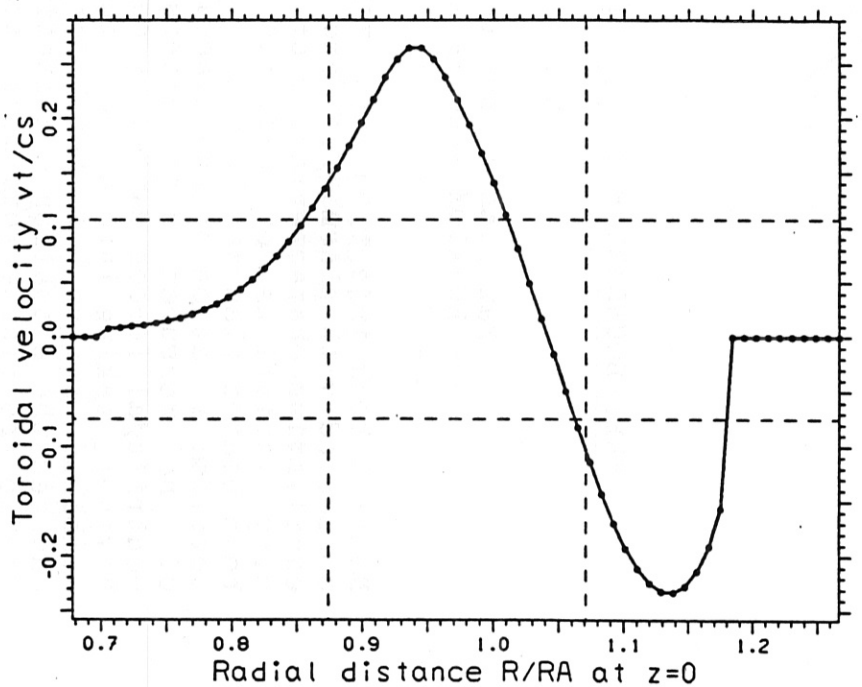

Fig. 4 Radial v_T/c_s profile

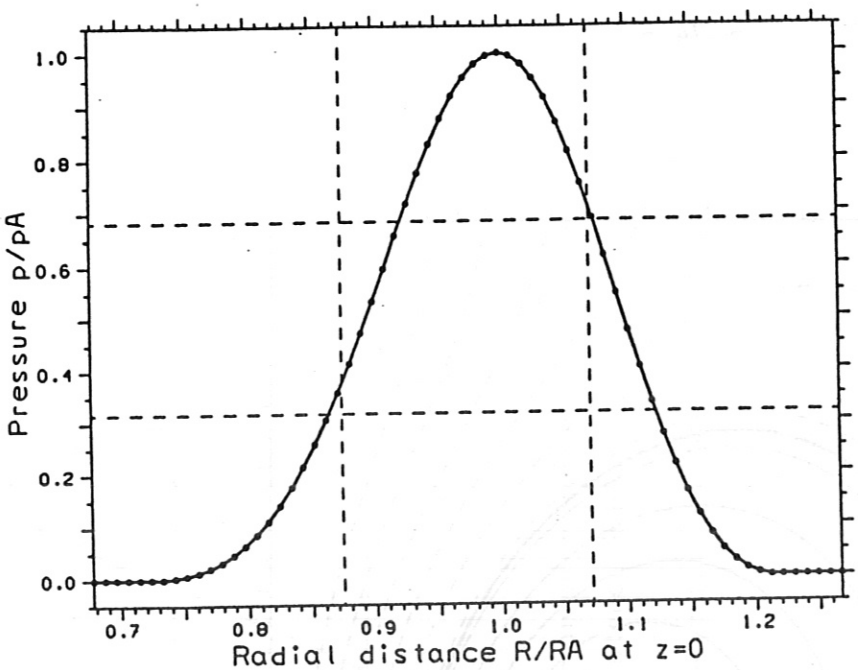

Fig. 5 Radial pressure profile (static equilibrium)

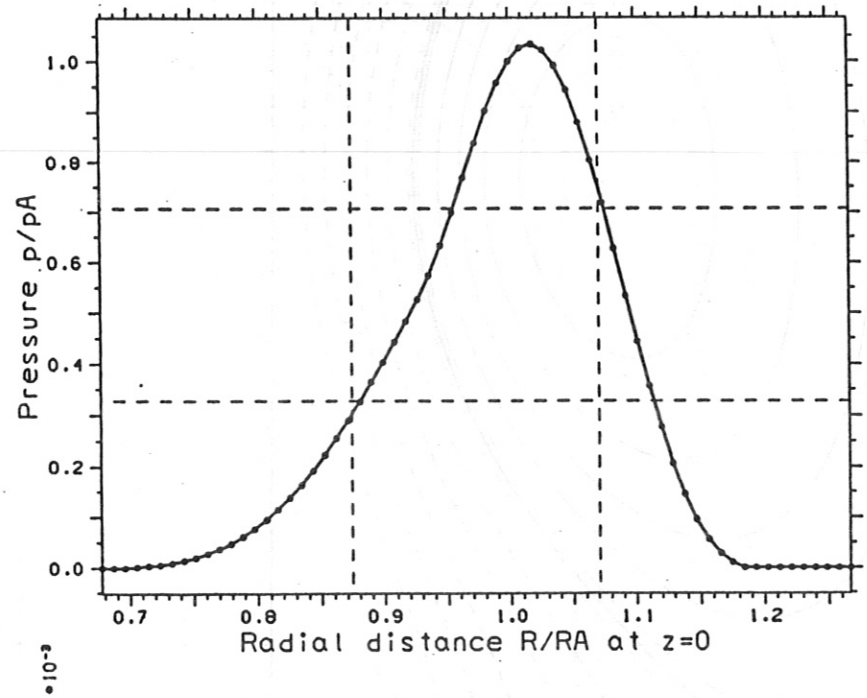

Fig. 6 Radial pressure profile (flow equilibrium)

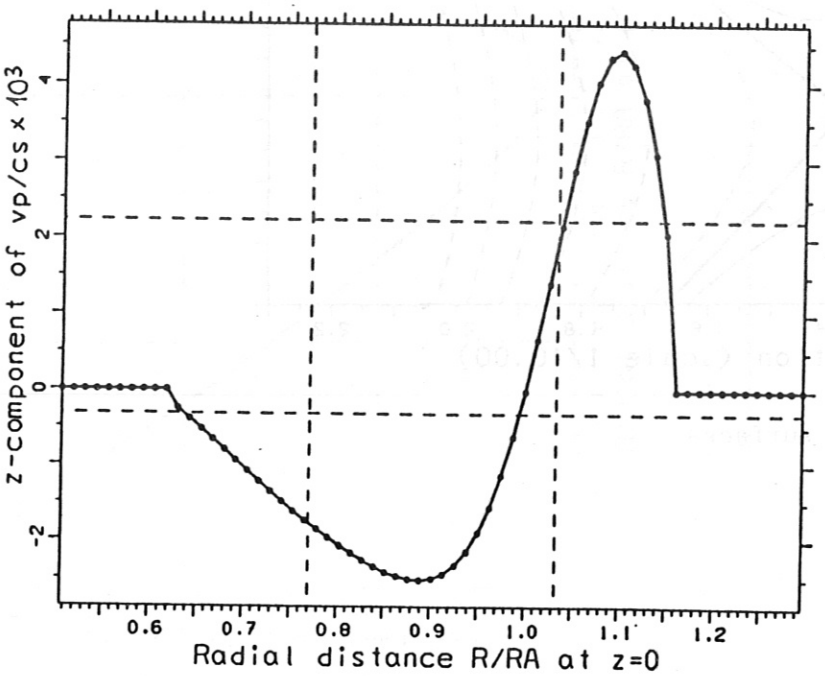

Fig. 8 Radial v_p/c_s-profile

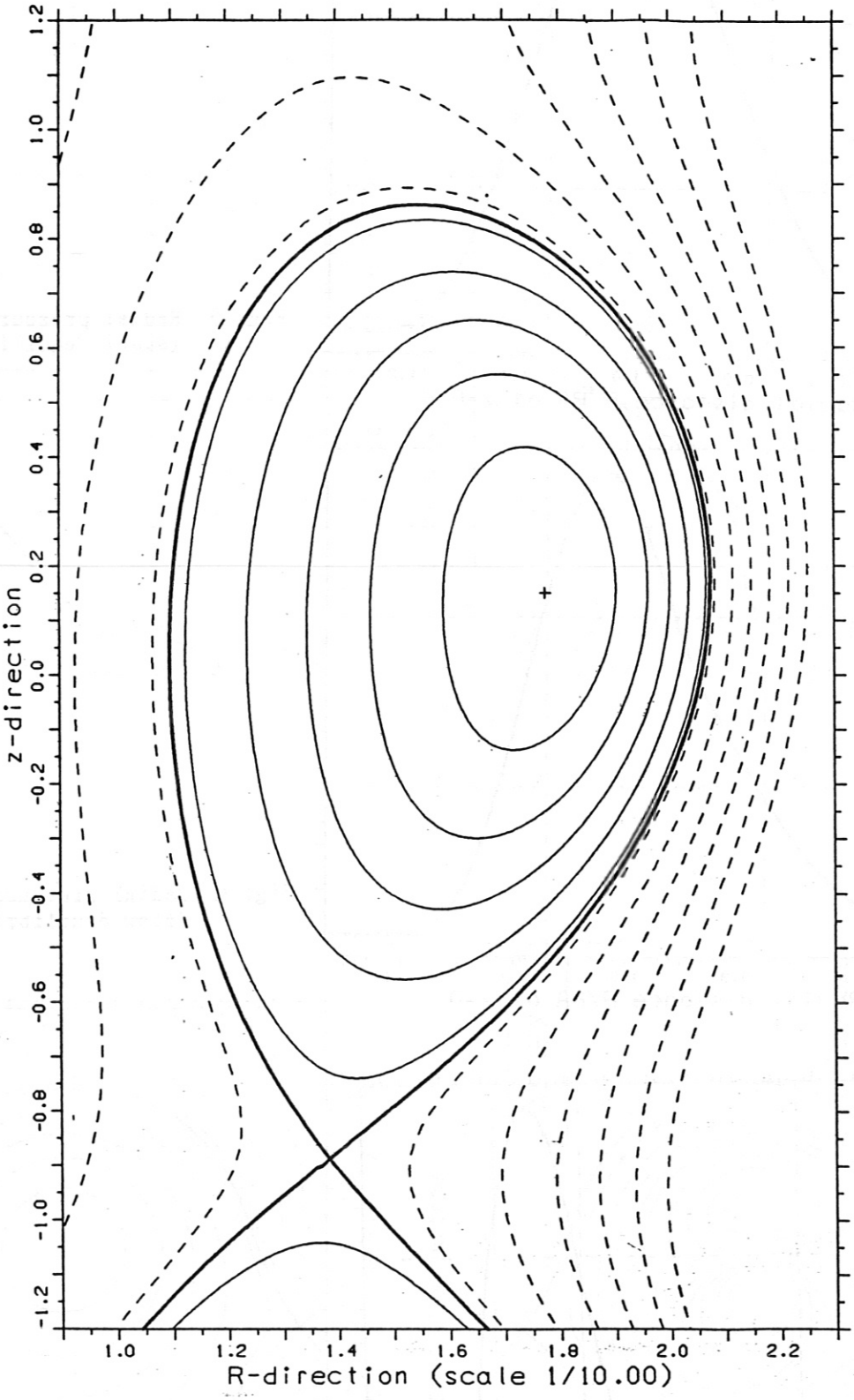

Fig. 7 ASDEX-UG flux surfaces

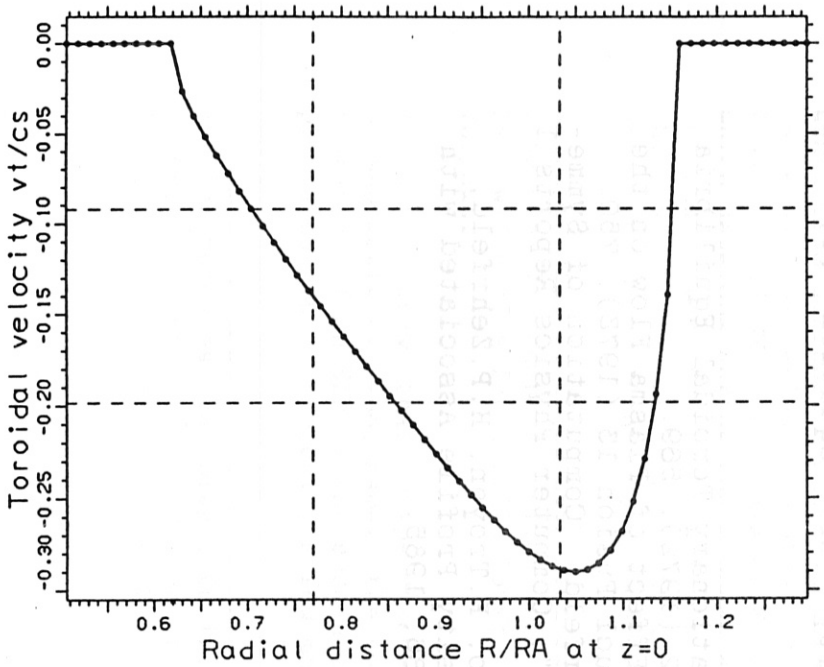

Fig. 9 Radial v_T/c_s-profile

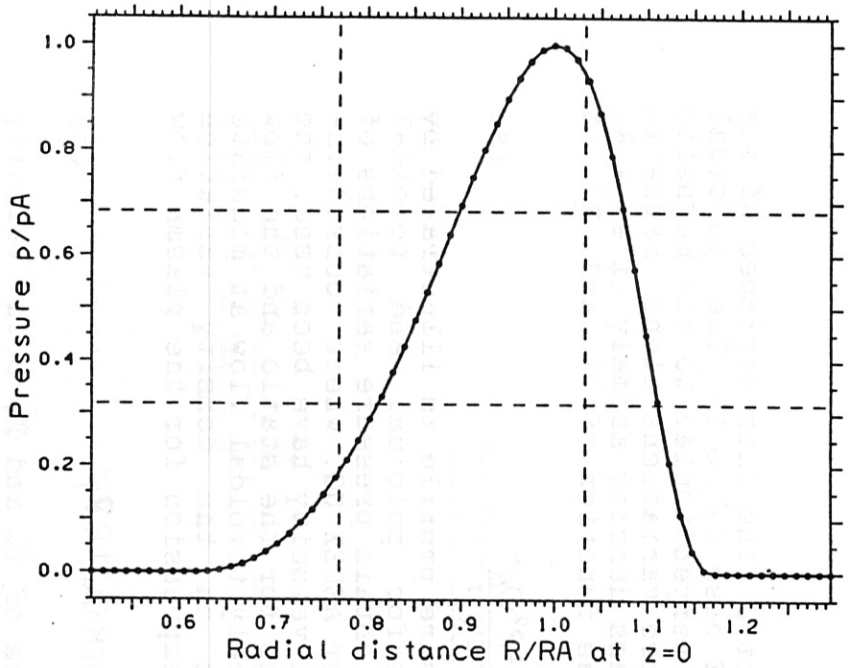

Fig. 10 Radial pressure profile (static equilibrium)

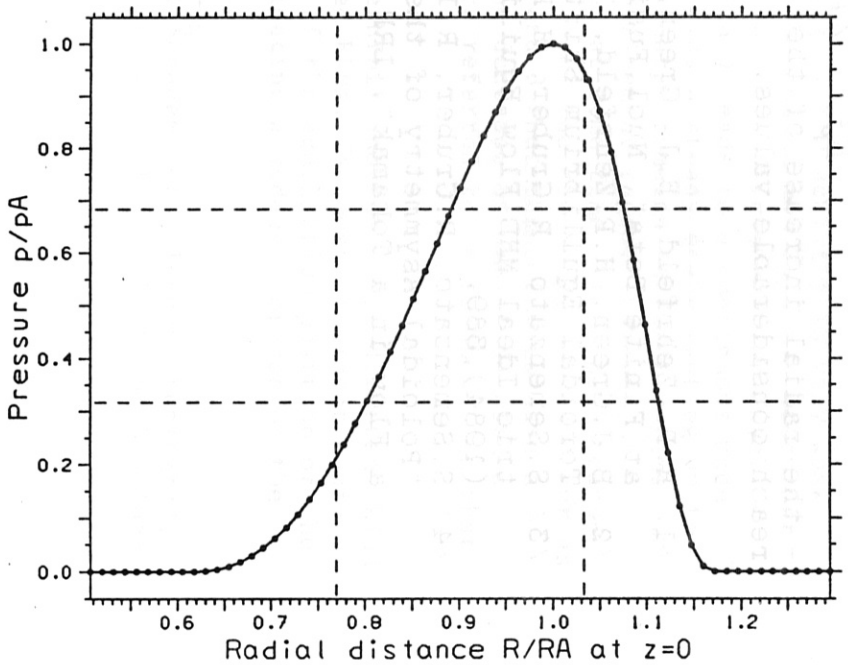

Fig. 11 Radial pressure profile (flow equilibrium)

Fig.3 shows surfaces of constant J (the flux surfaces of the current density field) for an ASDEX case ($\beta_p \approx 1$). The poloidal components of the current density perpendicular to the magnetic surfaces are responsible for pressure variations along magnetic field lines. The corresponding mass density anomaly (i.e. a R-dependence of ρ if ρ is conceived as function of Ψ and R) at the magnetic axis is given by

$$\frac{R}{\rho}\frac{\partial \rho}{\partial R} = \frac{B^2 \Psi_M'^2/\rho^2 + 4\pi^2 R^2 \Phi_M'^2}{(1-(B\Psi_M'/\rho c_s)^2)c_s^2} \qquad (5)$$

The anomaly of the radial pressure profile is illustrated by Figs. 5 and 6. For the Mach-numbers for poloidal and toroidal flow indicated in Figs.2 and 4 we obtain pressure variations of about 20% on a magnetic surface. For ASDEX-UG, where considerable smaller values for the poloidal velocity have been used, the corresponding pressure distributions for the static and the flow case are barely discernable - purely toroidal flow at moderate Mach-numbers has only small effect on the density variation along magnetic field lines. The expression for the plasma flow field

$$\mathbf{v} = \frac{\Psi_M'}{\rho}\mathbf{B}_p + \left\{\frac{\Psi_M'}{\rho}B_T + 2\pi R \Phi_M'\right\} R \nabla\varphi \qquad (6)$$

shows that for an appropriate choice of Ψ_M and Φ_M both velocity components can be small, whereas - approaching the boundary of the first elliptic regime of equation (1)

$$0 \leq \frac{\mu_0 \rho v_p^2}{B_p^2} < \frac{\beta}{1+\beta}, \quad \beta = \mu_0 \gamma p / B^2 \qquad (7)$$

- the radial increase of the density (cf. equation (5)) may reach considerable values.

/1/ H.P. Zehrfeld, B.J. Green, "Stationary Toroidal Equilibria at Finite Beta", Nucl.Fusion 12 (1972), 569.

/2/ B.J.Green, H.P.Zehrfeld, "The Effect of Plasma Flow on the Toroidal Equilibrium Shift", Nucl.Fusion 13 (1973), 750.

/3/ S.Semenzato, R.Gruber, H.P.Zehrfeld, "Computation of Symmetric Ideal MHD Flow Equilibria", Computer Physics Reports 1 (1984),389.

/4/ S.Semenzato, R.Gruber, R.Iacono, F.Troyon, H.P.Zehrfeld, "Poloidal Asymmetry of the Density Profile Associated with a Flow in a Tokamak", LRP 258/85, 1985.

MHD CHARACTERISTICS OF ASDEX H-TYPE DISCHARGES APPROACHING THE ß LIMIT

O. Klüber, J. Gernhardt, K. Grassie, J. Hofmann, M. Kornherr, R. Stambaugh[1], H. P. Zehrfeld and G. Becker, H. S. Bosch, H. Brocken, A. Eberhagen, G. Fussmann, O. Gehre, G.v.Gierke, E. Glock, O. Gruber, G. Haas, A. Izvozchikov[2], G. Janeschitz, F. Karger, M. Keilhacker[3], K. Lackner, M. Lenoci, G. Lisitano, F. Mast, H. M. Mayer, K. McCormick, D. Meisel, V. Mertens, E. R. Müller[3], H. Murmann, H. Niedermeyer, A. Pietrzyk[4], W. Poschenrieder, H. Rapp, H. Riedler, H. Röhr, J. Roth, F. Ryter[5], F. Schneider, C. Setzensack, G. Siller, P. Smeulders[3], F.X. Söldner, E. Speth, K.-H. Steuer, O. Vollmer, F. Wagner, D. Zasche

Max-Planck-Institut für Plasmaphysik
EURATOM Association, D-8046 Garching

1. Introduction

Due to the favourable confinement properties of the H regime, ß values close to the Troyon limit can be achieved in the ADSEX device at a neutral injection power level ~3 MW. In many cases, the ß limit is a soft one, i.e. ß attains a maximum and then decays smoothly up to the end of the injection pulse. Disruptions, however, may occur both during the rise and fall of ß.

2. Temporal evolution of MHD activity in the case of soft ß limit

The investigations presented below are mainly based on the analysis of Mirnov probe signals. Due to the divertor geometry, only a fraction of the poloidal circumference could be covered, namely 102° at the outside and 44° at the inside of the torus symmetric to the midplane. The toroidal mode number n is obtained from 5 probes placed in the midplane at the outer side distributed over a toroidal angle of 156°. Apart from a few n=2 cases not discussed in this paper, always n=1 is observed.

In ohmically heated ASDEX divertor discharges, MHD activity is very weak apart from disruptive ones; in this case the common m = 2, n = 1 precursor is seen. Application of neutral beam heating at sufficient power level (maximum 3.5 MW in the case of H_0 injection) leads to a continuous mode which develops during the L phase and attains a steady state lasting up to the end of the injection pulse if the discharge remains in the L regime. In the case of transition into the H-type confinement regime, however, the amplitude of the continuous mode decreases at some time after the H transition to a low level; in the further course of the discharge bursts occur as shown in Fig. 1. It is seen from Figs. 2 and 3 that these bursts have a fishbone-like character, i.e. increase and decrease of amplitude with a half-width of a few oscillations; they are referred to as fishbones in what follows.

It is well known that H-type discharges exhibit another quite different kind of MHD activity, too, namely the so-called ELMs. The most prominent manifestation of an ELM is the sudden change of the equilibrium position of the plasma column by typically a few mm (indicating a sudden decrease of the

---

[1]GA Technologies, San Diego, Calif., USA; [2]Academy of Sciences, Leningrad, USSR; [3]Present address: JET Joint Undertaking, England; [4]Univ. of Washington, Seattle, USA; [5]CEN Grenoble, France

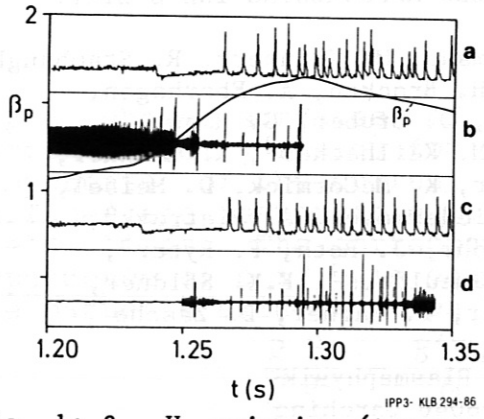

Fig. 1: β_p, H_α emission (traces a,c) and $\dot{\beta}_p$ (traces b,d) versus time for shots No. 18030 (a,b) and 18034 (c,d). Injection starts at 1.13 s and stops at 1.43 s. The temporal evolution of β_p is practically the same for both discharges.

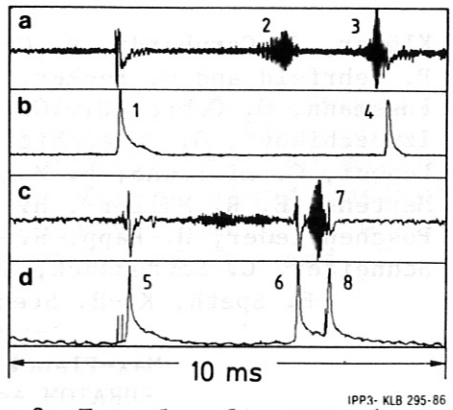

Fig.2: Examples for ELMs (events No. 1,4,5,6,8) and fishbones (events No. 2,3,7) recorded by Mirnov probes (traces a,c) and H_α monitor (traces b,d).

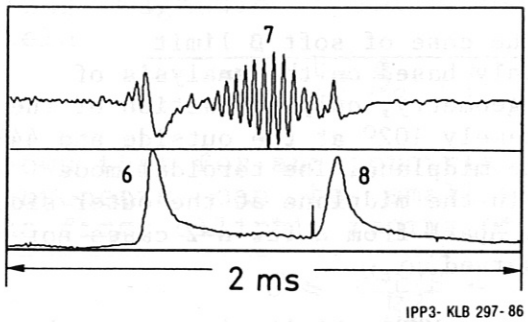

Fig. 3: Expansion of the sequence 6-7-8 from Fig. 2.

equilibrium parameter $\beta_p + l_i/2$) and a peak in the H_α emission. ELMs do not manifest, however, in the records of the Mirnov probes apart from the inward motion.
It is seen from Fig. 2 that ELMs and fishbones may occur independently from each other; on the other hand, fishbones appear to be triggered by ELMs in some cases and, more frequently, ELMs appear to be triggered by fishbones.

There are several features which are common to the continuous and the fishbone-like mode, namely

- The amplitudes measured at the outer side of the torus are much larger than those at the inner side. Amplitude ratios of 15 - 25 are typical; in many cases, the ratio must be even larger since no signals from the inner probes are obtained. Obviously, the determination of the poloidal mode number is particularly difficult in this situation.
- The frequency recorded by the soft X-ray diode cameras coincides with that of the Mirnov probe signals. During the continuous mode, an m = 1, n = 1 structure with frequency doubling is clearly seen. In the case of the fishbone-like events, the amplitudes are much smaller. In some cases, doubling of frequency was observed in near-center channels which indicates that the q = 1 surface may still be present.
- The mode propagates according to the toroidal rotation of the plasma applied by the unidirectional co-injection. Doppler shift measurement can only be obtained from a small zone at $R \sim R_o + 3a/4$. The velocity calculated from the mode frequency is systematically by a factor of 1.4 larger than the spectroscopic one. This discrepancy increases if an additional motion of the mode due to the diamagnetic drift is assumed. Thus, the mode frequency appears to be governed by the central rotation velocity.

It is seen from Fig. 1 that the repetition rate of the ELMs does not vary appreciably during the rise and the fall of ß. Fishbones appear more frequently in the ß decay phase. The duration of a fishbone-like burst, however, is less than 1 ms and the island size estimated from the amplitude of $\dot{B}$ is typically of the order of a few cms. Hence, for this type of shots, the observed MHD activity does not explain the decay of ß.

3. Discharges dominated by an m=2, n=1 mode

Another type is characterized by a dramatic change of the mode structure. A typical example is shown in Fig. 4. It is seen that at 1.29 s a continuous mode develops the amplitude of which increases suddenly at the inner side of the torus. A temporal expansion of this event is shown in Fig. 5. The change

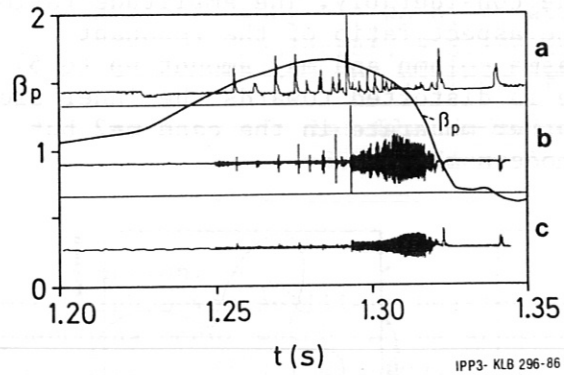

Fig. 4: $ß_p$ versus time for shot No. 18033. Injection starts at 1.13 s. The first disruption occurs at 1.32 s. Trace a: H_α emission. Trace b: $\dot{B}_\theta$ from a Mirnov probe located in the midplane at the outside of the torus. Trace c: Same for the inside.

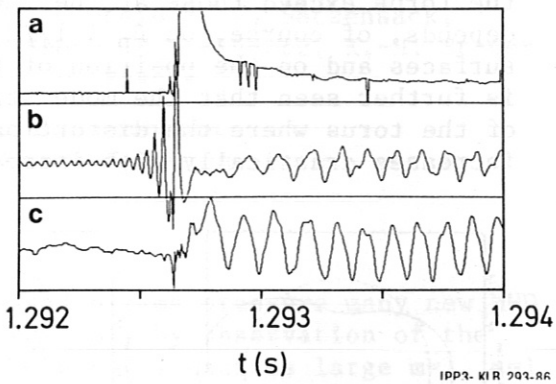

Fig. 5: Onset of the m=2 oscillation in shot No. 18033. Trace a: H_α signal (diode saturates). Trace b: Mirnov signal, midplane outside. Trace c: Mirnov signal, midplane inside. The amplitude is enhanced by a factor of 4 as compared to trace b.

of the mode structure is initiated by an ELM which is preceded by a fishbone. It is seen from Fig. 4 that the amplitude of the H_α spike of this particular ELM exceeds by far that of the preceding and the following ones. After the transition, the mode continues to propagate in the direction given by the toroidal rotation; the frequency of it decreases, however, by a factor between 2 and 4. Most remarkably, the ratio of the frequencies before and after the transition is close to an integral number. Furthermore, it is seen that the frequency recorded before the tansition remains with a small amplitude which lasts for typically 10 ms. Later on, only the "slow" mode is recorded. It is clearly an m = 2, n = 1 mode, as shown in Section 4.
In the case presented in Fig. 4, the m = 2 mode leads to a disruption after 30 ms. In the last ms before the onset of the disruption, the signal frequency decreases drastically. In other discharges, the m = 2, n = 1 mode may attain a saturated level and persist up to the end of the NI pulse. In both cases, the island size is large and may amount up to 20 % of the minor radius of the plasma column. It is seen from Fig. 4 that the onset of the m = 2, n = 1 mode leads to a violent decrease of $ß_p$.
Most frequently, the onset of the "large" m = 2 mode occurs nearly at the time at which ß attains its maximum. In some cases, however, this mode develops already in the phase of ß rise, in particular, if q_a is low.

4. Discussion of the poloidal mode structure

In the discharges considered here, the boundary q value is $3.5 < q_a < 4.5$. Hence the mode numbers m = 2,3 and 4 (if $q_a > 4$) are the candidates for the explanation of the mode structure. In a previous paper /1/, one of the authors investigated the effect of the toroidal curvature on the poloidal mode structure. In this model, the modes are created by surface currents flowing on rational magnetic surfaces parallel to the magnetic field. Typical examples for the modes m = 2,3 and 4, n = 1 are plotted in Fig. 6 where the phase is chosen such, that a maximum is located in the midplane at the outer side of the torus. It is seen that the amplitudes at the outer side of the torus exceed those at the inner side considerably. The amplitude ratio depends, of course, on $ß_p + l_i/2$, on the aspect ratio of the resonant surfaces and on the position of the plasma column and may amount up to 5. It is further seen that the mode structure is distorted towards the inner side of the torus where the distortion is rather moderate in the case m=2 but increases drastically with increasing mode number.

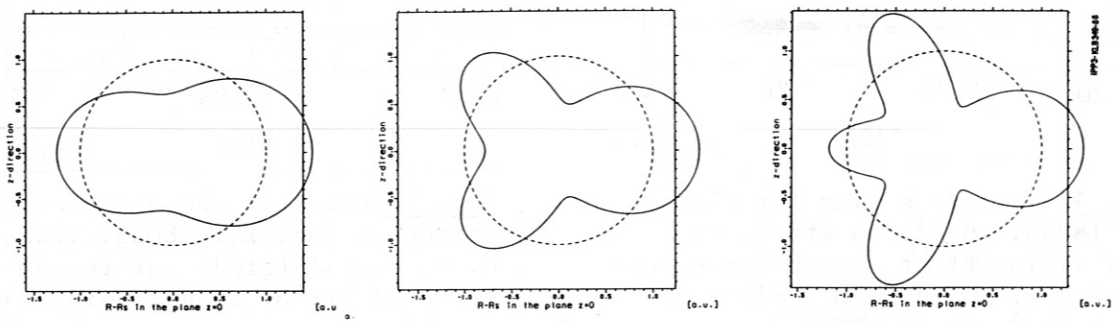

Fig. 6: Polar diagrams of the modes m = 2,3,4. The torus axis is on the left-hand side.

While the m=2 mode discussed in the preceding section fits quite well into this picture, the continuous and the fishbone-like mode cannot be explained by this model. The observed out-in amplitude ratios of 15 - 25 might be ascribed to the occurrence of two modes, an even and an odd one, coupled such that two maxima coincide in the midplane at the ouside. It is seen from Fig. 6, however, that all three modes pretend an m=2 structure as far as the outer side of the torus is concerned. This contradicts to the observed phase relations according to which phase reversal is obtained at poloidal angular distances between 45° and 60° (which would indicate a superposition of m=3 and m=4 if the geometry were cylindrical).
Obviously, rational magnetic surfaces with m > 4 are also present due to the separatrix. They are located, however, in a region with very large shear and hence very small island sizes. It is unlikely, therefore, that modes with appreciable amplitudes develop in this region.

5. Summary

- Three types of MHD oscillations were observed, a continuous, a fishbone-like and an m=2, n=1 mode.
- The decay of ß can be attributed to observable MHD activity only in the cases in which a strong m=2, n=1 mode develops.
- The continuous and the fishbone-like mode cannot be ascribed to currents flowing parallel to the magnetic field on rational surfaces.

Reference:

/1/ G.Fussmann, B.J.Green, H.P.Zehrfeld, Plasma Phys.and Contr.Nucl.Fus.Res. 1980 (Proc.10th Int.Conf.Brussels, 1980), Vol.I,IAEA, Vienna (1980) 353.

MHD-EFFECTS WITH NI AND ICRF HEATING ON ASDEX

M. Kornherr, A. Eberhagen, J. Gernhardt, O. Klüber, F. Wagner, G. Becker, H. S. Bosch, H. Brocken, G. Fussmann, O. Gehre, G.v.Gierke, E. Glock, O. Gruber, G. Haas, J. Hofmann, A. Izvozchikov[1], G. Janeschitz, F. Karger, M. Keilhacker[2], M. Kornherr, K. Lackner, M. Lenoci, G. Lisitano, F. Mast, H. M. Mayer, K. McCormick, D. Meisel, V. Mertens, E. R. Müller[2], H. Murmann, H. Niedermeyer, J.-M. Noterdaeme, A. Pietrzyk[3], W. Poschenrieder, H. Rapp, H. Riedler, H. Röhr, J. Roth, F. Ryter[4], F. Schneider, C. Setzensack, G. Siller, P. Smeulders[2], F.X. Söldner, E. Speth, K.Steinmetz, K.-H. Steuer, O. Vollmer, F. Wesner, D. Zasche

Max-Planck-Institut für Plasmaphysik
EURATOM Association, D-8046 Garching

Introduction

With high power auxiliary heating at increased plasma pressure many new MHD phenomena occur which can be studied most suitably by observation of the soft X-ray ("SX") radiation. In the plasma centre NI excites large m=1, n=1 oscillations, the detailed behaviour of which depends on external parameters. In divertor discharges with NI power $\lesssim$2 MW their occurrence is repetitive and terminated by sawteeth. When NI is combined with ICRH the m=1 mode often disappears after a first strong sawtooth which is followed by "precursor-free" large sawteeth.

The hot spot model

Detailed studies of the m=1 mode and of sawtooth activity have been made in ASDEX mainly based on the analysis of the signals of two SX diode cameras. In the case of a toroidal rotating plasma and disregarding a possible poloidal rotation these signals represent the projection of an asymmetric and helical radiation profile into the viewed poloidal cross section. From comparison with ECE measurements we conclude that the oscillating SX signals are mostly caused by varying electron temperatures.

Figure 1 shows an example of an m=1 mode during NI rotating opposite to the electron drift direction. The behaviour of the signals (doubled frequency, phase relations) can be well described by a rotating hot spot with an extension 2D, which is much larger than the distance Δ of its centre to the magnetic axis (Fig. 2). The hot spot centre describes a circle with radius Δ around the magnetic axis, the off-axis rotation of the hot spot affects a plasma roughly within the q = 1 zone.

Assuming growing values of Δ (at fixed D) we can distinguish three possibilities concerned to a chord with distance Z to the magnetic axis. These three cases and their characteristic different features are exhibited schematically in Fig. 3a,b,c (the dashed curves belong to parallel but opposite to the axis positioned chords with the same distance Z).

---

[1]Academy of Sciences, Leningrad, USSR; [2]Present address: JET Joint Undertaking, England; [3]Univ. of Washington, Seattle, USA; [4]CEN Grenoble, France

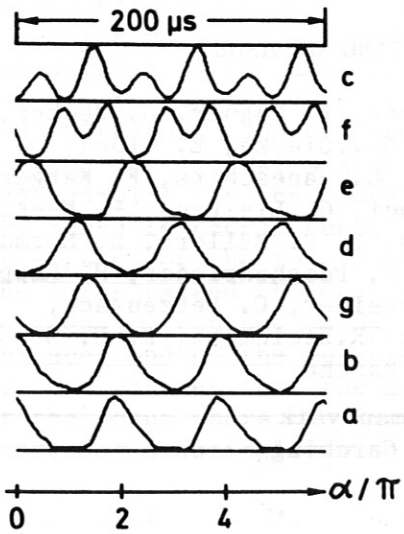

Fig. 1: SX traces of a m=1 mode with positions shown in Fig.2.

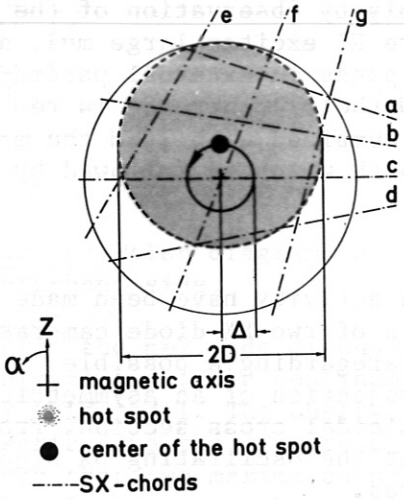

Fig. 2: The hot spot model.

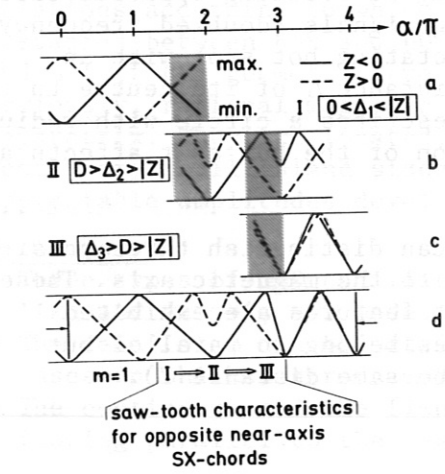

Fig. 3: Characteristics of the hot spot model for different cases with transitions (sectors hatched).

The sawtooth collapse

Near-axis SX chords show even during the conventionally defined period of the sawtooth collapse an oscillatory structure which seems to evolve from the m=1 mode with typical deviations from it. Such traces were interpreted as relaxation into an m=0 mode or a sudden change of direction of rotation.

With the assumption of a growing Δ, however, the observed behaviour as seen in the near-centre chords can well be described by the hot spot model.

Figure 3d exhibits the characteristic behaviour of two opposite chords during such a growth phase. The picture is "constructed" with the assumption of a transition from case I to case II and finally to case III each in a half period. Measured signals from two opposite SX channels with a radial distance R = 2.5 cm ($\approx$ Z) agree very well with this model - Fig. 4b demonstrates an example.

Another example is presented in Fig. 5 (an expended section of Fig. 6). While the central chord points toward a precursor-free sawtooth the near-axis chords show clearly the development of a weak m=1 mode which is followed after two periods by the sawtooth transition with the typical evolution described above (Fig. 5a). Opposite chords with a larger distance R from the axis exhibit this transition one half period later.

Heat wave propagation

The developed picture based on the hot spot model explains the spikes in the SX traces and their irregular nature as often seen when SX signals are plotted on a large time scale (Fig. 6). The traces of this example document that the hot spot does not reach the plasma edge and the mode is damped. The hot spot decays and a heat pulse propagates to the plasma edge on a time scale roughly two orders of magnitude larger than the collapse time and with a velocity of about 10^4 cm/sec.

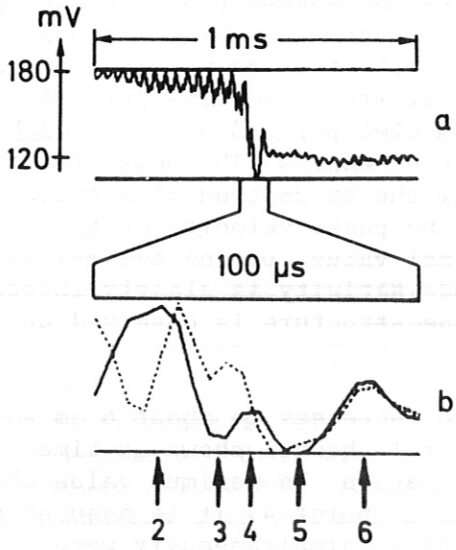

Fig. 4: a) The central signal from a sawtooth event with preceding m=1 mode. b) Vertically opposite near-axis signals during this sawtooth transition. The expended interval corresponds to the marked segment (by arrows) in Fig. 3d.

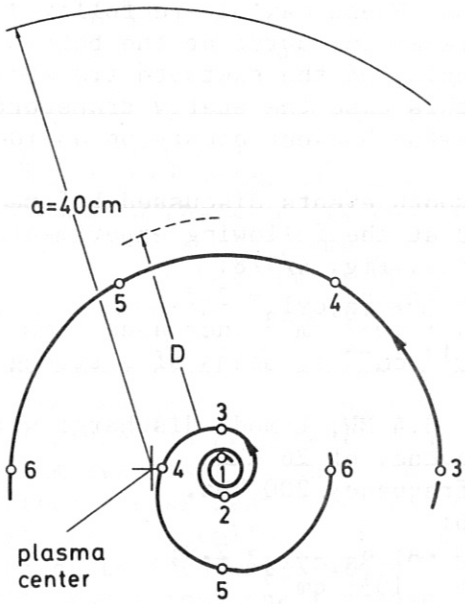

Fig. 7 The inner spiral represents the path of the hot spot centre during a sawtooth transition, the outer curve describes the movement of a second hot spot centre which is assumed to originate from the first one. The marked time points correspond to the arrows of Fig. 4b and 8.

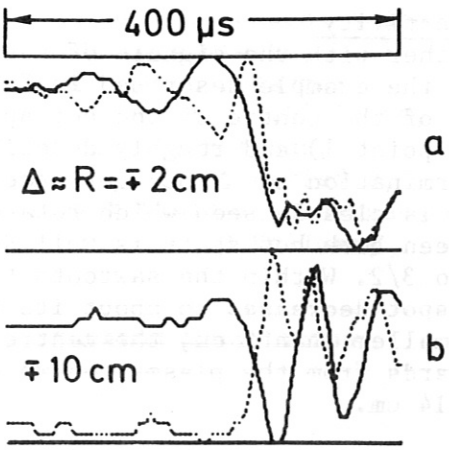

Fig. 5: A sawtooth transition after a weak but rapidly developing m=1 mode, shown for opposite channels at different distances from the magnetic axis.

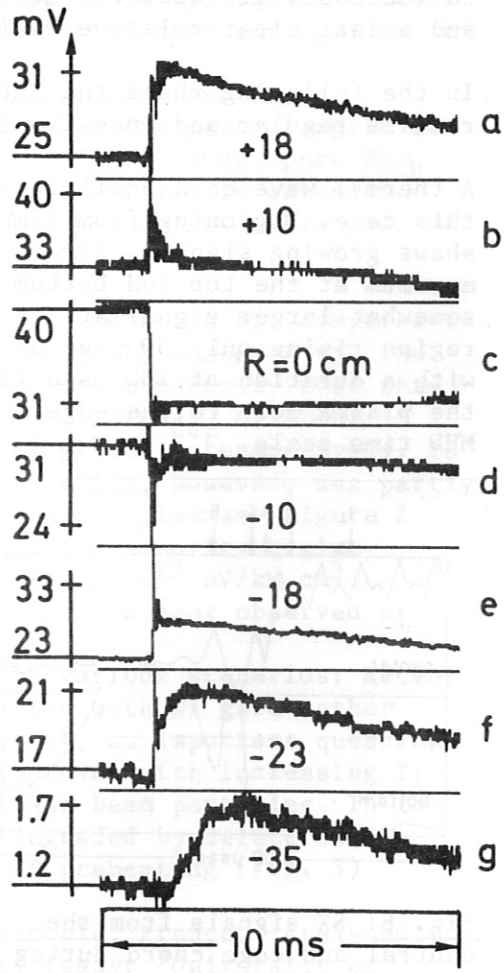

Fig. 6: A sawtooth collapse with typical spikes and the propagating heat pulse.

MHD activity

Together with the signals of a second camera the movement of the hot spot from the example described in Fig. 4 was reconstructed. Fig. 7 shows the path of the centre of the hot spot, which starts from an m=1 mode (marked time point 1) and roughly describes a spiral. After the time point 4 the determination of Δ becomes uncertain. From time point 3 on a second hot spot is clearly seen which rotates at a larger radius. The phase relation between both hot spots is well described by the assumption of a frequency ratio 3/2. Within the sawtooth transition the phase velocity of the inner hot spot decreases to about its half original value. During the m=1 mode Δ is smaller than 2 cm, the centre of the mode activity is clearly shifted outwards from the plasma centre and the mode structure is observed up to $r \approx 14$ cm.

Within the transition 2 to 3 the value of Δ increases to about 6 cm and the mode structure extends to $r \approx a/2$. The central channel shows at time point 3 a first distinct minimum and does not reach again its maximum value when the hot spot passes the horizontal channel at time point 4. It is assumed that the original hot spot is deformed and breaks up simultaneously when Δ starts to increase. Its absolute minimum shows the central channel at time point 5 and a last clear relative maximum is observed at time point 6.

In the following phase the MHD activity within a/2 becomes complicated but remains regular and ends finally in a stationary low frequency m=3 mode.

A thermal wave on a equilibrium transport time scale does not develop in this case. Beginning from time point 3 the outer plasma region ($r > a/2$) shows growing signals. Already at time point 5 these signals reach a first maximum at the top and bottom of the plasma. These maxima are followed by a somewhat larger signal at the top and a tremendous burst at the bottom region rising only 50 µsec after the beginning of the sawtooth transition with a duration of 200 µsec (Fig. 8). In this case the energy transport from the plasma core to the edge caused by a sawtooth event occurs on an ideal MHD time scale.

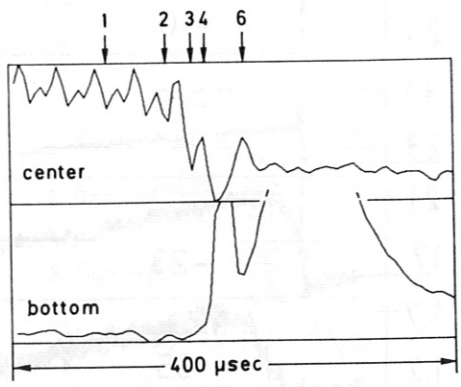

Fig. 8: SX signals from the central and edge chord during and after the sawtooth transition of Fig. 4b.

The sawtooth events discussed before were observed at the following experimental conditions. Fig. 4/7/8:
I_p = 380 kA, $q_{a,cyl}$ = 2.7;
$\bar{n}_e = 2.4 \cdot 10^{13}$ cm^{-3} increased from $1.5 \cdot 10^{13}$ cm^{-3} by means of a strong Ne puff;
NI power 3.4 MW; L-mode discharge with m=1 frequency of 26 kHz;
sample frequency 200 kHz.
Fig. 5/6:
I_p = 380 kA; $q_{a,cyl}$ = 2.9;
$\bar{n}_e = 3.5 \cdot 10^{13}$ cm^{-3}
NI power 1.7 MW + ICRH with 400 kW;
sample frequency 100 kHz.

ICRF H-MODE AND $2\Omega_{CH}$/D(H)-MINORITY HEATING ON ASDEX

K.Steinmetz, F.Wagner, F.Wesner, A.Izvozchikov[1], J.-M.Noterdaeme, F.Ryter[2], J.Bäumler, G.Becker, H.S.Bosch, M.Brambilla, F.Braun, H.Brocken, A.Eberhagen, R.Fritsch, G.Fussmann, O.Gehre, J.Gernhardt, G.v.Gierke, E.Glock, O.Gruber, G.Haas, J.Hofmann, F.Hofmeister, G.Janeschitz, F.Karger, M.Keilhacker[3], O.Klüber, M.Kornherr, K.Lackner, M.Lenoci[4], G.Lisitano, E.van Mark, F.Mast, H.M.Mayer, K.McCormick, D.Meisel, V.Mertens, E.R.Müller[3], H.Murmann, H.Niedermeyer, A.Pietrzyk[5], W.Poschenrieder, S.Puri, H.Rapp, H.Röhr, J.Roth, K.-H.Schmitter, F.Schneider, C.Setzensack, G.Siller, P.Smeulders[3], F.Söldner, E.Speth, K.-H.Steuer, O.Vollmer, H.Wedler, D.Zasche

Max-Planck-Institut für Plasmaphysik, Euratom Association,
D-8046 Garching, FRG

INTRODUCTION

ICRH experiments in the ASDEX divertor tokamak have now been operated in the $2\Omega_{CH}$ regime and D(H)-minority mode. This paper presents the status of these investigations and compares some of the most interesting features of the RF scenarios with neutral beam heating (NI) in the same machine under optimized and reproducible plasma parameters. The achievement of the H-mode with ICRH alone is reported. Considerations on possible synergetic effects of the combination of ICRH with NI /1/ and impurity studies during ICRH /2/ are presented separately.

$2\Omega_{CH}$ (67 MHz) and D(H)-heating (33.5 MHz) experiments are being routinely conducted in excess of 2 MW launched power for pulse lengths of up to 1 s. In addition to the combined scenarios of NI + ICRH, pure $2\Omega_{CH}$ and D(H) heating up to maximal power have now been applied in extensive studies of diverted discharges and in the case of carbonised walls /3/.

EXPERIMENTAL RESULTS

Electron and ion heating properties of both RF scenarios are compared in Figs. 1 and 2. Direct central electron heating (Fig. 1) measured via the initial slope of the sawteeth is clearly higher in the minority mode than at $2\Omega_{CH}$. The electron heating efficiencies, $\bar{n}_e \Delta T_e(0)/P^{IC}_{dep}$ of about 4.0 and $1.8 \cdot 10^{13}$ eV/kW cm^3, for D(H) and $2\Omega_{CH}$ (H-plasma), respectively, is also higher in the minority case ($n_H/n_e \sim 0.05$), which, however, was partly due to the better confinement properties of deuterium plasmas. Figure 2 presents the ion heating at RF power below 1 MW: The minority regime exhibits an efficiency as high as the NI H-mode ($4.2 \cdot 10^{13}$ eV/kW cm^3, $H^o \rightarrow D^+$) /4/, which is consistent with the good confinement observed at that RF power level (see Figs. 4 and 5).

Now to the global heating efficiencies of the various scenarios: Recent investigations on $2\Omega_{CH}$-heating and its combination with NI gave rather promising results /5/. When combining ICRH with NI, an important question is whether the RF heating efficiency becomes improved with increasing T_i (target) or by coupling of the IC wave to the fast beam particles. In the case of carbonised walls where heating is not degraded by deleterious impurity radiation, the increase of T_i due to NI preheating (Fig. 3)

---

[1]Academy of Sciences, Leningrad, USSR; [2]CEN Grenoble, France; [3]Assigned to JET Joint Undertaking, England; [4]ENEA Frascati, Italy; [5]University of Washington, Seattle, USA;

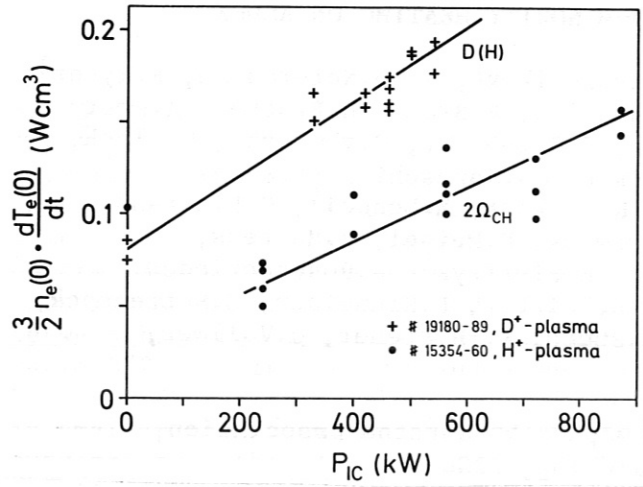

Fig. 1: Direct e-heating of $2\Omega_{CH}$ and D(H) scenarios.

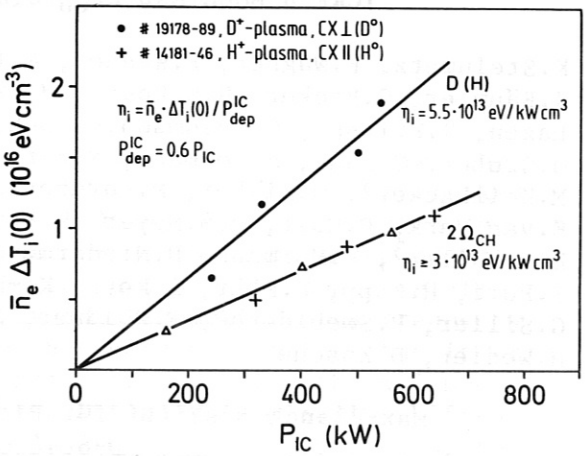

Fig. 2: Ion heating for both ICRF regimes.

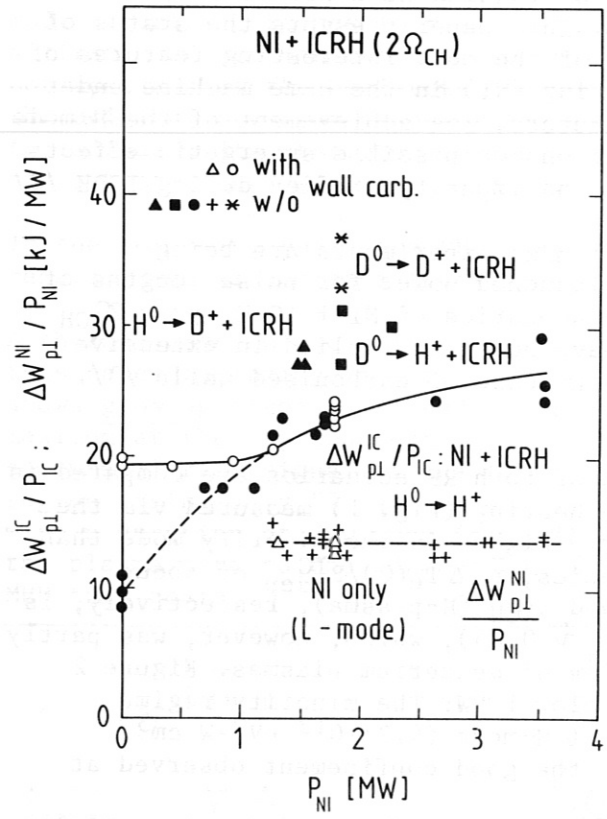

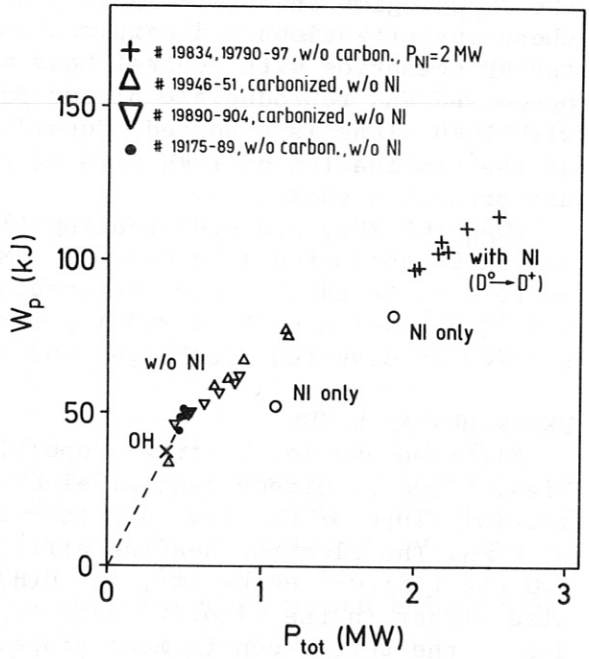

Fig. 4: Plasma energy versus total heating power for D(H), NI and NI+D(H) heating

Fig. 3: Heating efficiencies of $2\Omega_{CH}$, NI and NI+$2\Omega_{CH}$

improves the IC efficiency only by about 25 % from about 20 kJ/MW (w/o NI, $T_i \sim 0.7$ keV) to 25 kJ/MW at $P_{NI} = 3.5$ MW ($T_i \sim 2.2$ keV). Coupling of the IC wave to the beam is in fact observed in CX-spectra, but obviously to an extent which is not sufficient enough to improve the heating: On comparison of ICRH discharges with additional $H^0 \rightarrow D^+$ or $D^0 \rightarrow H^+$ (Fig. 3) the RF efficiency turns out to be independent of the beam species. Owing to the isotope effect on confinement $2\Omega_{CH}$-heated discharges in deuterium and helium with a small amount of hydrogen ($n_H/n_e > 10$ %) show even better efficiencies ($D^0 \rightarrow D^+$ + ICRH in Fig. 3). No heating at the fourth IC harmonics of D^+ and $^4He^{2+}$ could be noted.

As a general feature, energy and particle confinement of ICRH-heated plasmas are systematically better than those of the NI L-mode but appear still within the combined error bars. The plasma energy for minority heating at low power scales as well as the ohmic phase (Fig. 4). With increasing RF power W_p bends towards an L-mode behaviour, staying, however, at a slightly higher level than NI. In combination with NI, W_p and thus τ_E' are improved, too, a feature also observed at $2\Omega_{CH}$ /5/. The energy confinement times of $2\Omega_{CH}$, D(H) and NI(L) modes normalized to the ohmic values are presented in Fig. 5. Careful experimental investigations on the RF power absorption lead to $\alpha = 0.6$ and 0.7, without and with beam preheating respectively. For pure NI heating $\alpha = 0.8$ to 0.9 was found, in good agreement with the beam deposition calculations. As shown for various $2\Omega_{CH}$ regimes, carbonisation strongly reduces the central radiation /2, 3/, thus improving the confinement. At high power ($P_{IC} \sim 5\ P_{OH}$) both RF scenarios reach about equal τ_E' ($\sim 0.6\ \tau_E$) while below 700 kW the D(H)-confinement still remains as good as the ohmic one. Assuming equal global heating efficiencies (~ 20 kJ/MW) for the D(H) and 2Ω modes, but with W_p^{OH} (D(H), D^+-plasma) > W_p^{OH} ($2\Omega_{CH}$, H^+-plasma) the superior confinement of D(H) at low power in comparison to $2\Omega_{CH}$ can be explained.

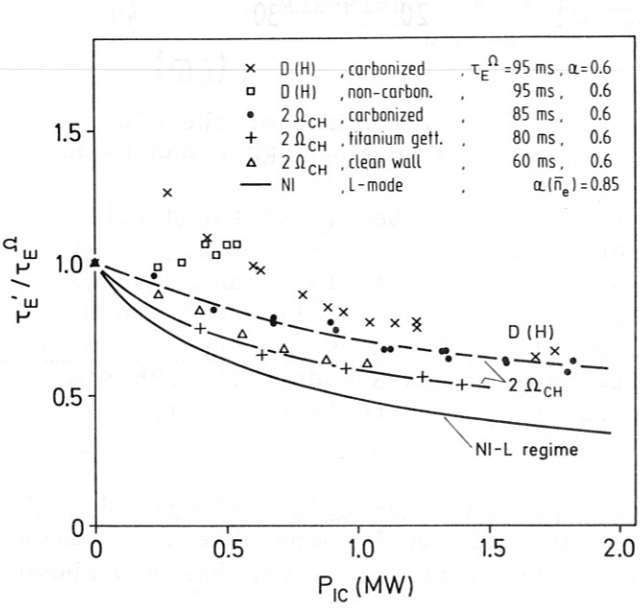

Fig. 5: Normalized confinement times versus launched RF power for various heating scenarios.

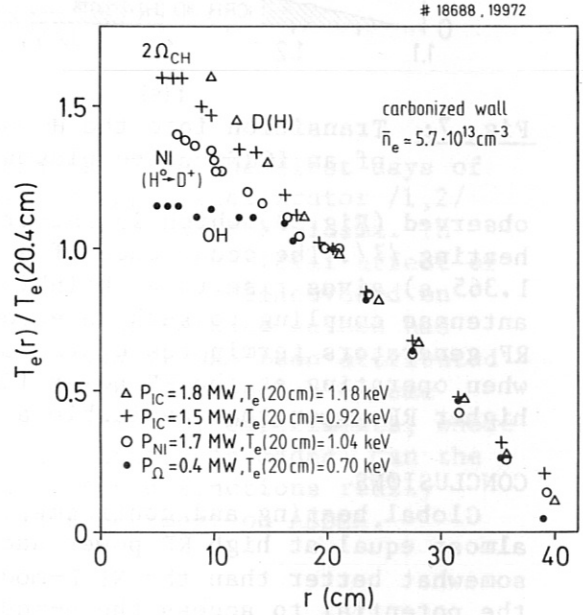

Fig. 6: Normalized T_e profiles of OH, NI, $2\Omega_{CH}$ and D(H)

Rather narrow power deposition profiles are expected theoretically for ICRF heating. In fact, ICRH is accompanied by T_e profiles strongly peaked on axis (Fig. 6) confirming a rather local power deposition. Well outside the q = 1 zone, however, the profiles of OH, ICRH (2Ω, D(H)) and NI appear to be almost invariant if normalized to T_e at $r \sim a/2$ indicating a 'profile consistency' within the so-called confinement zone /6/. When the IC resonance layer is shifted from the plasma centre to half radius, the T_e profile does not vary much while the global heating is maintained with slightly reduced sawteeth amplitude.

ICRF H-mode studies have been performed with and without NI. In combination with NI under optimized conditions the additional ICRF power can switch the plasma into the H-mode. For the first time, the H-mode has

been achieved with ICRH alone in the D(H)-minority regime at an absorbed RF power of about 1.1 MW. The H-mode is marginally reached showing all characteristic signatures of rising n_e and W_p, and frequent ELMs (Fig. 7). The typical development of an edge electron temperature pedestal is also

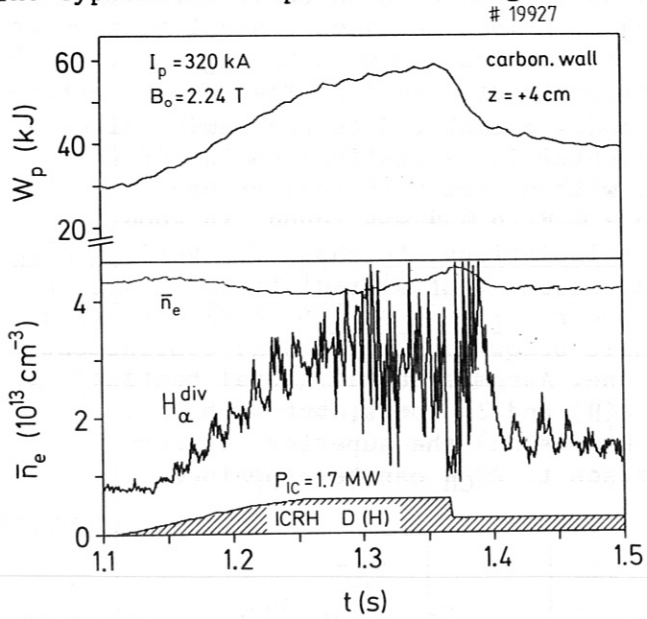

Fig. 7: Transition into the H-mode of an ICRF-heated plasma.

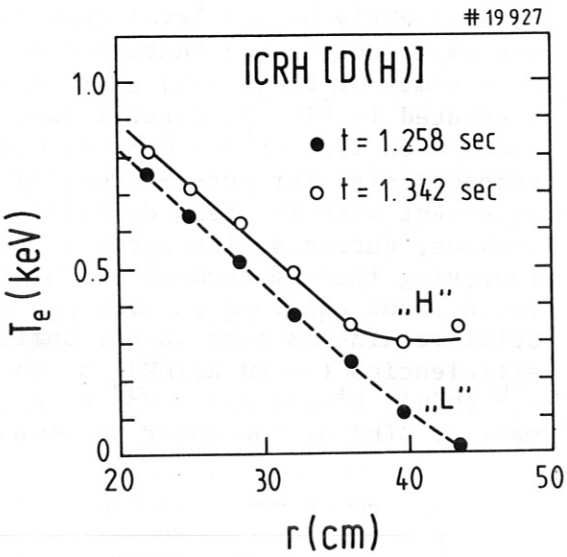

Fig. 8: Development of the edge T_e profile in the ICRH L and H-phase.

observed (Fig. 8) which is rather similar to the behaviour found with NI heating /7/. The occurrence of a short ELM-free H-phase (see Fig. 7 at t = 1.365 s) gives rise to a shrinking of the scrape-off-layer and changes the antennae coupling to such an extent, however, that in all cases one of the RF generators terminates operation by voltage breakdown in the vacuum line when operating at the RF power limit. To keep the H-mode with ICRH somewhat higher RF power than available at present appears to be necessary.

CONCLUSIONS

Global heating and confinement of $2\Omega_{CH}$ and D(H)-regimes are found to be almost equal at high RF power and appear to be well comparable to or even somewhat better than the NI L-mode. For the first time ICRH has now shown the potential to access the H-mode.

ACKNOWLEDGEMENTS

The kind help of J. Winter and P. Wienhold (KFA Jülich) in providing the CD_4-gas for carbonisation, and the excellent support of the ASDEX, ICRH and NI operation teams are gratefully acknowledged.

REFERENCES

/1/ F. Wagner et al., this conference.
/2/ G. Janeschitz et al., this conference.
/3/ W. Poschenrieder et al., this conference.
/4/ A. Stäbler et al., Proc. 4th Int. Symp. on Heating in Toroidal Plasmas, Rome, Vol. I (1984) 3.
/5/ K.Steinmetz et al., Plasma Physics and Controlled Fusion 28 (1986) 235.
/6/ H. Murmann et al., this conference.
/7/ M.Keilhacker et al., Plasma Physics and Controlled Fusion 26 (1984) 49.

Paper submitted to 13th Europ. Conf. on Controlled Fusion and Plasma Heating
Schliersee, April 1986

THE ROLE OF THE FARADAY SCREEN IN ICRF ANTENNAE:
Comparison of an optically open and optically closed screen in ASDEX

J.-M. Noterdaeme, R. Ryter*, M. Söll,
J. Bäumler, G. Becker, H.S. Bosch, M. Brambilla, F. Braun, H. Brocken,
A. Eberhagen, R. Fritsch, G. Fussmann, O. Gehre, J. Gernhardt, G. v.Gierke,
E. Glock, O. Gruber, G. Haas, J. Hofmann, F. Hofmeister, A. Izvozchikov[1],
G. Janeschitz, F. Karger, M. Keilhacker [2], O. Klüber, M. Kornherr,
K. Lackner, M. Lenoci[3], G. Lisitano, E. v.Mark, F. Mast, H.M. Mayer,
K. McCormick, D. Meisel, V. Mertens, E.R. Müller[2], H. Murmann,
H. Niedermeyer, A. Pietrzyk[4], W. Poschenrieder, S. Puri, H. Rapp,
H. Riedler, H. Röhr, J. Roth, F. Schneider, C. Setzensack, G. Siller,
P. Smeulders[2], F. Söldner, E. Speth, K. Steinmetz, K.-H. Steuer,
O. Vollmer, F. Wagner, F. Wesner, H. Wedler, D. Zasche

Max-Planck-Institut für Plasmaphysik,
D-8046 Garching, FRG

INTRODUCTION

A Faraday screen has been used on RF antennae since the first days of heating experiments with ICRF waves. Its use on the C-stellarator /1,2/ brought major improvements in the heating efficiency of the plasma. In subsequent heating experiments on other machines the beneficial effect of a Faraday screen, after initial trials without it, was rediscovered on TFR /3/, DIVA /4/ and ERASMUS /5/. Consequently the Faraday screen has become a mandatory component of ICRF antennae, and it has been attributed different functions. To fulfill those functions the screen has become increasingly complicated, and in the next generation of experiments, where the screen has to be cooled, a new round of complexity is added. Can the screen be simplified, and are some of its attributed functions really needed. Those questions were the basis for an experiment on ASDEX.

FUNCTIONS OF THE FARADAY SCREEN

They can be divided in three categories.

A first function is the protection of the antenna against the plasma: the screen should protect the antenna from particles and radiation from the plasma, in order to avoid parasitic loading of the antenna and to increase its voltage stand off. When a ceramic casing covers the antenna, the Faraday screen prevents the metallisation of the ceramic which could occur if Ti gettering is used.

A second function concerns the protection of the plasma: the Faraday screen should act as its name indicates and keep unwanted electric field components away from the plasma. The structure of the screen is chosen so as to allow the fast wave to go through but to short out electric fields along the magnetic field. The Faraday screen also may have a role in suppressing coaxial modes /6/.

A third function, which will not be further discussed is changing the electrical characteristic of the antenna: in order to minimise the voltage

---

[1]Academy of Sciences, Leningrad, USSR; [2]Assigned to JET Joint Undertaking, England; [3]ENEA Frascati, Italy; [4]University of Washington, Seattle, USA; *CEN Grenoble, France

on the transmission line, and to avoid as much as possible currents in the radial direction /7/, the electrical length of the antenna is adapted, by influencing the distributed capacitance, so that a current node appears at the feeding point. The Faraday shield is one component through which the distributed capacitance can be influenced.

ASDEX EXPERIMENT WITH OPEN SCREEN

In ASDEX two ICRH antennae are installed, 180° apart in the torus, on the low field side (Fig. 1). Each antenna is connected to 1.5 MW generator and consists of two /4 loops, fed top and bottom, and short circuited at the midplane (Fig. 2). One of the antennae was covered with an optically open Faraday screen (Fig. 3a), the other one with an optically closed screen (Fig. 3b). Over a large parameter range (300 kW $\leq P_{rf} \leq$ 1200 kW, $\bar{n} = 1.25 - 3.5 \times 10^{19}$ m^{-3}) a systematic comparison was made by firing the antennae alternately in successive shots. The experiments were performed at the second harmonic of hydrogen (67 MHz, 2.2 T) with uncarbonised and later with carbonised walls.

Concerning the first role of the screen (protection of the antenna) we found that we had no voltage stand off problem. The generator was pushed to its maximum power, and a voltage of 12 kV on the antenna was reached. Under some conditions of bad coupling higher voltages (15.5 kV) were reached, but a voltage limit would be encountered in the transmission line. Therefore we cannot say whether or not opening up the screen has changed the voltage standoff capabilities of the antenna voltages above this value. Two points would indicate that there are no problems with plasma getting into the antenna. We found no additional arcing traces on the central conductors after two month of operation, and there is no power dependence of the loading of the antenna. This is to be compared with limiter machines (TFR /3/, TEXTOR /8/) with an antenna crossing the resonance layer which have shown that a closed type Faraday screen is necessary.

The second role of the Faraday screen (protecting the plasma) seems to be sufficiently accomplished by an open type Faraday screen. In earlier experiments, without and with a Faraday screen on DIVA /4/large differences were seen on the plasma parameters. We however see no major systematic difference on the plasma centrum. Curves of ß, radiated power, soft X-ray radiation are similar for both antennae. No difference is seen on the flux of fast H° /9/. Central electron temperature curves are identical to the point of having the same sawtooth amplitude and frequency (Fig. 4)
The density is feedback controlled but there is a difference in the initial rate of increase of the density at the start of the ICRH. Values of 5 x 10^{20} m^{-3}/s at 900 kW and $n_e = 3.5 \times 10^{19}$ m^{-3} are found for the open screen antenna as compared with 8 x 10^{20} m^{-3}/s for the closed screen antenna. Occasionally, for the antenna with the closed screen this could lead to a different density evolution with larger impurity radiation and impurity lines (Fe XVI). The reason for this is unclear but could be related to the fact that the optically closed screen (originally coated with TiC) was already longer in the machine and may have become contaminated with Fe.

One domain where we have found a systematic difference is on the flux of neutral D particles from the edge. Those fluxes appear and disappear rapidly as the RF is turned off (τ=1-3 ms) showing that these ions are badly confined. A toroidal scan method already used for LH /10/ shows that they are accelerated near the plasma edge. It appears that the fluxes due

to the open screen antenna are much larger than those due to closed screen antenna. It has to be noticed that the actual tail begins for energies higher than 4 keV. For lower energy values the fluxes almost do not depend on ICRH (Fig. 6). Inverted sawteeth are clearly visible on the charge exchange signals: at low energies ($\lesssim$ 3 keV) for both antennae, at high energies ($\gtrsim$3 keV) only for the open screen antenna. The sawtooth modulation is correlated with the H_α/D_α light emitted by the plasma edge and is an effect of neutral density modification. The fact that the high energy channels are modulated only with the open screen antenna indicates, either that the fast ions are further outside the plasma for this antenna or that the mechanism which produces the fast ions for the open screen antenna is sensitive to plasma edge modifictaions.

The following points are further important in analysing the results: The analyser is toroidaly located between both antennae, the plasma current and toroidal magnetic field are parallel, and in the co-direction for the beams. The gas valve is close to open screen antenna. The particles received by the analyser are mostly bananas with large $v_\perp/v_{th}$ ratio and the geometry is such that they cannot be seen just after their acceleration in front of the open screen antenna. Other measurements have shown that the D^o fluxes are very sensitive to the magnetic field and that they can have large fluctuations during one shot, which do not seem to be correlated to any macroscopic parameter of the plasma. There is no indication that the measured D^o fluxes have a direct correlation with the impurity production, but it is clear, that they depend on the plasma capability to absorb the wave /11/.

In conclusion, these fast D^o tail could depend on the kind of Faraday shield used, but in the case of normal absorption of the wave in the plasma, they are only a parasitic effect without consequence on the plasma heating and impurity production.

SUMMARY

We can conclude from our experiment that in our geometry (divertor, antenna not crossing the resonance layer), the function of the Faraday screen as a shield against the plasma is not necessary.
In its function as a shield for the plasma against the unwanted fields from the antenna an open Faraday screen seems to be sufficient. We see no difference on the central plasma parameters and the boundary effect does not seem to be detrimental. We therefore believe that the Faraday shield can be simplified. However, many open questions still remain in this boundary domain between antenna and plasma.

/1/ M.A. Rothman et al., Plasma Physics (J.of Nucl.En., C) 8 (1966) 241
/2/ M.A. Rothman et al., Phys. Fluids 12 (1969) 2211
/3/ J.Jacquinot et al.,Int.Conf.on Plasma Physics, Nagoya 1980, Vol.2, 226
/4/ K. Odajima et al., Nucl. Fusion 20 (1980) 1330
/5/ V.P. Bhatnagar et al., Heat. in Tor. Plasma, Varenna 1978, Vol. 1, 133
/6/ A.M. Messiaen et al., Heat. in Tor. Plasmas, Rome 1984, Vol. 1, 315
/7/ A.M. Messiaen et al., Heat.in Tor.Plasmas, Grenoble 1982, Vol. 1, 243
/8/ R.R. Weynants et al., Radio Frequency Plasma Heating, Callaway Gardens 1985, 40 and private communication
/9/ F. Ryter et al., this conference
/10/ F. Ryter et al., Application of RF Waves to Tokamak Plasmas, Varenna 1985, Vol. 2, 746
/11/ G. Janeschitz et al., this conference

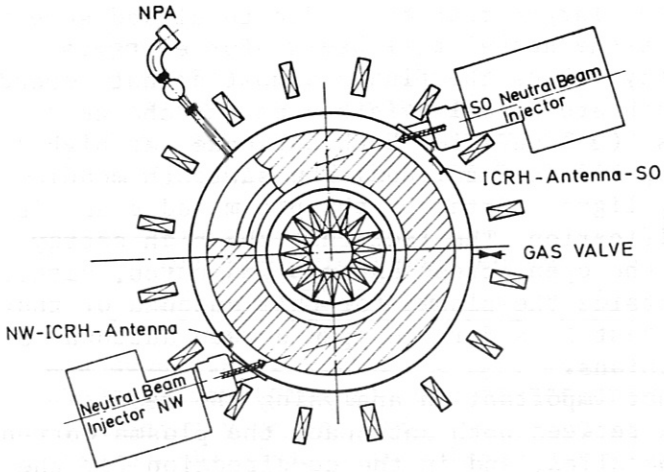

Fig.1: Horizontal cut through ASDEX, indicating the position of the NB-Injectors, the antennae, the neutral particle analyser and the gas valve.

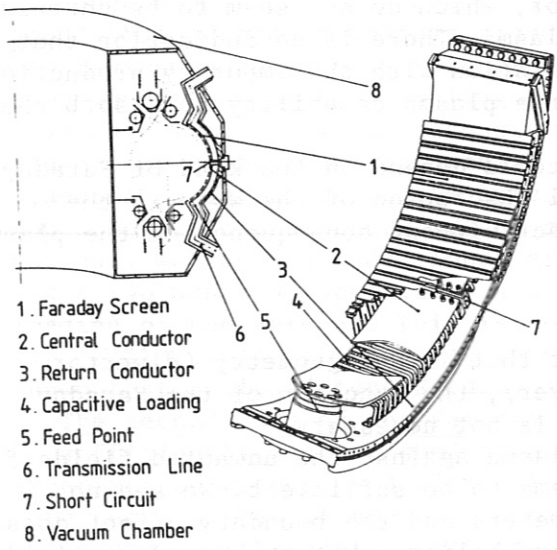

Fig. 2: Geometry of the ASDEX antenna.

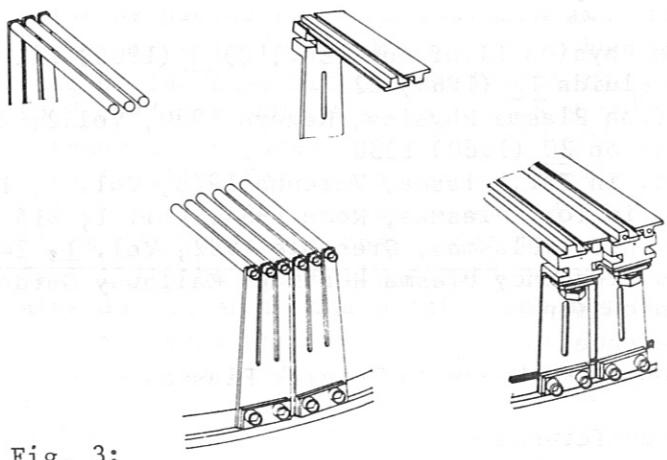

Fig. 3:
a) Optically open screen (SO Antenna)
b) Optically closed screen (NW Antenna).

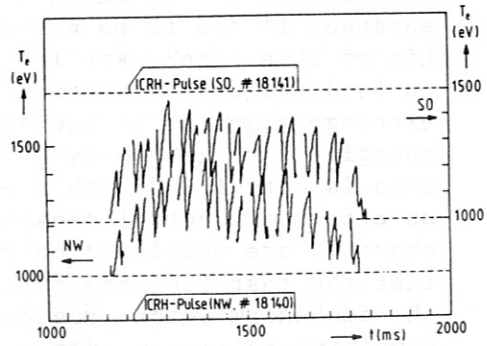

Fig. 4: Central electron temperature evolution. Note: Suppressed null line and its relative displacement for both antennae.

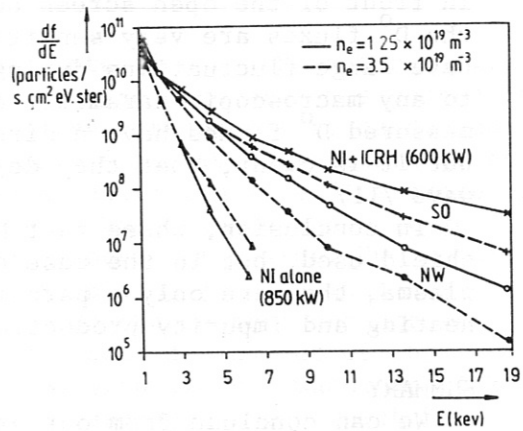

Fig. 5: Flux of D^o at the edge.

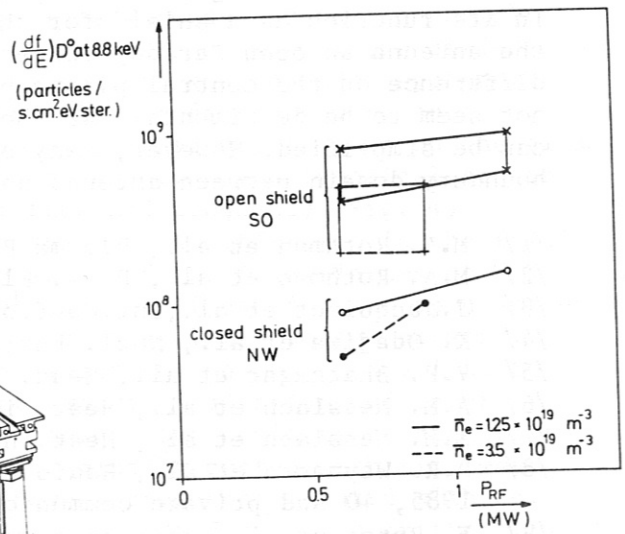

Fig. 6: Dependence of the flux D^o on power and density. For the open shield the modulation due to saw-teeth is shown.

COMPARISON OF ICRH AND LH ACCELERATED HYDROGEN IONS IN NI HEATED ASDEX PLASMAS

F. Ryter[1], H. Brocken, A. Izvozchikov[2], F. Leuterer, H. Maaßberg, H.M.Mayer, F. X. Söldner, K. Steinmetz, G. Becker, H. S. Bosch, A. Eberhagen, D. Eckhartt, G. Fussmann, O. Gehre, J. Gernhardt, G.v.Gierke, E. Glock, O. Gruber, G. Haas, J. Hofmann, G. Janeschitz, F. Karger, M. Keilhacker[3], O. Klüber, M. Kornherr, K. Lackner, M. Lenoci, G. Lisitano, F. Mast, K. McCormick, D. Meisel, V. Mertens, E.R. Müller[3], H.Murmann, H.Niedermeyer, J.-M. Noterdaeme, A. Pietrzyk[4], W. Poschenrieder, H. Rapp, H. Riedler, H. Röhr, J. Roth, F. Schneider, C. Setzensack, G. Siller, P. Smeulders[3], E. Speth, K.-H. Steuer, O. Vollmer, F. Wagner, F. Wesner, D. Zasche

Max-Planck-Institut für Plasmaphysik
EURATOM Association, D-8046 Garching

Introduction

In ASDEX, ICRH /1/ and LHH or LHCD /2/ have been applied separately to NI preheated plasmas in the L regime ($H^0 \rightarrow D^+$, energy E_B). The coupling of these waves to beam ions (H^+) have been studied with charge exchange diagnostics. Possible synergetic effects are discussed in /3/. Shots were made with E_B = 29 keV and E_B = 42 keV and in the latter case P_{NI} or P_{RF} were scanned.

1. Experimental set-up

Measurements were carried out with two neutral particle analysers. One "tangential" analyser (E = 0.1 - 55 keV) viewing opposite to the NI beam direction with the same tangency radius R_T at which the beam is injected (R_T = 145 cm R_o = 165 cm) and with one "perpendicular" analyser (E = 0.5 - 200 keV) which can be scanned vertically. Perpendicular measurements detect only particles with $V_{\parallel}/V \simeq 0$. Near the edge, however, banana ions are seen at the orbit tips. The energy upshift can be better studied in the case E_B = 29 keV because of the upper energy limit of the tangential analyser. For the 29 keV shots a diagnostic beam of hydrogen atoms was injected vertically in the poloidal plane of the perpendiular analyser and crossed the line of sight of the tangential one in the plasma centre.

2. Results

a) ICRH

The following features are observed with the tangential analyser when ICRH is applied: flux increase for $E > E_B$, flux decrease for $E < E_B$ (Fig.1). Fast atoms are detected in the highest energy channel (47 keV for E_B = 29 keV, 55 keV for E_B = 42 keV, Fig. 2). This signal has a rise time and a decay time of 30 ms. The diagnostic beam has no effect on this signal. In the perpendicular direction the active fluxes show a tail of fast ions up to 60 keV (Fig.3) and passive flux decay time is 30 ms at 40 keV. Passive fluxes at the plasma edge (r=a=40 cm) with E_B = 42 keV increase with P_{RF}/P_{NI} (Fig.4).

b) LH

In the tangential direction, fluxes increase for $E > E_B$, fluxes remain constant or increase (10 - 20 %) for $E < E_B$ (Fig. 1). Fast ions in the 47 keV channel, (55 keV for E_B = 42 keV) are detected (Fig. 2). This flux is twice as large for $\langle N_{\parallel} \rangle = 4$ than for $\langle N_{\parallel} \rangle = 2$. The decay seems to consist of a fast part (few ms) and a longer one (100 ms). For the E_B = 42 keV case, only the fast decay is clearly visible. As for ICRH the active flux is not

---

[1]CEN Grenoble, France; [2]Academy of Sciences, Leningrad, USSR; [3]Present address: JET Joint Undertaking, England; [4]Univ. of Washington, Seattle, USA

visible for $E > E_B$. In the perpendicular direction fluxes increase and ions are found till 60 keV. The 40 keV fluxes are twice as large for $\langle N_{\parallel} \rangle = 4$ than for $\langle N_{\parallel} \rangle = 2$ in the centre and equal at $r/a = 0.6$.

3. Discussion

Under our geometrical conditions (R_T(NI) = R_T (Analyser) = R_T) and with NI alone, the tangential analyser receives only passing co-particles originating from the maximum of the ion distribution for each magnetic surface (Fig. 5). This is due to the relation, valid both for injection and detection: $R_T/R = v_{\parallel}/v$ (R is the radius where the C.X. collision happens, $V_{\parallel}$ the parallel velocity and v the total velocity). Then, for each position R, the ion distribution is peaked at the injection angle defined by $v_{\parallel}/v = R_T/R$ which is the condition which must be fulfilled to receive neutrals from the position R. If the waves add perpendicular energy to some of the ions, a part of the distribution function is shifted to higher perpendicular velocities and the parallel analyser does not receive any more fluxes from the maximum for each magnetic surface. If no compensations occur from other regions, the signal for $E < E_B$ should drop. On the other hand, ions with $E > E_B$ must be found. They can be detected after acceleration and collisions which place them onto the detection line of the analyser, both geometrically and in velocity space. Estimation of the main collision times is given for the ICRH and LH cases for 30 keV ions ($n_e = 5 \cdot 10^{13}$ cm^{-3}, $T_e = 1.5$ keV and $n_e = 1.5 \cdot 10^{13}$ cm^{-3}, $T_e = 1.5$ keV correspondingly):

	slowing down on e^-	90° scattering	charge exchange n_o=10^7-10^8cm^{-3})
ICRH	25 ms	50 ms	1s to 100 ms
LH	60 ms	115 ms	1s to 100 ms

These characteristic times as well as the confinement define the decay time of the signal after the RF turn off.
For the perpendicular analyser a general flux increase is expected. The experimental results show that both ICRH and LH waves add perpendicular energy to ions which are clearly accelerated to high energies and nevertheless remain confined as discussed in the following.

a) ICRH
Ions which fulfil the relation $\Omega_{ICRF}(R) - 2\Omega_{CH} = k_{\parallel}.v_{\parallel}$ can be accelerated in the perpendicular direction. It happens in the resonance layer ($R = R_o \pm 4$cm) if they have $v_{\parallel} \simeq 0$. Some of them can be banana ions having their orbit tips in the resonance layer /4,5/. Ions can be accelerated outside of the resonance layer if they have enough $v_{\parallel}$ to fulfil the relation given above. These are passing or banana particles with large $v_{\parallel}/v$. Taking into account the $k_{\parallel}$ spectrum of the wave, we calculate that acceleration is possible till $r \simeq 12$ cm for $E_{\parallel} = 29$ keV and till $r \simeq 18$ cm for $E_{\parallel} = 42$ keV. Therefore beam ions (passing particles) can be directly accelerated only outside of the resonance layer. Beam ions first scatter to larger $v_{\perp}/v_{\parallel}$ before they can be accelerated in the resonance layer. Experimentally it is shown by the absence of active flux ($v_{\parallel} = 0.85$ v) in the tangential analyser: ICRH does not affect passing ions in the centre but off-axis acceleration is found. On the other hand, observations made with the perpendicular analyser show that accelerated ions with large $v_{\perp}/v_{\parallel}$ are present in the plasma centre.

b) LH
The LH interaction is not well located but particles must have enough perpendicular energy $E_{\perp}$ to fulfil the relation: $N_{\perp} \simeq 700\ (A/E_{\perp})^{1/2}$
($[E_{\perp}]$ = keV, A = atomic number)

The perpendicular index $N_\perp$ of the wave is calculated by ray tracing /6/ and the next tables compare the lowest $N_\perp$ values necessary for the interaction and the highest $N_\perp$ values given by the ray tracing method for different $N_\parallel$ values:

	$\langle N_\parallel \rangle$	2	4	resonance	$E_\perp$ 29 keV	42 keV
code	$N_\perp$	30-75	75-125	condition	$N_\perp$ 130	108

It appears that the $N_\perp$ values given by the code are too small to allow for interaction with beam ions particularly for the $\langle N_\parallel \rangle = 2$ spectrum. This general problem for the LH experiments will not be discussed here. As for ICRH the absence of active fluxes in the tangential direction shows that the interacting and accelerated ions in the centre have too large $E_\perp/E$ to be detected. This is confirmed by the perpendicular measurements which show an active flux increase in the centre due to LH.
Off axis acceleration happens and is enfavoured by the geometrical effect which provides the outer surfaces with beam ions having more $E_\perp$ than in the centre. The contribution of the non-central part to the fluxes could be large due to the high value of the neutral density and explain the flux increase for $E < E_B$. The life time of the ions generated off-axis is shorter due to higher losses (charge exchange, confinement) and could account for the fast part of the decay time. The non central effects are more favourable in the E_B =42keV case which provides the plasma edge with faster ions. Moreover interaction is expected further outside at higher density values. Shots made at 3×10^{13} cm^{-3} show flux increase of a factor 2 in the parallel direction for $E < E_B$ and very fast rise time and decay time. The perpendicular observations show large off-axis fluxes, similar to observed without NI /7/.

Conclusion

It appears from this analysis that for both the ICRH and the LH waves give perpendicular energy to beam ions:
- in the centre, to beam ions which have made 90^o pitch-angle scattering
- off-axis, to ions which come almost directly from the beam. This contribution to the fluxes seems to be larger for the LH case.

For ICRH in particular, these two populations are separated both geometrically and in velocity space and cannot mix strongly according to the collision times. The second population might improve somewhat the ICRH heating efficiency for NI preheated plasmas compared to that obtained in ohmic plasmas, nevertheless both for ICRH and LH the contribution of the accelerated ions to ß is small /1,3/.
The clear patterns shown in Fig. 4 as a function of P_{RF}/P_{NI} (RF power per injected particle) indicate probably that the interaction occurs mainly with beam ions. They show the global increase of the perpendicular energy of the ion distribution. For ICRH the contribution of the fast ions to the impurity production is very probable as discussed in /8/.
This work has been made in the frame of a collaboration between IPP-Garching and CEA-DRFC-SIG (Grenoble), and project boards in both laboratories are gratefully acknowledged as well as the assistance of the technical staff.

References

/1/ K. Steinmetz, et al., this conference and EPS Conf., Budapest, 1985.
/2/ F. Söldner, et al., EPS Conf., Budapest, 1985.
/3/ F. Wagner, invited paper at this conference.
/4/ T. Hellsten, et al., EPS Conf., Budapest, 1985.
/5/ G. W. Hammett, et al., Pine Mountain Conf., 1985.
/6/ M. Brambilla, private communication.
/7/ D. Eckhartt, et al, Proc.4thInt.Symp.on Heating in Toroidal Plasmas, Rome 1984.
/8/ G.Janeschitz, et al., this conference.

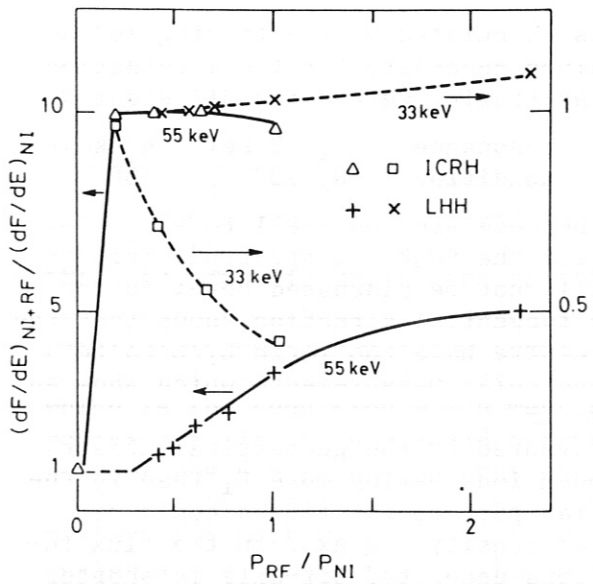

Fig. 1: H^o normalised fluxes for the tangential analyser versus P_{RF}/P_{NI} ($E_B = 42keV$).

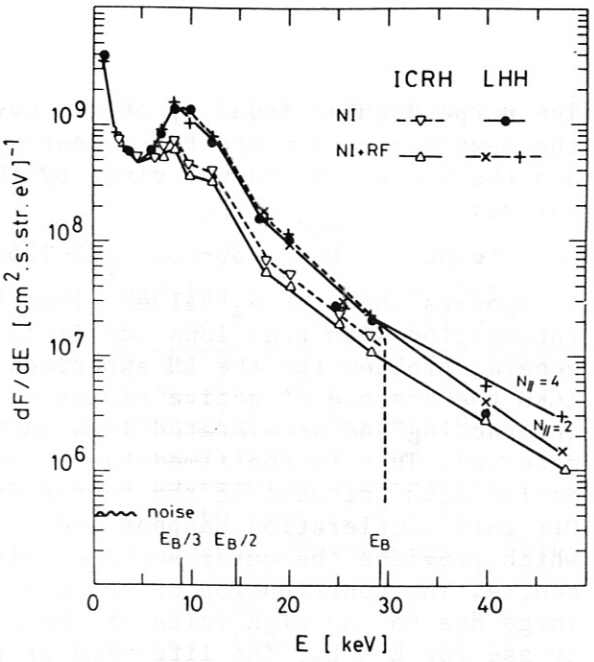

Fig.2: H^o energy spectra for the tangential analyser ($E_B = 29keV$).

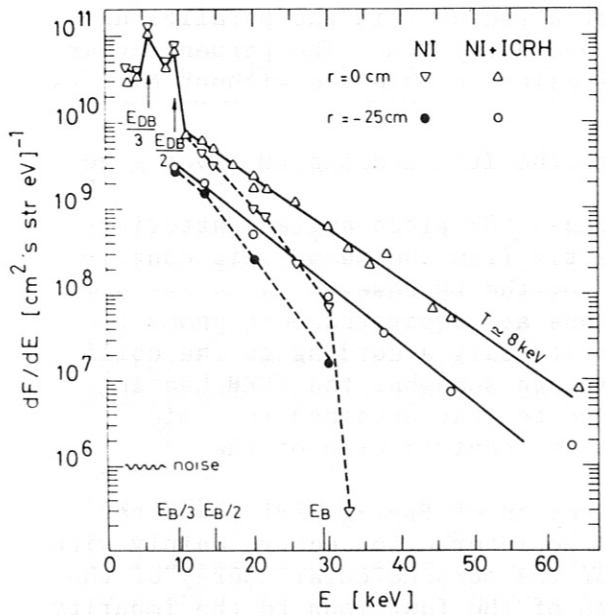

Fig. 3: Local H^o energy spectra for the perpendicular analyser ($E_B = 29keV$).

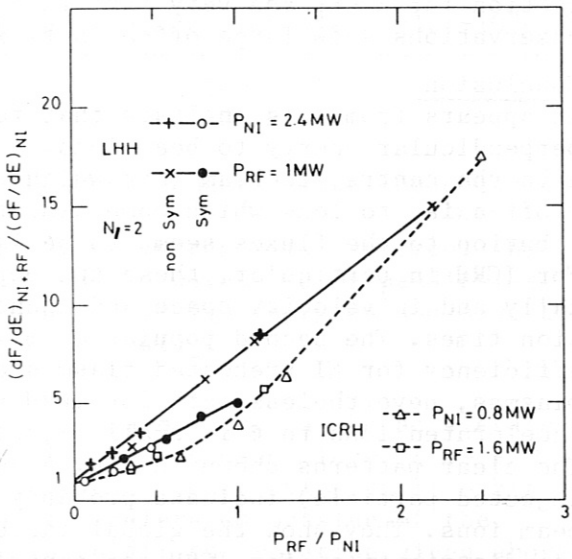

Fig. 4: H^o 17 keV normalized fluxes at r = 40 cm for the perpendicular analyser versus P_{RF}/P_{NI} (E = 17 keV is representative for the tail).

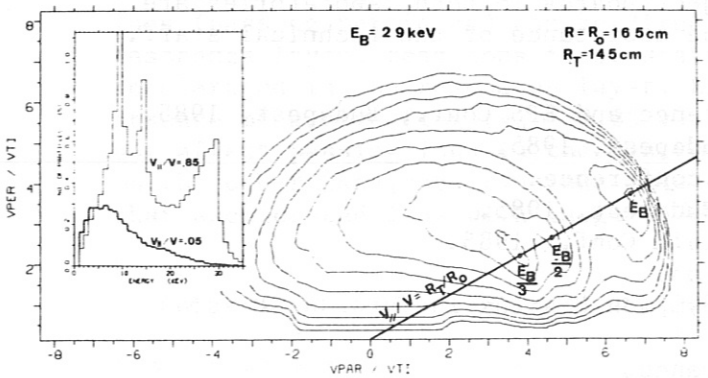

Fig. 5: Calculated ion distribution function with NI alone in the velocity space normalised to the thermal velocity. Energy spectra for two $v_{//}/v$ values are enclosed.

STABILISATION OF SAWTOOTH OSCILLATIONS BY LOWER HYBRID WAVES IN ASDEX

F. X. Söldner, D. Eckhartt, F. Leuterer, K. McCormick, G. Becker, H. S. Bosch, H. Brocken, H. Derfler, A. Eberhagen, G. Fussmann, O. Gehre, J. Gernhardt, G.v.Gierke, E. Glock, O. Gruber, G. Haas, J. Hofmann, A. Izvozchikov[1], G. Janeschitz, F. Karger, M. Keilhacker[2], O. Klüber, M. Kornherr, K. Lackner, M. Lenoci, G. Lisitano, F. Mast, H. M. Mayer, D. Meisel, V. Mertens, E. R. Müller[2], M. Münich, H. Murmann, H. Niedermeyer, A. Pietrzyk[3], W. Poschenrieder, H. Rapp, H. Riedler, H. Röhr, J. Roth, F. Ryter[4], F. Schneider, C. Setzensack, G. Siller, P. Smeulders[2], E. Speth, K.-H. Steuer, T. Vien, O. Vollmer, F. Wagner, D. Zasche, M. Zouhar

Max-Planck-Institut für Plasmaphysik
EURATOM Association, D-8046 Garching

Introduction:

Stabilisation of sawteeth has become a clue problem for high power additional heating in large tokamaks where the oscillations in the central electron temperature may be as high as 50 % /1/. In Lower Hybrid experiments the sawteeth of Ohmic discharges have been observed to disappear /2/, /3/. In this paper we study the parameter range for stabilisation of sawteeth accessible with the LH-system on ASDEX /4/, /5/. The role of the LH wave spectrum is discussed. For application to NBI heating the LH-power requirements and the benefits for the energy confinement in sawtooth-free discharges are investigated.

Stabilisation of sawteeth in OH-discharges

The sawtooth period τ_{st} rises upon injection of LH waves in a density range where the waves couple to suprathermal electrons ($\bar{n}_e \lesssim 3 \times 10^{13} cm^{-3}$). In the case of LH-current drive τ_{st} continues to change during the rf pulse. The values for the first sawtooth after start of the LH and for the saturated state are shown in Fig. 1 for a power scan at $\bar{n}_e = 1.6 \times 10^{13}$ cm^{-3}. At low power the sawtooth period rises continuously until the end of the rf. For $P_{LH} > 400$ kW τ_{st} first increases and then decreases, at high rf power even below the Ohmic value. Above a threshold P_{LH}^* the sawteeth finally disappear. The time delay τ_d between start of the LH and the last sawtooth collapse depends strongly on the density and it decreases with increasing rf power as shown in Fig. 2. The threshold P_{LH}^* there is marked by dashed lines. Stabilisation of sawteeth is possible only by applying LH-current drive spectra. With symmetric spectra in the LH-heating mode the sawtooth period may be changed but sawteeth remain present during the whole LH pulse ($\tau \leq 1.5$ s) even at rf powers more than a factor of 2 above the threshold P_{LH}^* with LH-current drive.

The mechanism for sawtooth stabilisation might therefore be seeked in the change of the current profile j(r) connected with LH current drive. The internal inductance l_i may be derived from magnetic measurements with some precautions. From the quantities $\beta_p^{equ} + l_i/2$ (derived from the equilibrium fields) and β_p^i (from diamagnetic measurements) l_i can only be determined if

---

[1]Academy of Sciences, Leningrad, USSR; [2]Present address: JET Joint Undertaking, England; [3]Univ. of Washington, Seattle USA; [5]CEN Grenoble, France

the pressure is isotropic. During heating and current drive with LH waves of high phase velocity ($\bar{v}_{ph,\parallel} = c/2$), however, the pressure may become highly anisotropic due to the generation of fast electrons parallel to the magnetic field /7/. Therefore direct measurements of j(r) were made for various modes of LH operation in ASDEX /8/, /9/. In the case of the LH power scan at $\bar{n}_e = 1.6 \times 10^{13}$ cm^{-3} (Figs. 1,2) the pressure anisotropy remains small and the stationary value of $(\beta_p^{equ} + l_i/2) - \beta_p^{\perp}$ then gives l_i. At low rf power l_i increases while it drops during LH current drive with $P_{LH} > 400$ kW as seen from Fig. 3. Consequently, the current profile is peaking during low power LH-current drive and the higher increase of the sawtooth period τ_{st} in Fig. 1 might then be explained by an expansion of the sawtooth-unstable region within r(q=1). The drop in l_i at higher power indicates a flattening of j(r) and the reduction in τ_{st} could be explained in like manner by a shrinking of the q=1-surface. With $P_{LH} > P_{LH}^*$ j(r) flattens to such an extent that the q=1 surface disappears and $q > 1$ in the entire plasma region /9/. Stabilisation of the sawteeth is therefore achieved if j(r) is modified such that the instability condition (q=1 at some radius) is removed. On ASDEX, so far, this is the only method how sawteeth could be suppressed by means of LH waves.

In the parameter range where sawteeth were stabilized about half of the rf power necessary for complete LH-current drive was required. For discharges with q(a) = 3.5 this can be seen from Fig. 4 where the relative reduction in Ohmic input $-\Delta P_{OH}^*/P_{OH}$ due to LH current drive at the stability margin with $P_{LH} = P_{LH}^*$ is plotted versus $\bar{n}_e$ together with the absorbable fraction $P_{LH,acc}^*$ of the rf power launched in these cases. Because of the uncertainty in the deposition profile two cases have been considered for accessibility to a/3 and 2a/3 /7/.

Stabilisation of sawteeth during NBI:
The sawtooth period τ_{st} during NBI increases with increasing beam power P_{NI} (Fig. 5) and above a certain threshold in P_{NI} which augments with $\bar{n}_e$ no sawteeth are observed during NBI. In sawtoothing discharges with NBI τ_{st} rises upon injection of LH power both in heating and current drive mode. Suppression of sawteeth is possible with LH current drive only. The mechanism of stabilisation is again related to a flattening of the current profile j(r) as indicated by a decrease of l_i. The drop in l_i does not depend on P_{NI} but only on P_{LH} and on the wave spectrum. The minimum rf power required for stabilisation P_{LH}^* is reduced for higher P_{NI} as seen from Fig. 5.

This suggests that the current profile is flattened in the central plasma region already by NBI alone and less LH-power is therefore required for higher P_{NI} to remove the q=1 surface from the plasma.

With counter-NBI the threshold power P_{LH}^* is even further reduced as seen in Fig. 5. Also with NBI alone sawteeth disappear already at lower power in this case. This seems to be mainly due to the broad $T_e(r)$ profiles which are observed with counter-NBI. The shorter sawtooth period (Fig. 5) might be also explained by this fact. A contribution from a counter-driven beam current reducing the net plasma current in the center and thereby flattening j(r) as proposed in a scenario for sawtooth suppression /10/ cannot be ruled out.

In sawtooth-free discharges with NBI higher central electron temperatures can be obtained. The $T_e(r)$ profiles are plotted in Fig. 6 for the Ohmic phase, NBI alone and for NBI combined with LH current drive. With $P_{LH} = 540$

kW which is below P_{LH}^* the $T_e(r)$ profiles still resemble the profiles with NBI alone. The additional LH power replaces mainly the drop in P_{OH} in this case. With $P_{LH} > P_{LH}^*$ (P_{LH} = 720 kW) sawteeth are suppressed and the central temperatures increase. The resulting increase in total energy content is small because of the small volume where sawteeth dominate the power loss. With lower q(a) the sawtooth-unstable region is larger and a larger gain for global plasma heating can be obtained. At q(a) = 2.75 (I_p = 380 kA, B_t = 2.2 T) sawtooth suppression with P_{LH} = 550 kW resulted in a 30 % increase of the total plasma energy content from NBI with P_{NI} = 1.8 MW. Improvement of the central confinement by stabilisation of the sawteeth therefore contributes also to an appreciable improvement of the global confinement.

References

/1/ J. Jacquinot, et al., Plasma Physics and Controlled Fus. 28, 1 (1986).
/2/ J.E. Stevens, R. Bell, S. Bernabei, et al., 12th Europ. Conf. on Contr. Fusion and Plasma Physics, Budapest, 1985, Vol. II, p. 192.
/3/ F. Parlange, et al., in Ref. /2/, Vol. II, p. 172.
/4/ D. Eckhartt, et al., 4th Int. Symposium on Heating in Toroidal Plasmas, Rome, 1984, Vol. I, p. 501.
/5/ F. Leuterer, F. Söldner, D. Eckhartt, et al., Plasma Physics and Controlled Fusion 27, 1399 (1985).
/6/ F. Leuterer, D. Eckhartt, F. Söldner, et al., in Ref. /2/, Vol. II, p. 240.
/7/ F. Söldner, D. Eckhartt, F. Leuterer, et al., in Ref. /2/, Vol. II, p. 244.
/8/ K. McCormick, et al., in Ref. /2/, Vol. I, p. 199.
/9/ K. McCormick, et al., this conference.
/10/ J. Jacquinot, private communication.

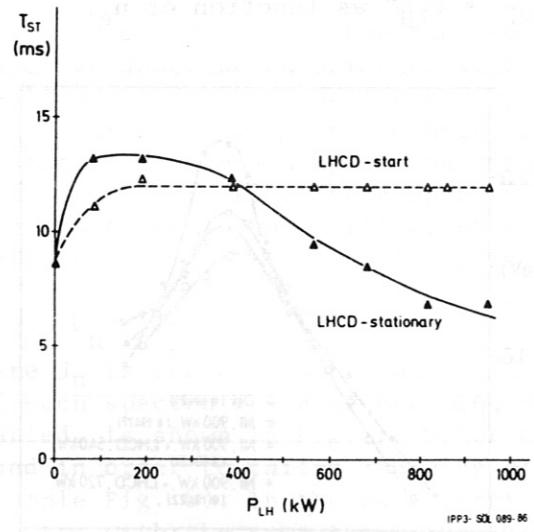

Fig. 1: Sawtooth period τ_{st} during LH-current drive versus LH-power.

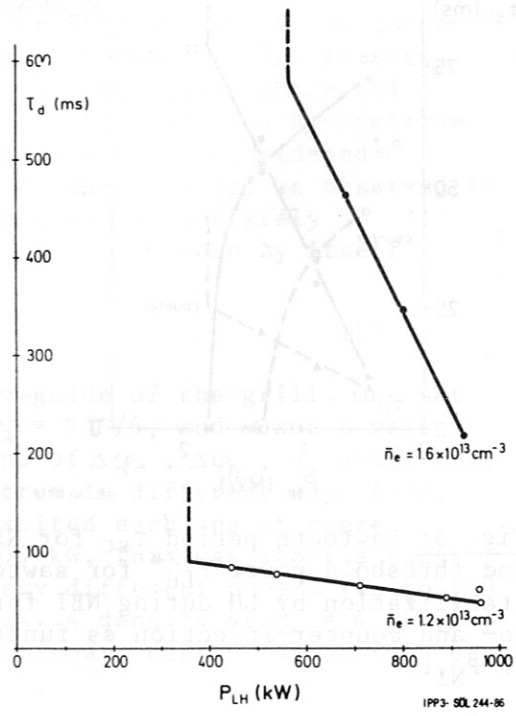

Fig. 2: Time delay τ_d for sawtooth suppression after start of LH versus LH-power.

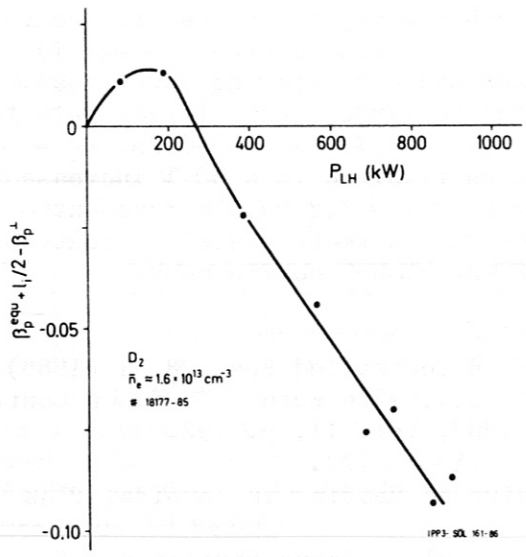

Fig. 3: Variation of the quantity $(\beta_p^{equ} + l_i/2) - \beta_p^{\perp}$ with P_{LH} during LH-current drive.

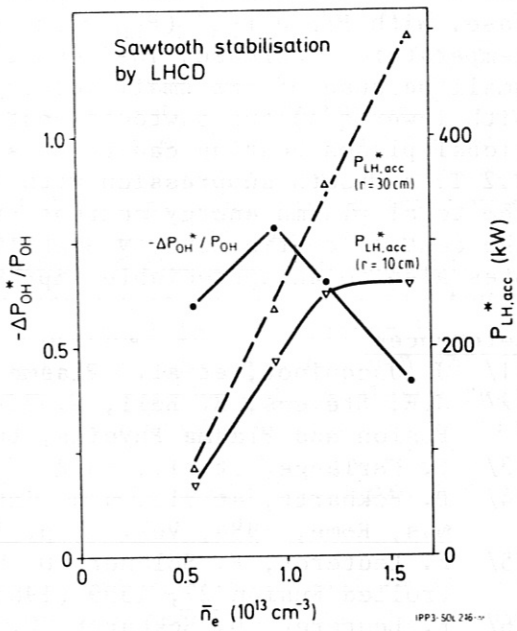

Fig. 4: Drop in ohmic power $-\Delta P_{OH}^*/P_{OH}$ and accessible fraction of LH-power $P^*_{LH,acc}$ at the margin for sawtooth stabilization $P_{LH} = P_{LH}^*$ as function of $\bar{n}_e$.

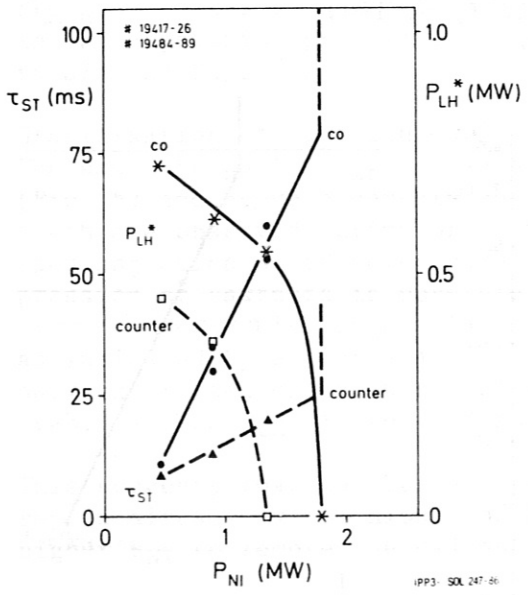

Fig. 5: Sawtooth period τ_{st} for NBI and threshold power P_{LH}^* for sawtooth stabilization by LH during NBI for co- and counter-injection as function of P_{NI}.

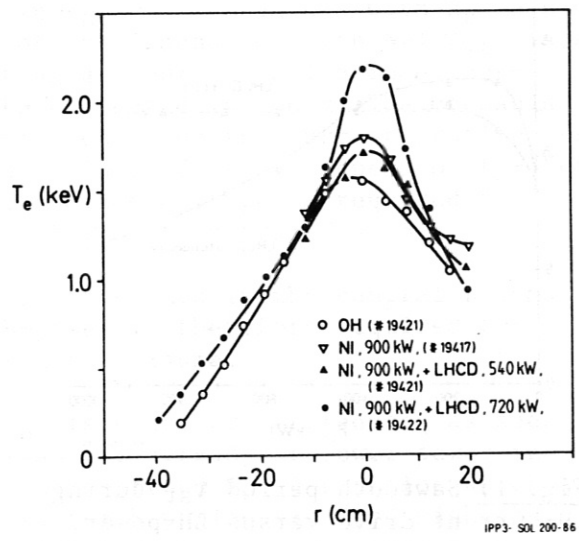

Fig. 6: $T_e(r)$ profiles during OH- and NBI-heating and for the sawtooth-free phase of NBI + LHCD (P_{LH} = 720 kW).

INFLUENCE OF THE N∥-SPECTRUM ON LOWER HYBRID CURRENT DRIVE IN ASDEX

F. Leuterer, M. Brambilla, D. Eckhartt, K. McCormick, M. Münich, F. Söldner, M. Zouhar, G. Becker, H.S. Bosch, H. Brocken, A. Eberhagen, G. Fussmann, O. Gehre, J. Gernhardt, G. v.Gierke, E. Glock, O. Gruber, G. Haas, J. Hofmann, A. Izvozchikov[1], G. Janeschitz, F. Karger, M. Keilhacker[2], O. Klüber, M. Kornherr, K. Lackner, M. Lenoci[3], G. Lisitano, F. Mast, H.M. Mayer, D. Meisel, V. Mertens, E.R. Müller[2], H. Murmann, H. Niedermeyer, A. Pietrzyk[4], W. Poschenrieder, H. Rapp, H. Röhr, J. Roth, F. Ryter[5], F. Schneider, C. Setzensack, G. Siller, P. Smeulders[2], K.-H. Steuer, F. Wagner, D. Zasche

Max-Planck-Institut für Plasmaphysik
EURATOM Association, D-8046 Garching

The lower hybrid current drive experiments in ASDEX so far have been performed mainly by operating successive waveguides of the grill at a relative phase of $\Delta\varphi = \pi/2$ and with equal amplitudes. The spectrum thus excited is considered in this paper as a reference spectrum and is shown as spectrum C 1 in Fig. 1. With such a spectrum it has been observed, like in many other related experiments, that the primary current rate of change, $-\dot{I}_{OH}$, necessary to maintain a constant plasma current I_p, decreased with increasing rf-power, P_{RF}. At a specific value of P_{RF}, depending on density and plasma current, $\dot{I}_{OH}$ becomes zero and the plasma current is driven by rf alone, while at higher powers the transformer gets recharged /1/. The scaling of these effects was found to depend on the accessibility of the lower hybrid waves and to agree with theoretical predictions /2, 3/. It was also shown that the current density profile j(r) for rf-current drive is different from that obtained for inductive current drive and is no longer directly determined by the electron temperature profile /4, 5/. In this paper we describe experiments with "tailored" spectra where phase and amplitude in each waveguide are specifically set to produce a N∥-spectrum with a definite wing at the high N∥-side. Such a wing is considered essential in explaining the magnitude of the driven currents as observed in the experiments /6/. These spectra are obtained by appropriately superimposing in the grill waveguides fields producing each by itself different N∥-spectra, resulting in

$$U_n = e^{i(n-1)\Delta\varphi_1} + a \cdot e^{i\alpha}\, e^{i(n-1)\Delta\varphi_2} \qquad (1)$$

Here U_n is the wave amplitude in the n-th waveguide of the grill. One set of such spectra where we used $\Delta\varphi_1 = \pi/2$, $\Delta\varphi_2 = 5\pi/6$, and α and a were varied, is shown in Fig. 1. Other combinations of $\Delta\varphi_1$, $\Delta\varphi_2$, a, and α were used in order to tailor the wing of the spectrum in different ways (for example Fig. 6). In the experiment we have excited each one of these spectra with the same total input power of 400 kW. This was about a power limit for those experiments because of the very different powers (up to 130 kW) to be applied to the individual waveguides. A density of $\bar{n}_e = 6 \times 10^{12}$ cm^{-3} was then chosen in order to obtain a stationary current drive ($\dot{I}_{OH,RF} = 0$) in the case of the reference spectrum C 1.

---

[1]Academy of Sciences, Leningrad, USSR; [2]Assigned to JET Joint Undertaking, England; [3]ENEA Frascati, Italy; [4]University of Washington, Seattle, USA; [5]CEN Grenoble, France

Figure 2 shows the primary current $I_{OH}(t)$ which is necessary to maintain a constant plasma current Ip before and during the application of LH-power with the spectra shown in Fig. 1. The curves are displaced for clarity. We recognise that for spectra with an increasing fraction of power at high $N_{\parallel}$ the current drive becomes less efficient, i.e. $-\dot{I}_{OH,RF}$ increases. The same $\dot{I}_{OH,RF}$ would be obtained with a smaller amount of power, $P^{o}_{RF,Cn}$, if the applied spectrum were the reference spectrum C 1. In Fig. 3 we plot the ratio $P^{o}_{RF,Cn}/P_{RF,C1}$ where $P_{RF,C1}$ is the power resulting in $\dot{I}_{OH,RF} = 0$ for the spectrum C 1. The LH-driven current scales, as:

$$I_{RF} \sim \mu \cdot g \cdot P_{RF}/\bar{n}_e ,$$

where

$$\mu = \int_{N_{\parallel 2}}^{N_{\parallel 4}} P(N_{\parallel})\,dN_{\parallel} \Big/ \int_{-\infty}^{+\infty} P(N_{\parallel})\,dN_{\parallel} \quad , \quad g = (N_{\parallel 4}^2/N_{\parallel 2}^2 - 1)\Big/(N_{\parallel 4}^2 \ln N_{\parallel 4}/N_{\parallel 2})$$

and $N_{\parallel 2}$ is determined by accessibility or the lower $N_{\parallel}$-boundary of the spectrum /7,8/. We therefore may write:

$$P^{o}_{RF,Cn}/P_{RF,C1} = (\mu \cdot g)_{Cn}/(\mu \cdot g)_{C1} .$$

The factor $(\mu \cdot g)$ depends of course on the choice of the spectrum boundaries $N_{\parallel 2}$ and $N_{\parallel 1}$. The two lines in Fig. 3 show the calculated ratio $(\mu g)_{Cn}/(\mu g)_{C1}$. For line a we chose $N_{\parallel 2} = N_{\parallel acc} = 1.5$ and the upper boundary $N_{\parallel 1}$ was determined by $r = \int_{0}^{N_{\parallel 4}} P(N_{\parallel})dN_{\parallel} / \int_{0}^{\infty} P(N_{\parallel})dN_{\parallel} = 0.97$. For line b $N_{\parallel 2}$ was either $N_{\parallel 2} = N_{\parallel acc} = 1.5$ or determined by $r = 0.1$ and $N_{\parallel 1}$ was determined by $r = 0.9$, thus shifting $N_{\parallel 2}$ to values greater than 1.5 for the spectra C 7 to C 13. We see that in the experiment the current drive efficiency is always greater than in the calculation b, while for calculation a this is true only for spectra C 3 and C 5, but less than calculated for C 9 to C 13. From this we conclude that in using the above equation for g, which is derived for a rectangular power spectrum /8/, we overemphasise the high $N_{\parallel}$-part of the spectrum while the low $N_{\parallel}$-part is more efficient with respect to current drive. To describe our experimental results in more detail we would thus need instead of the function g a function which does not only depend on the boundaries $N_{\parallel 2}$ and $N_{\parallel 1}$ of the spectrum but also upon its shape.

We further observed that the signal $\Lambda + 1$ as deduced from the equilibrium field depends remarkably upon the applied spectrum. As an example we show in Fig. 4 the difference between $\Lambda + 1 = \beta_p^{equ.} + l_i/2$ and $\beta_p^{\perp}$ (from the diamagnetic loop). This difference changes when LH-power is applied due to the wave generated anisotropy in the electron velocity distribution, $\beta_p^{equ.} - \beta_p^{\perp}$ which occurs on a fast time scale and is positive, and also because of a slowly decreasing l_i. The dependence of l_i as a function of the applied spectrum is shown in Fig. 5 for the set of spectra shown in Fig. 6. We see that $-\Delta l_i$ increases with increasing power in the high $N_{\parallel}$-part of the spectrum. This has also been observed in a phase scan where the shape of the spectrum remains roughly constant but the mean value $\langle N_{\parallel} \rangle$ is shifted from 2 to 4 with a directivity dropping to zero. The change in l_i is thus not only related to the amount of rf-driven current, but also to the shape of the spectrum, and the maximum Δl_i does not coincide with a maximum current drive efficiency. This suggests that the higher $N_{\parallel}$-part of

the spectrum is absorbed further radially outward than the low $N_{\parallel}$-part. The generated current density profile depends on the choice of the spectrum, and is not only determined by the direct rf-driven current, but also by an rf-modified conductivity profile due to bulk heating or suprathermal electrons.

We should also note that while l_i is decreasing additional power from the decreasing poloidal field energy is available in the plasma, leading to a further reduction in the loop voltage.

REFERENCES

/1/ F. Leuterer et al., Phys.Rev.Lett. 55 (1985) 75

/2/ F. Leuterer et al., Plasma Phys. and Contr. Fus. 27 (1985) 1399

/3/ F. Leuterer et al., Proc. 12th Europ. Conf. on Contr. Fusion an Plasma Physics, Budapest 1985, Vol. II, p. 240

/4/ K. McCormick, ibid., Vol. I, p. 199; also this conference

/5/ F. Söldner et al., this conference

/6/ S. Succi et al., Proc. 10th IAEA-Conf. Plasma Physics and Contr. Nucl. Fusion, London 1984, Vol. I, p. 549

/7/ G. Tonon, D. Moulin, 4th Int.Symp. Heating in Toroidal Plasma, Rome 1984, Vol. II, (1984) 1343

/8/ C.F. Karney, N. Fisch, Phys.Fluids 22 (1979) 1817

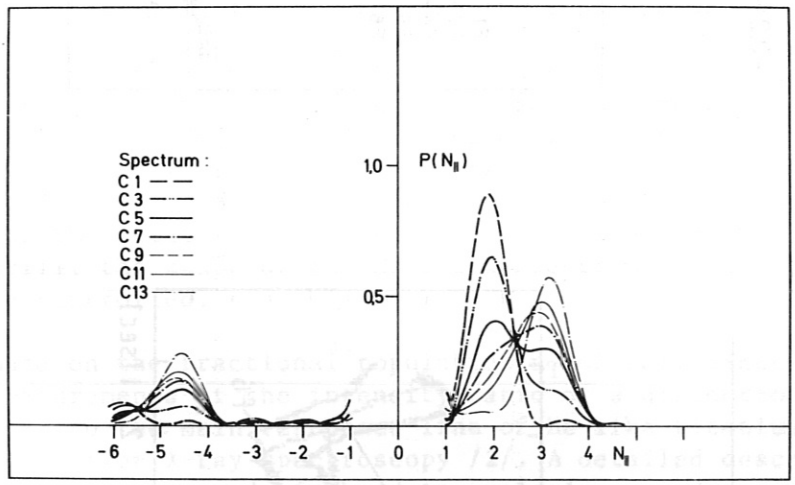

Fig. 1

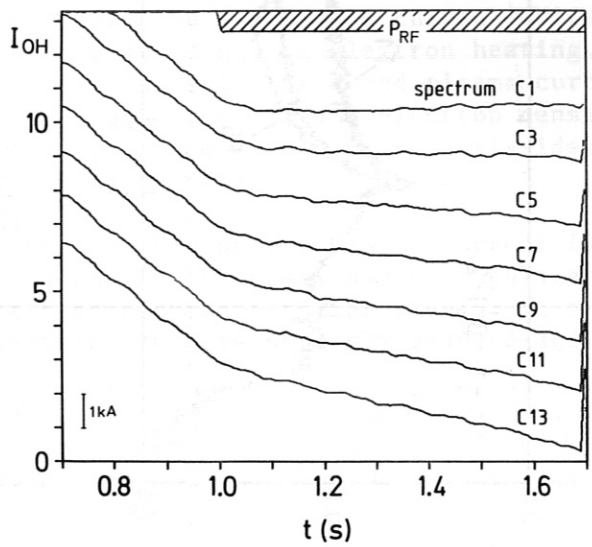

Fig. 2

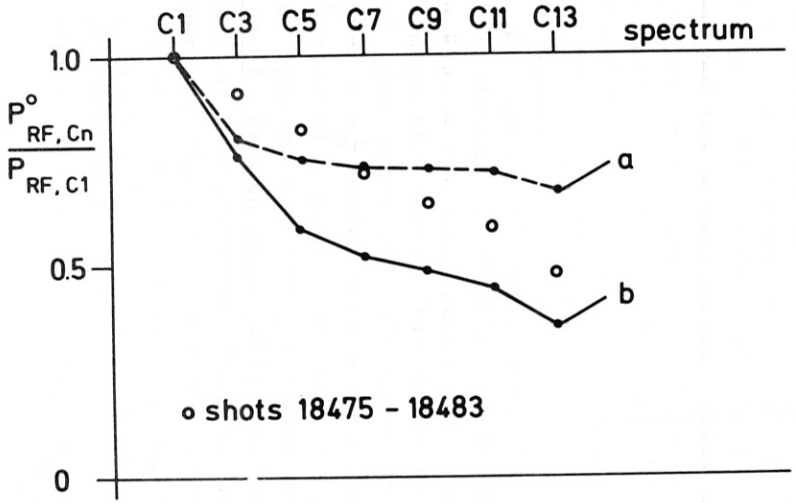

Fig. 3

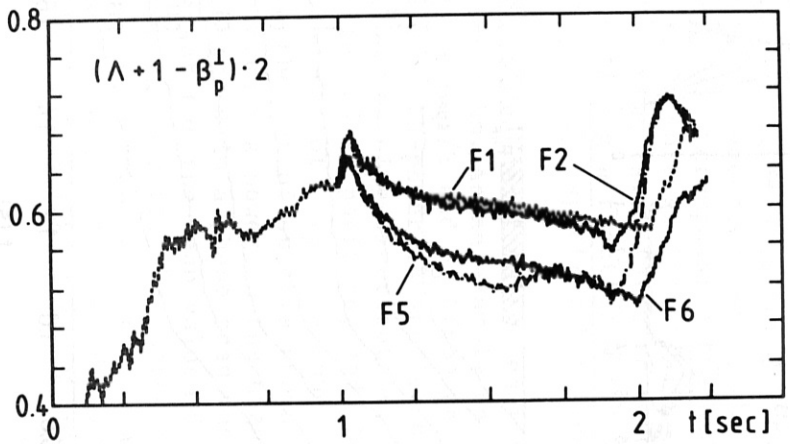

Fig. 4

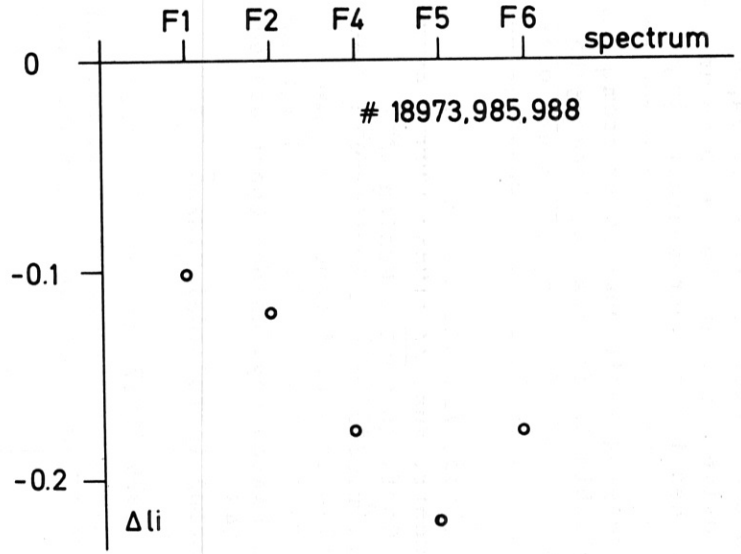

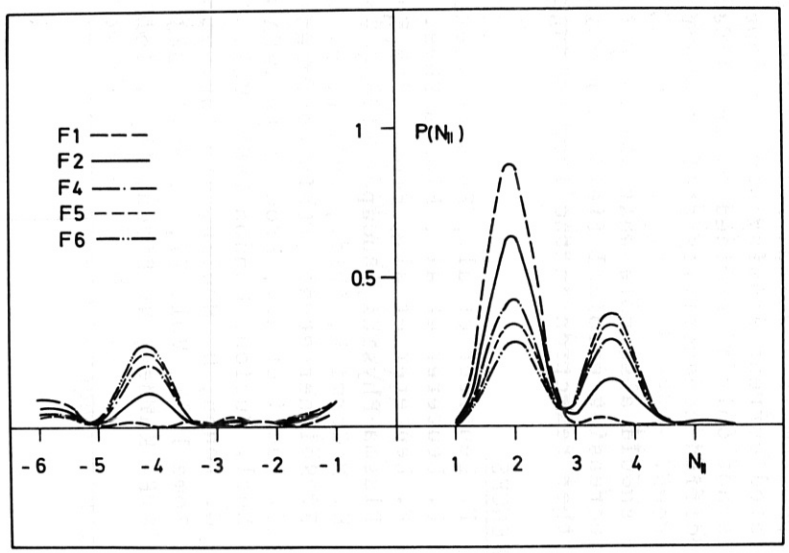

Fig. 6

MEASUREMENTS OF NON-THERMAL ELECTRON POPULATION DURING LOWER-HYBRID HEATING IN ASDEX

R. Bartiromo[1], M. Hesse[2], F. Söldner, R. Burhenn[3], G. Fussmann, F. Leuterer, H. Murmann, D. Eckhartt, A. Eberhagen, A. Giuliana[1], G. Becker, H. S. Bosch, M. Brambilla, H. Brocken, H. Derfler, O. Gehre, J. Gernhardt, G. v. Gierke, E. Glock, O. Gruber, G. Haas, J. Hofmann, A. Izvozchikov[4], G. Janeschitz, F. Karger, M. Keilhacker[5], O. Klüber, M. Kornherr, M. Lenoci, G. Lisitano, F. Mast, H. M. Mayer, K. McCormick, D. Meisel, V. Mertens, E. R. Müller[5], M. Münich, H. Niedermeyer, A. Pietrzyk[6], W. Poschenrieder, H. Rapp, H. Röhr, N. Ruhs, F. Ryter[2], F. Schneider, C. Setzensack, G. Siller, P. Smeulders[5], K.-H. Steuer, T. Vien, F. Wagner, F. v. Woyna, D. Zasche, M. Zouhar

Max-Planck-Institut für Plasmaphysik
EURATOM Association, D-8046 Garching

It has been recognized in recent years that e.m. waves in the lower hybrid (LH) frequency range can produce important effects when absorbed by plasma electrons like, for example, current generation, plasma heating and current profile modification. In these conditions the electron distribution function is not maxwellian but becomes enhanced at high energy depending on the power and phase velocity spectrum of the launched waves /1/.

The aim of the present paper is to study the plasma-wave interaction by experimentally determining the fractional population of non-thermal electrons under different plasma conditions. The experiments were carried out on the ASDEX divertor tokamak, where current drive and plasma heating can be studied up to an injected power of 1 MW at a frequency of 1.3 GHz. By changing the relative phase between successive elements in an eight-waveguide grill, the shape of the $N_{\parallel}$ index spectrum as well as its directionality can be controlled.

Data on the fractional population n_T of tail electrons were obtained from measurements of the intensity ratio of a dielectronically excited satellite line to the main resonance line of He-like titanium ions by means of high resolution X-ray spectroscopy /2/. A detailed description of the experimental apparatus and of the data analysis procedure can be found elsewhere /3/.

The results obtained in a current drive shot are compared in Fig. 1 with those obtained during electron heating. The two discharges have the same toroidal magnetic field and plasma current and nearly equal injected RF power ($P_{RF} \simeq 800$ kW) and electron density ($\bar{n}_e \simeq 1.2 \times 10^{13}$ cm^{-3}). The shape of the launched spectrum is nearly identical in the two cases and is characterized by $\langle N_{\parallel} \rangle = 2$.

In the first case the plasma current is almost completely driven by the RF waves and the feedback system regulates the ohmic power transformer to keep the plasma current to the pre-injection value; consequently the toroidal electric field is strongly reduced and comes near to zero. In these

---

[1]ENEA Frascati, Italy; [2]CEN Grenoble, France; [3]University of Bochum, W.-Germany; [4]Academy of Sciences, Leningrad, USSR, [5]Present address: JET Joint Undertaking, England; [6]University of Washington, Seattle, USA

conditions a rough estimate of the fractional population of tail electrons can be obtained by assuming from quasi-linear theory that a unidirectional plateau is formed in the toroidal direction in the velocity space from a low value V_1, a few times the thermal speed, up to a value $V_2 \gg V_1$, determined by the accessibility condition ($V_2 \simeq c/1.55$ for the present case). In this hypothesis the central current density is given by:

$$j_{RF}(0) = e \frac{V_2 + V_1}{2} n_{RF}(0)$$

where $n_{RF}(0)$ is the total density of RF-generated suprathermal electrons in the plasma center. This expression can be compared with the value obtained by assuming the q value in the plasma center close to unit, as, deduced from Li-beam measurements /4/:

$$j_{RF}(0) = \frac{2}{\mu_o} \frac{B_T}{R}$$

when R, the plasma major radius, is equal to 166 cm in ASDEX. When the value of the central electron density ($n_e(0) = 1.5 \times 10^{13}$ cm^{-3}) is taken into account we obtain for the current drive discharge $n_T(0) = 1$ % in good agreement with data in Fig. 1.

When we compare complete current drive with electron heating discharges we find a considerable enhancement of the non-thermal population in the latter case (Fig. 1). This could be explained by a better power absorption in the plasma, possibly due to small differences in the spectrum at high $N_{\parallel}$. However this should lead to an increase in the thermal energy content in heating discharges which is not observed.

Thus the higher content of non-thermal electrons in heating discharges seems to indicate that the tail extends to energies higher than in current drive discharges. However the minimum $N_{\parallel}$ accessible to the plasma center is nearly the same in the two cases and so the only possible explanation for the results is that the toroidal electric field, which is nearly vanishing only in the current drive case, is effective in accelerating the electron tail to higher energies. It is worth to note that in the heating discharges discussed here the value of the electric field is about 1.4 % of the critical runaway field. This results in a critical velocity of 0.56 c, which is lower than the upper limit of the quasilinear plateau, $V_2 = 0.62$ c, as deduced from accessibility condition.

Magnetic measurements also show that in the discharges considered here the plasma pressure becomes strongly anisotropic in the heating case while LH current drive leads to nearly isotropic heating (Fig. 2). The parallel and perpendicular components of the plasma pressure were derived from three independent measurements of β_p (diamagnetic beta), $\beta_p^{equ} + l_i/2$ (β_p^{equ} = equilibrium beta) and l_i /4/.

The influence of the shape of the $N_{\parallel}$ spectrum on the non-thermal population was also studied. A power scan with $\langle N_{\parallel} \rangle = 2$ and $\langle N_{\parallel} \rangle = 4$, (Fig. 3) shows for both cases a nearly linear dependence upon the injected power but faster waves are more effective in generating fast electrons. This is in agreement with observed heating efficiency as well as with current drive experiment results /5/.
Also shown in Fig. 3 are two measurements taken during opposite current drive experiments. In this case the waves have to push the electrons against

the applied toroidal field and consistently a lower number of tail electrons is observed.

A density scan was also performed at a medium power level ($P_{RF} \simeq 430$ kW). This is not enough to obtain complete current drive except at very low density. The results of the measurements are shown in Fig. 4. For $\bar{n}_e \geq 1 \times 10^{13}$ cm^{-3} the loop voltage is nearly equal for current drive and heating discharges with $\langle N_{\parallel} \rangle = 2$. The different behaviour in the partial current drive and heating cannot be due to electric field effects and is not fully understood. We note, however, that in this experiment heating discharges have a higher electron temperature.

At the highest density all the three spectra give nearly the same result. This corresponds to the point where the heating efficiency for the electrons is just starting to deteriorate because of the increasing ion absorption /5/. In these conditions we performed spatially resolved measurements for two values of the injected power at $\langle N_{\parallel} \rangle = 2$ (Fig. 5): we obtained hollow profile, showing a lack of wave penetration to the plasma center.

To check problem of wave accessibility to the plasma center, $\langle N_{\parallel} \rangle = 4$ spectrum was studied in the same plasma conditions, although at a reduced power level ($P_{RF} = 300$ kW), and the n_T profile was still found to be hollow. It can then be concluded that in the ion interaction regime the penetration of the waves to the plasma center is inhibited possibly due to the absorption by the plasma edge.

References

/1/ N.J. Fisch, Phys. Rev. Lett. 41, 873 (1978)
/2/ R. Bartiromo, et al., Phys. Rev. A32, 531 (1985)
/3/ R. Bartiromo, et al., to be published
/4/ K. McCormick, et al., Procs. 12th Europ. Conf. on Controlled Fusion and Plasma Physics, Budapest (1985), Vol. I, p. 189
/5/ F. Leuterer, et al., Plasma Phys. Controlled Fusion 27, 1399 (1985)

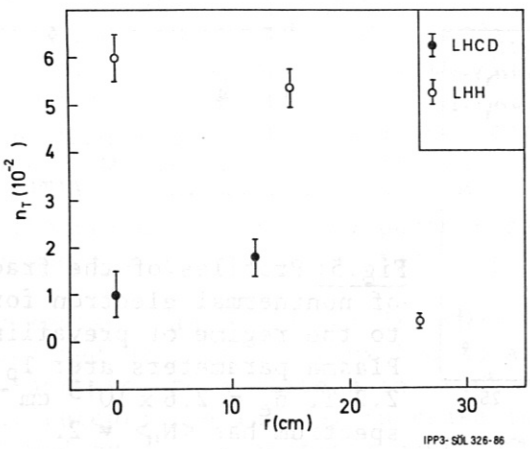

Fig. 1: The fractional population of non-thermal electrons is plotted versus the plasma radius for current drive and electron heating discharges. The plasma parameters are: $I_p = 300$ kA, $B_T = 2.4$ T. $\bar{n}_e = 1.2 \times 10^{13}$ cm^{-3} and $P_{RF} = 800$ kW. The launched spectrum has $\langle N_{\parallel} \rangle = 2$.

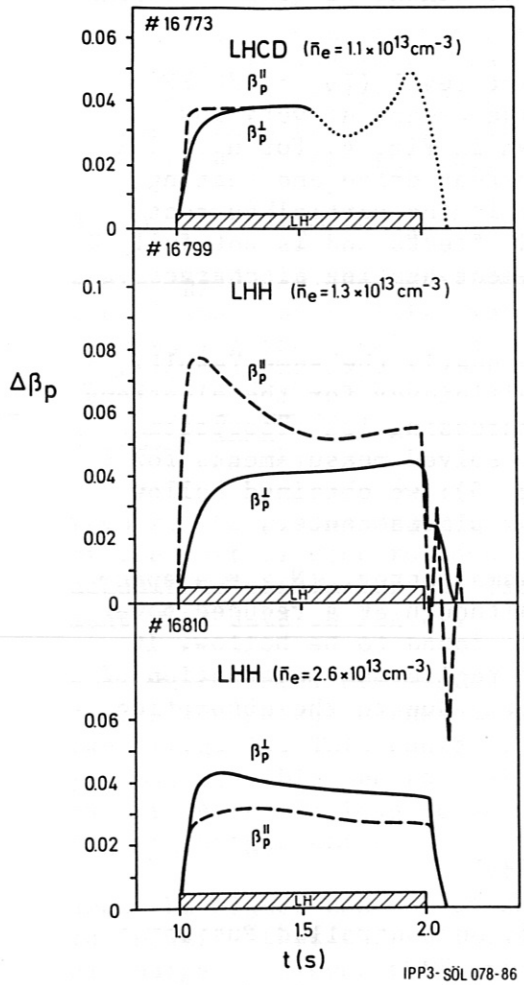

Fig. 2: Increment of $\beta_p^{\parallel}$ and β_p for LHCD and LHH at low and high electron density.

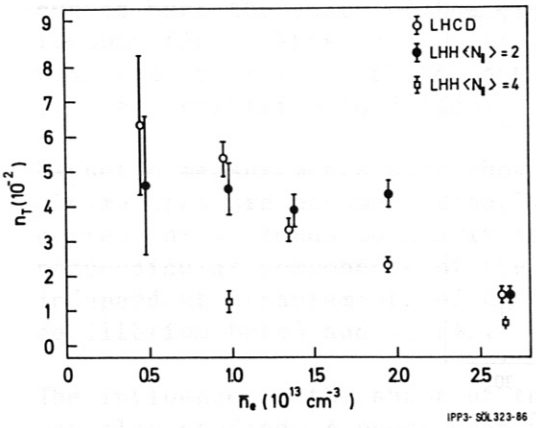

Fig. 4: Density scan for current drive with $\langle N_{\parallel} \rangle = 2$ and heating discharges with $\langle N_{\parallel} \rangle = 2$ and $\langle N_{\parallel} \rangle = 4$. Other plasma parameters are: $I_p = 300$ kA, $B_T = 2.2$ T, $P_{RF} = 430$ kW. Data refer to r = 11 cm.

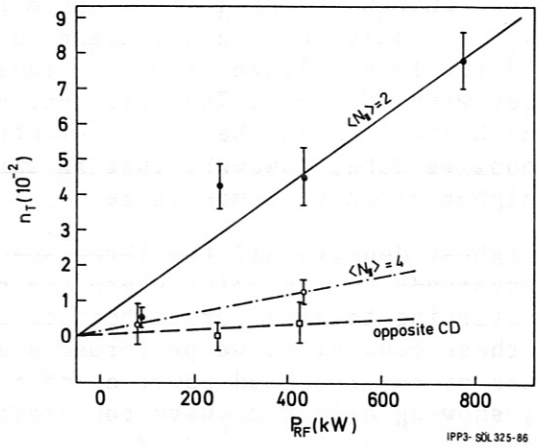

Fig. 3: Power scan for heating discharges with $\langle N_{\parallel} \rangle = 2$ and $\langle N_{\parallel} \rangle = 4$ and for opposite current drive. Plasma parameters are: $I_p = 300$ kA, $B_T = 2.2$ T, $\bar{n}_e = 1.0 \times 10^{13} cm^{-3}$. Data refer to r = 11 cm.

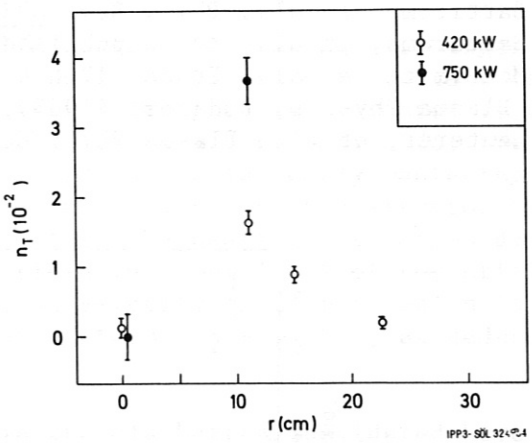

Fig.5: Profiles of the fractional population of nonthermal electron for discharges near to the regime of prevailing ion absorption. Plasma parameters are: $I_p = 300$ kA, $B_T = 2.2$ T, $\bar{n}_e = 2.6 \times 10^{13}$ cm^{-3}. The launched spectrum has $\langle N_{\parallel} \rangle = 2$.

INFLUENCE OF THE LOWER HYBRID WAVE SPECTRUM ON THE CURRENT DISTRIBUTION IN ASDEX

K. McCormick, F.X. Söldner, F. Leuterer, H. Murmann, D. Eckhartt, G. Becker, H. S. Bosch, H. Brocken, A. Eberhagen, G. Fussmann, O. Gehre, J. Gernhardt, G.v.Gierke, E. Glock, O. Gruber, G. Haas, J. Hofmann, A. Izvozchikov[1], G. Janeschitz, F. Karger, M. Keilhacker[2], O. Klüber, M. Kornherr, K. Lackner, M. Lenoci, G. Lisitano, F. Mast, H. M. Mayer, D. Meisel, V. Mertens, E. R. Müller[2], H. Niedermeyer, A. Pietrzyk[3], W. Poschenrieder, H. Rapp, H. Röhr, J. Roth, F. Ryter[4], F. Schneider, C. Setzensack, G. Siller, P. Smeulders[2], K.-H. Steuer, F. Wagner, D. Zasche

Max-Planck-Institut für Plasmaphysik
EURATOM Association, D-8046 Garching

Abstract: Measurements of the plasma current density distribution j(r) during injection of stationary or propagating lower hybrid wave spectra have been performed on ASDEX. Positive current drive leads to broader j(r) profiles - while $T_e(r)$ is peaking - coupled with an increase in q from $q \lesssim 1$ to $q > 1$. The other spectra influence j(r) only to the extent predicted from classical conductivity based on changes in $T_e(r)$ under the condition $q(0) \sim 1$.

Introduction: It has been demonstrated on various experiments that lower hybrid current drive (LHCD) can be used to suppress sawtooth oscillations /1-4/ or influence m/n = 2/1 tearing modes /2-4/. Based on magnetic signals and the monitoring of MHD activity it has been conjectured that these effects have their origin in an LHCD-induced broadening of the j(r) profile /2-4/. In the same way, magnetic signals have been interpreted as inferring a strong peaking of j(r), attained by appropriately adjusting the LH wave spectrum /4/. These points have been investigated on ASDEX by direct measurements of j(r) for a variety of LH spectra.

Experiment: ASDEX was operated in the divertor configuration with parameters: $\bar{n}_e = 1.2 \times 10^{13}$ cm^{-3} ($0\,\pi\,0\pi$: 8×10^{12} cm^{-3}), $I_p = 292 - 301$ kA, $B_T = 21.5$ kG, a ~ 39.4 cm and R ~ 167 cm. Approximately 560 kW ($0\,\pi\,0\,\pi$: 340 kW) of rf power was launched into the plasma via an 8-waveguide grill with a phase difference $\Delta\phi$ between the waveguides such that a spectrum with $\bar{N}_{\parallel} \sim 2$ ($0\,\pi\,0\,\pi$: $\bar{N}_{\parallel} \sim 4$) was generated symmetrically ($0\,0\,\pi\,\pi..$, $0\,\pi\,0\,\pi...$; LHH), parallel ($\Delta\phi = +\pi/2$, LHCD) or antiparallel ($\Delta\phi = -\pi/2$) to the plasma current /5/. Z_{eff} in the ohmic heating (OH) phase - deduced assuming neoclassical conductivity - and the OH/LH loop voltages V_L are given in Table I.

The resulting incremental changes in the diamagnetic beta signal $\Delta\beta_{p\perp}$ and $\Delta(\beta_p^{equ} + l_i/2)$ (measured by poloidal flux loops) are depicted in Fig. 2. It is seen that $\Delta\beta_{p\perp}$ increases to a plateau in ~100 - 150 ms. The behavior in $\Delta(\beta_p^{eq} + l_i/2)$ is different; the initial increase in this quantity, common to all cases, is followed by a slow decrease over ~300 ms to a plateau below the OH value for $+\pi/2$ and $0\,\pi\,0\pi$. We note that $\beta_{p\perp}$ is sensitive only to the perpendicular energy $W_\perp$ and β_p^{eq} to the entire energy $W=(W_\perp+W_{\parallel})/2$, so that $D = \Delta(\beta_p^{eq} + l_i/2) - \Delta\beta_{p\perp} = \Delta(W_{\parallel}-W_\perp)/2 + \Delta l_i/2$. Hence, the discrepancies D

---

[1]Academy of Sciences, Leningrad, USSR; [2]Present address: JET Joint Undertaking, England; [3]Univ. of Washington, Seattle, USA; [4]CEN Grenoble, France

seen between $\Delta\beta_{p\perp}$ and $\Delta(\beta_p^{eq} + l_i/2)$ in Fig. 2 can be ascribed to the production of a pressure anisotropy between the directions perpendicular and parallel to the magnetic field, and/or to a change in Δl_i, i.e. to a redistribution in j(r).

The effect on j(r) was determined directly by means of a neutral lithium beam probe which measures the magnetic field pitch angle $\theta_p = \tan^{-1}(B_p/B_T)$ at the intersection between the beam and optical axis of the detecting system (Fig. 1) /6-7/; j(r) can be calculated using $\theta_p(r)$ in conjunction with Maxwell's equations. $T_e(z)$ is registered along a vertical chord (not passing through the magnetic axis) by a 60 Hz pulsed Thomson scattering system (Fig. 1) /8/.

Results: The measured pitch angle profiles θ_p^c, adjusted to cylindrical geometry, for $+\pi/2$ are plotted vs. the flux-surface radius r_f in Fig. 2 (top, right) for the OH and steady-state LHCD phases along with the corresponding q(r) and j(r) profiles (top, left). It should be noted that the OH points are well documented with two points each at r_f = -1.7, +10.3, 14.3 and 29.2 cm. The indicated error bars on θ_p^c reflect the noise level associated with the base line of θ_p^c and of θ_p^c itself. For OH, the q=1 radius is in rough agreement with the ECE sawtooth inversion radius (hatched region) r_{st}. The application of LHCD leads to a broadening of the j(r) profile (from which $\Delta l_i \sim -0.12$ is computed) and an associated increase in q(0) from $0.98 + 0.03/-0.01$ to ~ 1.14, in concord with previous results /7/. While T_e profiles are not available for this series, the experience is always that T_e peaks with LHCD in the fashion seen with 0 0 π π, thereby demonstrating that the LH-driven current is decoupled from the classical conductivity profile.

The (Fig. 3) θ_p^c and T_e profiles for $-\pi/2$ exhibit no significant change between the OH and LH phases, i.e. D is due solely to a large anisotropy in the non-thermal electron population in favor of the component parallel to the magnetic field. A comparison between the experimental θ_p^c points and the curves predicted from Spitzer or neoclassical (neo) conductivity (assuming Z_{eff} and the electric field E are constant) shows no consistent agreement with either case. (Fig. 3 - the curve spread reflects the T_e error bars.) However, neither model correctly predicts r_{st}: neo gives q(0) values far below the q(0) ~ 0.96 determined from the lithium beam, whereas Spitzer generally yields q ~ 1 only very near the axis. If a central zone of anomalous resistivity or a smaller E is postulated such that q ~ 1 is fulfilled, then neoclassical conductivity would describe the experimental points reasonably well in the q > 1 region. However, for fiducial purposes the Spitzer curves are used in comparison hereafter.

The failure of the experimental θ_p^c curves to cross the axis at r_f = 0 for both $-\pi/2$ and 0 0 π π (consecutive series) is probably due to a slight (~0.3°) beam misalignment. The systematic trend of the $r_f < 0$ θ_p^c points to increase for $-\pi/2$ is not understood, as a symmetric behavior for $r_f \sim 10$ cm is not observed.

The heating spectrum 0 0 π π produces a pronounced peaking in $T_e(r)$, but no distinct change in θ_p^c. In contrast to the OH phase, the Spitzer θ_p^{LH} profiles lie above the experimental θ_p^c points, demonstrating that j(r) has not tracked the $T_e(r)$ change - suggestive that a mechanism which always maintains q(0) ~ 1 is operative.

The 0 π 0 π T_e^{OH} profile is broader in the central region compared to 0 0 π π, leading to a narrower j(r) distribution (synonymous with higher θ_p^c values) as corroborated by the Li-beam measurements. LHH produces a decrease in T_e ($r \leq a/2$), which j(r) follows up to $\Delta t_{LH} \sim 300 - 400$ ms as confirmed by θ_p^c from experiment (Fig. 3). Hence j(r) has been altered by affecting the bulk thermal electron population, changing $q^{OH}(0)$ from ~0.97 to $q^{LH}(0) \sim 1.06$ and 1_i^{OH} from 1.35 to $1_i^{LH} \sim 1.15$. The behavior after $\Delta t_{LH} \sim 400$ ms cannot be considered here.

Discussion: Table I summarizes the experimentally determined changes in q(0) and l_i, from which we see that $q^{OH}(0) = 0.96 - 0.98$. This implies that only a few per cent of the current inside the q = 1 surface needs be displaced outwards in order to achieve q > 1 and an associated suppression of sawteeth. Such a small change can take place inside one sawtooth period, which is congruous with the observed invariance of r_{st} up to the moment of sawtooth disappearance described elsewhere /1/.

Taking the experimental Δl_i it is possible to compute $\Delta\beta_p^{eq}$ for all cases, the values of which are indicated on Fig. 2 by arrows. Accordingly, +π/2 produces a nearly isotropic pressure (i.e. $\Delta\beta_p^{eq} \gtrsim \Delta\beta_{p_\perp}$), whereas -π/2 exhibits an extreme anisotropy and 0 0 π π lies in between. These deduced trends are consistent with direct measurements of the non-thermal electron population on ASDEX /9/.

In passing it should be mentioned that the profiles discussed here are interesting candidates for a "profile consistency" analysis /10/ inasmuch as $T_e(r)$ and j(r) are loosely coupled for 0 0 π π and decoupled for π/2, but both yield approximately the same T_e profile. Further, for 0 π 0 π, LHH produces a large, coupled change in $T_e(r)$ and j(r).

Finally, the Li-beam measurements reported here support the thesis /11/ that sawtooth stabilization on ASDEX occurs only when the condition q > 1 prevails in the central region.

References:

/1/ J.E. Stevens, et al., 12th Eur. Conf. on Contr. Fusion and Plasma Physics 2, 192 (Budapest, 1985).
/2/ F. Parlange, et al., Ref. /1/, 2, 172.
/3/ D. van Houtte, et al., Nucl. Fusion Lett. 24, 1485 (1984).
/4/ D. van Houtte, et al., Course/Workshop on "Tokamak Startup-Problems and Scenarios related to the transient phases of ignited tokamak operations" (Erice, 1985).
/5/ F. Leuterer, F. X. Söldner, et al., Plas. Phys. 27, 1399 (1985).
/6/ K. McCormick, M. Kick, et al., 8th Eur. Conf. on Contr. Fusion and Plasma Physics, 140 (Prague, 1977).
/7/ K. McCormick, et al., Ref. /1/, 1, 199.
/8/ D. Meisel, H. Murmann, H. Röhr, K.-H. Steuer, this conference.
/9/ R. Bartiromo, M. Hesse, et al., this conference.
/10/ B. Coppi, Comments Plas. Phys. Contr. Fusion 5, 201 (1980).
/11/ F. X. Söldner, et al., this conference.

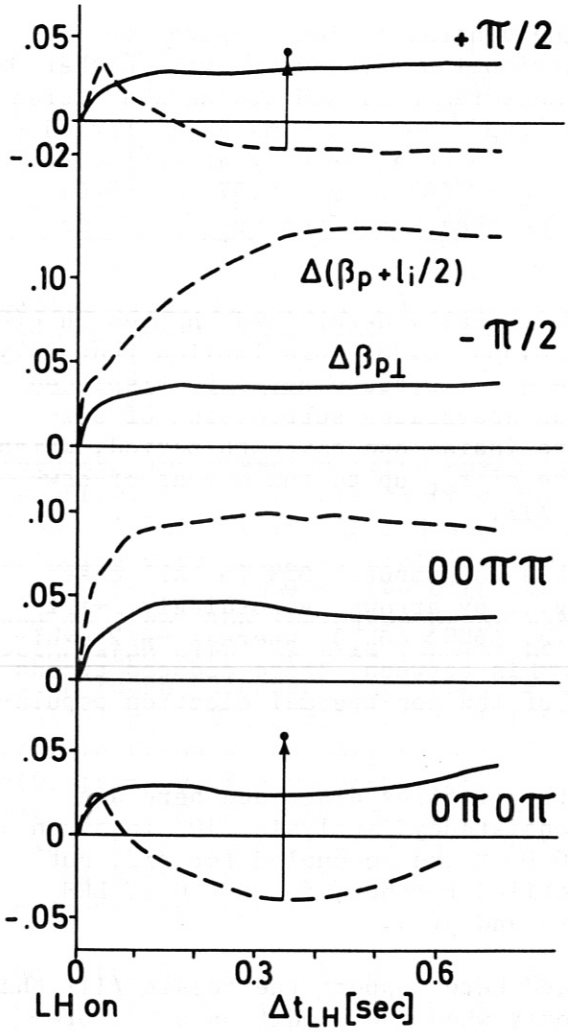

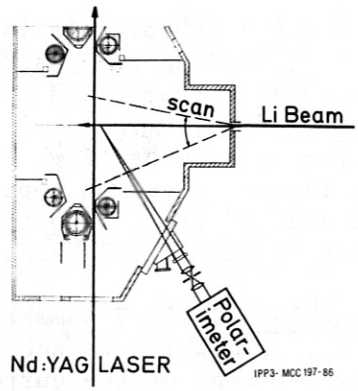

Fig.1
Diagnostic
Layout

Fig. 2: The incremental change in $ß_{p\perp}$(-) and $ß_p + l_i/2$(--) arising from LH. The arrows and points indicate the Li-beam derived values for $-\Delta l_i/2$ and $\Delta ß_p^{eq}$, respectively. OH values: $ß_{p\perp} \sim 0.2$, $(ß_p + l_i/2) \sim 0.9$.

Table I: Experimental Results

	Z_{eff}^{neo}	$V_L^{OH}:V_L^{LH}$	$q^{OH}(0)$	$q^{LH}(0)$	Δl_i
π/2	?	0.9:0.3	0.98	1.14	-0.12
-π/2	2.4	0.9:0.62	0.96	0.99	0
0 0 π π	"	0.9:0.57	"	0.96	0
0 π 0π	4.0	1.0:0.54	0.97	1.06(?)	-0.2

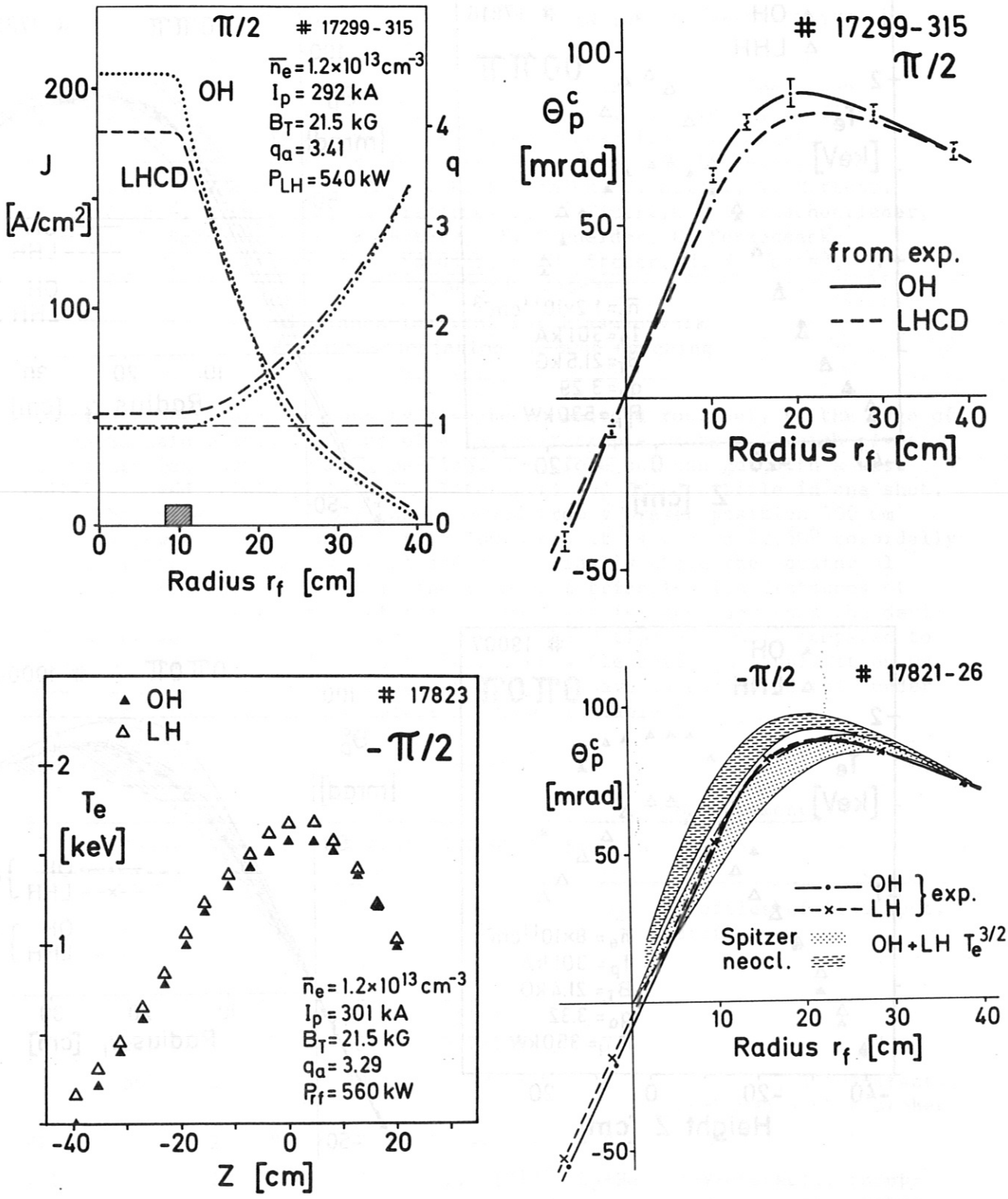

Fig. 3: j(r) and q(r) profiles (top, left) derived from the experimental pitch angle curves (top, right) for OH and LHCD. Successively, the T_e and experimental θ_p^c profiles (on the left and right, respectively) for the OH and LH discharge phases are shown for opposite current drive -π/2, and on the next page the heating spectra, 0 0 π π, 0 π 0 π.

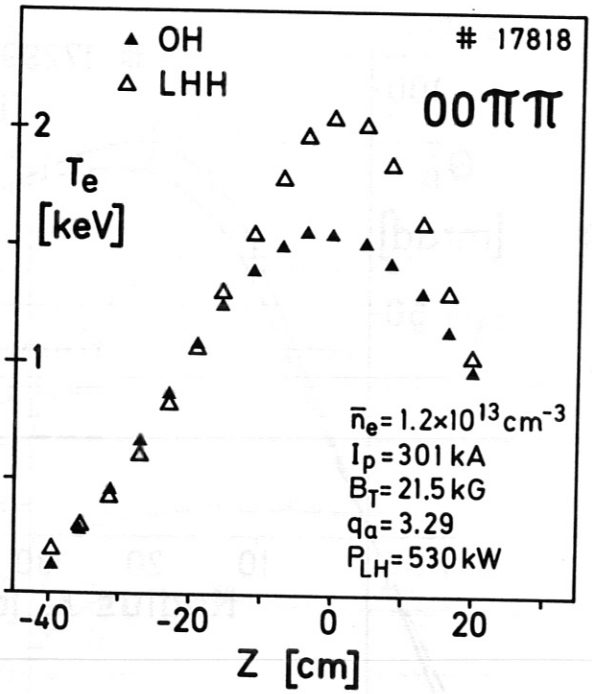
▲ OH
△ LHH
17818
00ππ
Te [keV]
2
1
$\bar{n}_e$= 1.2×10^{13}cm^{-3}
I_p= 301 kA
B_T= 21.5 kG
q_a= 3.29
P_{LH}= 530 kW
-40
-20
0
20
Z [cm]

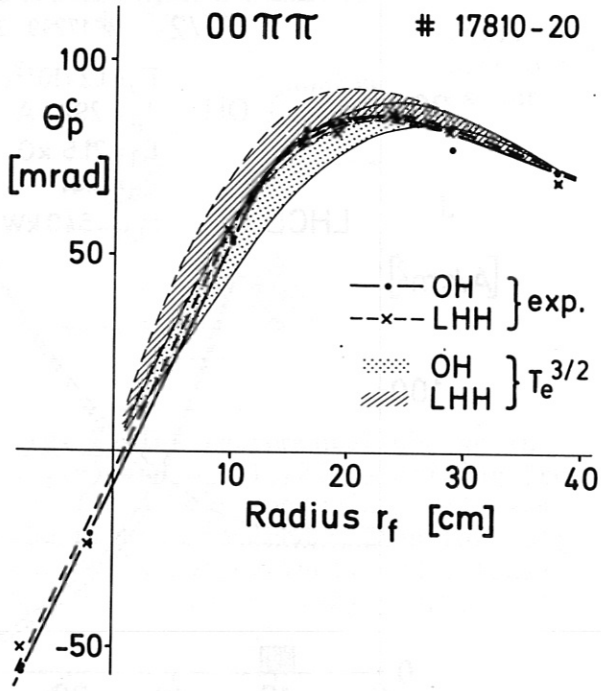
00ππ
17810-20
100
Θ_p^c [mrad]
50
-50
OH
LHH
exp.
OH
LHH
$T_e^{3/2}$
10
20
30
40
Radius r_f [cm]

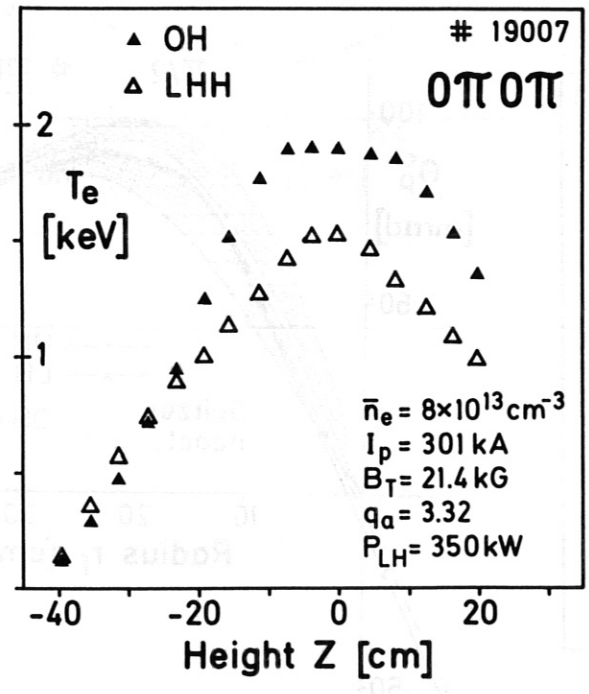
▲ OH
△ LHH
19007
0π0π
Te [keV]
2
1
$\bar{n}_e$= 8×10^{13}cm^{-3}
I_p= 301 kA
B_T= 21.4 kG
q_a= 3.32
P_{LH}= 350 kW
-40
-20
0
20
Height Z [cm]

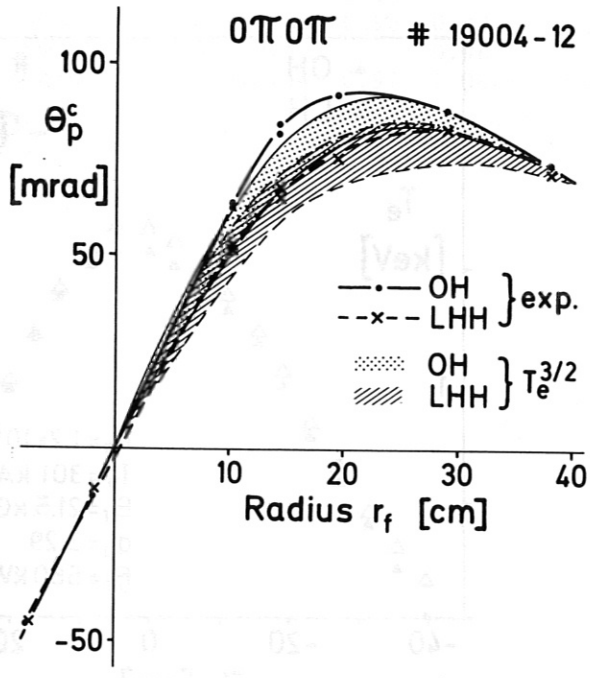
0π0π
19004-12
100
Θ_p^c [mrad]
50
-50
OH
LHH
exp.
OH
LHH
$T_e^{3/2}$
10
20
30
40
Radius r_f [cm]

Fig. 3

PROBE MEASUREMENTS OF PLASMA INHOMOGENEITIES IN THE SCRAPE-OFF LAYER OF ASDEX DURING LH

M. Lenoci, G. Haas, G. Becker, H. S. Bosch, H. Brocken, A. Eberhagen, D. Eckhartt, G. Fussmann, O. Gehre, J. Gernhardt, G.v.Gierke, E. Glock, O. Gruber, J. Hofmann, A. Izvozchikov[1], G. Janeschitz, F. Karger, M. Keilhacker[2], O. Klüber, M. Kornherr, K. Lackner, F. Leuterer, G. Lisitano, F. Mast, H. M. Mayer, K. McCormick, D. Meisel, V. Mertens, E. R. Müller[2], H. Murmann, H. Niedermeyer, A. Pietrzyk[3], W. Poschenrieder, H. Rapp, H. Röhr, J. Roth, F. Ryter[4], F. Schneider, C. Setzensack, G. Siller, P. Smeulders[2], F.X. Söldner, K.-H. Steuer, N. N. Tsois[5], F. Wagner, D. Zasche

Max-Planck-Institut für Plasmaphysik
EURATOM Association, D-8046 Garching

Electron temperature and density have been measured routinely at the edge of the ASDEX main plasma by means of a Langmuir triple probe /1/ which gives the saturation current and T_e on-line. Therefore one can get with a fast radially moved triple probe a complete $n_e(r)$ and $T_e(r)$ profile in one shot. The probe installed in ASDEX can be moved from a preset position 100 mm radially inward and backward within 200 msec. It is placed 22.50° toroidally away from the LH launching grill and 5° poloidally above the equatorial plane; the tips are arranged in the form of a triangle with distances of 7 mm. For a proper function of triple probes it is necessary that the deviations between the floating potentials of the 3 tips are small compared to T_e/e. In ohmic discharges this is fulfilled while during LH application we observed differences of the order of T_e/e. We have investigated this under different plasma and LH parameters as shown in Table 1.

Table 1

Series	LH		Plasma				Measurements
	Power (kW)	$n_{\parallel}$	B_T(T)	I_p(kA)	$\bar{n}_e$(cm^{-3})	Species	
I	770	2	2.37	300	1.4×10^{13}	D_2	profiles of float.pot. diff.
II	750	2	"	"	2.7×10^{13}	"	" "
III	370	4	2.18	"	2.1×10^{13}	"	" "
IV	275	4	"	380	2.7×10^{13}	"	" "
V	500	2	"	300	1.4×10^{13}	"	" , I-V-charact., combined double probes
VI	"	2	"	"	2.9×10^{13}	"	" "
VII	"	2	"	"	1.4×10^{13}	D_2+He	I-V-charact., independent double probes
VIII	"	2	"	"	2.9×10^{13}	"	explorative, independent double probes

[1]Academy of Sciences, Leningrad, USSR; [2]Present address: JET Joint Undertaking, England; [3]Univ. of Washington, Seattle, USA; [4]CEN Grenoble, France; [5]NRC Democritos, Athens, Greece

From the floating potential differences we have constructed the electric field vector. The direction and absolute value of this show a strong radial dependence (Fig. 1, 2). In the series I, II, V, VI we found a large component parallel to the magnetic field at the innermost radial position. At the radial position of the grill the absolute value of the vector is much smaller. Despite of the different main plasma density in the series V and VI we found a very similar radial dependence of the direction. The same we got for the two series III and IV with lower RF power, for which the absolute value of the vector was always rather small. The reason for the deviations in floating potentials may be local inhomogeneities in electron temperature or in plasma potential or in flux of suprathermal eletrons. These can arise from effects connected to decay processes inbetween the grill and the separatrix described e.g. by Derfler /2/ or by Motley and Glanz /3/.

In order to distinguish between these possible explanations we operated for the series V, VI, VII and VIII couples of tips of the triple probe as double probes. The fast movement was modified in such a way that the probe stays for about 100 msec at the innermost position where the I-V characteristics were taken. In series V and VI we measured with two combined double probes with tip 3 as common reference tip. Under these conditions tip 3 has to carry the sum of the currents of tip 1 and 2 and from the characteristics one cannot find floating potential differences. They have to be measured independently. The characteristics (Fig. 3, 4) show only small differences between high and low main plasma density (corresponding to the ion-RF and the electron-RF interaction regime resp.) and indicate for couple 1-3 a lower temperature than for couple 2-3. This is in agreement with the direct floating potential measurements (Fig. 1,2), but not with the relative shift of the two characteristics.

For series VII with parameters like series V but with a changed plasma composition we have increased the voltage range to 0 - 600 V in order to reach well the saturation. We have used the two couples 1-3 and 2-3 alternatively and not connected. In this case we find again a lower temperature for the couple 1-3 than for couple 2-3 (Fig. 5) (67 and 80 eV resp.). Now the floating potential difference derived from the shift of the characteristics (30 V) is within 30 % in agreement with the temperature difference.

In addition to this series in the electron regime we have done also some explorative measurements in the ion regime but otherwise under the same conditions (series VIII). We have found again no significant difference between high and low density. This may indicate that a plasma exists inbetween the LH-grill and the separatrix dominated by the LH-wave or by any decay waves and decoupled from the main plasma.

In other exlorative measurements we have investigated for comparison purpose ohmically heated discharges with plasma parameters like series VI and VIII. We have found much lower electron temperature (15 eV instead of 65-80 eV) and higher electron densities (2.5 - 3 x 10^{12} cm^{-3}) (Fig. 6). This is at least for the electron regime in agreement with mesurements done by Pericoli on FT /4/ and El Shaer on ASDEX /5/ who found a strong redution of the density in front of the LH grill during RF application.

Conclusion

We have observed during LH application on ASDEX with a Langmuir probe having 3 tips strong poloidal and toroidal deviations in the floating potential. The probe was positioned roughly 1 m away from the LH-grill in a magnetic

flux bundle directly connected to the space in front of the RF-coupler. These deviations exist at all plasma and LH conditions investigated until now and can inhibit the operation of a triple probe at all. But other fast moved elctrostatic probes may also be disturbed too, since the radial dependence of the floating potential differences acts like a temporal change of the probe potential which cannot be controlled. The most important reasons for these deviations are changes in the electron temperature of typically 10 - 20 eV over a distance of 7 mm. But some findings like an additional shift in the I-V characteristic or large components of the floating potential differences parallel to the magnetic field lines cannot be explained by temperature differences. One has to assume also locally inhomogeneous fluxes of suprathermal electrons and differences in the plasma potential.

References:

/1/ S. L. Chen, T. Sekiguchi, J. Appl. Phys. 36, 2363 (1965).
M. Kamitsuma, S.L. Chen, J.S. Chang, J. Phys. D 10, 1065 (1977).
/2/ H. Derfler, private communication.
/3/ R. W. Motley, J. Glanz, Phys. Fluids 25, 2107 (1982).
/4/ V. Pericoli-Ridolfini, Plasma Phys. and Contr. Fus. 27, 709 (1985).
/5/ M. El Shaer, IPP Garching Report IPP III/96 (1984).

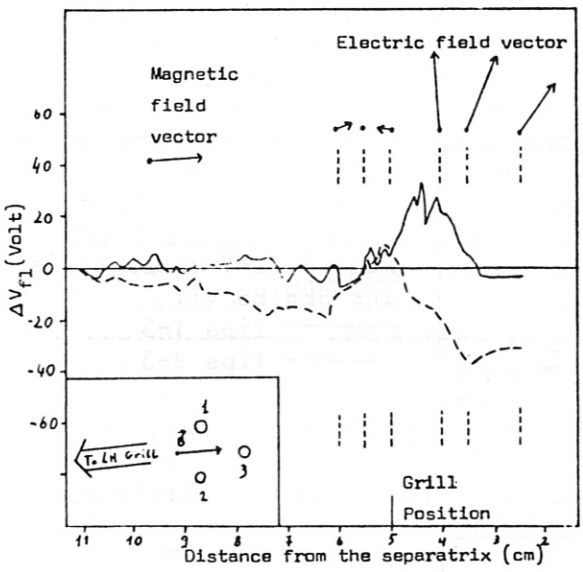

Fig. 1: Radial profiles of floating potential differences. SERIES VI
——— tips 1-3
------- tips 2-3

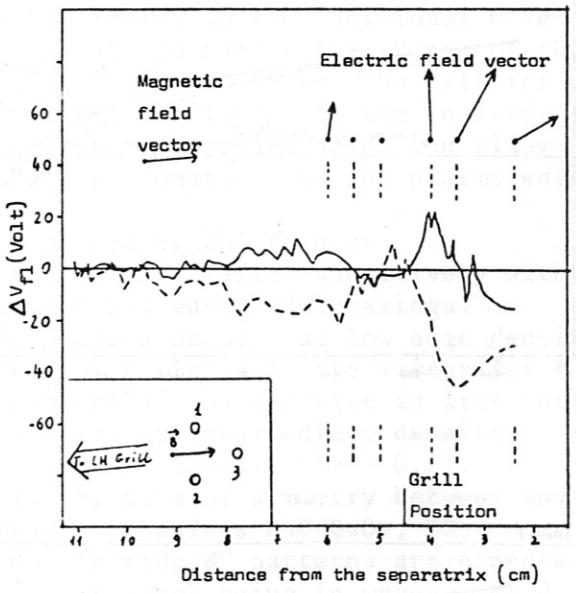

Fig. 2: Radial profiles of floating potential differences. SERIES V
——— tips 1-3
------- tips 2-3

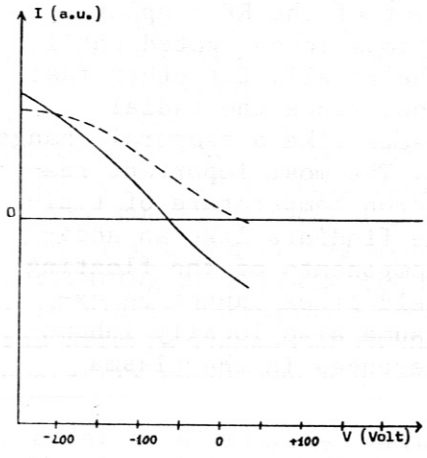

Fig. 3: I-V characteristics SERIES VI
——— Tips 1-3
------- Tips 2-3

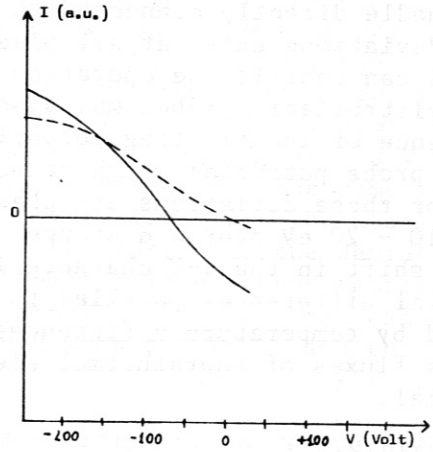

Fig. 4: I-V characteristics SERIES V
——— Tips 1-3
------ Tips 2-3

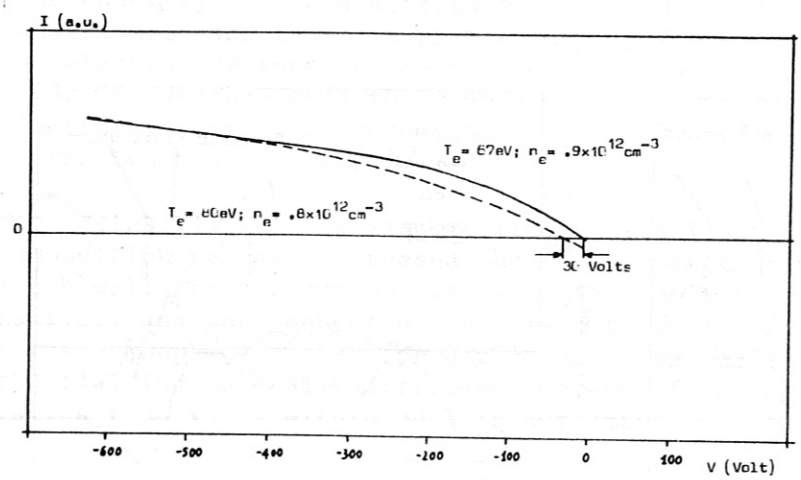

Fig. 5: I-V characteristics SERIES VII
——— Tips 1-3
------- Tips 2-3

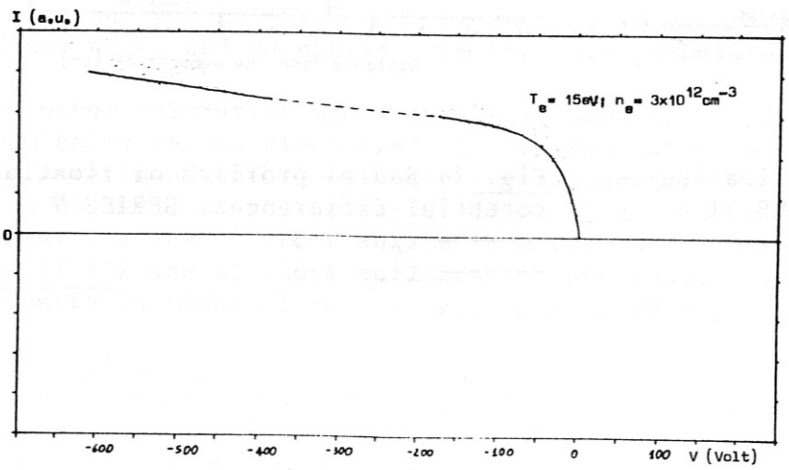

Fig. 6: I-V characteristics OH-discharge
$\bar{n}_e = 2.9 \times 10^{13}$ cm^{-3}

COUPLING OF LOWER HYBRID WAVES TO THE ASDEX PLASMA

M. Zouhar, T. Vien, F. Leuterer, M. Muenich, M. Brambilla, H. Derfler, D. Eckhartt, F. v.Woyna and ASDEX-Team

Max-Planck-Institut für Plasmaphysik, EURATOM Association, D-8046 Garching,FRG

1. Introduction

The ASDEX Lower-Hybrid experiment uses an eight waveguide grill antenna to launch the waves. A mean power reflection coefficient as low as $\langle R \rangle = 0.1$ is attainable in all modes of operation. However the reflection coefficients R_k in the individual waveguides may vary over a great range (up to 0.9). This paper aims at depicting the reflection patterns $R_k = f(k)$ and comparing measurement with theory.

At high power levels (above 140 kW/waveguide) a breakdown occurs. The sequence of phenomena relating to this breakdown is documented and commented on .

2. Calculated reflection patterns

Each of the reflection patterns depicted in the diagrams below consists of eight values R_k (power reflection coefficients) in the individual waveguides. Lines are drawn between adjacent points to render the shapes of the patterns prominent; they have no physical meaning otherwise. The patterns dealt with here all result from equal incident amplitudes in the individual waveguides. In each of the diagrams representing computed data, the plasma density gradient in front of the grill is kept constant and the plasma edge density is considered as a parameter.

The following characteristics are predicted by the theory:

- in general the R_k-patterns are expected to vary fairly sensitively with the plasma edge density. This is true for all waveguide phasings.
- a characteristic transition in the R_k-pattern occurs: at low edge density the edge waveguides exhibit low reflection while in centre waveguides reflection is relatively high ("ridge-pattern"). The opposite is true for high density ("valley-pattern"). In between an intermediate density exists with low reflection in all waveguides (overall $\langle R \rangle = 0.1$).
- symmetric reflection patterns R_k (k=1...8, axis of symmetry between waveguides 4 and 5) are expected for waveguide phasings $0\pi0\pi0\pi0\pi$, $00\pi\pi00\pi\pi$, $00\pi\pi\pi\pi00$, $0000\pi\pi\pi\pi$. Characteristic "double-ridged" patterns are expected for $00\pi\pi00\pi\pi$ and $0\pi0\pi0\pi0\pi$ phasings, the "ridges" being in waveguides 3 & 6 and 2 & 7 respectively.
- asymmetric reflection patterns are expected for 90 degrees difference between adjacent waveguides (+90 deg denoted "current drive" phasing, -90 deg "opposite current drive", i.e. opposite to the sense of the OH-current) and for similar phasings (120 deg, 60 deg, etc.).
- the phasings $00\pi\pi\pi\pi00$ and $0000\pi\pi\pi\pi$ have little importance for plasma heating. However, the accompanying R_k-patterns are very particular and fairly pronounced in magnitude. They offer an additional convenient opportunity to verify the theory.
- the computed R_k-patterns are depicted in Figs. 3a through 7a.

3. Experimental reflection patterns

Good qualitative agreement between experimental and theoretical data was observed:

- the measured R_k-patterns are shown in Figs. 3b through 7b. In most cases data of shots with varying edge density are presented.
- the characteristic shapes of the R_k-patterns are clearly distinguished. Relative plasma density changes in front of the grill were measured by means of a microwave interferometer (at 136 GHz). The R_k-patterns vary with density as anticipated.
- the agreement in magnitude is rather coarse. It should be noted however that no absolute values n_{edge} and ∇n were taken. In addition, the theoretical boundary conditions are not really those of the experiment (infinite plane conducting wall surrounding the grill, parallel plate geometry).
- all theoretically symmetric R_k-patterns experienced some experimental asymmetry. Possibly the alignment of the grill relative to the plasma torus was not perfect.

4. Breakdown in front of the grill

At high power levels (above 140 kW/waveguide at low densities) a breakdown in front of the grill was detected. This breakdown was studied in more detail by testing a single waveguide (Figs. 1 and 2).

- at first (time t = 0), light is detected by the photo-diode PD1 viewing all along the waveguide into the plasma (Fig. 2, first trace, positive signal).
- coincidentally several phenomena occur:
  a. A pronounced reflection of RF-power is indicated by directional coupler DC3 (outside the grill vacuum section, trace 3, negative).
  b. At the grill mouth coupler DC1 and the grill coupler DC2 (both being sidewall couplers within the grill vacuum section, both indicating incident waves, both signals negative) amplitude modulation due to the poor directivity of these couplers is clearly visible. The fact that the DC1-signal exhibits just one trough and one crest implies that the locus of the reflection originates in some distance from DC1 and propagates backward. In passing DC1 it causes the DC1-signal to vanish (trace 5). The same happens later at DC2 (trace 6).
- 250 microseconds after t = 0: light appears at photo-diode PD2 viewing perpendicularly into the waveguide (trace 2, positive, plateau resulting from saturation).
- 750 microseconds after t = 0: the incident wave is switched off (visible at DC3, trace 3, negative) as soon as light appears at PD3 (arc detector).

A possible explanation of this sequence of phenomena is:

- breakdown at the edge of the grill.
- reflection layer (plasma) moving back to the transmitter at a speed of about 3000 m/s, driven by the combined action of ponderomotive force and the force caused by the local magnetic field gradient.

The physics of the breakdown, however, has not yet been identified.

REFERENCES

/1/ Brambilla M., Nucl. Fusion 16 (1976) 47

/2/ Stevens J. et al., Nucl. Fusion 21 (1981) 1259

Breakdown in front of the grill

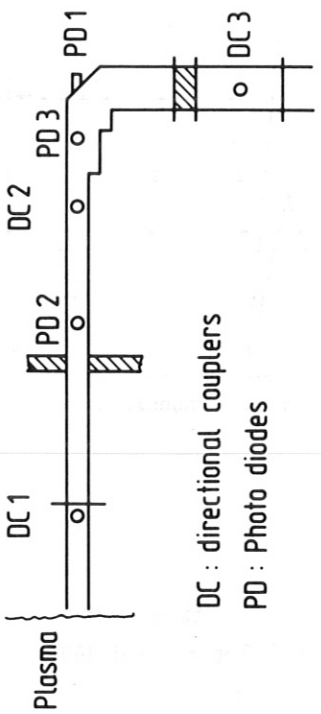

Fig. 1

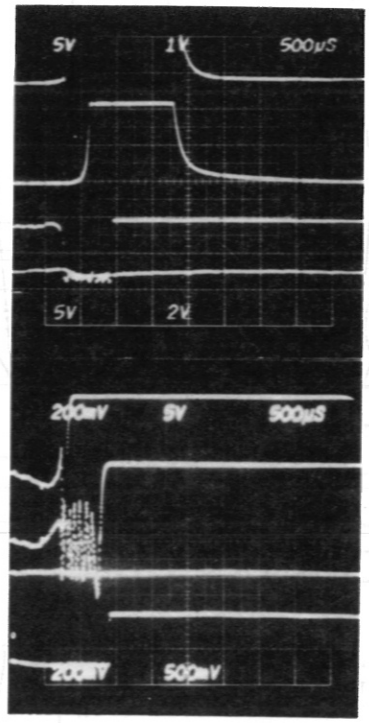

PD 1

PD 2
DC 3 , reflection

DC 1
DC 2

DC 3 , incident wave

Fig. 2

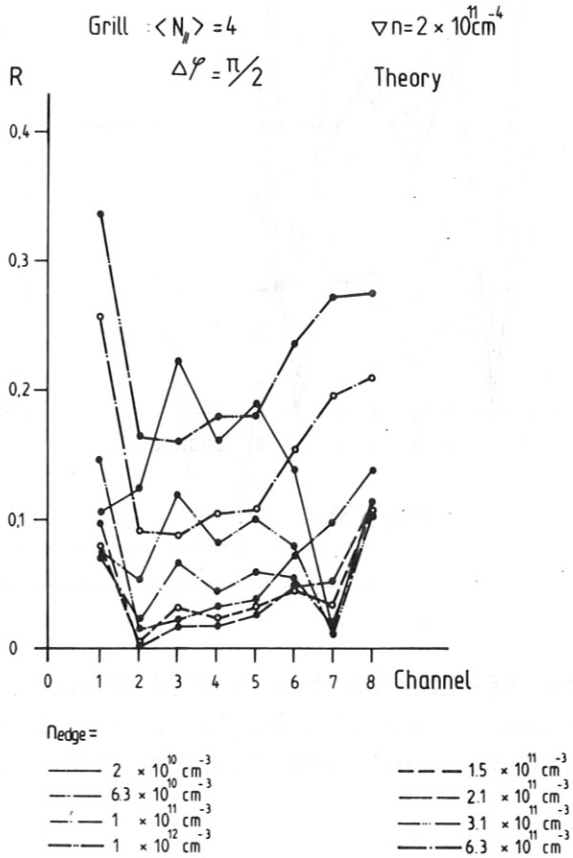

Fig.3a

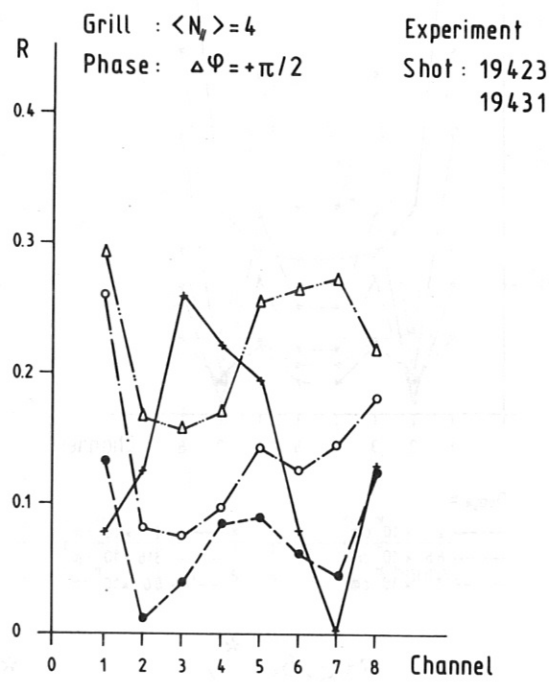

Fig.3b

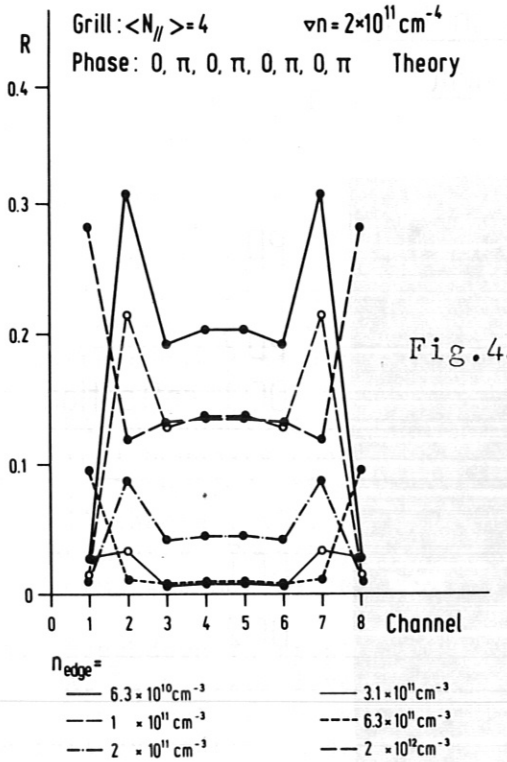

Fig.4a

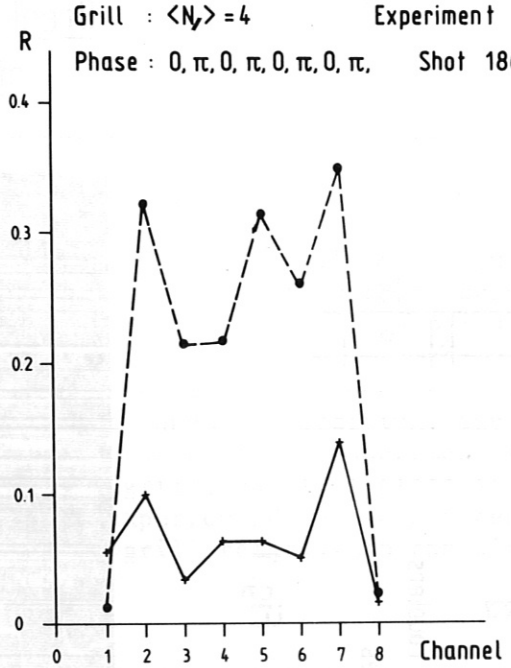

Fig.4b

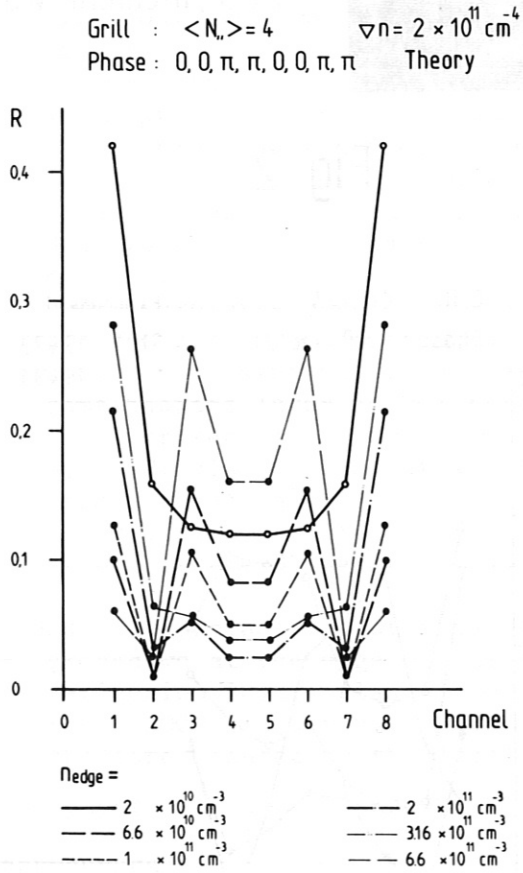

Fig.5a *)

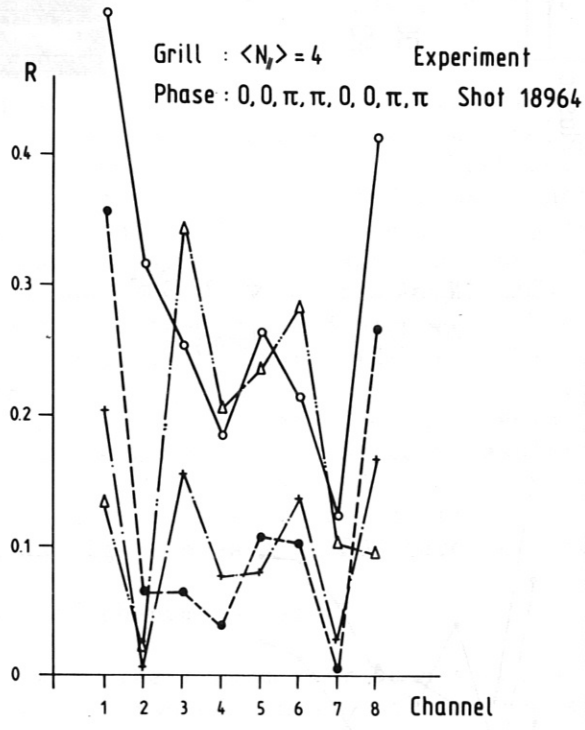

Fig.5b

*) : In figure 5a the solid line stands for the highest density, the dashed line for the lowest.

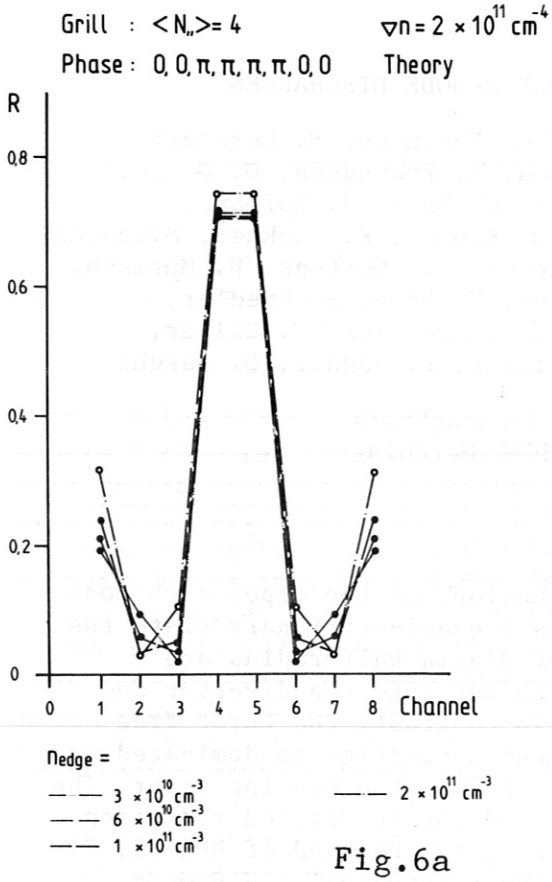

Fig.6a

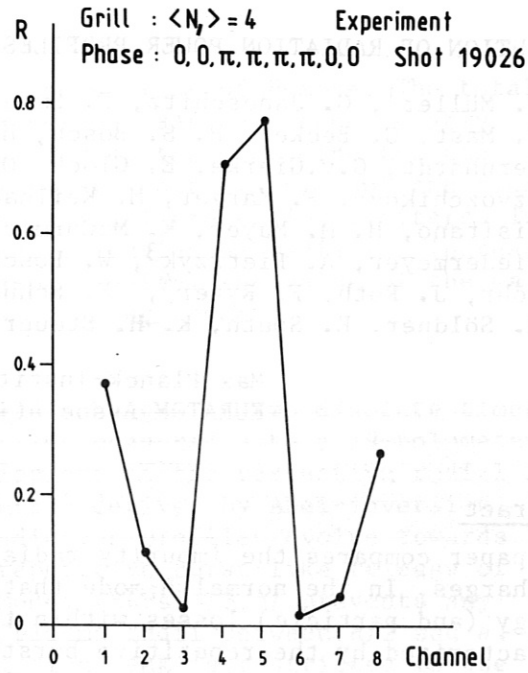

Fig.6b

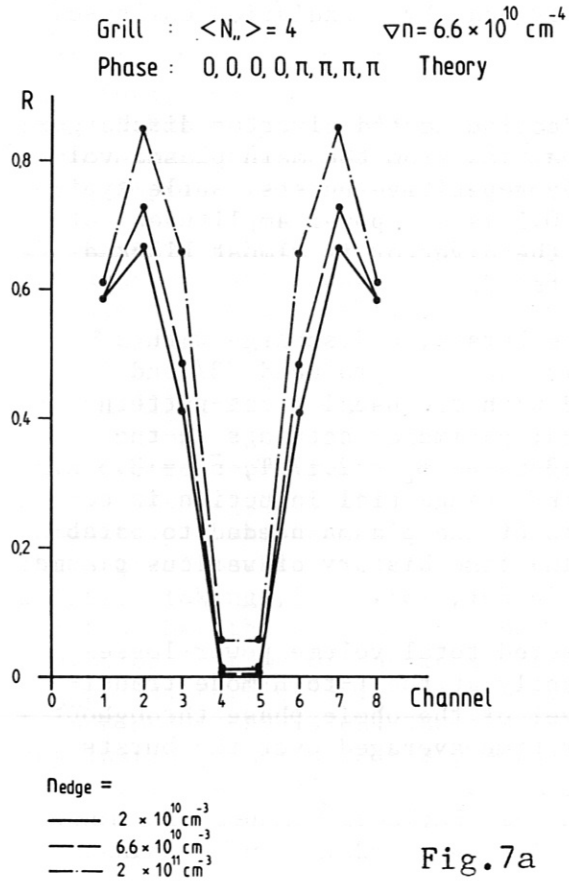

Fig.7a

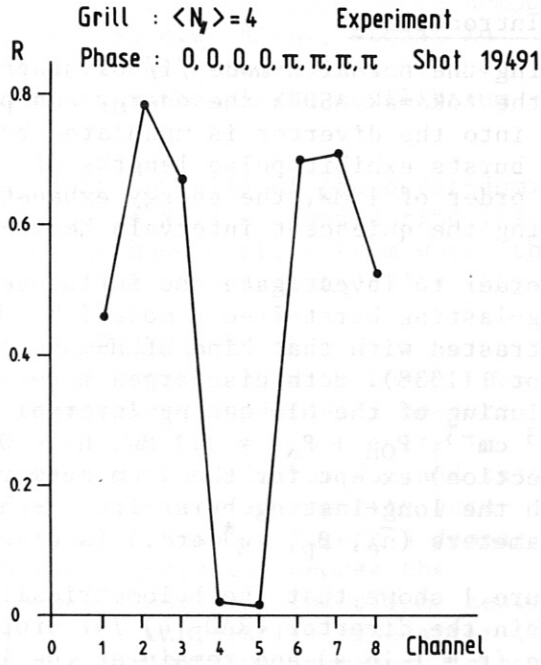

Fig.7b

EVOLUTION OF RADIATION POWER PROFILES IN ASDEX H-MODE DISCHARGES

E. R. Müller[1], G. Janeschitz, P. Smeulders[1], G. Fussmann, M. Kornherr, K. F. Mast, G. Becker, H. S. Bosch, H. Brocken, A. Eberhagen, O. Gehre, J. Gernhardt, G.v.Gierke, E. Glock, O. Gruber, G. Haas, J. Hofmann, A. Izvozchikov[2], F. Karger, M. Keilhacker[1], O. Klüber, K. Lackner, M.Lenoci, G. Lisitano, H. M. Mayer, K. McCormick, D. Meisel, V. Mertens, H. Murmann, H. Niedermeyer, A. Pietrzyk[3], W. Poschenrieder, H. Rapp, H. Riedler, H. Röhr, J. Roth, F. Ryter[4], F. Schneider, C. Setzensack, G. Siller, F. X. Söldner, E. Speth, K.-H. Steuer, O. Vollmer, F. Wagner, D. Zasche

Max-Planck-Institut für Plasmaphysik
EURATOM Association, D-8046 Garching

Abstract

The paper compares the impurity radiation behaviour of two types of H-mode discharges. In the normal H-mode that reaches a quasi-stationary state the energy (and particle) losses within the outer plasma half-radius are characterized by the repetitive burst-like exhaust into the divertor and constantly moderate radiation power losses. In contrast, the burst-free variant of the H-mode with superior confinement properties is dominated by radiation losses growing continuously up to 100 % of the heating power. The time evolution of the impurity concentration and the associated radiation losses at the plasma centre is hardly influenced by the kind of H-mode. If the concentration of medium-heavy metals in the burst-dominated H-mode plasma is raised to sufficiently high values, e.g. by the accumulation of intrinsic iron, the burst-free (or burst-deficient) H-mode is triggered which after a new accumulation period usually ends by a radiation collapse.

1. Introduction

During the normal H-mode /1/ of neutral-injection heated divertor discharges in the tokamak ASDEX the energy and particle flow from the main plasma volume into the divertor is modulated by highly repetitive bursts. While typical bursts exhibit pulse lengths of around 0.5 ms and power amplitudes of the order of 1 MW, the energy exhaust into the divertor is almost blocked during the quiescent intervals between bursts /2/.

In order to investigate the influence of the bursts, a discharge with a long-lasting burst-free H-mode (shot # 11447) has been produced /3/ and is contrasted with that kind of H-mode endowed with the usual burst-pattern (shot # 11338). Both discharges have identical parameter settings at the beginning of the NI-heating interval (I_p = 320 kA, B_t = 2.17 T, $\bar{n}_e$ = 3.5 x 10^{13} cm^{-3}, $P_{OH} + P_{NI}$ = 3.3 MW, $H^o \rightarrow D^+$ (40 kV) tangential injection in co-direction) except for the 4 cm outward shift of the plasma needed to establish the long-lasting burst-free H-phase. The time history of various plasma parameters ($\bar{n}_e$, β_p, τ_E^* etc.) is discussed in Ref. /3/.

Figure 1 shows that the bolometrically measured total volume power losses within the divertor (RAD_{DIV}) /4/ drop instantly at the L-to-H mode transition (t = 1.16 s) and remain at the low level of the ohmic phase throughout the burst-free H-mode, whereas they recover time-averaged over the bursts

---

[1]Present address: JET Joint Undertaking, Culham, England; [2]Academy of Sciences, Leningrad, USSR; [3]Univ. of Washington, Seattle, USA; [4]CEN Grenoble, France

with growing burst activity during the second variant of H-mode. The total radiation power losses of the main plasma volume (RAD) are considerably higher in the burst-free H-discharge, even during the preceding L-phase. This radiation enhancement indicates an impurity contamination of the plasma produced by its shift to the outer stainless-steel protection limiters. The burst-free H-mode is terminated when, after a continuous radiation increase accelerated by a simultaneous rise of plasma density, the value of the main plasma radiation (RAD) equalizes the total heating power.

2. Radiation power profiles

Figure 2 compares the two types of H-mode discharges at two discrete times with regard to their chord-intensity profiles measured with a 19-bolometer array, and Fig. 3 presents the time development of the respective radial profiles of radiation power density ($P_{RAD}(r)$) derived by Abel-inversion method. During each kind of H-mode the radiation profiles evolve towards shapes peaked at the plasma centre. The repetitive burst-like release of plasma energy due to the Edge Localized Modes (ELMs) /3,5/ prevents any long-term increase of radiation power at plasma radii between a/2 and a. In this case, the growth of the central radiation peak is restricted to the inner half-radius and at t = 1.260 s it is reversed into a decay towards an equilibrium profile identical to that at t = 1.215 s. In contrast, during the burst-free H-mode, where the energy outflow into the divertor is permanently suppressed, the radiation power losses grow unimpeded over nearly the whole plasma cross-section until the radiation collapse converts the discharge back into the L-mode. The burst activity and the radiation enhancement thus act mutually exclusively as additional important energy loss mechanisms within the outer plasma half-radius and, depending on the class of H-mode, both quantitatively substitute each other. The main plasma radiation becomes the dominant energy loss channel in the burst-free H-mode. Therefore, the energy flow into the divertor (see e.g. RAD_{DIV} signal in Fig. 1) keeps low and does not restore the previous L-mode level as one would expect for transport-dominated losses after the plasma equilibrium (with improved confinement) is re-established.

It is important to note that the chord-intensity profile of the burst-dominated H-mode which ends up quasi-stationary stays always, even during its transient central peaking, distinctly below the base profile from which the fatal radiation increase of the burst-free H-mode starts at t=1.215s (Fig.2).

3. Radiation and impurity accumulation at the plasma centre

Correlation of the bolometric radiation profiles (Fig. 3) with those from VUV spectroscopy, soft X-ray tomography, temperature and density measurements makes evident that the radiation emission at the plasma centre is completely dominated by line radiation of highly ionized iron /3/ and that the central peaking of the radiation profiles reflects an impurity accumulation taking place irrespective of the type of H-mode. Figure 4 demonstrates that the presence or absence of bursts hardly influences the evolution in time of the local radiation power density at the plasma centre ($P_{RAD}(0)$), particularly the time-constant of the exponential rise after the L-to-H-mode conversion. The absolute magnitude of $P_{RAD}(0)$, however, is at any instant, including the preceding L-phase, about three times higher in the burst-free H-discharges as compared with the burst-dominated one, due to the initial iron contamination. The iron concentration at the plasma centre, displayed in Fig. 5, is derived from $P_{RAD}(0)$ by applying the temperature-dependent radiative power loss function for iron $P_{Fe}(T_e)$ /6/, that includes charge-exchange recombination with beam neutrals ($n_o/n_e = 10^{-5}$).

4. Internal triggering of the burst-free H-mode

Shot # 12218 (Figs. 6 and 7) shows that the burst-dominated H-mode with moderate radiation losses may turn into the burst-deficient H-mode with disastrous consequences. The mode conversion occurs when the accumulation of intrinsic metal impurities during the burst-dominated H-phase raises the bolometric centre-chord intensity up to the threshold value of the burst-deficient H-mode. The first and the last step in the profile evolution depicted in Fig. 7 resemble strikingly their burst-dominated and burst-free counter-parts in Fig. 2, respectively, because the burst frequency in the burst-deficient H-mode seems to be too low to slow down the impurity accumulation. Our interpretation that a sufficient degree of plasma contamination with medium-heavy metals is needed to establish the long-lasting burst-free H-mode agrees with the experimental observation that the burst-free H-mode can be triggered externally by the laser blow-off injection of metals such as chromium and copper /7/.

References:

/1/ Wagner, F., et al., Phys. Rev. Lett. 49 (1982) 1408.
/2/ Müller, E.R., et al., Journ. Nucl. Mat. 121 (1984) 138.
/3/ Keilhacker, M., et al., in Plasma Physics and Contr. Nuclear Fusion Res. (Proc. 10th Int. Conf. London, 1984) Vol.1, IAEA, Vienna (1985) 71.
/4/ Müller, E.R., Behringer, K., Niedermeyer, H., Nucl. Fus. 22 (1982) 1651.
/5/ Wagner, F., et al., Phys. Rev. Lett. 53 (1984) 1453.
/6/ Hulse, R.A., Post D.E., Mikkelsen, D.R., J. Phys. B: Atom. Molec. Phys. 13 (1980) 3895.
/7/ Keilhacker, M., et al., Plasma Phys. and Contr. Fusion, 28, (1986) 29.

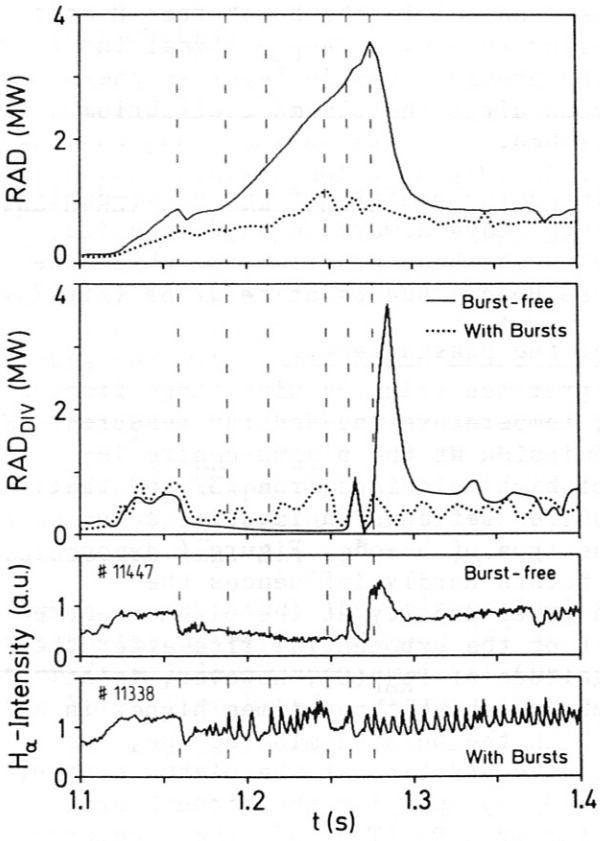

Fig. 1 (left): Time history of the bolometer signals RAD and RAD$_{DIV}$ (electronic integration-time ≈10 ms) for both kinds of H-mode discharges.

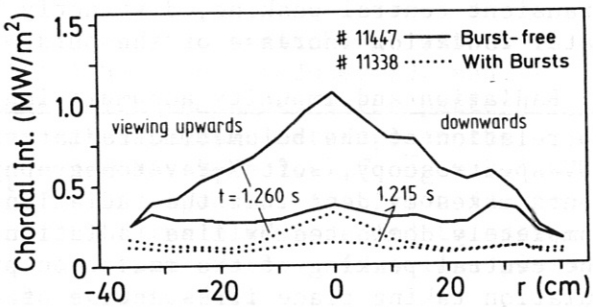

Fig. 2 (above): The bolometric chord-intensity profiles characteristic of either type of H-mode at two discrete times.

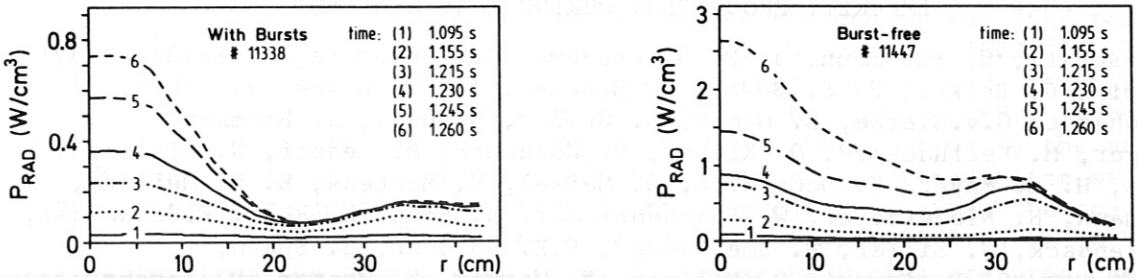

Fig.3: Time evolution of the radial profile of radiation power density during the burst-dominated (left) and the burst-free (right) H-mode discharge (note the different radiation scales).

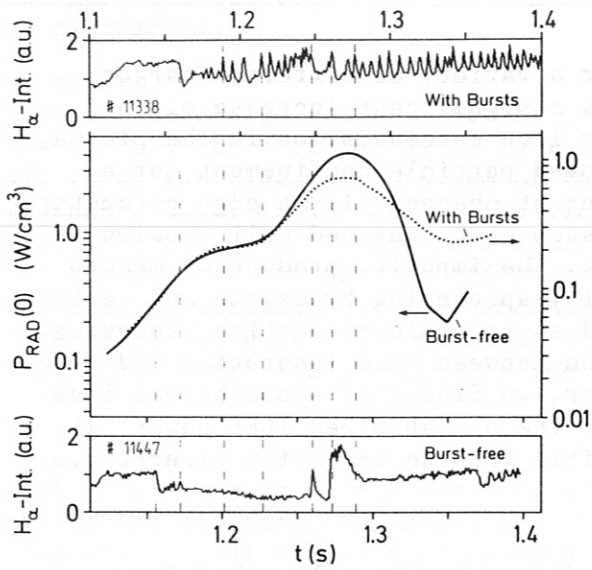

Fig. 4: Dynamic behaviour of the radiation power densities at the plasma centre.

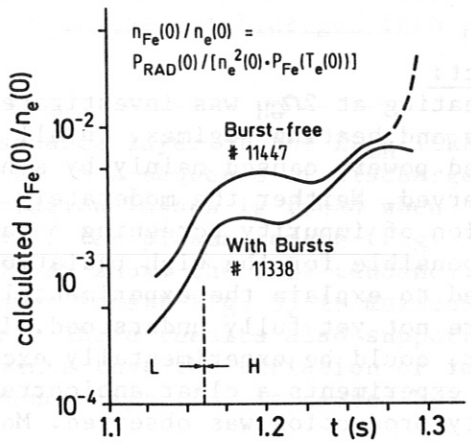

Fig. 5: Variation in time of the calculated iron concentrations at the plasma centre.

Fig. 6 (right): Time development of various plasma parameters during shot #12218 converting from a burst-dominated into a burst-deficient H-mode.

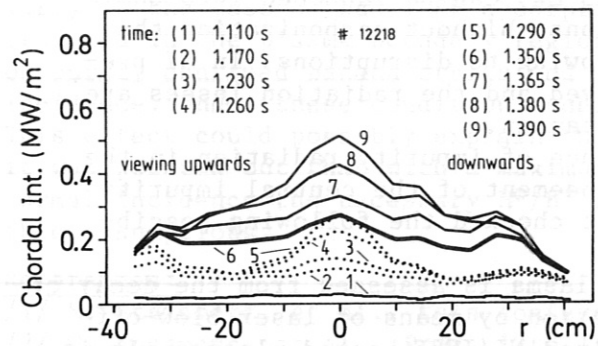

Fig. 7 (above): The evolution of the bolometric chord-intensity profile during shot #12218.

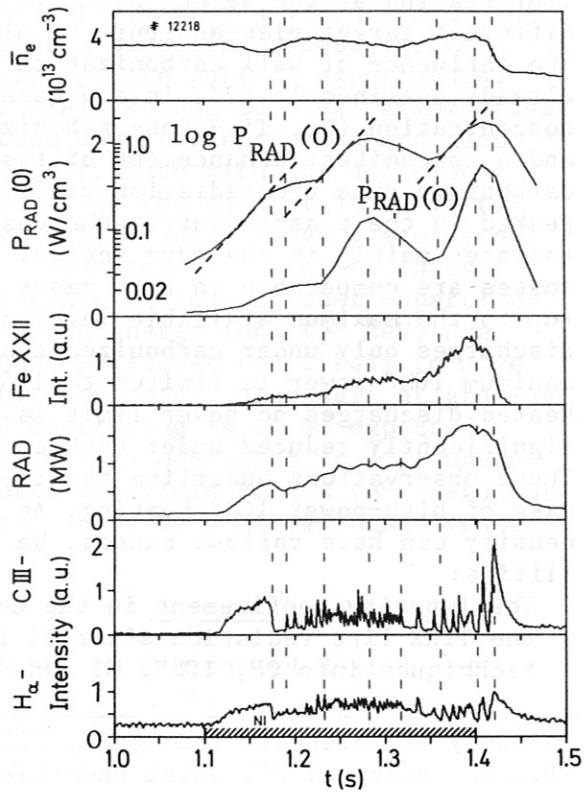

IMPURITY PRODUCTION DURING ICRF HEATING

G. Janeschitz, G. Fussmann, J.-M. Noterdaeme, K. Steinmetz, A. Izvozchikov[1], F. Ryter[2], G. Becker, H. S. Bosch, H. Brocken, A. Eberhagen, O. Gehre, J. Gernhardt, G.v.Gierke, E. Glock, O. Gruber, G. Haas, J. Hofmann, F. Karger, M. Keilhacker[3], O. Klüber, M. Kornherr, M. Lenoci, G. Lisitano, F. Mast, H. M. Mayer, K. McCormick, D. Meisel, V. Mertens, E. R. Müller[3], H. Murmann, H. Niedermeyer, W. Poschenrieder, H. Rapp, H. Röhr, F.Schneider, C. Setzensack, G. Siller, P. Smeulders[3], F.X. Söldner, E. Speth, K.-H. Steuer, S. Ugniewski, O. Vollmer, F. Wagner, F. Wesner, D. Zasche

Max-Planck-Institut für Plasmaphysik
EURATOM Association, D-8046 Garching

Abstract:
ICRF heating at $2\Omega_{CH}$ was investigated for a variety of different target plasmas and heating regimes. In all cases a significant increase of the radiated power, caused mainly by a higher iron concentration in the plasma, is observed. Neither the moderately improved particle confinement nor a reduction of impurity screening on account of changed plasma edge parameters is responsible for the high radiation losses, but enhanced wall erosion is required to explain the experimental data. The impurity production mechanisms are not yet fully understood. Impurity sputtering by oxygen and carbon, however, could be experimentally excluded as possible production processes. In all experiments a clear anticorrelation between wave absorption and impurity production was observed. Moreover, we find that suprathermal ions are produced in the plasma edge region by the non-absorbed ICRF power. It is assumed that these particles are responsible for the excessive impurity production.

General statements and features

ICRF heating at the second harmonic of hydrogen has been launched into different target plasmas (pure H, mixed H/D, and He; OH and NI preheated). The influence of wall carbonization has also been investigated /1/. As already outlined in /2/, in any case a significant increase of the impurity concentration (Fe, Ti - non-carbonized; C, Ti - carbonized) in the plasma and a concomitant enhancement of the radiation losses are found. In the non carbonized case the radiation profiles measured by a bolometer array are peaked in the plasma centre, whereas with carbonized walls the plasma radiates mainly in the edge region. Though the volume-integrated radiation losses are comparable in both cases (45 % of input power), high-power ICRH (up to the maximum available level of 2.5 MW) can be launched into ohmic discharges only under carbonized conditions. Without carbonization the maximum ICRF power is limited to 1.5 MW owing to disruptions. In NI preheated discharges no power limit is oberved and the radiation losses are significantly reduced under both circumstances.
These observations underline the importance of impurity radiation in the case of high-power ICRF heating. An enhancement of the central impurity density can have various causes. We first checked the following possibilities:

- The impurity confinement in the core plasma is assessed from the decay of the TiXX line radiation after Ti injection by means of laser blow-off techniques into OH, ICRF, NI and combined NI/ICRF-heated plasmas. It is

[1]Academy of Sciences, Leningrad, USSR; [2]CEN Grenoble, France;
[3]Present address: JET Joint Undertaking, England;

reduced by factors of 2 and 4, respectively, at the end of the ICRH period. In this case the H_α divertor intensity does not change when ICRH (200 kW) is applied, indicating a power flow into the divertor during ICRH comparable to the OH phase. A similar type of discharge heated by 500 kW ICRF is presented in Fig. 2. In this case we stop hydrogen blowing 200 ms prior to the end of the ICRF pulse. As is clearly demonstrated in Fig. 2, all radiation signals (FeXVI, bolometer, soft X-ray) start to rise immediately after the end of H_2 puffing. A similar increase is found in the H^o CX-particle flux at 10 keV originating from the plasma edge (Fig. 2). These particles are produced by the wave and can be assumed to be representative of the behaviour of the non-confined high energy ions.
It is important to note that in contrast to the above-described relations no changes were observed when puffing deuterium instead of hydrogen into pure He discharges.

B_T-scans

In order to change the position of the resonance layer of the $2\Omega_{CH}$ ICRF in the plasma, the toroidal field B_T was varied in a sequence of discharges. In all these experiments a minimum of the radiation losses is found when the resonance layer is located in the vicinity of the plasma centre (Fig. 3). Furthermore, the H^o CX particle flux at 17 keV shows the same tendency. On the other hand, the heating efficiency (lower insert Fig. 3) is maximum for the optimum position of the resonance layer. These results also support the interpretation deduced from the He experiments that the variation of impurity density with the position of the resonance layer /3/ is caused by changes of the wave absorption.

Conclusions

ICRF heating in He discharges revealed a clear anticorrelation between wave absorption and impurity production. Consistently with these observations, we find strong indications that changes of the impurity density as a function of the resonance layer position can also be explained by a variation of the absorption conditions. Impurity sputtering as a possible process for enhanced wall erosion could be excluded by appropriate puffing experiments. Spectroscopic Fe-flux measurements did not yield strong poloidal asymmetries in the accessible range at the top and bottom divertor entrances and inner wall region. The observed Fe fluxes roughly correlate with the additional power input but no excessive increase is found in the case of ICRH. Therefore, it must be assumed that the excessive wall erosion takes place either at a closer distance to the antennae or at the outer wall regions which could not be observed. From CX-flux measurements we learned that - particularly in the case of bad ICRH absorption - high-energy ions ($\gtrsim$5 keV) are produced in the plasma boundary region. These particles are likely to move on purely confined banana orbits and may hit the outer torus wall at grazing incidence. Under these conditions enhanced sputtering is to be expected. This effect could possibly explain the discrepancy mentioned in /2/, where it was pointed out that with a maximum sputtering yield of 1 % (H^o - Fe) for normal incidence the necessary H^o/H^+ fluxes cannot be achieved under reasonable assumptions.

References:

/1/ K. Steinmetz, et al., this conference.
/2/ G. Fussmann, et al., Proc. 12th Int. Conf. on Controlled Fusion and Plasma Physics, Budapest (1985), Part I, A P Th 002.
/3/ K. Steinmetz, et al., Plasma Physics and Controlled Fusion, Vol. 28, No. 1A, pp. 235-238, 1986.

found that the corresponding impurity confinement times (τ_I in the case of OH: 49 ms, NI: 19 ms, ICRH: 32 ms, NI + ICRH: 33 ms) are increased by a factor of ~1.5 when ICRH is added ($P_{NI} = P_{ICRH} = 0.8$ MW). This marginal improvement of central confinement cannot explain on its own the enhancement of the radiation losses.

- Larger changes of the plasma edge parameters, which could result in a deterioration of the screening efficiency could not be substantiated by edge diagnostics.

Consequently, enhanced wall erosion is required to explain our findings. The first hypothesis on impurity production mentioned in /3/ assumed that vertically drifting ions are accelerated in the resonance layer and release impurities at structural elements in the vicinity of the upper stagnation point. This hypothesis, however, had to be discarded on the basis of more extended investigations including spectroscopic Fe-flux measurements described below. In the following we present new experimental results with respect to the impurity production mechanisms.

Fe flux measurements

A double mirror system, specially developed for poloidal scanning, was used to measure spectroscopically the Fe fluxes originating in the vicinity of the upper and lower stagnation points, as well as from the inner wall (Fig. 1). The spectrometer used was a 1.5 m Cerny-Turner visible monochromator equipped with an OMA diode-array camera providing a high resolution (1000 channels, $\lambda/\Delta\lambda = 6000$). The evaluation of the spectra is rendered difficult by blending of the weak FeI lines with strong light impurity lines. For evaluation we used the 3719.9 Å and the 3734.9 Å FeI resonance lines. The system allows measurements during NI and combined NI + ICRF heating phases, but fails because of intensity problems during the OH phase. As seen from Fig. 1, no drastic increase of the FeI fluxes with the onset of ICRH occurs in contrast to the strong enhancement of the Fe concentration in the core plasma. Furthermore, in striking contradiction to the hypothesis mentioned in /3/ no up-down asymmetry in the fluxes is found (Fig. 1).

Sputtering by impurities

The possibility of sputtering by highly ionized light impurity ions, such as O^{+8} and C^{+6}, which compared with H^+ and D^+ have a much higher sputtering yield (~20 % instead of ~1 % for H^+), was checked by puffing oxygen and methane during the ICRH pulse. According to CX recombination/line intensity measurements of CVI and OVIII the concentrations of these light impurities were increased by a factor of 1.5. No change, however, of the Fe density (deduced from the FeXVI intensity) in the plasma could be seen. Self-sputtering of iron as a dominating mechanism can also be excluded, since under these circumstances the Fe signals should increase exponentially during the ICRF pulse, whereas generally a stationary behaviour is seen.

$2\Omega_{CH}$-heating in pure He plasmas

ICRH at $2\Omega_{CH}$ was applied to a pure helium plasma ($n_H^+/n_{He}^{++} \lesssim 3$ %). In this case no heating could be established and a low power limit at 200 kW exists. The FeXVI line intensity, the total radiation losses and the eletron density rise steadily during the whole ICRF pulse. In accordance with this behaviour we observe a reduction of the H_α divertor radiation, which is representative of the power flow into the divertor. Puffing hydrogen during the ICRF pulse, in order to increase the H^+ concentration to $n_H^+/n_{He}^{++} \sim 10$ %, results in a moderate heating of the plasma and the power limit is shifted up to 500 kW. The radiation losses and the FeXVI line intensity become stationary and are

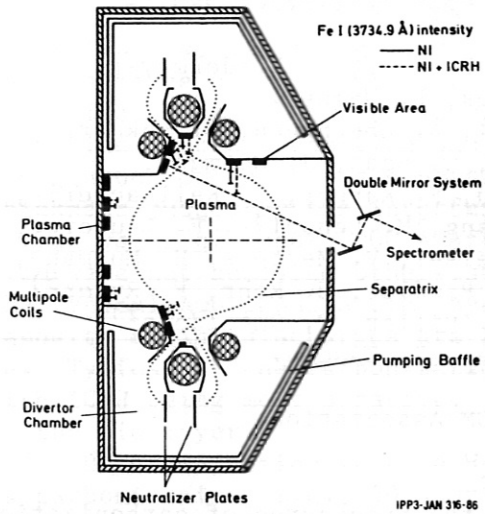

Fig. 1: Spectroscopic arrangement for Fe-flux measurements. The Fe I fluxes measured are proportional to the lengths of the bars perpendicular to the indicated areas.

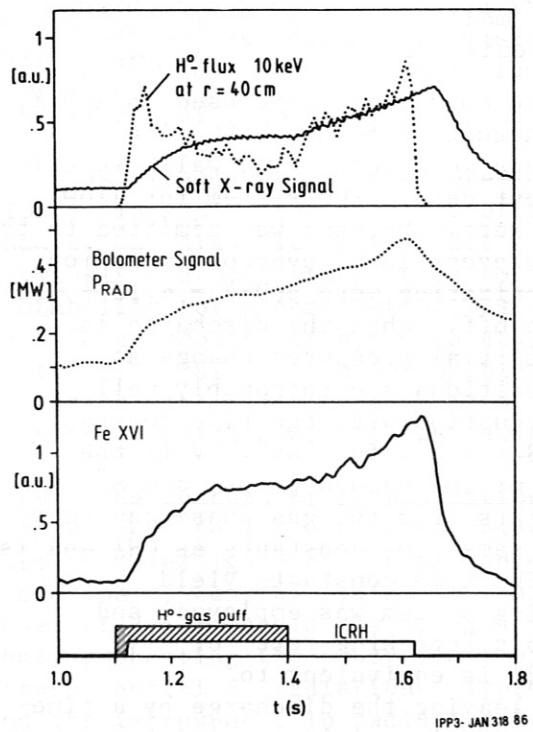

Fig. 2: Fe XVI line intensity, bolometer signal, soft X-ray signal, and the 10 keV H^0-CX flux, demonstrating the anticorrelation of impurity production and hydrogen concentration in a He discharge during ICRF heating (2 Ω_{CH}).

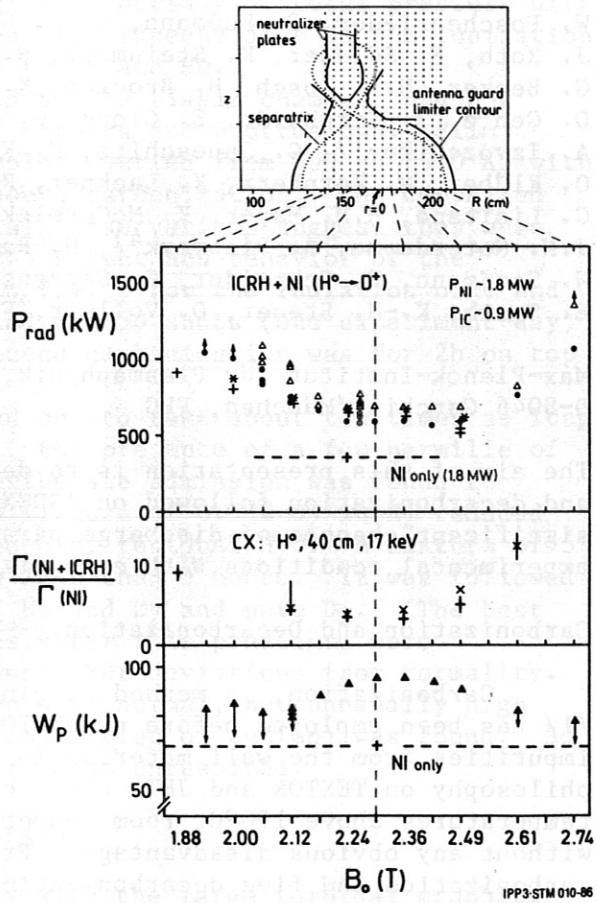

Fig. 3: Various plasma parameters during ICRH: total radiation losses (bolometer), relative fluxes of fast protons at the plasma edge and plasma energy content as a function of the position of the resonance layer (B_T-scan). Arrows in the W_p-plot indicate the increment of W_p due to increased ohmic input.

Wall Carbonization in ASDEX: A Collation of Characteristic Results

W. Poschenrieder, G. Fußmann, G. v. Gierke, F. Mast, H. Niedermeyer, J. Roth, F. Söldner, K. Steinmetz, H. Verbeek, F. Wagner. G. Becker, H.S. Bosch, H. Brocken, K. Büchel, A. Eberhagen, D. Eckhartt, O. Gehre, J. Gernhardt, E. Glock, O. Gruber, G. Haas, J. Hofmann, A. Izvozchikov[1)], G. Janeschitz, M. Kaufmann, F. Karger, M. Keilhacker[2)], O. Klüber, M. Kornherr, K. Lackner, R.,S. Lang, M. Lenoci[3)], F. Leuterer, G. Lisitano, H.M. Mayer, K. McCormick, D. Meisel, V. Mertens, H. Murmann, J.N. Noterdaeme, A. Pietrzyk[4)], H. Rapp, H. Riedler, H. Röhr, F. Ryter[5)], W. Sandmann, F. Schneider, C. Setzensack, G. Siller, P. Smeulders[2)], E. Speth, K.-H. Steuer, O. Vollmer, F. Wesner, D. Zasche.

Max-Planck-Institut für Plasmaphysik, EURATOM-Association
D-8046 Garching/München, FRG

The aim of this presentation is to describe the procedures of carbonization and decarbonization followed on ASDEX, and to summarize the most significant changes of discharge parameters observed under the various experimental conditions with carbonized walls.

Carbonization and Decarbonization.

Carbonization, a method originally proposed by the Jülich IPP Group /1/ has been employed before on TEXTOR /2/ and JET /3/ to reduce high Z impurities from the wall material in discharges. In contrast to the philosophy on TEXTOR and JET, where carbonization was executed with wall temperatures above 150°C, room temperature conditions were used on ASDEX, without any obvious disadvantage. From August 85 to March 86 nine carbonization and five decarbonization runs were done. The walls were in carbonized condition on thirteen experiment days. The system for glow discharge cleaning /4/ was also employed here. Methane was admitted to the D_2 or H_2 discharge via the divertors to prevent local overconcentration. Typical discharge parameters during carbonization were $p(D_2) = 4.10^{-1}$ Pa and $p(CH_4) = 9.10^{-2}$ Pa with the discharge off. When the discharge is switched on (U = 400 V, I = 2.0 A) the partial pressures change as depicted in Fig. 1. The exponential transitions are reasonably well described by a first-order differential equation with the time constant given by $\tau^* = V/S$ for "off" and $\tau^* = V/(S_V + S^*)$ for "on". V is the vessel volume (26 m^3), S_V is the speed of the vacuum pumps, and S^* represents the speed by which CH_4 disappears from the gas phase caused by the discharge. H_2 shows practically the same time constants as CH_4 and is obviously produced by cracking of CH_4. The time constants yield S_V = 2600 1/s (only 1/4 of the full pumping system was employed) and S^* = 1500 1/s. The latter corresponds to a "cracking rate" of $3.5\ 10^{19}$ molec./s, while the current of 2A is equivalent to $1.2 \cdot 10^{19}$ ions/s. An analysis of the ions leaving the discharge by a time-of-flight analysis indicates that the current is mainly carried by hydrocarbon ions. Consistent with this is the observed deposition rate based on the table of interference colors as given by the Jülich group /5/. Obviously, CH_4 is more cracked than is directly deposited. The radicals

---

[1]Academy of Sciences, Lenigrad, USSR; [2]Assigned to JET Joint Undertaking, England; [3]ENEA Frascati, Italy; [4]University of Washington, Seattle, USA; [5]CEN Grenoble, France.

formed in the gas phase do not lead to carbonization on contact with the wall but seem to react to C_mH_n as indicated by the mass spectrum. A detailed particle balance was not attempted, but summing up the partial pressures of fig. 1 yields a slight increase of total pressure with the discharge on. It also explains the simultaneous drop in the ionization gauge indication since CH_4 is replaced by H_2 and HD.

The carbon deposition was limited to the plasma chamber, and not homogeneous owing to its geometry with corners and protrusions. Film thickness judged by the interference colors varied from 500 to 1500 Å, with a mean value of about 1000 Å after 6 hours carbonization. The deposited film were not analyzed otherwise, but all observations suggest they were the typical amorphous a-C:H layers /1/. Effect and behavior of the deposits during discharges are shown in fig. 2 for the radiation of C and Fe. Typically, one carbonization lasted for 50 shots (one experiment-day) with ICRH being most abrasive. The second carbonization was for 2h on top of the old layer.

Decarbonization in pure H_2 turned out to take about ten times as long as carbonization, i.e., 60 hours. But, the presence of a few permille of oxygen from residual H_2O, a leak or deliberate admission was found to considerably speed up the cleaning. A mixture of 0.5 % O_2 in H_2 reduced the time to 12 h, but lead to an increase of residual H_2O. A mixture of 5 to 10% O_2 in He cleaned the machine in less than 3 hours. It was followed by a deoxidation phase in a mixture of He and D_2 and pure D_2. (The best deoxidant is CH_4.) However, discharges after this procedure were characterized by poor density limits and other deviations from normality. Still, global radiation and O radiation were normal, but unusually high radiation of fluor (probably from decomposition of teflon) was found. So far, the actual origin of the problem remains unresolved.

The effects of carbonization on discharges

As already experienced previously with the large toroidal graphite limiter in ASDEX, the presence of large amounts of carbon in the plasma chamber can significantly affect the recycling behavior of hydrogen. Obviously, hydrogen atoms stick to the carbon surface without a high probability for recombination, as compared to steel at room temperature, thus large amounts of hydrogen stay in the vessel between shots. But, in contrast to JET, only minor problems with density control at very low densities were experienced. This is certainly due to the fact that the divertors, which dominate the recycling flux, remained uncarbonized.

ICRH: The success of carbonization reported from TEXTOR /2/, especially with respect to ion cyclotron resonance heating, was a strong motivation also to investigate carbonization on ASDEX. Indeed, concomitant with a reduction of central radiation from Fe by a factor of ten, the total ICRH power of 2.4 MW could now be launched. Without carbonization and only ohmic preheating the power limit was 1.1 MW due to disruptions caused by strong central Fe radiation. Typical values of P_{rad}/P_{tot} = 20 % were found and the improvement in radiation losses is also evident from Fig. 3 showing the fractional radiation increase per ICRH power coupled into the plasma for various wall conditions. Also, the degradation in τ_E during 1 MW of ICRH was only down to 70 % of the ohmic value, instead of 60 % for uncarbonized walls. A comparison of radiation profiles shows slightly increased boundary radiation for the carbonized case being mostly due to C radiation.

OH+NI: In the ohmic phase preceeding neutral injection, spectroscopic data show a 2.5-fold increase in C-radiation with carbonization, a slight decrease in O-radiation and a reduction of Fe-radiation by a factor of ten, still, the global radiation is little affected. Increased τ_E in the saturation regime ($n_e > 3\ 10^{19}\ m^{-3}$) as depicted in figure 4 indicates a reduced share of central radiation. This is fully corroborated by the radiation profiles showing the shift of major radiation to the boundary. Also for NI the degradation of energy confinement in the L-regime was less severe (figure 4), and the power limits for obtaining the H-regime in D_2-discharges were hardly influenced by carbonization. However, the H-regime was not of the same quality showing a higher and more stochastic ELM frequency. The difference is particularly obvious in the values of the poloidal beta, which reached only values of 55 % of the critical value instead of 70 % before carbonization. This behaviour might be associated with the increase in global radiation which is essentially due to high boundary radiation of C under carbonization.

LH: Also lower hybrid heating has profited from carbonization extending the working range to $5\ 10^{19}\ m^{-3}$. Radiation showed now a much smaller increase with $\bar{n}_e$ and LH-Power. Previously, the strong influence of Fe, caused by generated fast ions at higher density ($\bar{n}_e > 2\ 10^{19}\ m^{-3}$), had led to disruptions at $\bar{n}_e = 3.5 \times 10^{19}\ m^{-3}$. Problems with density control below $1.2\ 10^{19}\ m^{-3}$ limited the operation regime for experiments with current drive.

Pellet injection: Extremely high central densities of $2.2\ 10^{20}\ m^{-3}$ could now be reached as the reduced Fe-influx eliminated the thermal collapse observed without carbonization. The regime, thus attained, showed unusually long energy and particle confinement. The Murakami-parameter $\bar{n}\ R/B_T$ for $q = 2.7$ increased from $6\ 10^{19}\ m^{-2}\ T^{-1}$ (without carbonization) to $8.5\ 10^{19}\ m^{-2}\ T^{-1}$.

In conclusion, we see ICRH as the main beneficiary of carbonization but the reduced influx of heavy wall impurities extended the operational range quite generally. Only in the quality of the H-regime are negative effects of the increased boundary radiation seen. Carbonization can be regarded as a rather simple and efficient tool to change wall conditions and study plasma wall interaction. Though divertor discharges are less susceptible to impurities the results on ASDEX confirm those of TEXTOR and JET, all of which show that, for the time being, carbon is the best wall material.

References

/1/ Winter, Waelbroeck, Wienhold, Esser, Könen, Banno, Rota and Clausing, Journal of Nuclear Materials 122/123 (1984) 1187.
/2/ Schlüter, Graffmann, Könen, Waelbroeck, G. Waidmann, J. Winter and TEXTOR-Team, Proceed. 12th Europ. Conf. Controlled Fusion and Plasma Physics, Budapest (1985).
/3/ Bickerton et al. JET Report JET-P(85) 15.
/4/ Poschenrieder, Staudenmaier and Staib, Journal of Nuclear Materials 93/94 (1980) 322.
/5/ Winter, Wienhold, Besocke, Littmark, Esser, Banno, Waelbroeck, Kaleck and Tschersich, to be published.

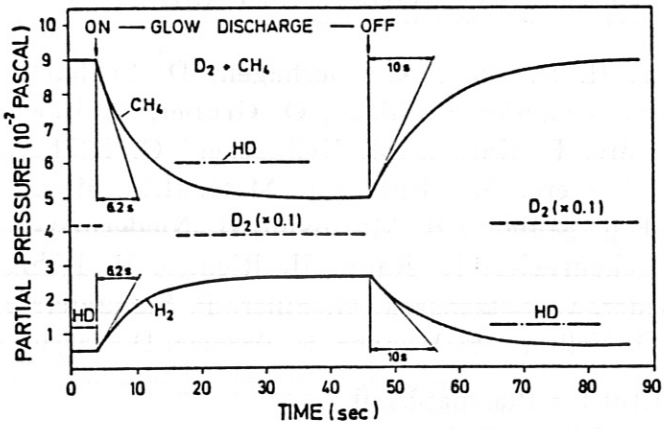

Fig.2: Variation of partial pressures of a D_2 + CH_4 mixture under stationary flow conditions, when the discharge is switched on.

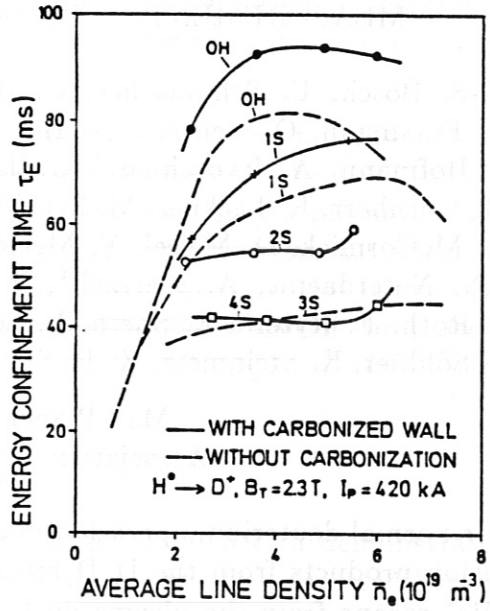

Fig. 4: Improvement of energy confinement with carbonization for OH- and NI-discharges (S: number of sources).

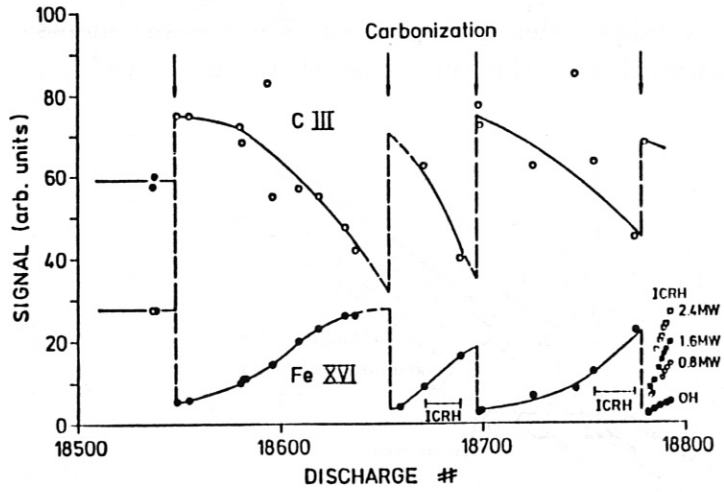

Fig.2: Effect of discharges on the carbon deposit, shown for Fe- and C-radiation. Points represent ohmic standard discharges where not indicated otherwise.

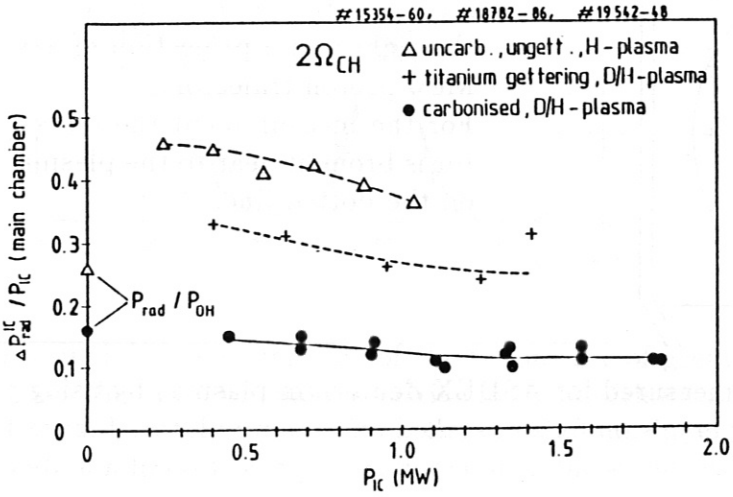

Fig. 3: Reduction of radiation increase during ICRH with carbonization.

MEASUREMENTS OF CHARGED FUSION PRODUCTS IN ASDEX

H.-S. Bosch, U. Schumacher, G. Becker, H. Brocken, A. Eberhagen, D. Eckhartt, G. Fussmann, O. Gehre, J. Gernhardt, G. v.Gierke, E. Glock, O. Gruber, G. Haas, J. Hofmann, A. Izvozchikov[1] G. Janeschitz, F. Karger, M. Keilhacker[2] O. Klüber, M. Kornherr, K. Lackner, M. Lenoci[3], F. Leuterer, G. Lisitano, F. Mast, H.M. Mayer, K. McCormick, D. Meisel, V. Mertens, E.R. Müller[2], H. Murmann, H. Niedermayer, J.N. Noterdaeme, A. Pietrzyk[4], W. Poschenrieder, H. Rapp, H. Riedler, H. Röhr, J. Roth, F. Ryter[5], E. Speth, F. Schneider, C. Setzensack, G. Siller, P. Smeulders[2], F. Söldner, K. Steinmetz, K.-H. Steuer, O. Vollmer, F. Wagner, F. Wesner, D. Zasche

Max-Planck-Institut für Plasmaphysik
Association Euratom-IPP, D-8046 Garching

For normal deuterium operation in ASDEX (A = 4.1, I_p = 250 - 400 kA) the charged fusion products from the D–D reactions (3 MeV proton, 1 MeV triton and 0.8 MeV ^{3}He) escape from the plasma on helical orbits to the upper part of the vessel. Since slowing–down can be neglected in ASDEX, the protons and tritons escape on identical orbits, because the trajectory depends only on the product $m \cdot \vec{v}$. The measurements of the charged fusion products give information on the ion temperature, fusion yield, and plasma behaviour [**1**,2].

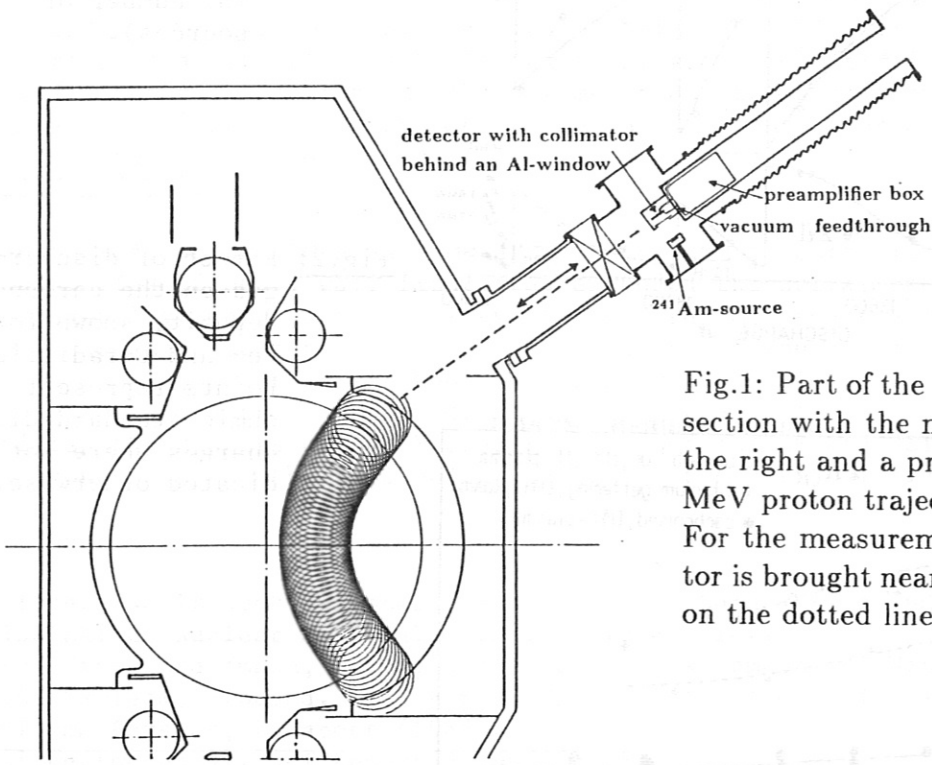

Fig.1: Part of the ASDEX cross–section with the manipulator on the right and a projection of a 3 MeV proton trajectory.
For the measurement the detector is brought near to the plasma on the dotted line.

The charged fusion products were measured for ASDEX deuterium plasmas by using a surface barrier detector or nuclear emulsion foils, installed on a manipulator. Figure 1 shows the ASDEX cross–section with the movable detector and a projection of a 3 MeV

[1] Academy of Sciences, Leningrad, USSR, [2] assigned to JET Joint Undertaking, [3] ENEA Frascati, Italy, [4] University of Washington, Seattle, USA, [5] CEN Grenoble, France

proton trajectory. For measurements with the surface barrier detector it is necessary to have sufficient electrical shielding and to keep the distance between the detector and the preamplifier short.

With the surface barrier detector , it is possible to measure the flux and the energy spectrum of the 3 MeV protons, and that of the 1 MeV tritons, either. The electric and magnetic distortions of the spectrum (about 50 keV) are monitored by a pulser signal, that is additionally fed into the preamplifier. By fitting the spectra with a Gaussian profile, we get a spectral width, that can be corrected with respect to the straggling in the Al foil and the noise broadening, which is measured by the width of the pulser peak. This corrected width, for the protons as well as for the tritons, is related to the ion temperature by the equation

$$\Delta E\ (FWHM) = 91.6 \cdot \sqrt{T_i},\quad \Delta E, T_i\ in\ keV.$$

Figure 2 gives examples of a proton and a triton spectrum. The spectra demonstrate that both widths (not yet corrected for the straggling) are about the same, and hence they yield the same ion temperature. The time dependence of the temperature, evaluated from the proton spectra for a neutral-beam (H^0)-heated discharge in deuterium, is given in Fig. 3 in comparison with the temperature deduced from the neutron flux.

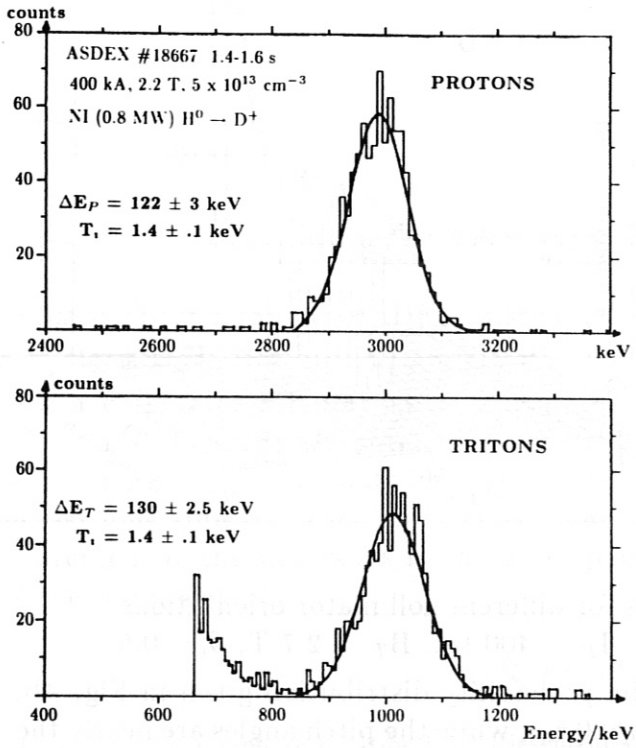

Fig.2: Spectra of protons and tritons

Fig.3: T_i from proton spectra and neutron flux

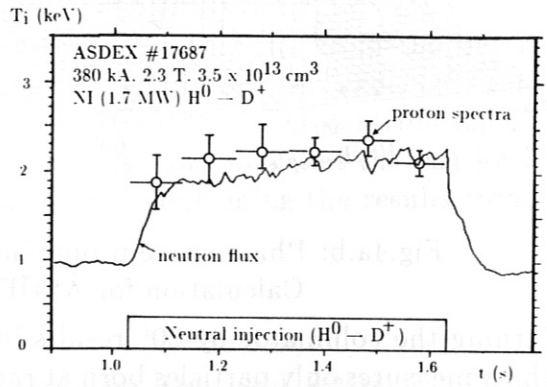

In principle, measurements of the tritons are of great interest, since their lower energy makes the spectrum more sensitive to the reaction conditions than the proton spectrum. However, the observation of the tritons is only possible in discharges with a low level of X-rays because these cause a background at the low energies that may cover the triton spectrum. Moreover, the surface barrier detector application is limited by the saturation of the preamplifier in discharges with high background levels.

Because of the influence of the strong magnetic fields in a tokamak the measurements of charged fusion products have to be supported by detailed particle trajectory calculations. They describe the phase space transformation of the charged fusion particles from the plasma to the detector. For measurements of the particle fluxes it is necessary to calculate the efficiency of the collimated detector [**3**], and for the spectra it is important to know which particles (characterized by birth radius and pitch angle) can reach the detector. To get this information about the phase space of the observed charged fusion particles, we calculate their trajectories in the opposite direction, i.e. from the detector into the plasma. For each point of the orbit the distance from the plasma centre and the pitch angle are calculated and then the point is stored in a matrix of these phase space coordinates. This is done for different directions through the collimator, weighted with the collimator transparency. Doing this, one gets a phase space probability for the measurement of charged fusion products that depends on the charge and energy of the particle, on the magnetic fields in the plasma, and on the orientation of the collimator. An example of such a probability calculation is given in fig. 4a, and it is obvious, that in this case the detector measures particles from the whole plasma volume, mainly starting perpendicularly to the plasma axis. In this case (pitch angle of about 90°) the influence of the poloidal field is very small, and so the details of the current distribution are of no importance. Measurements of the ion temperature are done with this collimator orientation.

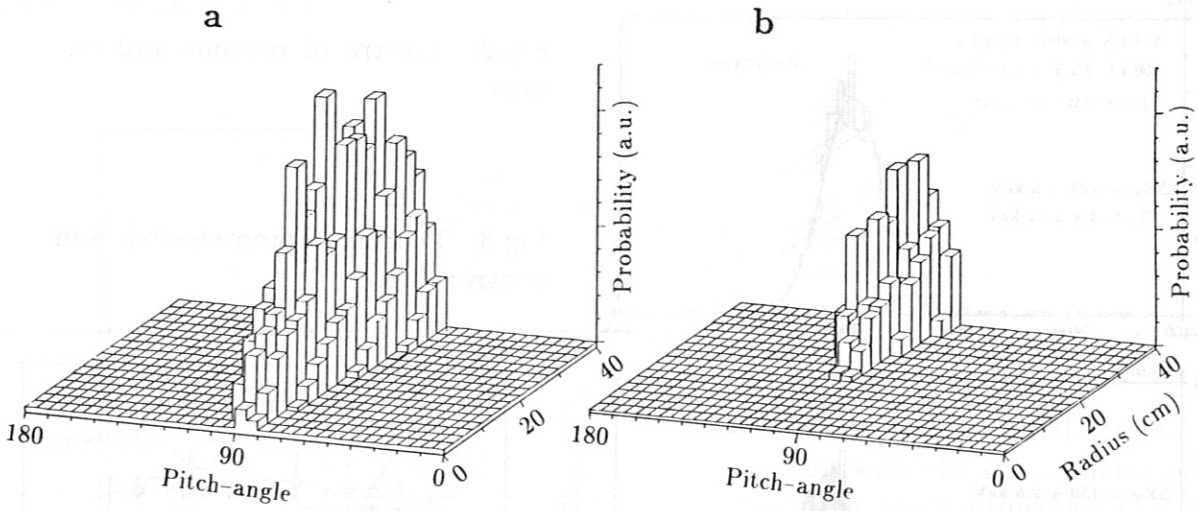

Fig.4a,b: Phase space probabilities for different collimator orientations
Calculation for ASDEX, I_P = 400 kA, B_T = 2.7 T, β_p= 0.5

Turning the collimator by 20° results in the probability distribution given in Fig. 4b, which measures only particles born at radii ≥20 cm, while the pitch angles are nearly the same as in Fig. 4a. This dependence of the phase space distribution on the collimator orientation can be used to deduce the fusion emission profile from the flux measurements at different orientations.

This procedure can be applied to look for the fast deuterium ions created by LH waves in ASDEX at densities above about 2.8 x 10^{13} cm^{-3} [**4**]. Figure 5a gives an example of a typical spectrum from such a discharge at a collimator orientation as in Figure 4a. The spectrum of the protons and that of the tritons show a superposition of a

on the expected thermal peak. These central peaks (ΔE about 100 keV) correspond to the Maxwellian plasma bulk with an ion temperature of about 700 eV. The wider parts of the spectra (about 600 keV wide) are produced by the fast ions generated by the LH waves. The velocity of these deuterium ions is mainly directed in the poloidal plane and their energy is in the range of 25 keV. Since the fusion reactivity at these energies is about 5 orders of magnitude higher than at 700 eV the number of these fast ions must be correspondingly smaller.

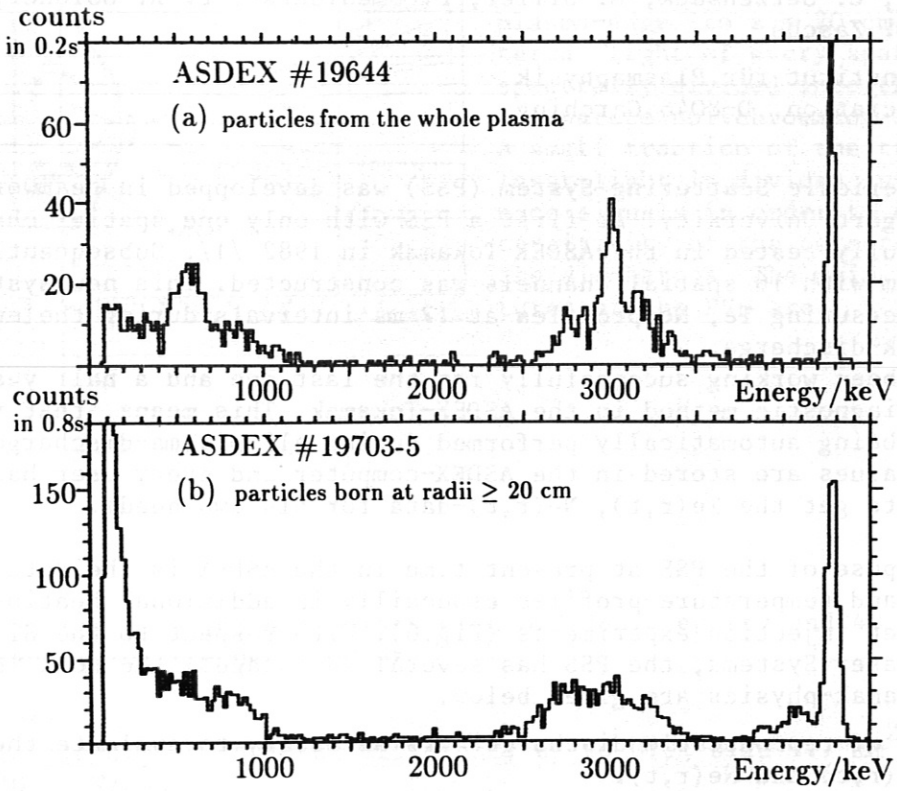

Fig.5a,b: Spectra for two ASDEX-discharges with different collimator orientations. I_P = 400 kA, B_t = 2.7 T, n_e = 3.9 x 10^{13} cm^{-3}. LH (1.3 GHz) P_{RF} = 900 kW

With a collimator orientation as in Figure 4b (where only particles from the outer regions are detected) we obtain the spectrum given in Figure 5b. As expected, the spectra generated by the bulk ions are not detected any more. Since the contribution of the fast ions appears nearly unchanged, however, one must conclude that the fast ions are created by the LH waves in the outer plasma regions, confirming the results from CX measurements [5].

REFERENCES

1. Nagle D.E., Quinn W.E., Ribe F.L., Riesenfeld W.B., Phys.Rev. **119** (1960), 857-862.
2. Strachan J.D., in "Diagnostics for Fusion Reactor Conditions", EUR 8351-I-EN, Varenna, 1982, pp. 383-400.
3. Heidbrink W.W., Strachan J.D., Rev. Sci. Instr. **56** (1985), 501-518.
4. Eckhartt D., et al., 4th Int. Symp. Heating in toroidal Plasmas, Rome 1984 **I**, 501-512.
5. Ryter F., in "RF-Applications to Tokamaks", EUR 10333-EN, Varenna, 1985, pp. 746-751.

PERIODIC THOMSON SCATTERING DIAGNOSTIC WITH 16 SPATIAL CHANNELS ON ASDEX

D. Meisel, H. Murmann, H. Röhr, K.-H. Steuer, G. Becker, H.S. Bosch, H. Brocken, A. Eberhagen, G. Fussmann, O. Gehre, J. Gernhardt, G. v. Gierke, E. Glock, O. Gruber, G. Haas, J. Hofmann, A. Izvozchikov[1], G. Janeschitz, F. Karger, M. Keilhacker[2], O. Klüber, M. Kornherr, K. Lackner, M. Lenoci, G. Lisitano, F. Mast, H. M. Mayer, K. McCormick, V. Mertens, E. R. Müller[2], H. Niedermeyer, A. Pietrzyk[3], W. Poschenrieder, H.Rapp, J. Roth, F. Ryter[4], F. Schneider, C. Setzensack, G. Siller, P. Smeulders[2], F. X. Söldner, F. Wagner, D. Zasche

Max-Planck-Institut für Plasmaphysik
EURATOM Association, D-8046 Garching

The Nd-YAG Periodic Scattering System (PSS) was developped in teamwork with IPF of Stuttgart-University. At first a PSS with only one spatial channel was successfully tested in the ASDEX-Tokamak in 1982 /1/. Subsequently an upgraded system with 16 spatial channels was constructed. This new system is capable of measuring Te, Ne-profiles at 17 ms intervals during the entire ASDEX-Tokamak-discharge.
The PSS has been working successfully for the last one and a half years as a standard diagnostic method in the ASDEX-Tokamak. This means, that the measurement is being automatically performed during all plasma-discharges. The Te- and Ne-values are stored in the ASDEX-computer and every user has the possibility to get the Te(r,t), Ne(r,t)-data for his own needs.

The main purpose of the PSS at present time in the ASDEX is the determination of density- and temperature-profiles especailly in additional heating (Fig.3, 4,5) or pellet injection-experiments (Fig.6). With respect to the Single-Pulse-Ruby-Laser-Systems, the PSS has several advantages, the most important ones for Tokamak-physics are given below:

1. No series of reproducable discharges are necessary to evaluate the behavior of Te(r,t) and Ne(r,t).
2. The combination of Nd-YAG-Laser with detectors of high quantum-efficiency together with an optics of high luminosity, leads to a scattering device, where the photon-noise of the signals is sufficiently small at normal Tokamak-densities. The additional plasma-light-noise is also smaller than in Ruby-scattering devices, because plasma light is decreasing from the visible to the IR-region.
3. The large number of scattering and background signals can be used to make a calculation of the error-bars of the measurements. The PSS can reach an accuracy of about 5 % in Te- and 3 % in Ne-measurements in the normal Tokamak-regime.
4. The detectors (Si-Avalanche-Diodes) give an extremely linear response. Thus the PSS can work in a wide range without saturation effects, e.g. at high densities or high levels of plasma light. Magnetic fields do not influence the sensitivity of the diodes.

In some special discharges, the QSS is the only diagnostic method available for the reliable evaluation of Te, Ne-profiles, e.g. in the slide-away-region (Fig. 5) or during rapid density variations.

---

[1]Academy of Sciences, Leningrad, USSR; [2]Present address: JET Joint Undertaking, England; [3]Univ. of Washington, Seattle, USA; [4]CEN Grenoble, France

MAIN FEATURES OF THE PERIODIC THOMSON SCATTERING SYSTEM (PSS) ON ASDEX

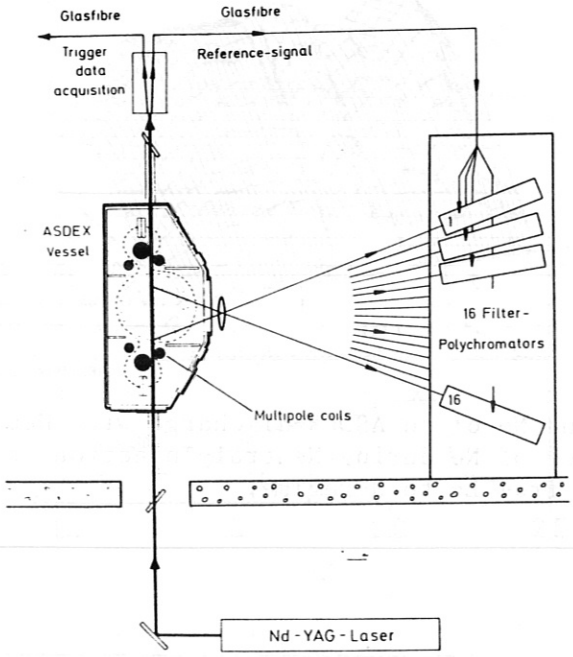

Fig. 1: Schematic of the optical set-up of the QSS.

The PSS simultaneously measures Te,Ne at 16 spatial points distributed over 3/4 of the diameter of the plasma-column (from z = -40 cm at the lower plasma-edge to z = 20 cm). The scattered light of every spatial point is spectrally divided into three parts by a separate polychromator (see Fig. 2). A small fraction of the transmitted laser-light is divided into 48 reference signals in order to calibrate the sensitivity of the detectors during the discharges. The main technical features of the PSS are:

Laser:
Nd-YAG at λ = 1.06 μm; 400 pulses with 0.8 Joule energy and 40 ns duration each. Repetition frequency 60 Hz.

Detectors:
Si-Avalanche-diodes; quantum efficiency up to 0.9; size 1.7 mm^2; NEP 1.6 x 10^{-13} $W/\sqrt{Hz}$.

Range of Te- and Ne-measurements of the ASDEX-PSS:
The PSS is capable of measuring kTe in the range of 150 eV (at the plasma-edge) up to 5 keV (in the plasma-centre) using two matched types of filter polychromators. The lower density-limit is a few x 10^{12} cm^{-3}. This limit can be further improved by averaging signals with respect to time.

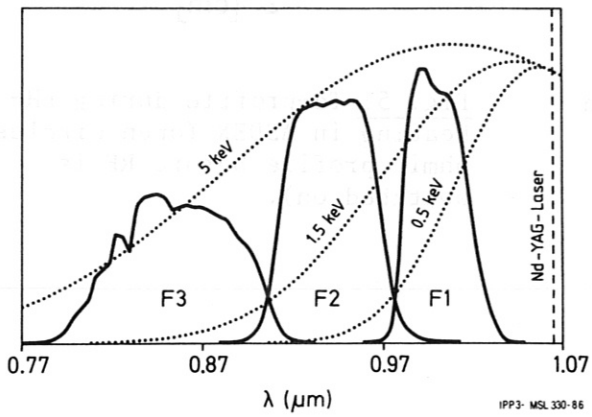

Fig. 2: Spectral sensitivity of the filter-polychromator for the central plasma region. The ratio of the signals F2/F1 is the basis for the calculation of kTe up to 1.5 keV; at higher Te, the ratio F3/(F1 + F2) is used. The system is density-calibrated by Anti-Stokes Raman-scattering in hydrogen /2/.

EVALUATION OF TE(r,t) AND NE(r,t) BY PSS DURING ADDITIONAL HEATING IN ASDEX

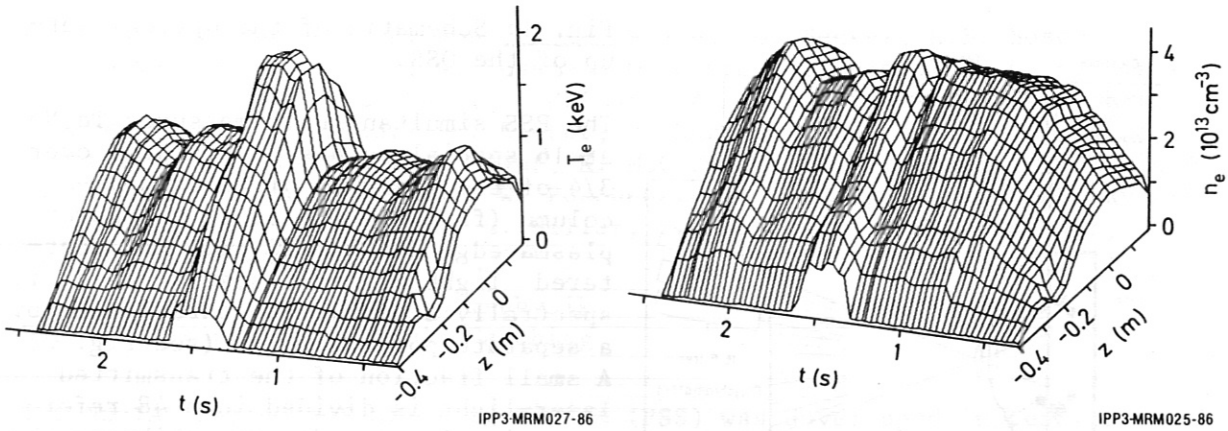

Fig. 3: Three-dimensional plots of Te and Ne of an ASDEX-discharge with Neutral Injection (P_{NI} = 3 MW). The behavior of Ne during Neutral-Injection indicates, that the discharge has changed from L- to H-regime.

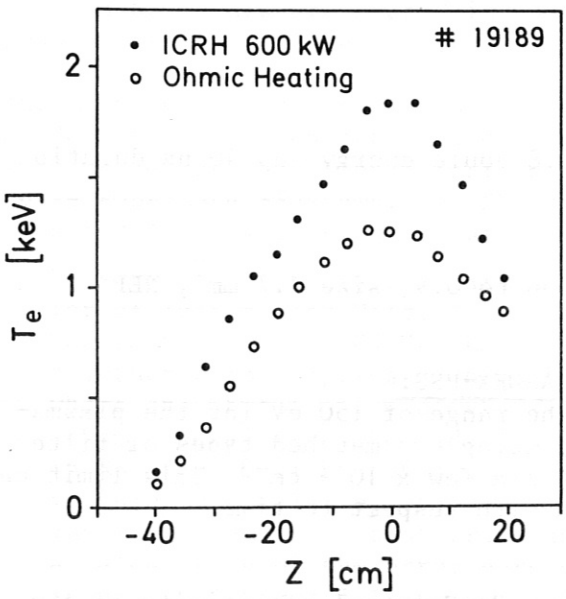

Fig. 4: Comparison of Te-profiles in an ASDEX-discharge during ohmic heating and during ICRH-minority heating (deuterium in hydrogen) with 600 kW RF-power.

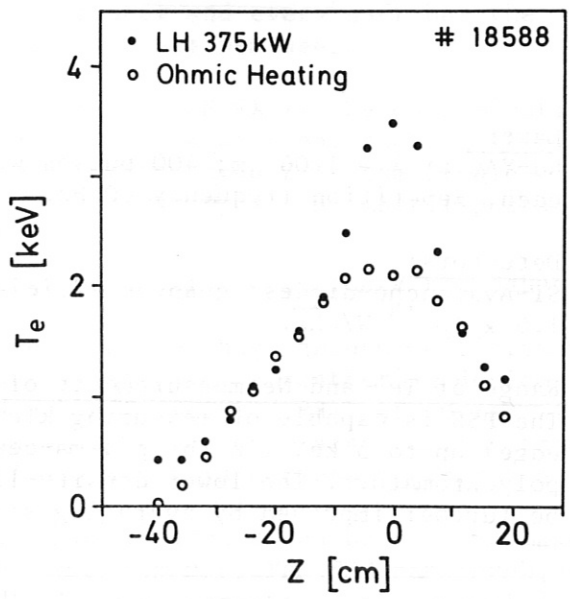

Fig. 5: Te-profile during LH-heating in ASDEX (open circles: ohmic profile before RF is switched on).

EVALUATION OF PLASMA-PARAMETERS DURING PELLET-INJECTION

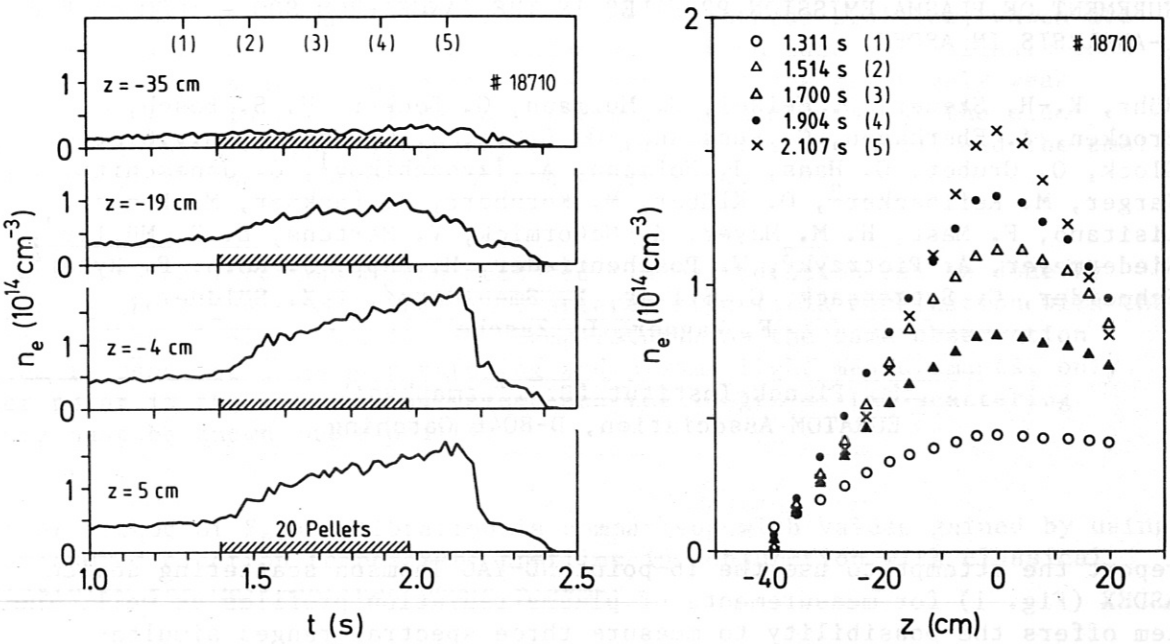

Fig. 6: Density increase of up to 1.5 x 10^{14} cm^{-3} by an injection of a series of pellets using a centrifuge. Time-evolution of Ne at different radii (Fig. 6a) as well as the corresponding Ne-profiles show, that the density raise occurs mainly in the plasma-centre, even when the pellet-injection has been discontinued.

The PSS-results are the basis for further calculations of plasma-parameters, e.g. heat-conductivity of electrons, diffusion-coefficients and so on. Profile measurements, which we have shown in a few examples, are necessary for any plasma-simulation by computer-codes or determination of the energy-balance of a Tokamak plasma. The PSS can deliver at present technical state the wanted parameters in a wide range of discharge-conditions.

References:

/1/ H. Röhr, K.-H. Steuer, G. Schramm, K. Hirsch, H. Salzmann, Nucl. Fus., Vol. 22, No. 8 (1982) 1099-1102.

/2/ H. Röhr, Phys. Letts., Vol. 81 A, No. 8 (1981) 451-53.

MEASUREMENT OF PLASMA EMISSION PROFILES IN THE RANGE FROM 800 - 1000 nm FOR Z_{EFF}-ANALYSIS IN ASDEX

H. Röhr, K.-H. Steuer, D. Meisel, H. Murmann, G. Becker, H. S. Bosch, H. Brocken, A. Eberhagen, G. Fussmann, O. Gehre, J. Gernhardt, G.v.Gierke, E. Glock, O. Gruber, G. Haas, J. Hofmann, A. Izvozchikov[1], G. Janeschitz, F. Karger, M. Keilhacker[2], O. Klüber, M. Kornherr, K. Lackner, M. Lenoci, G. Lisitano, F. Mast, H. M. Mayer, K. McCormick, V. Mertens, E. R. Müller[2], H. Niedermeyer, A. Pietrzyk[3], W. Poschenrieder, H. Rapp, J. Roth, F. Ryter[4], F. Schneider, C. Setzensack, G. Siller, P. Smeulders[2], F.X. Söldner, F. Wagner, D. Zasche

Max-Planck-Institut für Plasmaphysik
EURATOM Association, D-8046 Garching

We report the attempt to use the 16-point ND-YAG Thomson scattering device on ASDEX (Fig. 1) for measurements of plasma radiation profiles as well. The system offers the possibility to measure three spectral ranges simultaneously: 780 - 880 nm, 900 - 970 nm and 985 - 1020 nm.

The plasma light can be analysed in two different ways:

As the Thomson scattering system is only transparent to high-frequency signals because of the AC coupling of the avalanche diodes, direct measurement of the plasma light calls for a fast chopping technique. This is achieved by a special chopper wheel (Fig. 2) in front of the large observation lens which interrupts the plasma radiation fast enough (chopper frequency 3 kHz).

On the other hand, without the installation of the wheel, it is possible to determine the plasma radiation by analysing the radiation shot noise signal (Fig. 3) which is necessarily detected during each Thomson measurement.

Both of the two possibilities have been applied. The first has the advantage of delivering the time evaluation of radiation profiles. The installation of the chopper wheel in the present form, however, doesn't allow simultaneous measurements of the Thomson scattering, and the lack of n_e, T_e profiles prevents direct comparison of the measured radiation with bremsstrahlung in the same discharge.

The second method yields averaged results during selectable time intervals of the order of a few 100 msec or more. The calibration of the noise signals is done by illuminating the avalanche diodes by LED's with different intensities. Owing to the simultaneously measured Thomson scattering profiles this method allows comparison with actual bremsstrahlungs profiles.

---

[1]Academy of Sciences, Leningrad, USSR; [2]Present address: JET Joint Undertaking, England; [3]Univ. of Washington, Seattle, USA; [4]CEN Grenoble, France

The two methods show rough agreement of the brightness profiles, which are nearly the same in the 3 spectral channels. In both cases the signals show relatively large statistical errors. The reason is the relatively weak plasma radiation in the infrared and the poor transmission of the electronics even at a chopper frequency of 3 kHz, on the one hand, and the small amplitude of the noise signals, on the other hand.

The absolute calibration of the measured plasma radiation can be done by comparing the signals with Thomson scattered signals in combination with the corresponding electron density and temperature. As the same observation system is used for Thomson scattering and plasma light measurements, only laser power in the observation volume and the length of the scattering volume must be known additionally.

Another method of Z_{eff} calibration is comparison with values gained by using the measured electron temperature profiles in conjunction with classical resistivity for well-defined ohmic plasmas.

As an example, we show the brightness and Z_{eff} profiles before and after pellet injection in ASDEX. Figure 4 shows the time behaviour of the central electron density measured simultaneously by Thomson scattering. About 12 pellets are injected into the discharge between 1.4 and 1.8 sec. After pellet injection the density keeps the high value for about 0.3 sec without any gas puffing. Figure 5a shows the Abel-inverted radiation profile averaged over the 3 spectral channels in the ohmic phase (averaged from 0.5 - 1.3 sec), and Fig. 5b the profile in the high-density phase from 1.7 - 2.0 sec. The radiation increases by a factor of more than 20 and scales as $n^2/\sqrt{T}$ (bremsstrahlung). The scaling already indicates that there is no essential change of Z_{eff} due to pellet injection. The corresponding Z_{eff} profiles are shown in Fig. 6a,b.

The results show that combined measurement of Thomson scattering and plasma radiation profiles is possible and reasonable. In a new system, e.g. for ASDEX Upgrade, we include this method by adding a second exit with dc-coupling for measuring plasma radiation directly without the complications of high-frequency coupling.

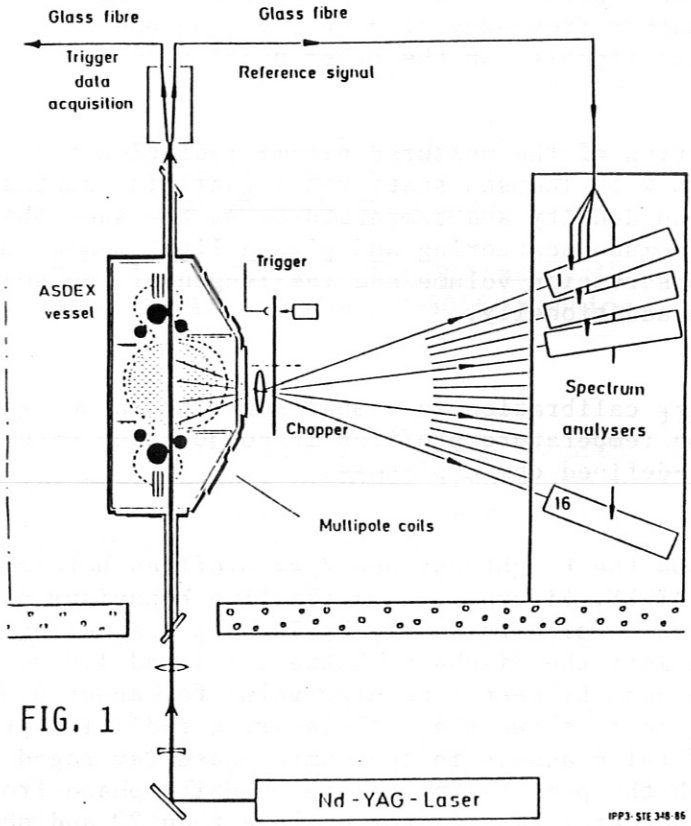

FIG. 1

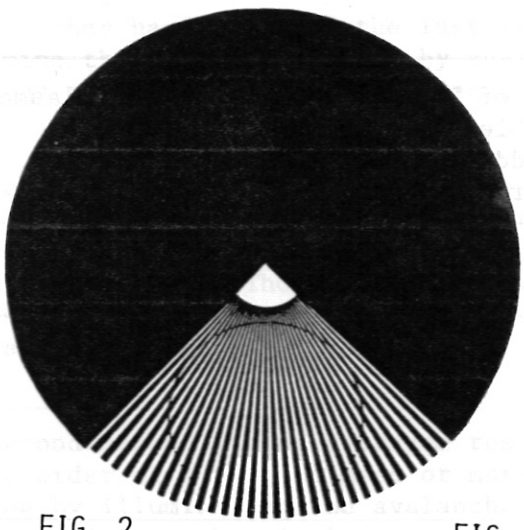

FIG. 2

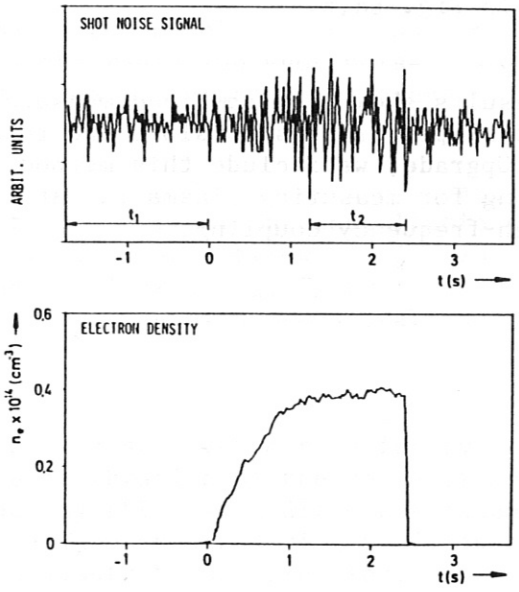

FIG. 3

PELLET INJECTION

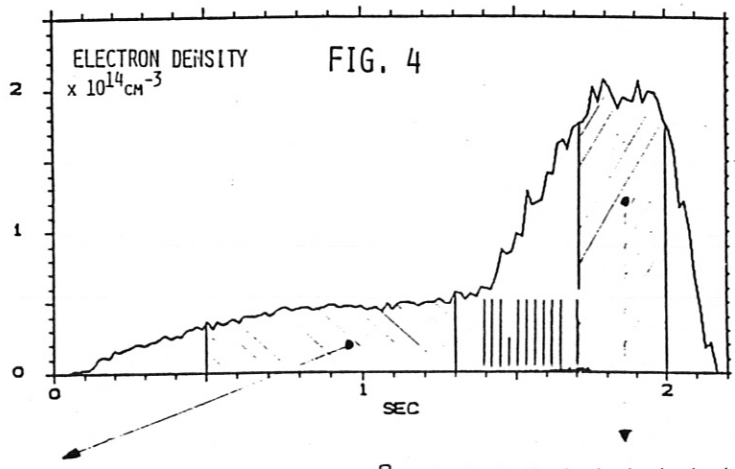

FIG. 4

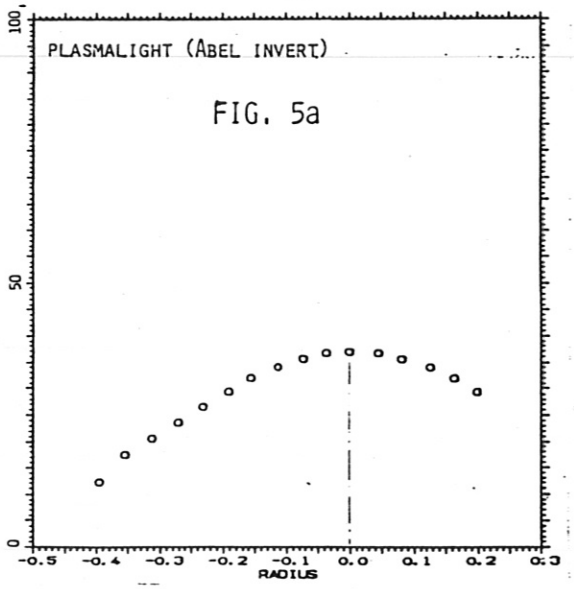

FIG. 5a

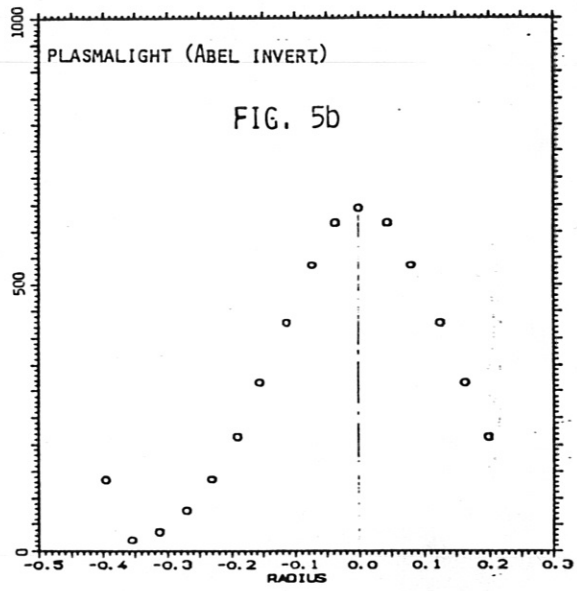

FIG. 5b

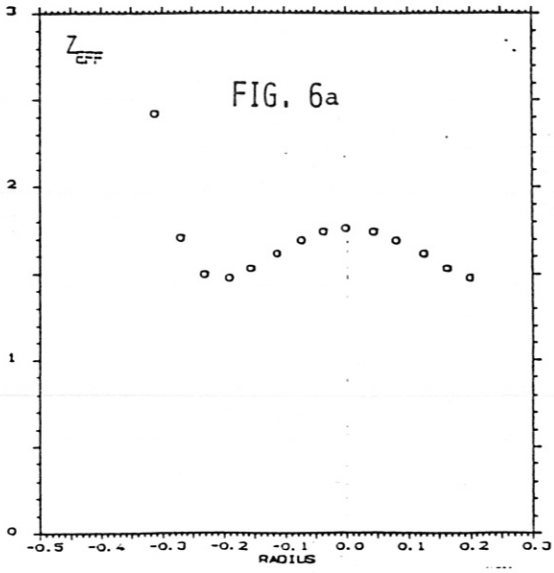

FIG. 6a

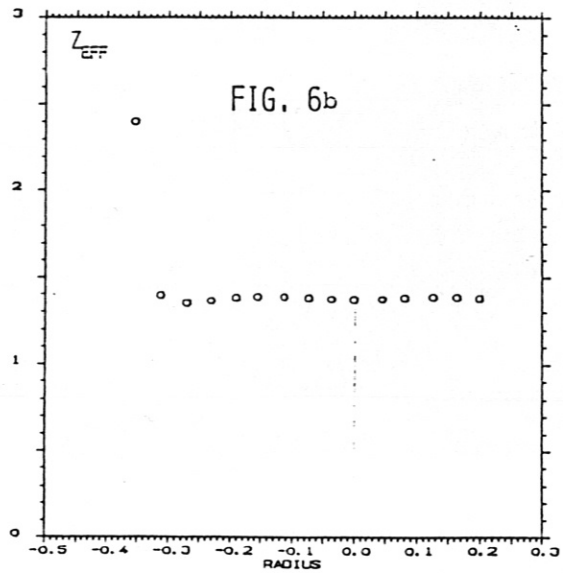

FIG. 6b

RATIO PLASMALIGHT / BREMSSTRAHLUNG